NASA ARMD Subsonic Fixed Wing Project

Acoustic Prediction Methodology and Test Validation for an Efficient Low-Noise Hybrid Wing Body Subsonic Transport

Final Report for NASA Contract Number NNL07AA54C

February 25, 2011

Compiled by

R.T. Kawai

Principal Investigator

Prepared for

NASA Langley Research Center, Hampton, VA

The Boeing Company

Boeing Research and Technology

Huntington Beach, CA

FOREWORD

This investigation was conducted by Boeing Research and Technology in Huntington Beach California for the Subsonic Fixed Wing Project, Fundamental Aeronautics Program in the Aeronautics Research Mission Directorate of the National Aeronautics and Space Administration. This investigation titled “Acoustic Prediction Methodology and Test Validation for an Efficient Low-Noise Hybrid Wing Body Subsonic Transport” was performed under NASA Contract Number NNL07AA54C during the time period October 1, 2007 through January 31, 2011. This contract was awarded under NRA NNH06ZEA001N, Amendment 4 Round 2 Appendix A.2 Topic A.2.4 – Hybrid wing/body Technologies released March, 2007. The investigation was a team effort led by Boeing Research & Technology with major contributions from NASA Langley Research Center, NASA Glenn Research Center, Massachusetts Institute of Technology, University of California Irvine, and United Technologies Research Center.

Any opinions, findings, and conclusions or recommendations expressed in this material are those of the author(s) and do not necessarily reflect the views of the National Aeronautics and Space Administration.

ACKNOWLEDGEMENTS

This document summarizes a contract conducted for the NASA Langley Research Center from October 1, 2007 through December 31, 2010 by Boeing Research & Technology, Huntington Beach, CA. The NASA LaRC COTRS were Florence Hutcheson for Aero Acoustics and Greg Gatlin for Low Speed Aerodynamics

The authors acknowledge the valuable contributions and information from:

NASA Langley Research Center:

Dr. Russell Thomas
Dr. Florence Hutcheson
Gregory Gatlin
Dr. Thomas Brooks
Harry Haskins
Craig Nickol
Casey Burley
Frank Quinto

NASA Glenn Research Center:

Jeffrey Berton
Hyun Dae Kim
William Haller
Scott Jones
Mike Tong
Dr. Robert F. Handschuh
James E. Bridges
Daniel L. Sutliff

The Boeing Company:

Principle Investigator.....Ron Kawai
BWB Chief Engineer.....Derrell Brown
BWB Program Manager .....Bob Liebeck
Aerodynamic Design .....Peter Camacho, Dave Bruns
Aerodynamic Performance .....Alan Okazaki, Ron Mairs
Vehicle Configurations.....Dick Odle
Computational Fluid Dynamics.....Dino Roman, Yoram Yadlin, Pichuraman Sundaram, Doug Friedman, Eric Unger
Stability and Control.....Dhar Patel
Mass Properties.....Tony Gonzales, Brandin Northrop, Bruce Kimoto
Wind Tunnel Definition.....Dave Pitera, Brian Sheen Gary Ige, Jan Murphy
Supplier Management.....Chris Garcia, Neal Harrison, Kevin Mcgann, Bob Welge, Gale Winans, Terry Monahan, Sam Gompsi, Janet Hewson
Business Manager.....Bill Vargo, Kris Monroe

Massachusetts Institute of Technology Gas Turbine Laboratory:

Professor .....Zolti Spakovszky
Graduate Students.....Leo Ng, Philip Andrew Weed, D. Colas, K. Strominger E. de la Rosa Blanco

University of California Irvine Mechanical and Aerospace Engineering Department:

Professor .....Dimtri Papamoschou
Graduate Student .....Salvador Mayoral

Changzheng Huang (postdoc)

Additional contributors .....Juntao Xiong and Sara Rostamimonjezi

United Technologies Research Center

Wind Tunnel Test Planning .....R.H. Schlinker, J.C. Simonich

TABLE OF CONTENTS

Appendices

SUMMARY

This investigation was conducted to: (1) Develop a hybrid wing body subsonic transport configuration with noise prediction methods to meet the circa 2007 NASA Subsonic Fixed Wing (SFW) N+2 noise goal of -52 dB cum relative to FAR 36 Stage 3 while achieving a -25% fuel burned compared to current transports (re :B737/B767); (2) Develop improved noise prediction methods for ANOPP2 for use in predicting FAR 36 noise; (3) Design and fabricate a wind tunnel model for testing in the LaRC 14 x 22 ft low speed wind tunnel to validate predictions; (4) Supplementary goal to assess low-speed characteristics of a very low noise HWB configuration.

In Phase I, a medium wide body cargo freighter was selected to represent a logical need for an initial operational capability in the 2020 time frame. MIT developed the starting point planform and airfoils for a configuration meeting ICAO Annex 14 Code E span limits from the CMI SAX 40. This starting point was refined by Boeing R&T to improve structural design and low speed characteristics. NASA GRC developed the propulsion data for 2020 technology engines. In Phase I, a N2A configuration with podded engine nacelles and a N2B with embedded engines using boundary layer ingestion inlets were sized and mission performance data developed with the Boeing Integrated Vehicle Design System (BIVDS). The N2A configuration was predicted to be able to meet the NASA SFW N+2 fuel burn goal based on a “clean wing” analyses and was +5.3dB off from meeting the noise goal, assuming high speed aero integration penalties would be negligible.

In Phase II Boeing refined the configuration with higher fidelity RANS CFD analyses for the integrated propulsion aerodynamic integration including the nacelle/pylon/hybrid wing body to assure the model represented an efficient transonic configuration. The Efficient Low Noise Hybrid Wing Body (ELNHWB) configuration N2A-EXTE was evolved to meet the circa 2007 NRA N+2 fuel burn and noise goals. The key features of the –EXTE configuration were moving nacelles aft and extending the centerbody trailing edge. UCI small scale tests made improvements in jet noise compression shielding and UCI developed a prediction method for partially shielding the axial and spatially distributed noise source from a jet. MIT developed a rapid diffraction turbomachinery noise shielding method of ANOPP2. BIVDS analyses for mission analyses and noise predictions by MIT incorporating the UCI results showed the N2A-EXTE can meet the N+2 fuel burn and noise goals. A fan pressure ratio study resulted in surpassing the fuel burn and noise goals by going to a geared turbofan but was judged to be EIS 2025 as to the EIS 2020 technology ground rule for this investigation.

The N2A-EXTE was used to define the Quiet Ultra Integrated Efficient Test Research Aircraft #1 (QUIET-R1) that is a 12 ft 5.8% scale wind tunnel model for noise and low speed aero testing in the LaRC 14 x 22 wind tunnel. The wind tunnel model is designed and built for testing configuration changes. The model is modular allowing for

variations of airframe noise shielding (positions of engine noise simulators, verticals, and elevons) and airframe noise sources (elevon angles, leading edge slat, and removable landing gear). Removable flow through nacelles are also designed and built for low speed aero testing.

Detailed model design and fab was under a subcontract to ATK in Tullahoma TN. UTRC reviewed the test objectives and provided recommendations for acoustic testing in the 14 x 22 wind tunnel.

1.0 INTRODUCTION

This is the final report for NASA Contract Number NNL07AA54C. This NASA contract activity was conducted towards developing technologies towards meeting the NASA Aeronautics Research Mission Directorate (ARMD) goals for future transport aircraft. This contract was awarded under the Reference 1 NRA NNH06ZEA001N, Amendment 4 Round 2 Appendix A.2 Topic A.2.4 – Hybrid wing/body Technologies. The contract was under the NASA Fundamental Aeronautics Program Subsonic Fixed Wing (SFW) Project towards meeting the N+2 goals that were being in place when the contract was initiated. The objectives are: (1) to define a representative Hybrid Wing Body (HWB) capable of meeting the NASA N+2 goals for a cum -52dB relative to FAR 36 Stage 3 and -25% fuel burn relative to B737/767 technology (2) improve ANOPP2 noise prediction methods with propulsive noise shielding; and (3) design and fabricate a low noise highly fuel efficient scale model for NASA to conduct acoustic and low-speed aerodynamic wind tunnel tests in the NASA Langley 14 x 22 ft low speed wind tunnel to validate noise prediction methods and determine the low speed aero characteristics of the efficient low noise HWB configuration.

This activity was led by Boeing Research & Technology (BR&T) with the NASA Langley Research Center (LaRC) as the technical monitor. NASA Glenn Research Center (GRC) developed the propulsion data. University of California Irvine (UCI) developed the prediction for jet noise with shielding using noise source compression. Massachusetts Institute of Technology (MIT) conducted the noise assessment relative to FAR 36 including use of the MIT developed turbo machinery noise shielding module for ANOPP2. The investigation was conducted in 2 Phases. Phase I developed the initial configuration concepts with noise shielding prediction methods by UCI and MIT. Phase II conducted higher fidelity refinements for the N+2 HWB configuration and noise prediction methods from which a low noise efficient HWB wind tunnel model was fabrication by ATK as the model supplier. United Technologies Research Center (UTRC) has provided recommendations related to the planned acoustic testing in the 14 x 22 wind tunnel.

UCI, MIT, and UTRC final reports are Appendices A, B, and C to this report.

2.0 N+2 CONFIGURATION DEVELOPMENT

2.1 SFW N+2 Requirements

2.1.1 Goals

The HWB configuration was evolved to meet the circa 2007 NASA Subsonic Fixed Wing project N+2 goals shown in Figure 1 with an Entry Into Service (EIS) year 2020.

	"N+1" Generation Conventional 2012-2014	"N+2" Generation Hybrid Wing 2018-2020
Noise (cum below Stage 3)	- 42 dB	- 52 dB
Emissions (LTO NOx) (below CAEP/2)	- 70%	- 80%
Performance: Aircraft Fuel Burn (relative to 737/CFM56)	- 15%	- 25%

Figure 0 NASA Subsonic Fixed Wing N+2 Amendment 4 Goals

This investigation focused on the noise and fuel burn goals. The reduction in NOX using the CAEP index is based on thrust and this technology is being developed by the engine manufacturers. The fuel burn evaluation is being based on an equivalent technology reference because then study size is a larger aircraft. The Blended Wing Body (BWB) type of Hybrid Wing-Body (HWB) airplane configuration was selected because of a large background knowledge base where past studies have shown fuel burn improvements exceeding 25% for equal payload-range. The BWB eliminates the empennage and, with body lift, has a better span-wise load distribution than a conventional tube-and-wing configuration. The BWB type configuration has inherently lower noise characteristics and, based on the NASA study that established the N+2 goal, a large noise reduction potential should result by employing airframe shielding of propulsion noise. Improved noise prediction methods are needed to optimize propulsion/airframe integration. For this MIT and UCI were tasked with developing improved noise prediction methods when employing noise shielding.

2.1.2 Mission Requirements

Boeing continually updates a market outlook for the purposes of product development strategy. During Phase I, the BR&T N+2 team reviewed this forecast and noted that the demand for cargo air traffic was forecast to grow at a higher rate than passenger airliners. This Boeing forecast from Reference 2 is shown in Figure 2. Airbus has published similar forecasts in Reference 3.

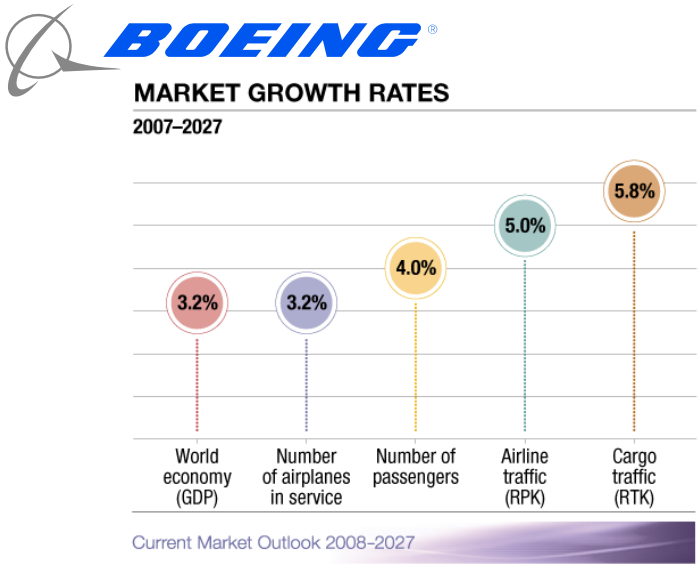

Figure 2 Air Cargo Growth Forecast Greater than Passenger Growth

A very quiet hybrid wing body airplane would enable night operations into noise sensitive airports, which in combination with market elasticity from improved economics, would further stimulate cargo growth requiring more such aircraft. Furthermore, a cargo freighter does not have perceived issues with ride quality or limited number of windows for a hybrid wing type of configuration. It was judged to be reasonable that a new aircraft, designed for very low noise deliverable in the 2020 timeframe, would be a cargo freighter with potential dual use as a military platform. Therefore a cargo freighter was selected as the 'N+2' metric base. The vehicle mission parameters were determined using the international average Freight Tonne Miles (FTK's) projected in the 2026 timeframe. This information, illustrated in Figure 3, shows that cargo air traffic growth is heavily dominated by international trade with nearly 50% of all traffic being Asia-US and Asia-Europe routes. Previous studies with inputs from cargo operators had shown appropriate design range for these routes to be between 5500 and 6000-nm. Some of the city pairs (range w/85% annual winds) are Anchorage – Narita (3,250 nm), Hong Kong – Anchorage (4,400 nm), Charles de Gaul – Memphis (4,400 nm), Anchorage – Hong Kong (4,400 nm), Rome – LAX (5,900 nm), and Singapore – Amsterdam (6,000 nm). The SAX-40 with its large internal fuel volume is ideal for these long routes.

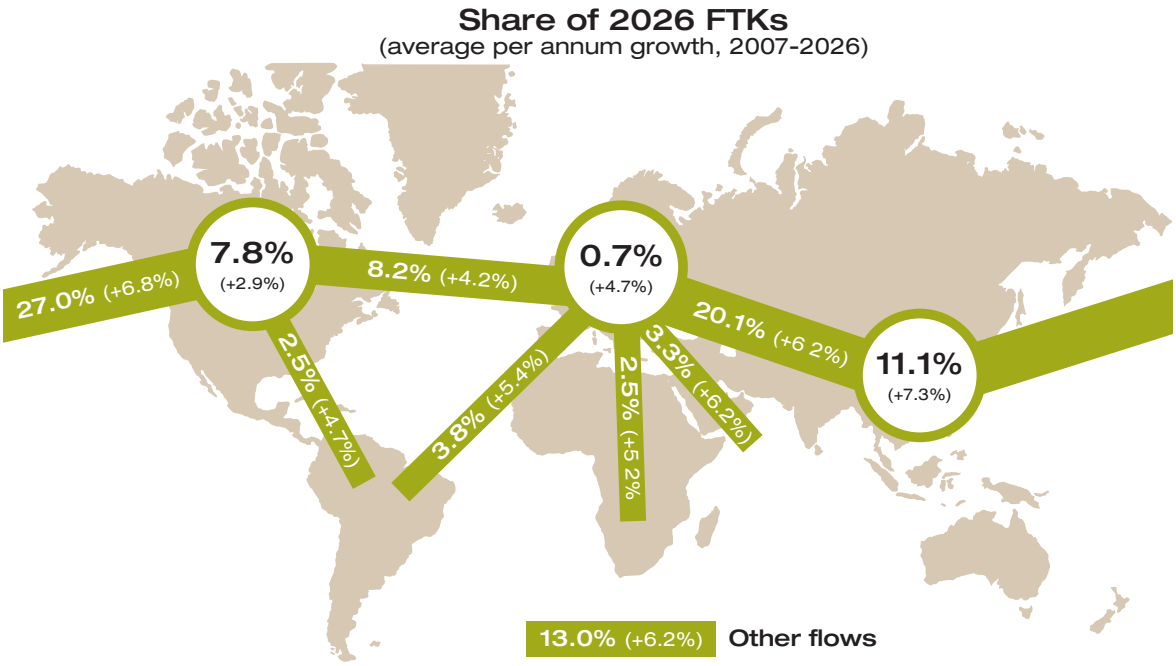

Figure 3 Majority of International Freight Traffic is Between the US and Asia

The requirements drawn from these sources and Boeings McDonnell Douglas heritage knowledge of air traffic needs concluded:

- Payload of 100,000 pounds
- Range of 6,000 nm
- Initial Cruise Altitude (ICA) 35,000ft or higher
- Time to Climb to 31K ft no greater than 30 minutes
- Cruise Mach number of 0.8
- Field length of 10,000 ft or less

The NASA NRA required that all results be open, and therefore the Cambridge MIT Institute (CMI) SAX-40 (Reference 4), a non-proprietary configuration, was provided by MIT as the starting point. The SAX-40 was developed for an EIS of 2025 under the United Kingdom sponsored Silent Aircraft Initiative (SAI) over a 3-year period. 2 concepts were derived from the SAX-40 for an earlier time frame EIS of 2020. A low risk version designated a the N2A with podded engines, and the other retaining the SAX 40 type embedded engines designated as the N2B.

2.2 Design Process and Tools

2.2.1 Boeing Integrated Design System

The Boeing Integrated Vehicle and Design System (BIVDS) tool suite provided the means to perform vehicle sizing, assess performance, and execute trade study tasks.

As a Boeing Research & Technology (BR&T) standard tool, BIVDS is routinely applied to current and advanced aircraft configurations as part of internal and contracted research and development studies. The modules selected from the tool suite library and applied to the study are empirical or physics-based, depending upon the maturity level of the technology being assessed. BIVDS represents Boeing best practices, and is built on a modern multi-platform integration framework drawing upon selected tools from Boeing and from company mergers, heritage McDonnell Douglas and North American Rockwell.

BIVDS incorporates the tools that perform the design synthesis and analysis process, shown in Figure 4. After populating the database with aerodynamic, propulsion, and mass properties information, the vehicle is "flown" through the design mission profile from takeoff to landing. The takeoff gross weight, wing area, and engine thrust can be scaled to meet field length requirements for both takeoff and landing with engine out, fuel volume required, and landing approach speed. Takeoff, climb-out, and approach landing flight path data are also calculated to FAR 36 rules for noise assessments.

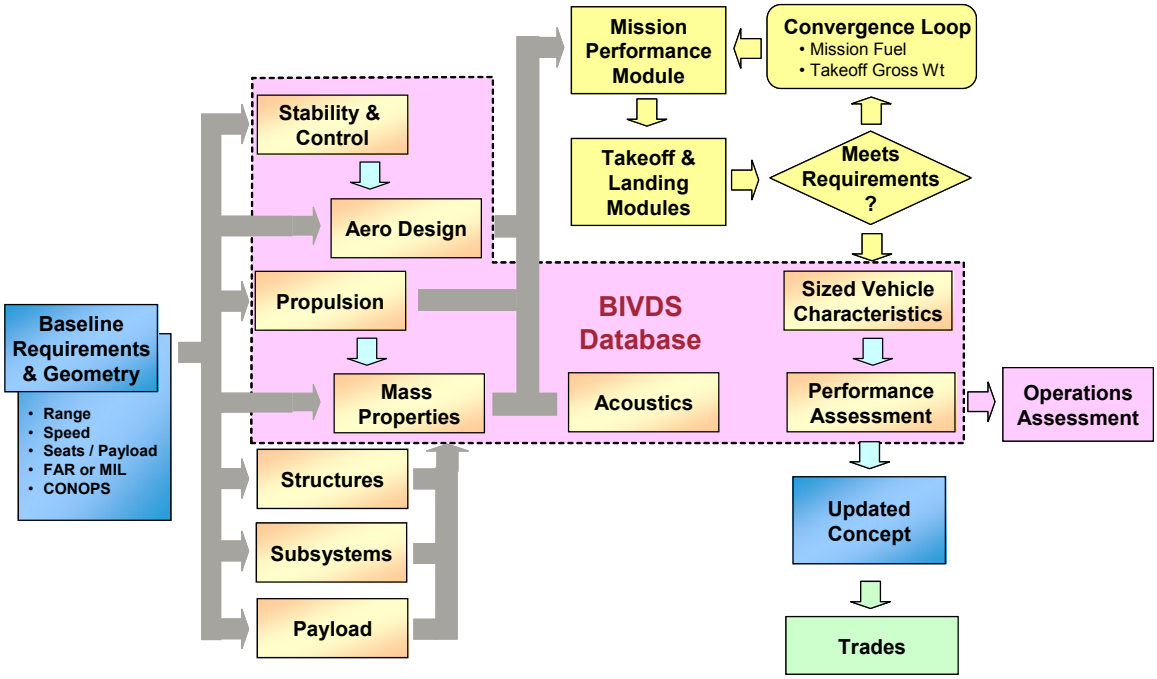

Figure 4 Air Vehicle Integrated Design Synthesis and Analysis Process

The geometric definition of the vehicle was generated using Unigraphics NX5. This includes generation of a vehicles rough Outer Mold Line (OML) and internal and structural arrangement.

BR&T proprietary mass properties methodology includes sensitivities to geometric and load parameters for the concomitant level of analysis under consideration. These tools are continuously updated and calibrated with new methods and with data from actual vehicles and from higher fidelity substructures and subsystems analyses.

BR&T heritage performance routines are based on K5JA (Mission Performance), J5G2 (Takeoff), B4RB (Landing), and the F2SC (Flight Path for Acoustics) programs.

BR&T uses existing engine decks when appropriate or substitutes parametric engine decks where needed. For this study, five different engine decks were used; four for the N2A configuration and one for the N2B configuration. These engine decks were created from the data files for 2020 technology engines developed by NASA GRC. NASA GRC developed the engine definition and performance using the NASA Numerical Propulsion System Simulation (NPSS) that is a standard tool used by engine companies.

2.2.2 Field Length

Field length was evaluated for Engine-Out Balanced Field and All-Engine takeoff conditions. The FAR rules observed for this study are summarized in Figure 5 and Figure 6. Additional requirements not shown in the figures include a sea level standard day plus 27°F. No credit/decrement was taken for head/tail winds or runway gradients.

- **$V_1 = V_{EF}$ + (Recognition and Reaction Time) = V_{EF} + 1 second**
- **$V_1 \geq V_{MCG}$; $V_1 \leq V_R$ or V_{MBE}**
- **V_R must at max rotation rate provide $V_{LOF} \geq 1.1\ V_{MU\text{-}AE}$ and $V_{LO} \geq 1.05\ V_{MU\text{-}EO}$**
- **V_2 = Engine Out Speed at 35 foot height**
- **$V_{2min} \geq 1.13\ V_{SR}$ and $V_{2min} \geq 1.1\ V_{MCA}$**

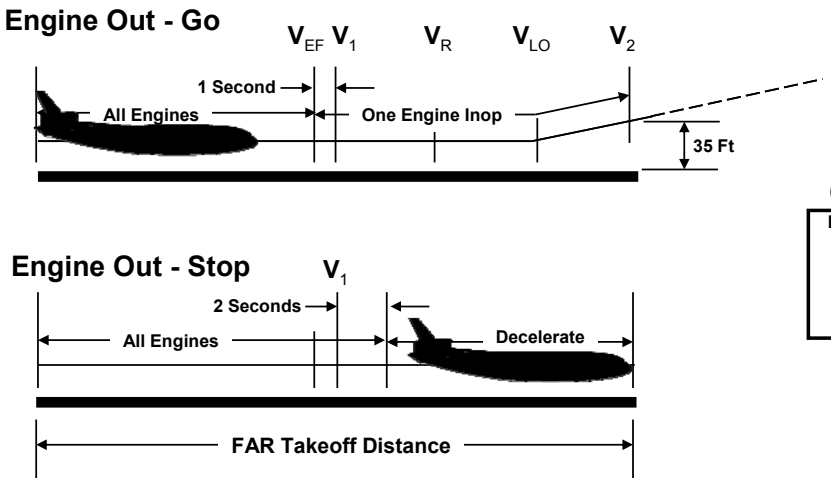

Climb Gradients Out of Ground Effect

Engines	Gear Down V_{LO}	Gear Up V_2
4	0.5%	3.0%
3	0.3%	2.7%
2	Positive	2.4%

Figure 5 FAR Engine-Out Takeoff Performance Rules

- **V_R must be the same for both All Engine and Engine Out cases**
- **Takeoff Field Length is the largest of:**
  - 115% of All Engine distance to 35 feet
  - Engine Out Distance to 35 feet
  - Engine Out Accelerate - Stop Distance
  - All Engine Accelerate - Stop Distance

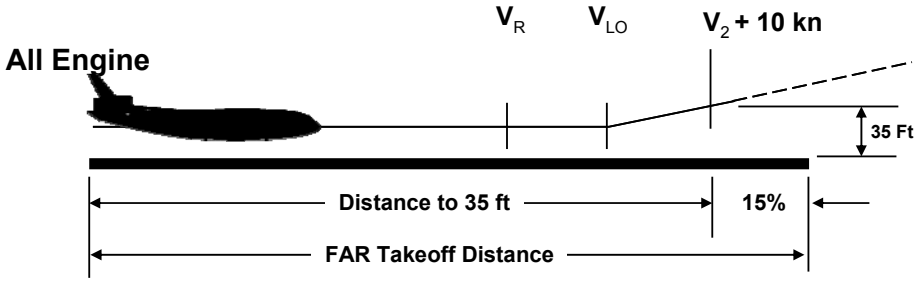

Figure 6 FAR All-Engine Takeoff Performance Rules

2.2.3 Fuel Efficiency

Mission performance was evaluated assuming US Standard Day atmospheric conditions, zero wind, and FAR rules for a westbound IFR altitude sequence. A definition of the mission profile for Phase I, including reserves, is presented in Figure 7. In Phase II, it was assumed that the Next Generation Air Transportation System (NGATS) would be in place and new aircraft would incorporate the navigations systems that would allow continuous climb cruise. Continuous Climb Cruise (CCC) offers 2 benefits. CCC improves fuel efficiency by cruising at the best Breguet factor, i.e. maintaining the best M x (L/D) / SFC and also benefits transonic propulsion/airframe integration by cruising at a higher continuous inlet mass flow ratio. Continuous operation at a higher average inlet mass flow ratio reduces the inlet spillage flow that occurs with a reduced power setting as fuel is burned off and gross weight drops if constant altitude cruise is used. This allows designing for a reduced inlet cowl thickness and reduces flow in the nacelle/pylon/centerbody channel making in easier to avoid strong shocks on the cowling and in the channel.

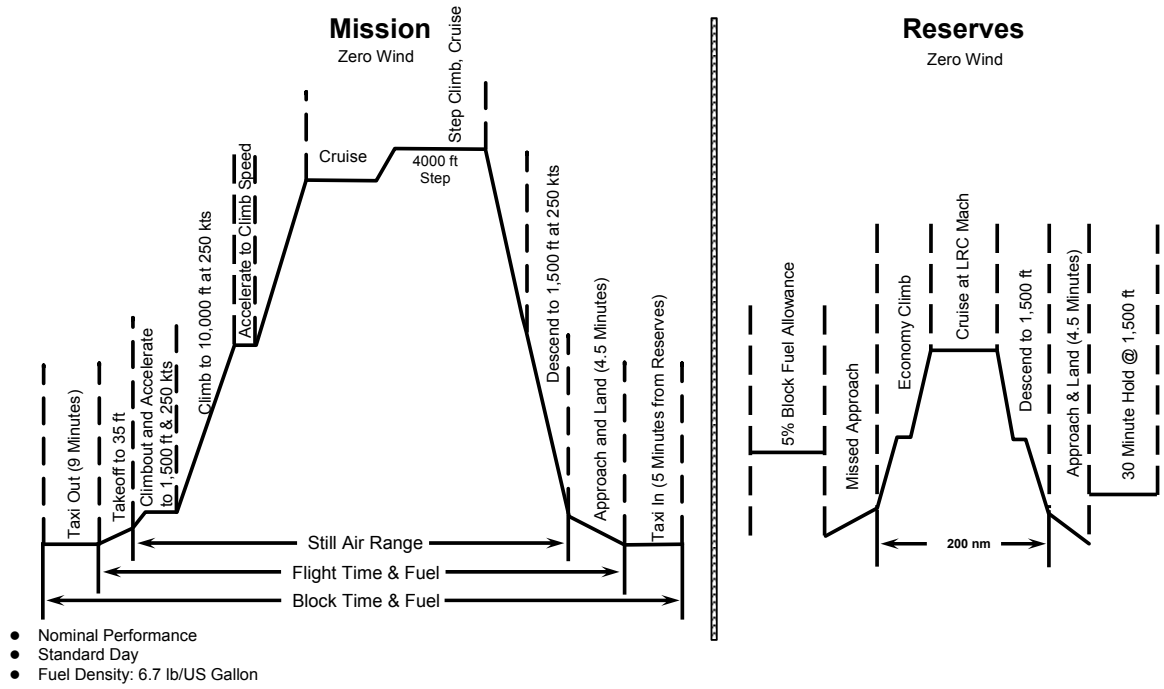

Figure 7 Mission and Reserve Profile

2.2.4 Flyover Noise

The estimation on FAR 36 noise was accomplished by the team with BR&T providing the configuration definition and flight profiles. Noise estimates were then made by the team as depicted in Figure 8.

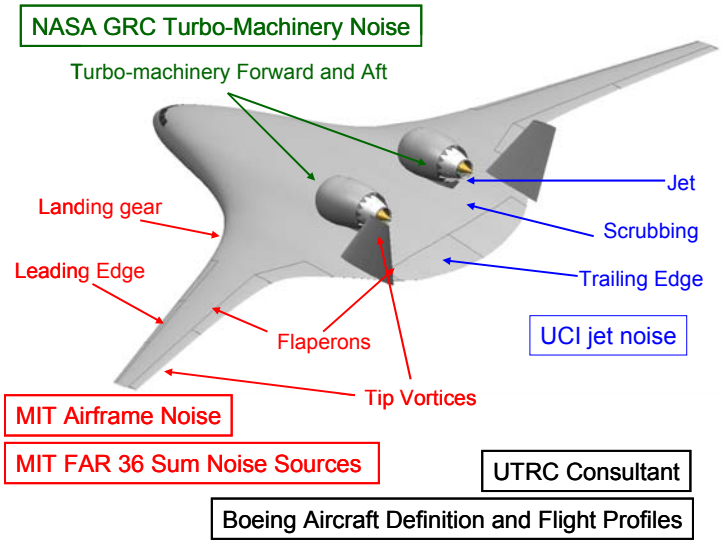

Figure 8 Noise Prediction Team

Jet noise prediction methods incorporating exhaust nozzles designed to enhance jet noise shielding were evolved in Phase I and refined in Phase II. UCI conducted small scale model tests showing that jet noise is spatially distributed and directional for which there was no method available to adequately predict jet noise shielding. Small scale model tests were therefore conducted and used as the basis for improving jet noise shielding and developing a jet noise shielding prediction method. This prediction method was initiated in Phase I with continuing development in Phase II. UCI provided the shielded jet noise estimates to MIT. The UCI work is documented in Appendix A.

Overall noise estimates for FAR 36 were made by MIT using ANOPP based methods supplemented were necessary. A rapid turbo-machinery noise shielding method for ANOPP2 was developed by MIT and used. Detailed description of the method and results are described in Reference 5 Appendix C for Phase I and in Appendix B of this report for Phase II.

2.3 Phase I Configurations

A fuel efficient HWB was synthesized and evaluated using the Boeing Integrated Vehicle Design System. Phase I was at fidelity Level 1. This Level 1effort used a concept design level drag build up based on the summation of airframe and propulsion components to determine the potential efficiency for a good design. These Phase I

estimates were without propulsion/airframe integration analyses. An initial assessment determined that refinements were needed to minimize the nacelle/pylon/centerbody integrated transonic drag. Phase II conducted RANS CFD based propulsion/airframe aero integration analyses including power on to refine the podded configuration to minimize transonic drag.

Reducing noise, particularly for flyover and sideline, is limited by the aft engine noise floor. Two approaches towards lowering the aft noise floor were investigated. One was to locate the nozzle exit forward of the HWB trailing edge for aft noise shielding. This approach uses podded nacelles (i.e. bottom pylon-mounted). The other was using a low fan pressure ratio with a core flow mixer nozzle in a long fan duct with extensive acoustic treatment. . This later approach was taken in the Silent Aircraft Initiative SAX-40.

These two approaches were investigated based on technologies for 2020 initial operational capability as to the later 2025 technologies in the CMI SAX 40. Operational capability in 2020 assumed a need to be at TRL 6 by 2011-2012 for a TRL 7 flight demonstration to precede a 7-year span from initial market exploration through flight development and certification for an all new advanced concept airplane. The configurations are identified as N2 for the N+2 goals with the podded engines identified as N2A and the embedded engines as N2B.

As shown in Figure 9 the CMI estimate in the SAI program was for a cumulative -81 EPNdB, with the flyover at -29 EPNdB. The NASA goal is also shown in the figure, for which the -52 EPNdB has a -18 EPNdB flyover.

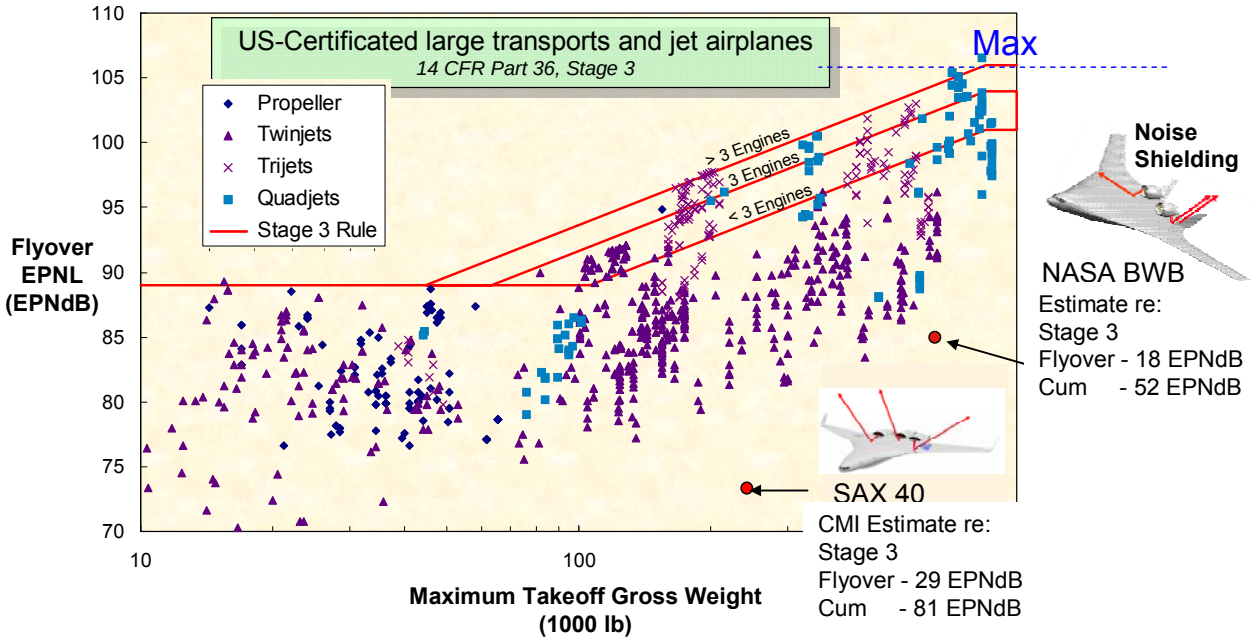

Figure 9 HWB Predicted Low Noise Potential

The CMI SAX-40 incorporated a novel concept employing a cambered forward center-body that increased the forward lift so that the outer wing airfoils could be more highly

aft-loaded (supercritical type) and still be trimmed at cruise without undue drag from pitch trimming with elevon. This, in turn, allowed a lower sweep with a thicker but lighter outer wing. This concept was incorporated into the Efficient Low Noise Hybrid Wing Body (ELNHWB) configuration identified as N2, used to meet the N+2 noise and fuel burn goals. The SAI very low noise level was achieved employing technologies judged to be beyond the time frame for this study and also used a steep approach that is not included in FAR 36 which specifies a 3^{o} glide slope. The GRANTA engine concept in the SAX 40 employed vectoring/reversing variable area nozzles with 60% changes in area to match with continuous modulation during take-off to maximize thrust for acceleration while reducing fan pressure ratio after lift off to reduce sideline and flyover noise. The vectoring was used for pitch trim to lower elevon deflection noise. In this investigation, conventional propulsion and flight control characteristics were assumed to determine airplane configuration design methods for low noise as opposed to employing and evaluating operational procedures.

Noise prediction elements in the SAI assessment were also proprietary. For non-proprietary noise prediction methods development, the NASA Aircraft Noise Prediction Program (ANOPP) was the logical base with propulsion source noise data from NASA GRC.

2.3.1 Evolving Configurations

The initial SAX-40 cargo aircraft from MIT had a wingspan of 221.6 feet. To be competitive, for 2020 this size class vehicle should operate from ICAO Annex 14 Code E airports. The wing span was therefore reduced to 65 meters to be within the Code E airport limit. The revised design, referred to as the SAX-40F is shown in Figure 10 with a wing span of 213 feet. As part of this revision, the mission was established at 103,000 pounds payload for a range of 6,000 nm. This payload was based on the interior volume available for containers with an average density of 8 lbs/cubic ft on the upper deck and 10 lbs/cubic ft in the lower deck. MIT conducted an analysis of the revised configuration, working with Boeing, which is now identified as N2 for the N+2 noise goal and specifically as N2A for podded engines and N2B for embedded engines.

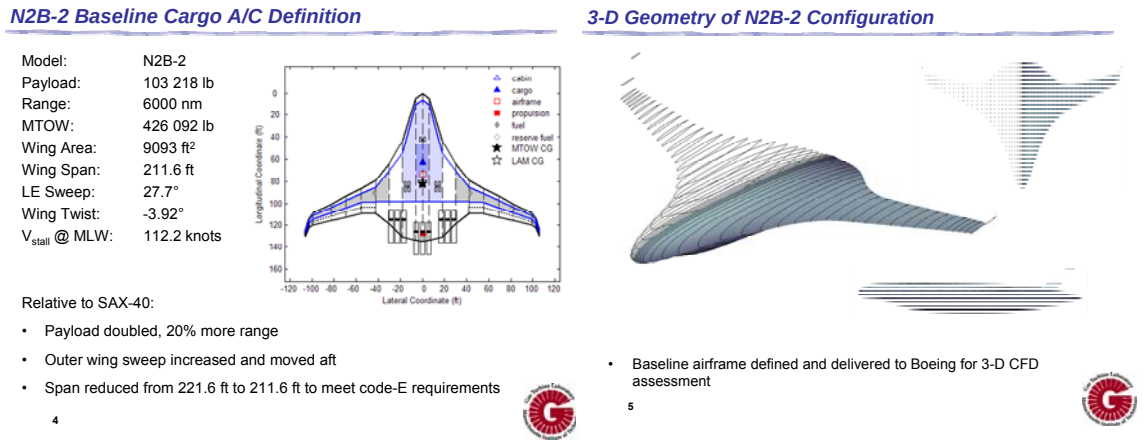

Figure 10 SAX-40F Configuration

The initial geometry for these study aircraft was transmitted to Boeing from MIT via IGES and STEP files. These files were utilized in Boeing's UniGraphics CAD system, versions NX4 and NX5. An "airfoil stack" was used to loft the "clean wing." The stack is derived from 20 to 24 chord-wise sections across the semi-span. The term "clean wing" means the wing only, without winglets, verticals, or propulsion system. The clean wing geometry was analyzed and initial L/D, spanload, and pitching moment characteristics were determined by a Reynolds Averaged Navier-Stokes (RANS) Computational Fluid Dynamics (CFD) analysis using the CFL3D code. The reference quantities used for the analysis are shown in Figure 11.

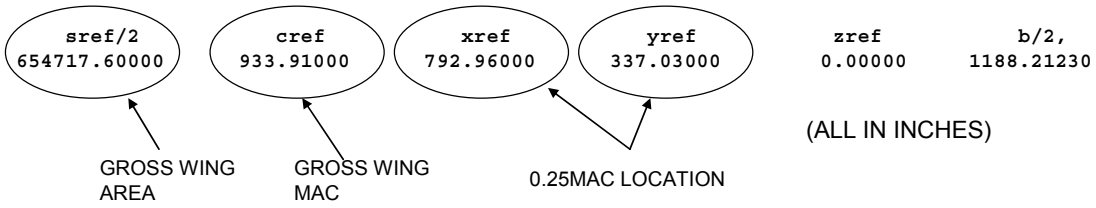

NOTE:
MOMENT REFERENCE FOR AERO DATA IS AT THE CG, 46%MAC
AERO DATA SHOWN FOR RN_{mac}=119.2M (M=0.8/40KFT)

Figure 11 Reference Quantities Used for Initial SAX-40F CFD Analysis

The initial airfoil stack had an untrimmed cruise L/D of 23.5 at a Mach number of 0.80 and C_L=0.27 as illustrated in Figure 12.

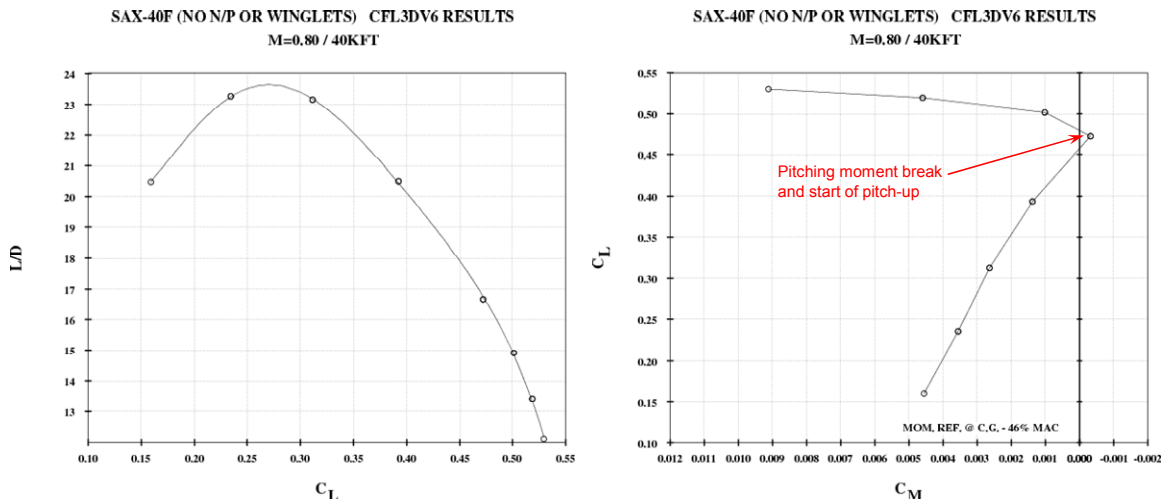

Figure 12 Lift-to-Drag Ratio and Pitching Moment from Initial SAX-40F CFD Analysis

The analysis revealed a drag divergence Mach number of 0.83 seen in Figure 13. This indicates a higher Mach capability than required. The pitching moment curve shows a stable configuration with more than adequate buffet margin, where buffet is assumed to occur at the pitching moment break. Based on past experience with blended

configurations, trimming effects are estimated to be negligible and can be addressed through careful tailoring of airfoil shape and spanload.

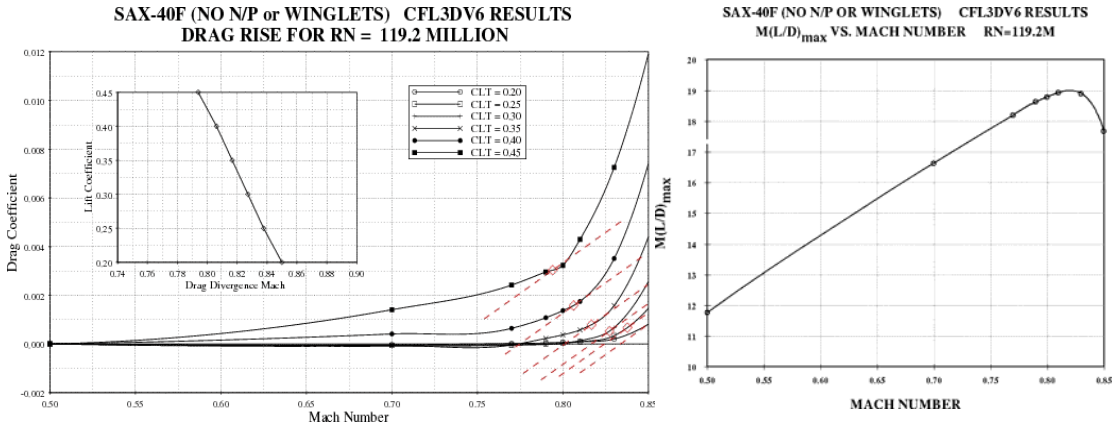

Figure 13 Mach Number Capability of SAX-40F

These higher order CFD results are compared to those of a quasi 3-D method in Figure 14. Based on the figure, the quasi 3-D Method is adequate for design space exploration and baseline definition.

Comparison: Quasi-3D Method vs CFL3DV6

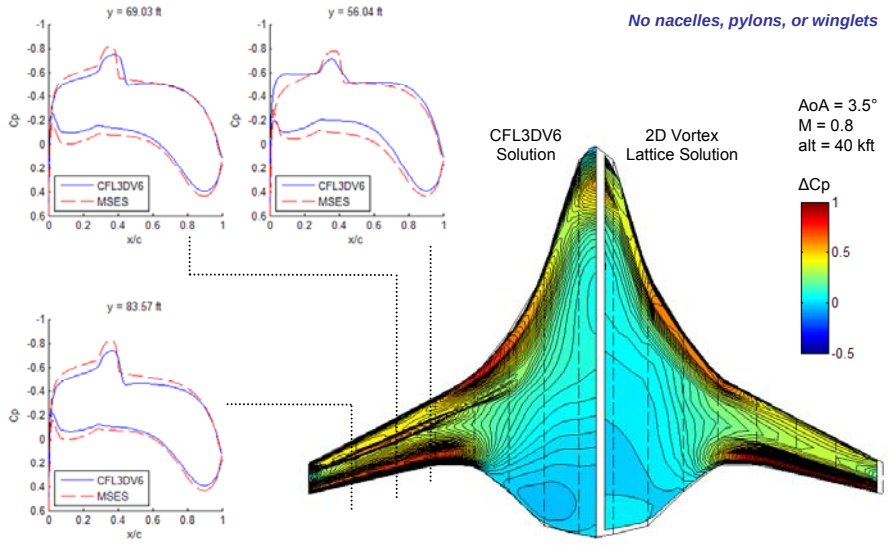

7

Lift / Drag Comparison: Quasi-3D Method vs CFL3DV6

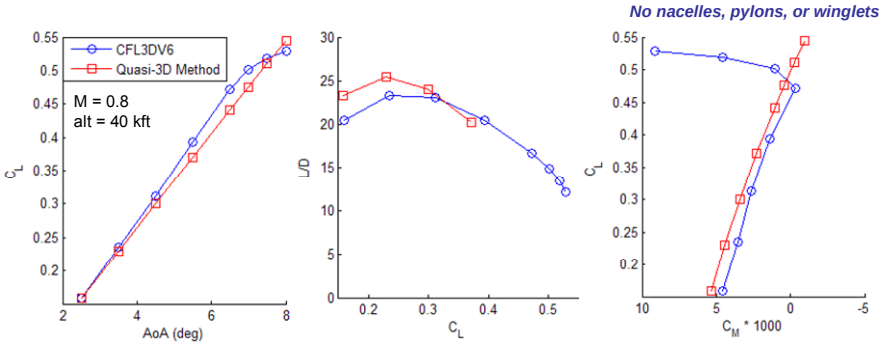

- CL and L/D trends agree, 10% over-prediction in max L/D by Q3D method
- Aircraft is statically stable for C_L upto 0.47 - pitching moment break not captured by Q3D method
- Overall, Q3D method adequate for design space exploration and to set baseline N2B-2 configuration

8

Figure 14 Comparison to Quasi-3D Method

Low Speed C_{Lmax} was estimated using a Boeing higher-order panel method (DACVINE) coupled with an empirically derived method for predicting C_{Lmax} known as the Pressure Difference Rule Figure , shows the clean wing can sustain an untrimmed C_{Lmax} of 0.7 at 13 degrees angle of attack. A simple 17.5% chord, 30-degree drooped leading edge slat extending from 33.5% span outboard increases the C_{Lmax} capability to slightly over 1.0 at 20 degrees angle of attack. Based on past experience with blended configurations, this level is deemed to be adequate. Note that a 20 degree deflection is not sufficient to protect the wing leading edge. A concern that is evident from the Figure 15 is that the entire outboard wing becomes critical at the same time which could lead to severe pitch-up. This issue can be addressed through leading edge droop, leading edge radius modification and/or spanload tailoring.

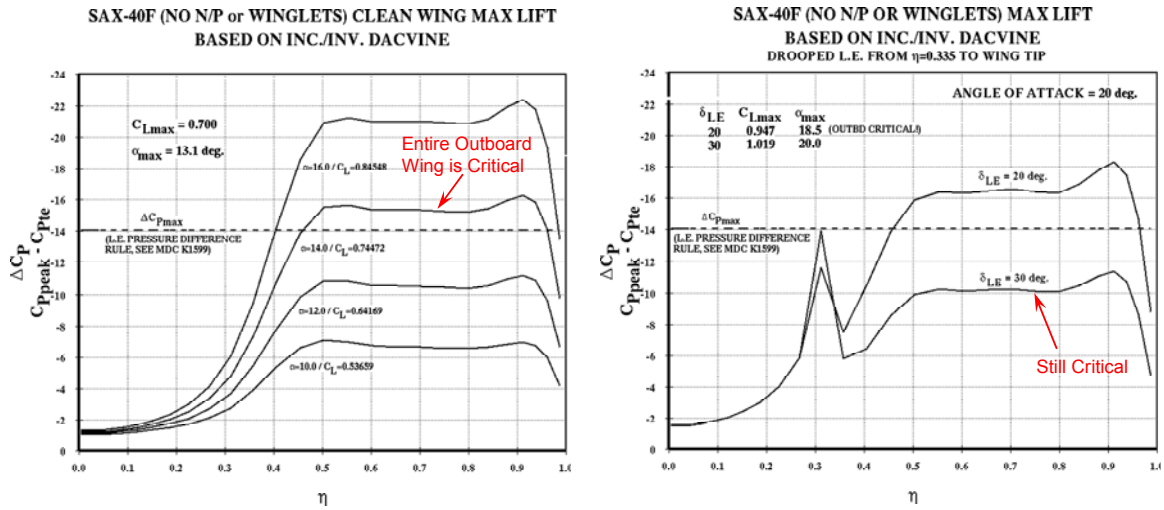

Figure 15 Low Speed C_{Lmax} Capability

While this initial configuration satisfies the most basic requirements, as shown above, and is a viable configuration for further development, several issues were uncovered that needed to be addressed before further design work was done. As shown in Figure 16, the average outboard wing thickness-to-chord ratio of 0.07 is extremely low which was deemed unsatisfactory from a practical structural standpoint and has aerodynamic implications. While a thin wing will improve high speed cruise performance as shown, it will also add unnecessary weight to the configuration and could effect low speed/high lift characteristics. Recall that the entire outboard wing is critical in the C_{Lmax} analysis discussed previously. Accordingly, the outboard wing thickness was increased to 8.5% based on past experience with blended configurations.

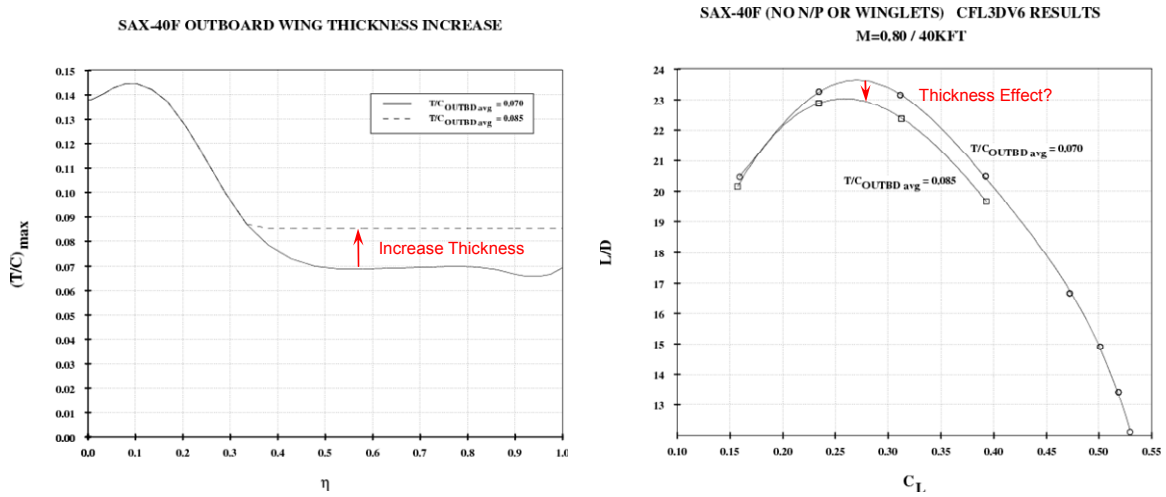

Figure 16 Increased Thickness Effect

Another anomaly discovered was a curvature discontinuity on the upper and lower surface of the wing, Figure 17.

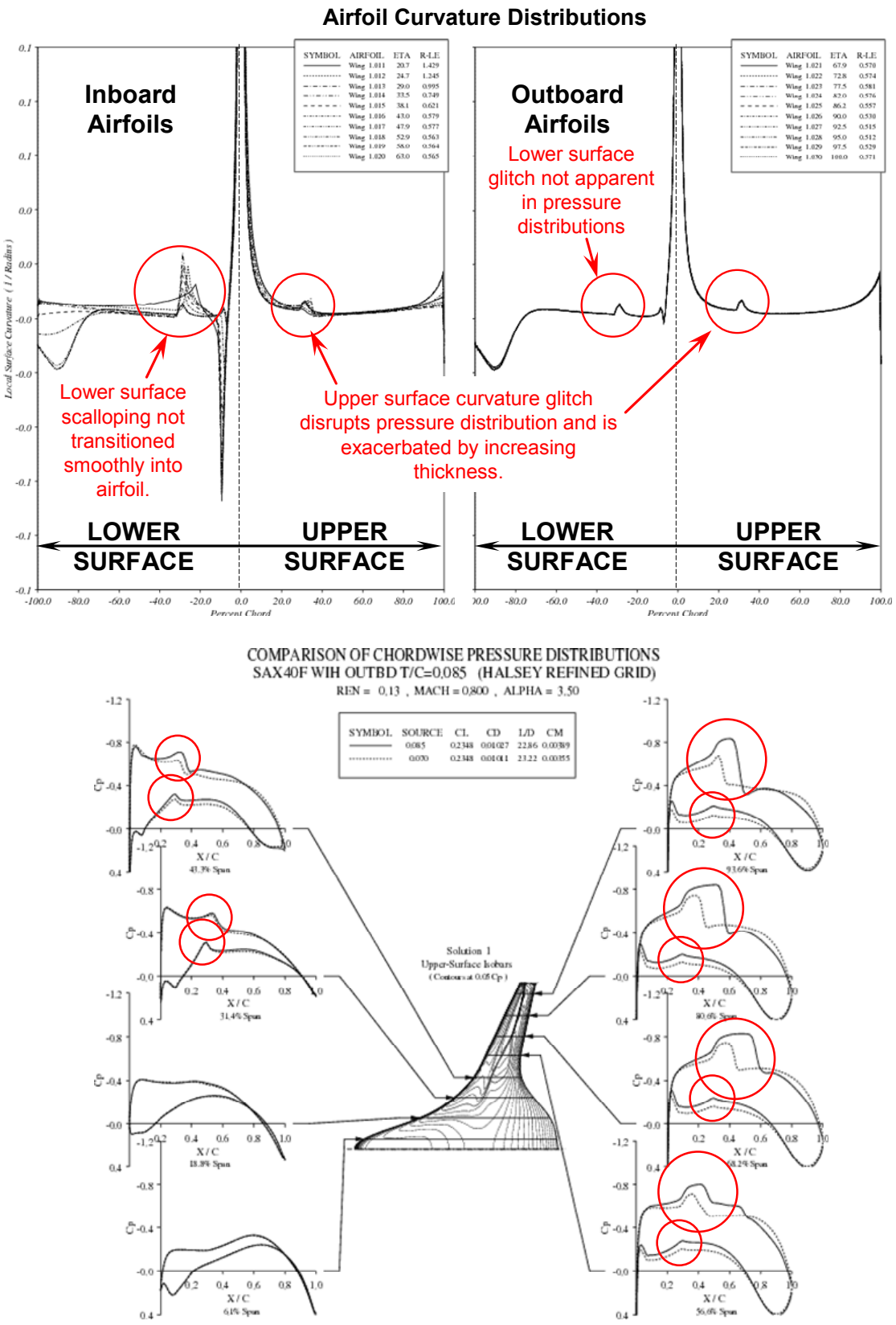

Figure 17 Surface Curvature Discontinuity Effect Exacerbated at Higher Thickness

This discontinuity is reflected in the wing pressure distributions and its effect is exacerbated at the higher outboard wing thickness as shown in the Figure 18. Therefore, the L/D increment shown above may not be solely a result of the increased wing thickness.

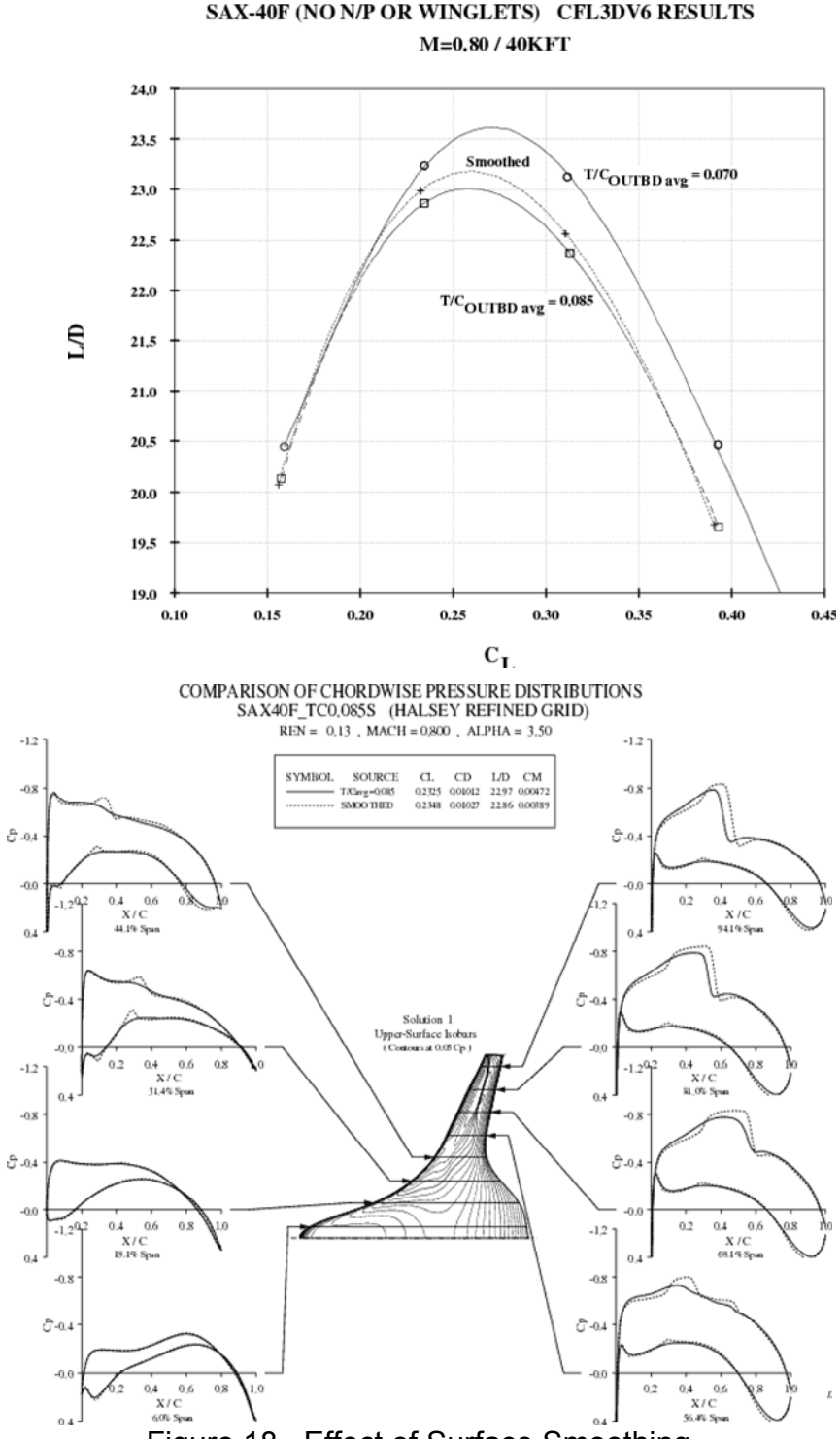

Figure 18 Effect of Surface Smoothing

The surface discontinuity was deemed unacceptable and the geometry was smoothed to remove the discontinuity. The results of the smoothing are shown in Figure 18.

The spanload of the SAX-40F as seen in Figure 19 is nearly elliptic. Again this is deemed unacceptable from a practical structural standpoint and could be contributing to the severity of the high speed pitching moment break and to the entire outboard wing being critical at low speed C_{Lmax}.

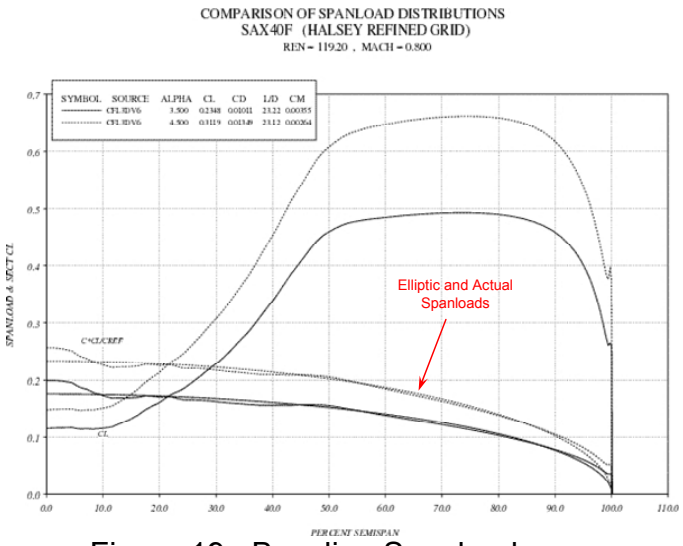

Figure 19 Baseline Spanload

The final configuration for this study was re-twisted to match a more practical spanwise loading based on past experience with blended configurations and has been designated as the N2 for the N+2 goals.

2.3.2 N2A Planform

All the modifications discussed in Section 2.3.1 were incorporated, the span was increased to 211.6 feet (later refined to 213.0 feet). The aerodynamic lines for this configuration were designated HWB-1.6X. The reference altitude for aerodynamic performance quoted in the following figures was lowered from 40,000 ft. to 35,000 ft. to be more in line with current blended configuration databases existing at Boeing. Reference quantities used in the analysis and high speed results are shown in Figure 20.

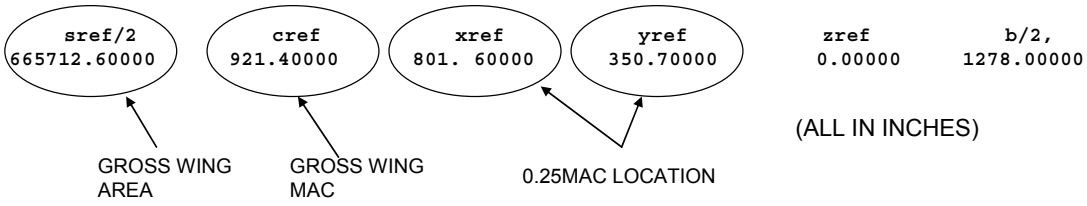

NOTE:
MOMENT REFERENCE FOR AERO DATA IS AT THE CG, 46%MAC
AERO DATA SHOWN FOR RN_{mac}=147.5M (M=0.8/35KFT)

Figure 20 Reference Quantities Used for HWB-1.6X CFD Analysis

The aerodynamic properties for the N2 are illustrated in Figure 21

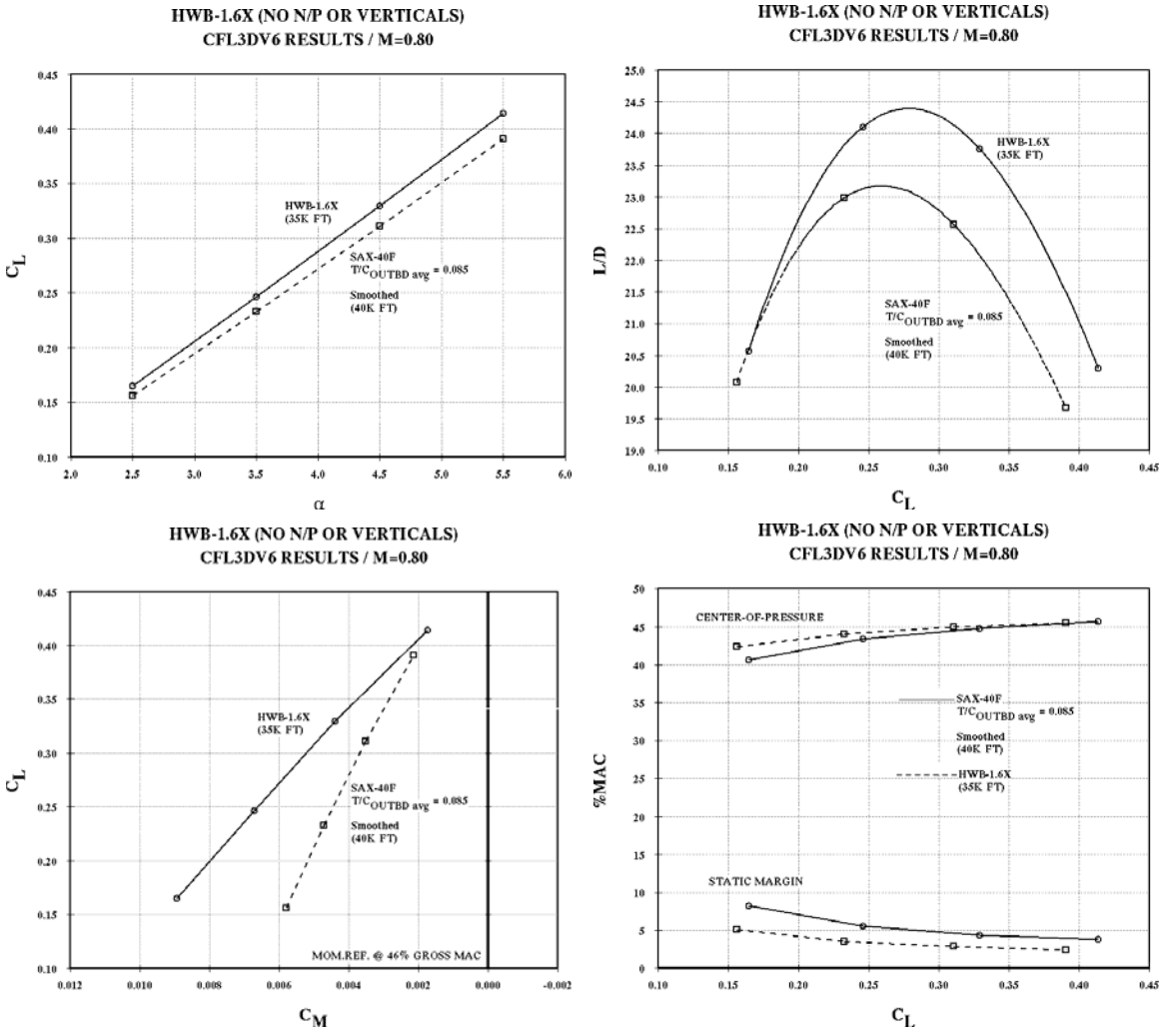

Figure 21 HWB-1.6X High Speed Aerodynamics

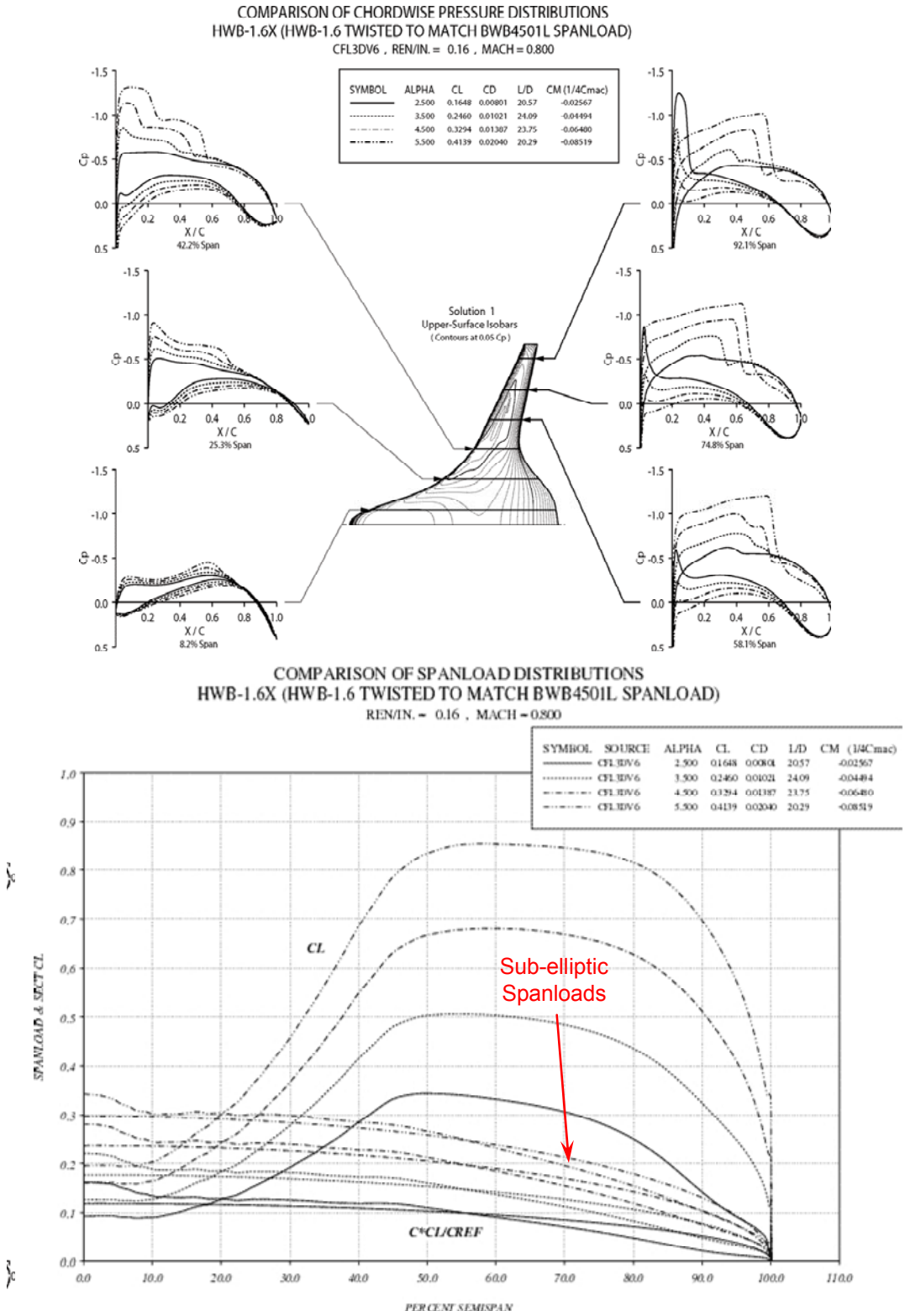

Figure 22 HWB-1.6X Pressure Distributions and Spanload

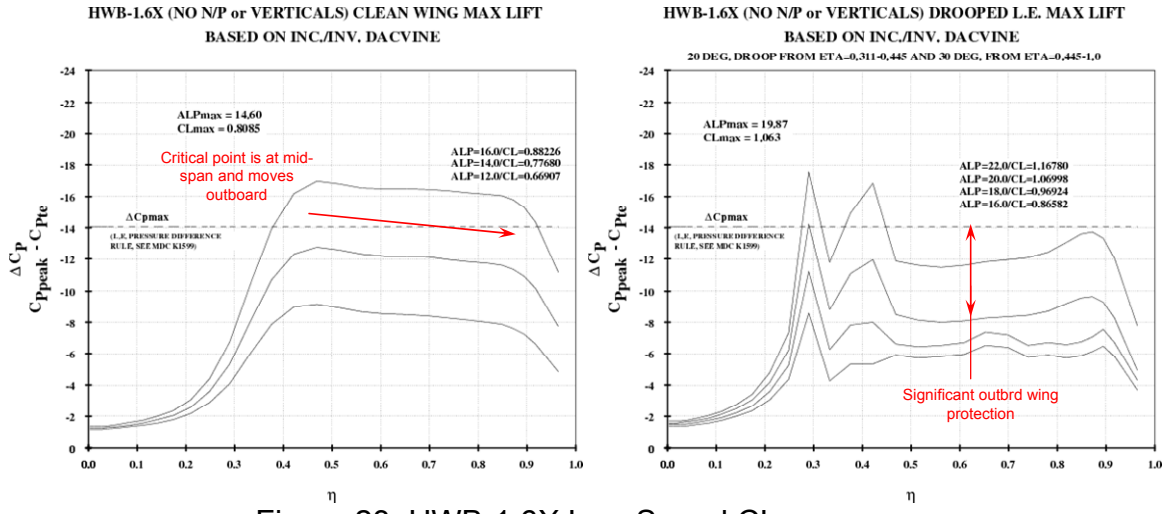

Figure 23 HWB-1.6X Low Speed CLmax

The wing geometry was then refined to improve the performance characteristics and returned a new wing airfoil stack to be re-lofted. The refined wing geometry included changes in airfoil camber, twist and thickness. The basic planform of the wing was not changed. This geometry was used to begin integration of the various aircraft systems, including propulsion, landing gear, payloads, winglets, verticals, and structure. Upon completion of this work, a new airfoil stack was sent back for further analysis. Preliminary sizing and locations were determined for the verticals.

2.3.3 Podded Engines N2A

Two propulsion concepts were developed. The N2A with podded engine in nacelles described in this Section depicted in Figure 24 and the N2B with embedded engines described in Section 2.3.4.

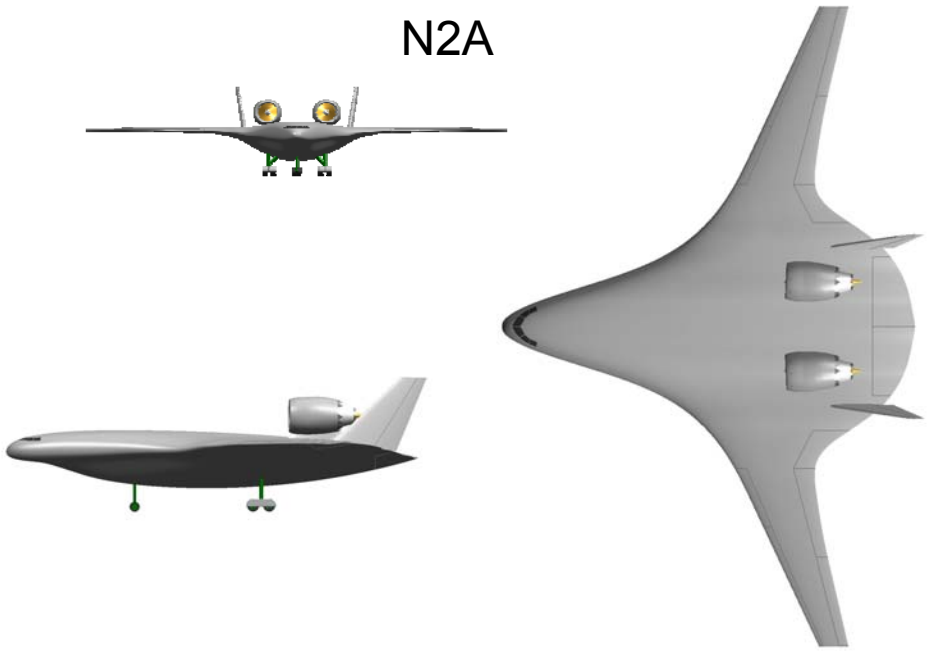

Figure 24 N2A Podded Engines

Low Speed C_{Lmax} was estimated using the BR&T higher-order panel method (DACVINE) coupled with an empirically derived method for predicting CLmax known as the Pressure Difference Rule (MDC K1519). The analysis as seen in Figure 25 showed the low-speed clean wing C_{Lmax} was too low and a simple droop leading edge device was designed to enable a C_{Lmax} of about 1.. The above methods were also used to generate center of pressure plots. Phase II will require modifications to the airfoil cross section shapes for high speed aerodynamics.

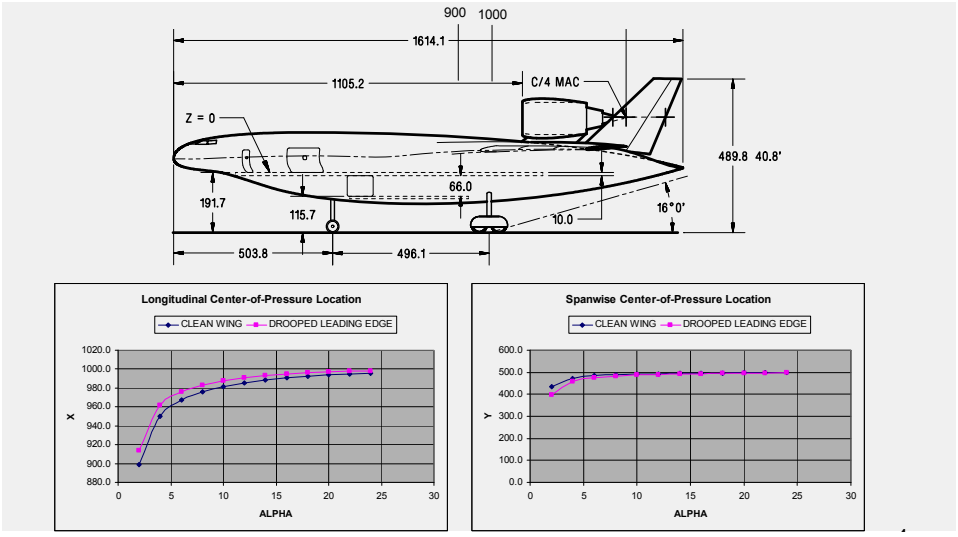

Figure 25 N2 Low Speed DACVINE C_p (without nacelles). X,Y,Z dimensions given in inches unless otherwise noted.

2.3.3.1 NASA GRC N2A Propulsion Data

The engine data requirements were established with the data matrix needed to conduct sizing and mission analyses using the Boeing Integrated Vehicle Design System (BIVDS) submitted to NASA GRC. NASA GRC used the Numerical Propulsion Simulation System (NPSS) to create the engine data needed for fan pressure ratios of 1.4 and 1.5 geared fans and 1.6 and 1.7 direct drive fans as shown in Figure 26. The detailed description of these data is presented in Appendix D of Reference 5.

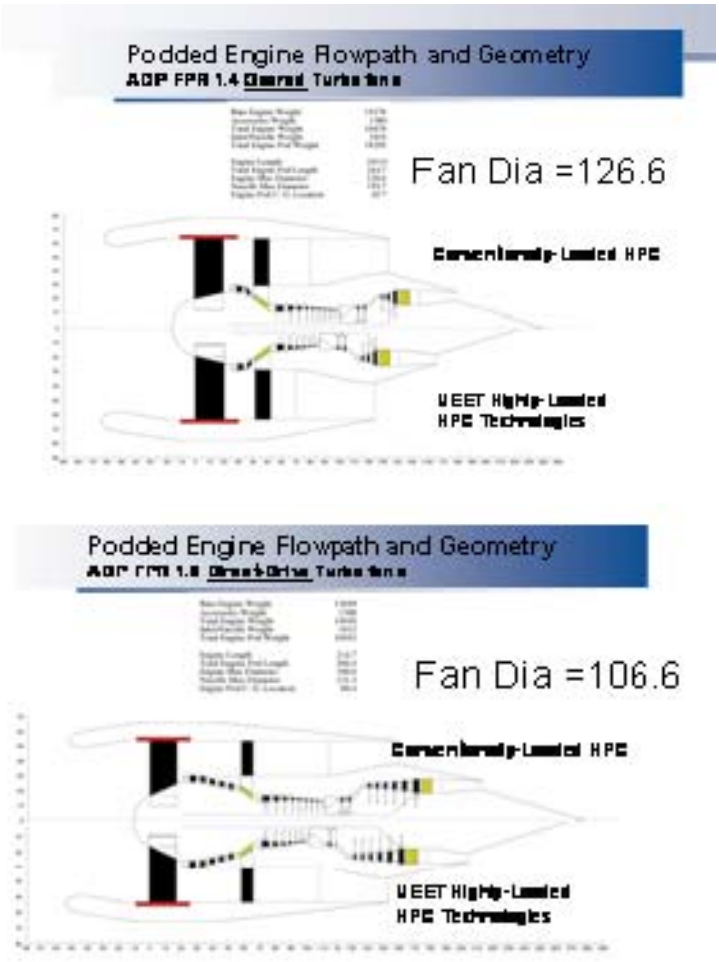

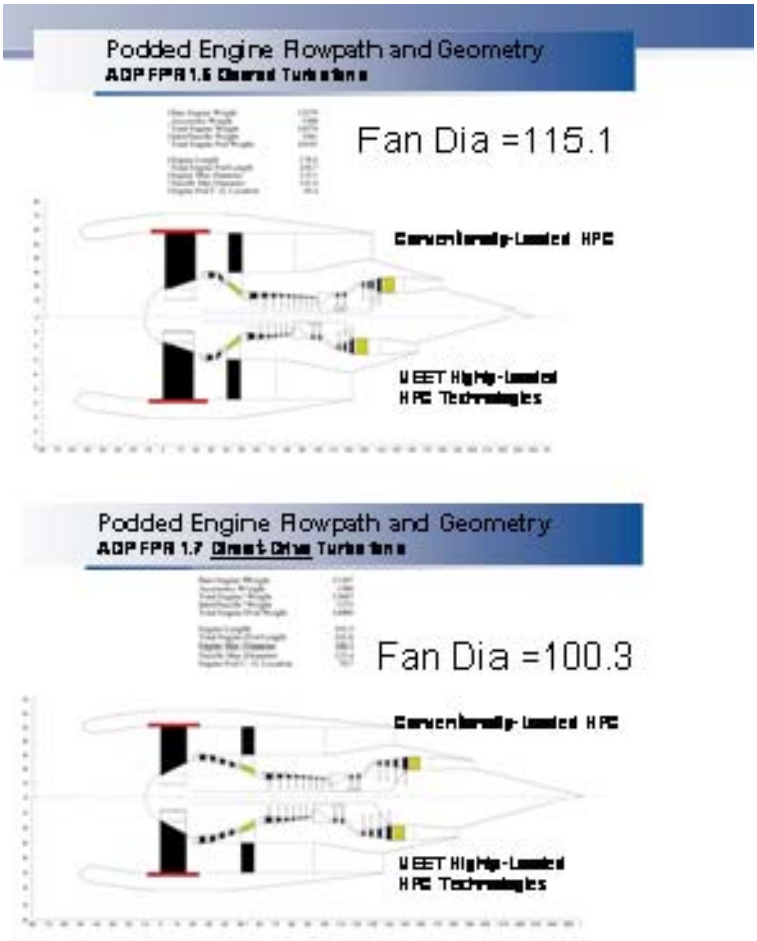

Figure 26 GRC N2A Engines

Data was provided for both highly loaded and conventional turbo machinery stage loadings (a complete description is presented Reference 5 Phase I Final Report Appendix D). It was mutually agreed between NASA GRC and BR&T that the small differences in weight and overall dimensions would not compensate for the overall efficiency degradation with the highly loaded engines. Engine data modules were created and a mini-trade study was conducted using BIVDS for the Fan Pressure Ratio (FPR) sweep. The results of this trade are shown in Table 1 and compared to other vehicles.

Table 1 Fuel Burn Comparison of NASA GRC Engines

Ground Rules: • 6,000 nm Range • 30 min Time to Climb through 32,000 ft • 35,000 ft ICA • TO + 27°F					
Fan Pressure Ratio	1.4	1.5	1.6	1.7	1.5
MTOGW (lb)	464,700	460,700	461,500	463,700	460,000
Payload (lb)	103,000	103,000	103,000	103,000	103,000
Ton-nm/lbf	2.606	2.555	2.471	2.393	2.568
Static Sea Level Thrust (lb)	74,862	71,837	69,757	68,258	71,837
OEI Field Length (ft)	6,214	5,942	6,196	6,320	

The FPR 1.6 as shown in paragraph 3.5.1 meets the fuel burned goal. While the lower FPR had a lower fuel burned, it was a geared fan and entailed increased risk for the 2020 IOC time frame. While considerable technology development had been underway for the geared turbofan by Pratt & Whitney, it had been directed towards a 20K lbs thrust class engines. There is no known technology development for a 60 – 70K lbs thrust class flight weight gear drive system and a geared fan in this thrust class was judged to be higher risk since a TRL Level 6 would need to achieved in the 2011-2012 time frame for a 2020 IOC (Initial Operating Configuration). Consequently the direct drive FPR 1.6 was selected for continuing configuration updating. The cruise SFC for the FPR 1.6 configuration is shown in Figure 27.

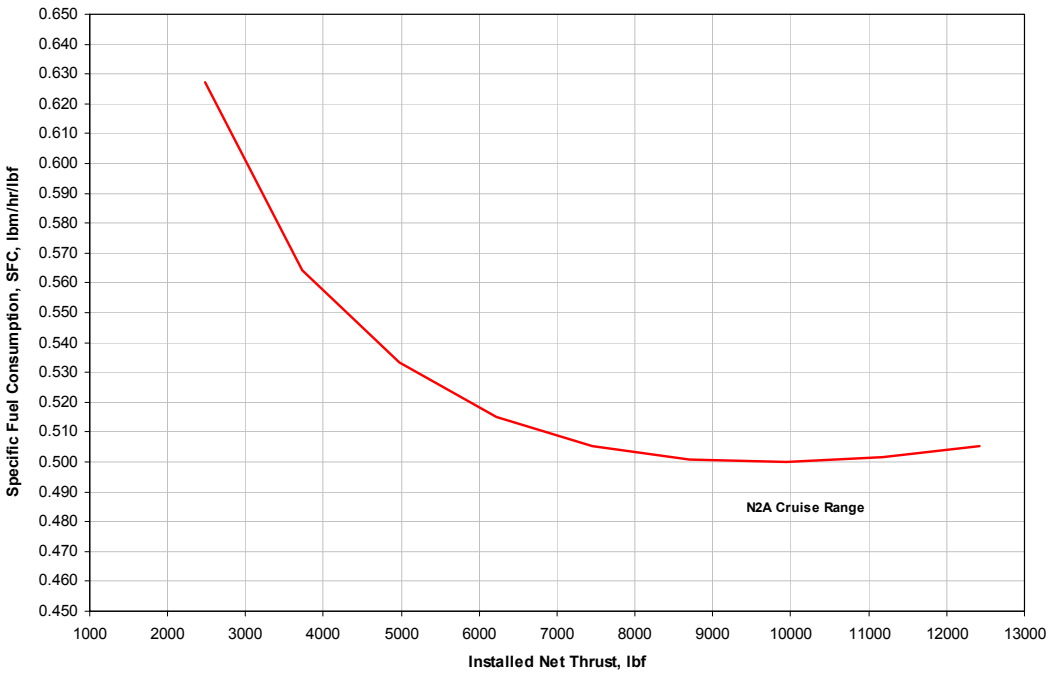

Figure 27 N2A Cruise SFC at 35,000 feet and 0.80 Mach Number

Subsystems including landing gear, flight deck and windscreen, cargo decks, preliminary structure, doors and windows and control surfaces were identified, sized and located. From this preliminary knowledge base a General Arrangement drawing shown in Figure 28 was completed and issued to the appropriate analysts for their work. The actual model file from UniGraphics was released as well for their use.

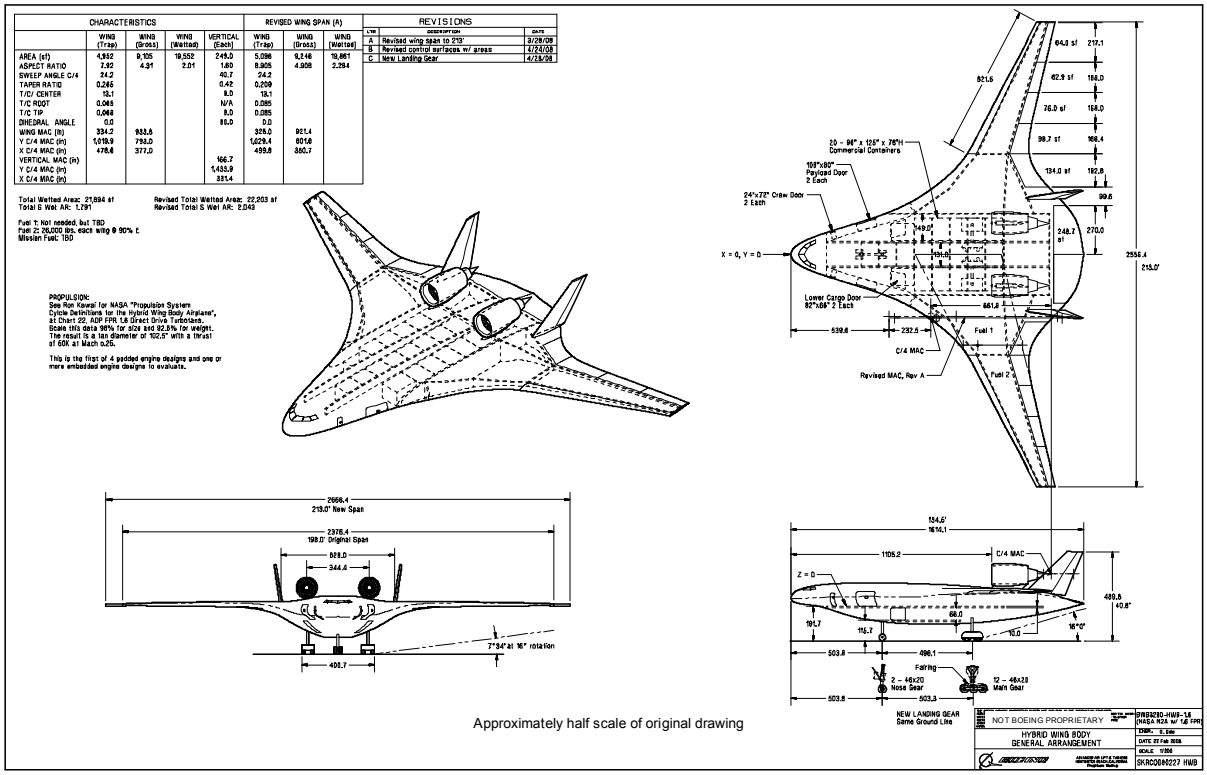

Figure 28 N2A General Arrangement Drawing

This airplane database was then used to “cycle” the N2A podded engine configuration. Figure 29 shows the updated N2A baseline.

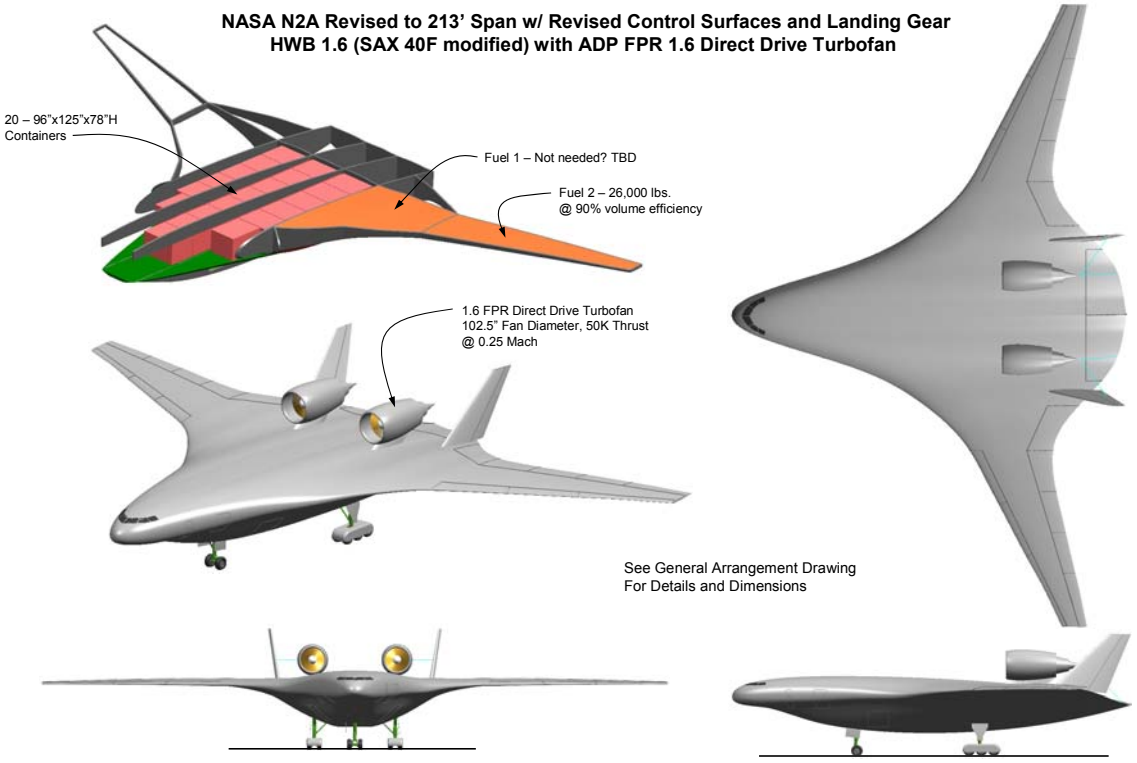

Figure 29 Updated N2A Baseline

The drag polar for N2A is shown in Figure 30.

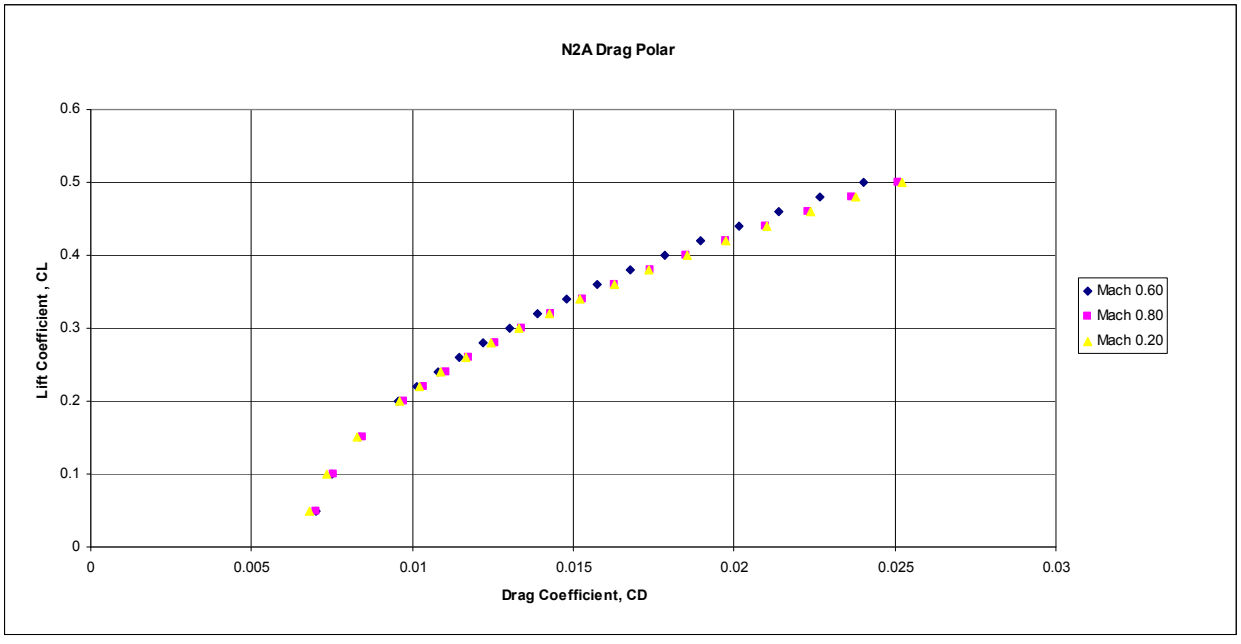

Figure 30 N2A Drag Polar

2.3.4 Embedded Engines N2B

The second propulsion concept retains the SAX 40 type embedded engines as shown in Figure 31.

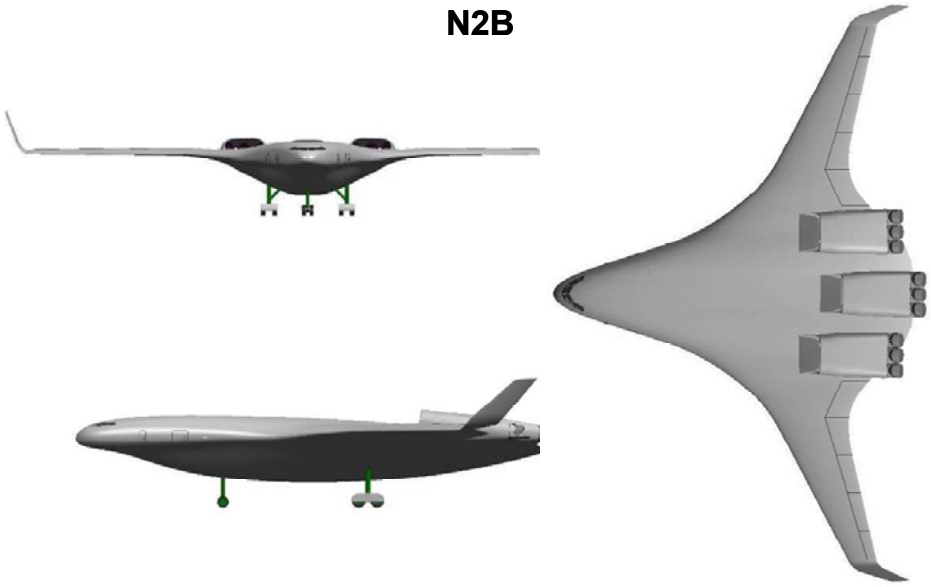

Figure 31 N2B Embedded Engines

The propulsion system configuration was developed starting from systems descriptions from the CMI SAX-40 and the engine cycle descriptions. The SAX-40 contained engine company proprietary data, therefore NASA Glenn Research Center (GRC) developed the engine data including engine source noise with nacelle duct attenuation. The concept was derived from the SAX-40 GRANTA which had three propulsion modules that were each composed of a gas generator that drove an inline fan and two additional fans through a mechanical drive train.

2.3.4.1 NASA GRC N2B Propulsion Data

GRC started with component sizing by using NPSS to provide the Mach 0.25 and climb thrust levels estimated by Boeing. The overall architecture was developed by NASA GRC and the power transfer design requirements determined as shown in Figure 32.

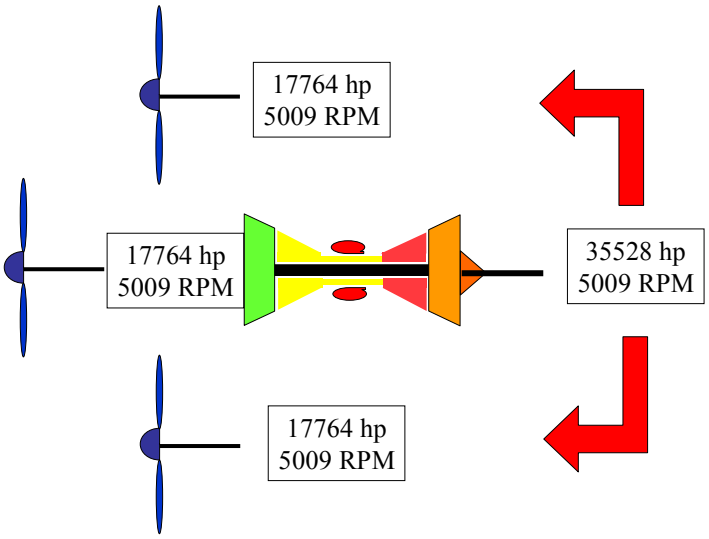

Figure 32 Propulsion Drive System Requirements

The layout for estimating performance and weights is shown in Figure 33. The mechanical drive train was designed to be powered from the gas turbine low pressure turbines through angle gearboxes to adjacent fans.

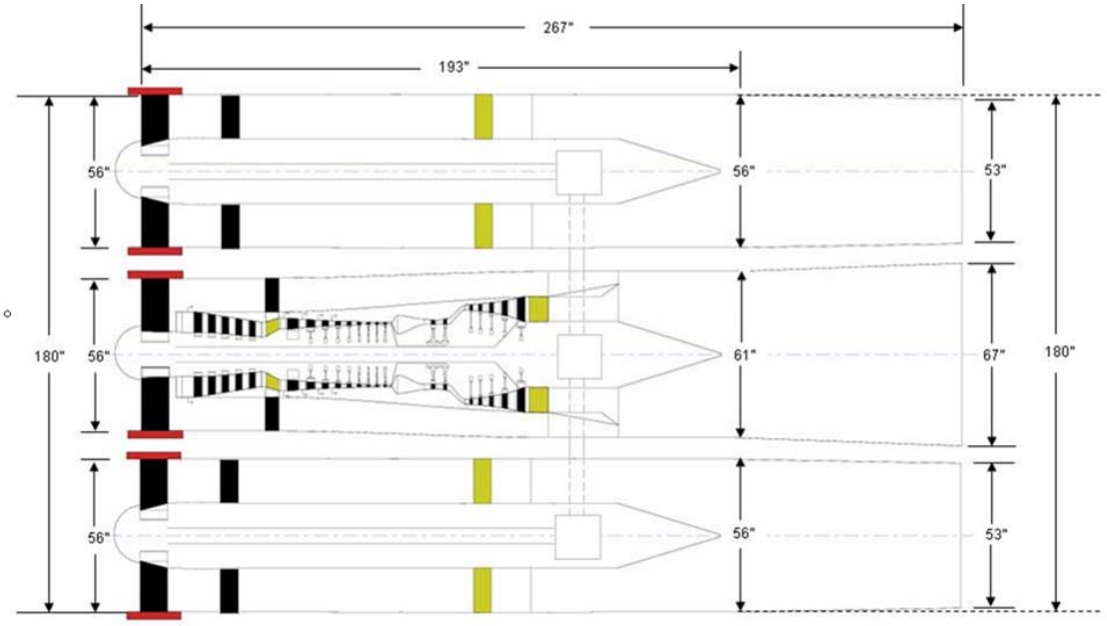

Figure 33 Embedded Engine Internal Layout

Three shaft drive system arrangements were studied at NASA GRC and the arrangement shown in Figure 34 selected.

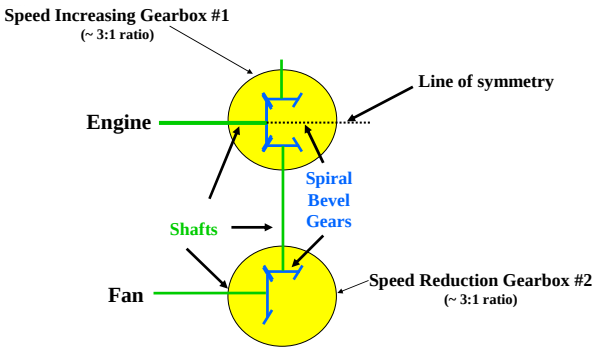

Figure 34 BWB Tri-Fain Configuration #3

The power train weights and sizing data was developed at NASA GRC. A graph showing the weights based on parametric values is shown in Figure 35.

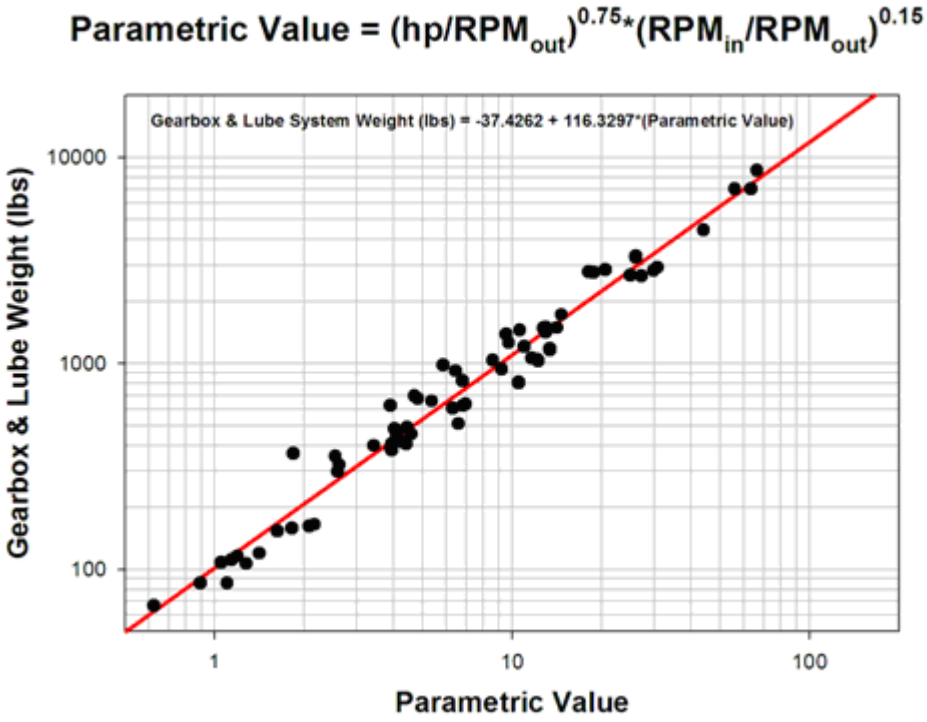

Figure 35 Rotocraft Transmission and Lubricant System Weight Data

The performance for the N2B was developed by NASA GRC.for the cycle summarized in Figure 36.

	SLS (ISA+27F)	RTO (M0.25/SL/ISA+27F)	ADP (M0.80/31kft/ISA+0)	Top of Climb (M0.80/35kft/ISA+0)	Throttled Cruise, 90% FN (M0.80/35kft/ISA+0)
Net Thrust (lb)	49060	36000	10000	8286	7458
SFC (lb/hr/lb)	0.288	0.398	0.564	0.553	0.556
BPR (core only)	3.2	3.2	3.1	3.1	3.3
BPR (effective)	11.5	11.7	11.3	11.3	11.8
OPR	45	43	46	46	43
N1 (%)	98	97	100	100	96
N2 (%)	99	99	100	100	99
T3 (R)	1706	1710	1476	1430	1398
T4 (R)	3460	3460	3010	2920	2844
T41 (R)	3310	3310	2876	2789	2716
T49 (R)	2460	2460	2113	2044	1986

Figure 36 NASA Embedded Engine Cycle Information

The N2B data was generated by NASA GRC using NPSS with the inlet pressures recoveries from Boeing with all losses in the outer fan flow only. The inlet recoveries were determined from the mass average total pressure of the inlet capture flow at the inlet highlight. This was calculated from the RANS CFL3D clean wing analyses of total pressure with an additional 0.6% inlet diffuser loss. This internal loss was from a prior study based on use of fixed vane vortex generators to redistribute the low energy flow. This increases radial distortion to achieve an acceptable level of circumferential distortion. The embedded N2B propulsion system is further described with the data location at the NASA GRC website in Reference 5 Appendix D.

Boeing then developed the nacelle installation of the engines into the N2B airframe as shown in Figure 37 using a conceptually similar design from the Boeing YC-14 that employed a surface mounted over wing nacelle with a variable area thrust reverser nozzle.

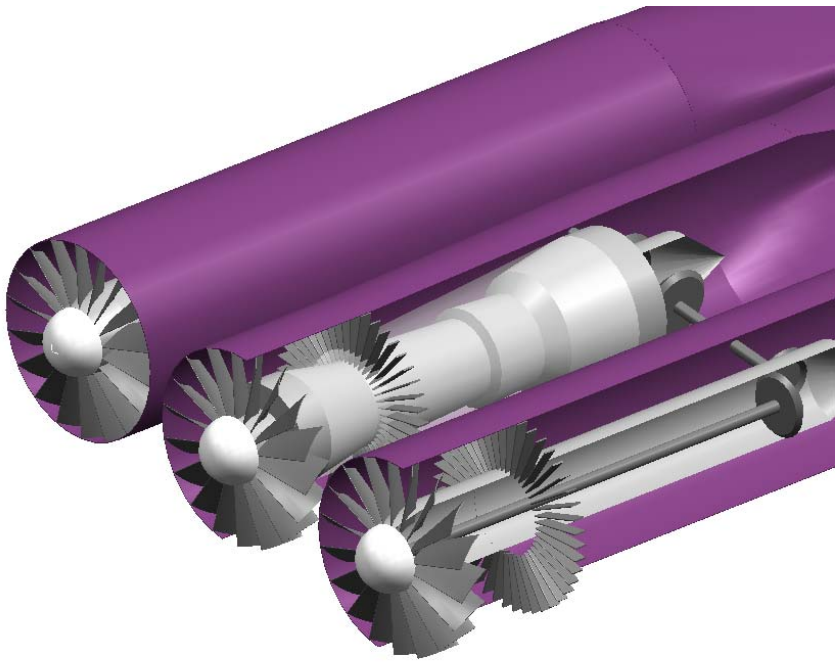

Figure 37 N2B Engine Installation

Figure 38 illustrates the variable area thrust vectoring/reversing concept developed for the N2B configuration.

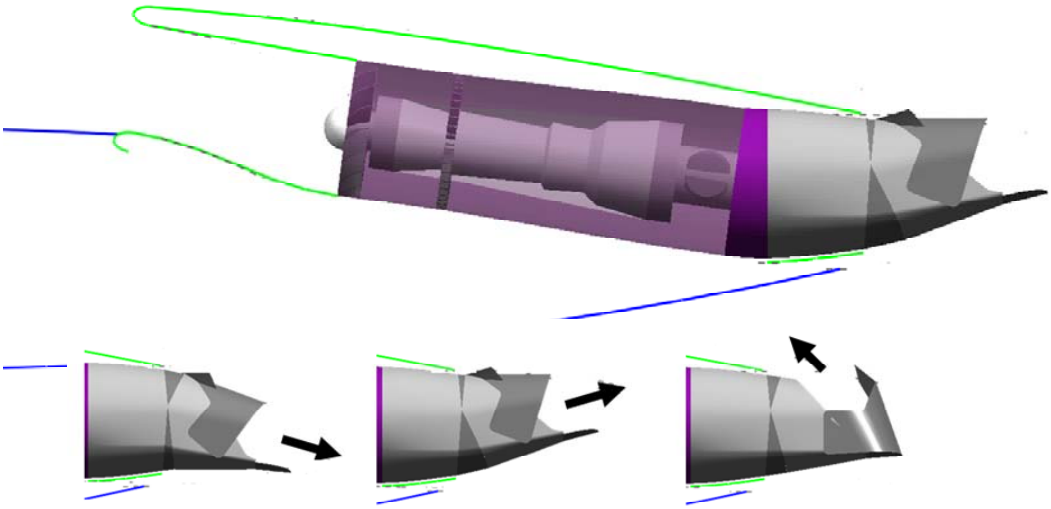

Figure 38 N2B Thrust Vectoring/Reversing Nozzle

The NASA N2B engine performance module with the boundary layer ingestion inlet was developed for BIVDS by reducing the ram drag in the NASA GRC data sets. The ram drag reduction with boundary layer ingestion was determined by the method in Reference 6 where the change in inlet momentum is calculated from the change on

mass-averaged pressure recovery of the inlet capture flow. The mass-averaged inlet pressure recovery for Mach 0.80, 35K ft altitude resulted in a ram drag reduction of 6.2% of the net thrust.

A sanity check that was made by determining the approximate viscous drag for the flow entering the inlet as a percent of total HWB drag along the climb and cruise flight path. assuming the inlet forebody scrubbing is longitudinal into the inlet highlight. Since the boundary layer ingestion flow pressure loss is primarily from viscous drag, the climb benefit was estimated by corrected at lower flight speed by factoring with the freestream dynamic pressure.

The results are shown in Figure 39. The cruise fraction was 6.9% applied to the wing/body drag compared to the 6.2% based on the momentum change calculated from the mass average pressure recovery. This is reasonable since minimum drag occurs when parasite drag equals induced drag. Parasite drag is primarily viscous drag and approximately split between the top and bottom of a HWB. Ram drag reduction from ingestion of the upper surface boundary layer would then at most be about 25% if all the upper surface flow were ingested. The fraction of ingested wetted surface area applied to the total viscous drag provides an approximate measure of the boundary layer ingestion benefit.

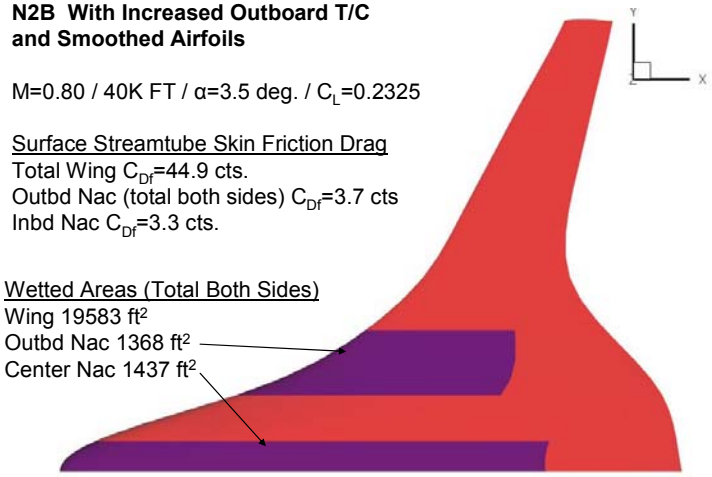

Total Drag CD = 100.9 counts

Total Viscous loss stream tube into inlet is 7 / 110.9 = 6.94%

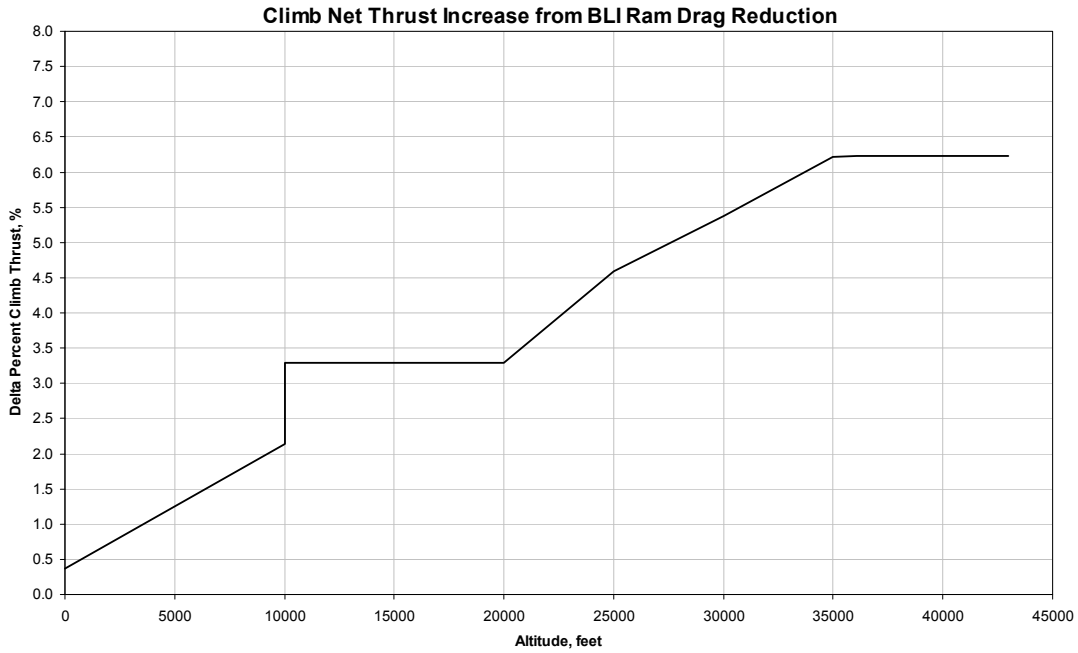

Figure 39 Viscous Loss in Agreement with Change in Net Thrust

Performance of engines with low fan pressure ratios is also very sensitive to inlet pressure recovery losses. The cruise SFC with the net effect of ram drag reduction from boundary layer ingestion with performance loss from the attendant loss in inlet total pressure recovery is shown in Figure 40.

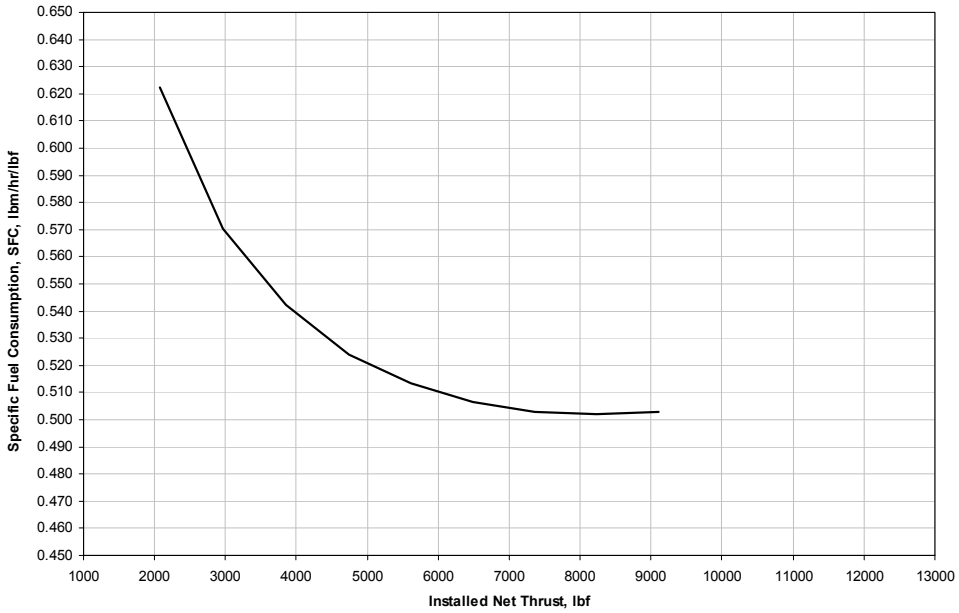

Figure 40 N2B Specific Fuel Consumption at 35,000 ft Mach 0.80

A view of the propulsion system as integrated into the airframe is shown in the general arrangement drawing, Figure 41. ,

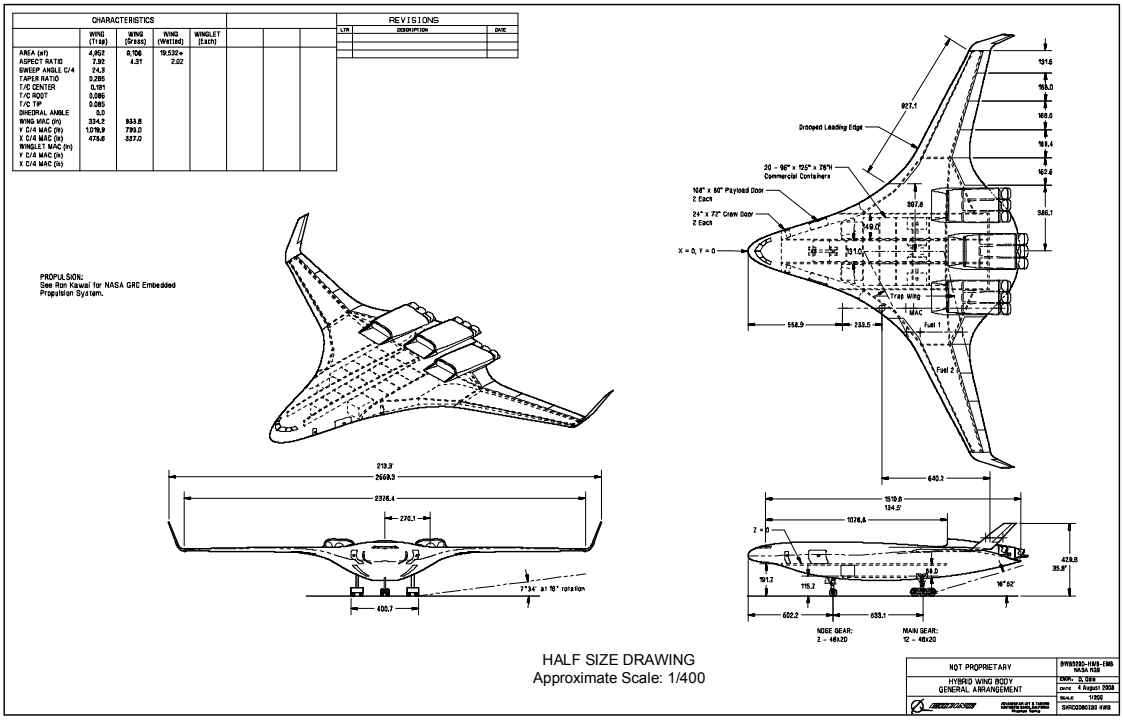

Figure 41 N2B General Arrangement Drawing

An isometric view is shown in Figure 42.

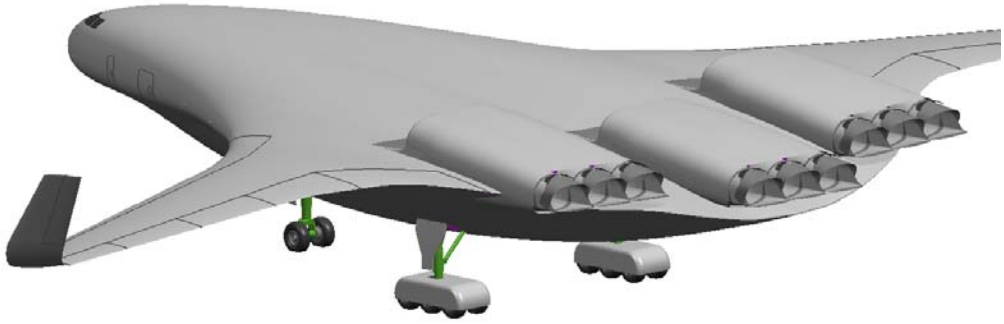

Figure 42 N2B Propulsion System Installation

The drag polar for the N2B was developed from the CFL3D clean wing with the nacelle and winglet drag then added. The N2B polar is shown in Figure 43.

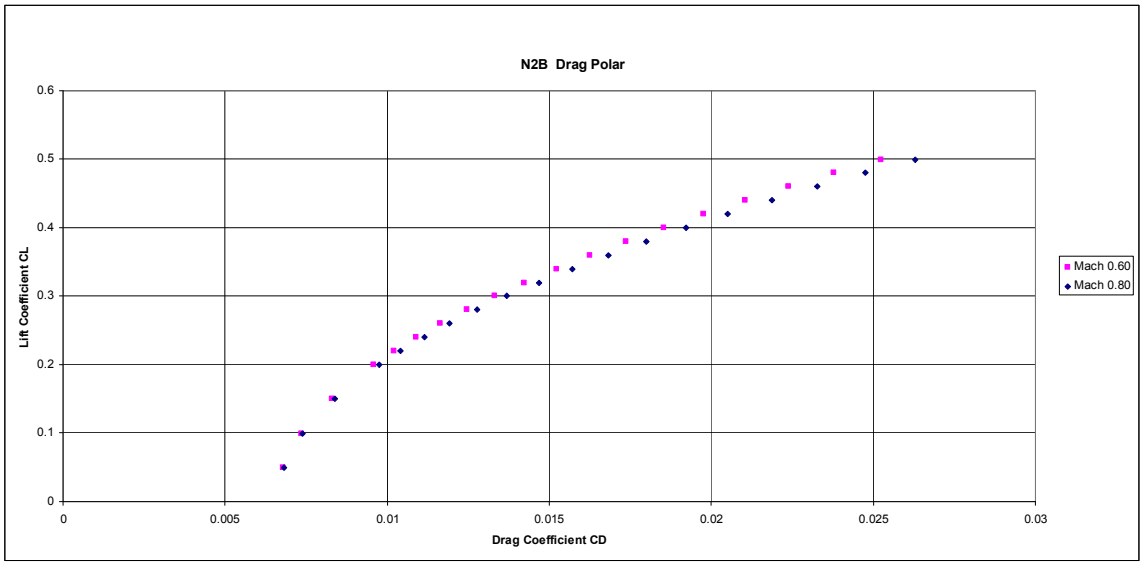

Figure 43 N2B Drag Polar

2.3.5 Conceptual Mass Properties Analysis

2.3.5.1 Weights

The mass properties task for this study was to analyze two different BWB type airplane engine integration concepts using a comparable geometric BWB planform, design requirements and ground rules, and weight estimating methodology.

Details from the general arrangement drawings (3-view) for the two concepts were used to provide input data for the weight estimating algorithms and to assess weight penalties to account for discrete concept features. The general arrangement drawings are:

- Podded Engine Concept, SKRCO080227 HWB, BWB3290-HWB-1.6 (NASA N2A w/ 1.6 FPR), dated 2/27/2008 in Figure 28.
- Embedded Engine Concept, SKRCO080730 HWB, BWB3290-HWB-EMB (NASA N2B), dated 8/4/2008 in Figure 41.

The conceptual cargo airplane group weights were derived, for the NASA (2) two engine N2A top body mounted conventional podded engine concept and the (3) three engine N2B fuselage body embedded engine concept, based on a common in-house BWB weight methodology. The weight methodology was developed using weight results from prior in-house BWB configuration development programs and NASA advanced composite structure development contract experiences.

The propulsion system geometry and weight for the N2A podded engine concept is based on NASA GRC ADP Direct Drive Turbofan engine with a FPR of 1.6. The propulsion system weight was obtained from data presented and shown in GRC Propulsion-Datav2 Rev Mar 10.ppt, page 21 (Reference 5 Appendix D page D-11). The base reference installed SLS (Sea-Level Static) thrust used for the NASA podded FPR 1.6 engine was 69,757 lbs per engine. The total bare engine, nacelle pod, thrust reverser, exhaust nozzle and engine accessories weight, less 1,300 lbs of accessories, was used as provided by NASA GRC. The 1,300 lbs of accessories was removed for the analysis because it is assumed that the subsystem and accessories weight were already accounted for in the individual functional aircraft subsystem weights. The engine pylon and attach structure weight is based on in-house engine pylon weight estimation methodology.

The base reference engine geometry and weights for the N2B embedded engine concept were also attained from NASA GRC . The base reference SLS thrust for the NASA embedded engine is 51,780 lbs per engine cluster. The engine weights for each engine cluster included the bare engine (one core and 3 fans, fan air ducting and core flow mixer, engine EBU (Engine Build-up Unit) and engine accessory and subsystems, gearboxes and drive shafts) and (3) three fan and primary exhaust ducting and variable area nozzles which includes (3) thrust reversers. The inlet, nacelle, exhaust acoustic liner and engine attach structure weight penalties were estimated with in-house weight estimating tools and engineering judgment. The total engine, nacelle, exhaust nozzle, thrust reverser, gear box, drive shaft and engine accessories weights were scaled to the mission performance sized thrust of 48,320 lbs per engine cluster.

For distinct concept features, weight penalties were assessed based on engineering judgment. Also, the conceptual group weights also presumes employing projected weight savings achieved from future composite materials and design advancement reflecting Year 2012 technology.

The mission performance sized airplane weight results of the Podded Engine Concept and the Embedded Engine Concept are shown in Table 2. The airplane OEW is categorized in three weight groupings.

The Structure Group weight includes the outer wing, aerodynamic control surfaces, body/fuselage sections, winglet/vertical tails, and engine pylon/engine to body support and attach weight penalties.

The Propulsion System Group weight represents items listed in SAWE RP No. 8-Part II, Detail Weight Statement sections: engine section or nacelle group, air induction group, and propulsion group, except for the pylon/engine attach structure weight penalties and the fuel system weight. For simplicity of weight definition and allocation, the podded engine pylon structure weight and the embedded engine support and attach structure weight penalties are accounted for in the structure group weight and the fuel system weight is included in the sub-system group weight.

The Remaining Sub-Systems Group weight includes the landing gear system, outer wing fuel system, flight controls system, hydraulics system, pneumatics system, APU system, electrical system, instruments system, avionics and auto flight system, environmental control system, and anti-ice system. The Furnishing Group weight represents a typical cargo/freighter configuration which includes cockpit seats, consoles, paneling, lavatory and galley accommodation for a three person crew, freighter type main cargo deck acoustic insulation, sidewall panels and floor covering, main deck cargo loading system, lower cargo compartment flooring and sidewall lining, and crew oxygen and emergency equipment.

Table 2 N2A and N2B Weight Summary

Configurations	N2A	N2B
Drawing No. (see Fig 28 and 41)	SKRCO080227	SKRCO080730
Propulsion System Concept	Podded	Embedded
3 View Geometry Data		
Gross Wing Area (ft^2)	9,246.0	9,106.0
Wing Span (ft)	213.0	198.0
Body Length (ft)t	134.5	134.5
Number of Engines	2	3
Performance Sized Thrust @TOSLS / Engine Pod	69,750	48,320
Sub Component Weight		
Structure Group (incl wing, body, winglet/vert stab, pod to body attach) (lb)	122,364	112,971
Propulsion System Group (less pylon/engine attach, fuel sys) (lb)	26,320	44,443
Remaining Sub Systems, Furnishings and Operational Items Group (lb)	69,915	67,139
Vehicle Weight		
Operational Empty Weight (lb)	218,600	227,600
Payload Weight (lb)	103,000	103,000
Zero Fuel Weight (lb)	321,600	330,600
Mission Fuel (lb)	139,900	146,800
Takeoff Gross Weight (lb)	461,500	477,400
Max Landing Weight (lb)	337,400	347,900
CG Limits		
Fwd S&C CG limit % MAC	39.5	43.0
Aft S&C CG limit % MAC	48.0	50.0

2.3.6.2 Balance

Balance analysis was performed for both the N2A and N2B and the results are shown in Figure 44 and Figure 45. The forward and aft CG limits for the both concept were

chosen to place the configuration loadability extremes, which occur at the OEW and MZFW conditions, within the forward and aft CG limits. The balance diagram % MAC values are determined based on the wing gross MAC.

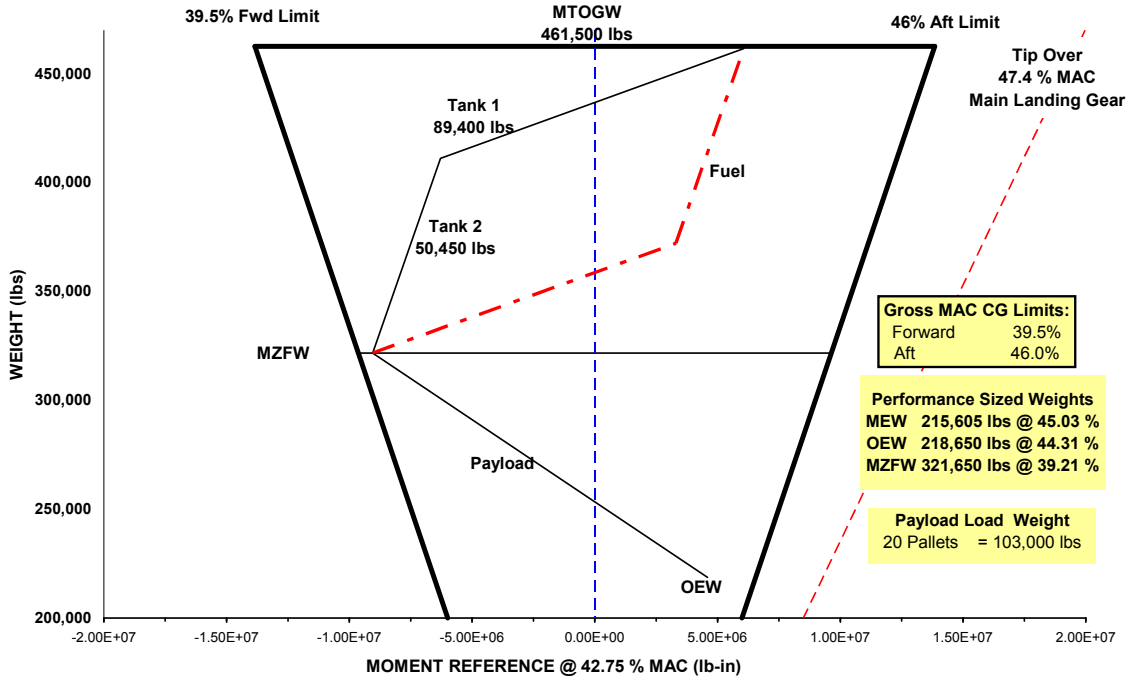

Figure 44 Conceptual N2A Balance Diagram

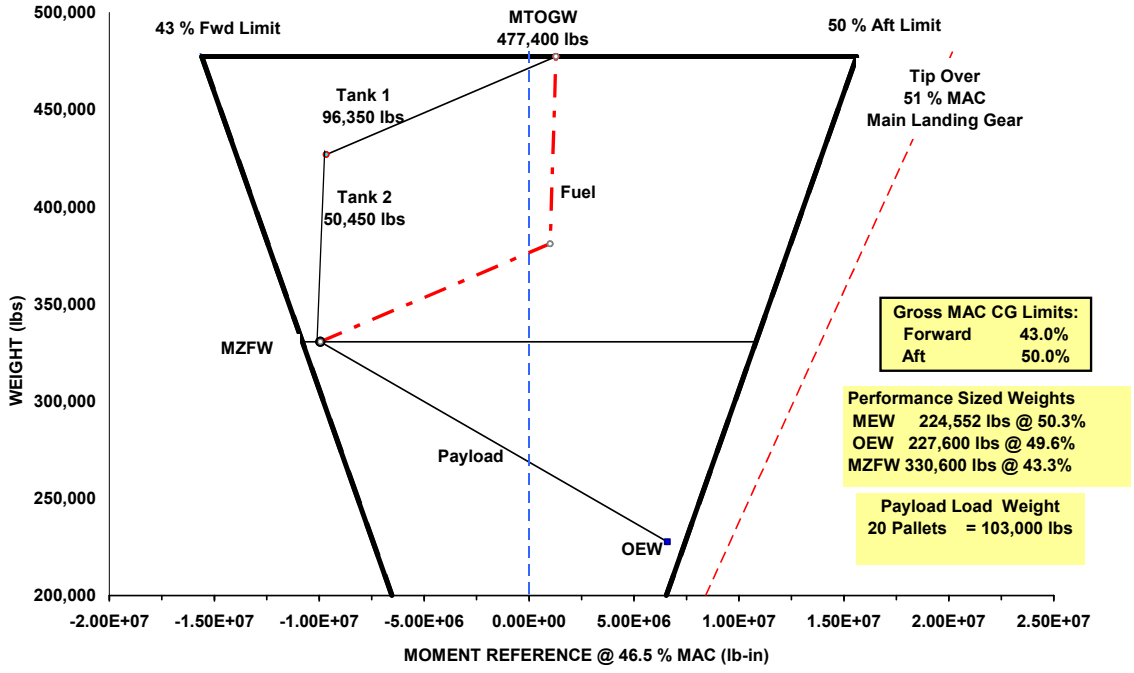

Figure 45 Conceptual N2B Balance Diagram

For this initial conceptual design balance analysis, the N2A forward limit is estimated at 39.5% MAC and the aft limit is estimated at 46% MAC. The N2B forward limit is estimated at 43% MAC and the aft limit is estimated at 50% MAC.

A cursory tip over assessment was made to assure that the MEW (Manufacturer's Empty Weight) CG and all other CG conditions fell forward of the main landing gear centerline.

2.3.5.3 Control Authority Assessment

2.3.5.3.1 N2A CG Control Limits Analysis

Following the development of the aerodynamic data, mass properties, and engine performance for the HWB N2A configuration, an evaluation of the Center of Gravity (CG) control limits was conducted.

Based on previous experience with Blended Wing Body configurations, three conditions were assumed to be the critical cases which determine the forward and aft limits. These cases are summarized in Table 3.

Table 3 Critical Cases for Establishing CG Limits

Critical Case	CG Limit	Mass Case
Nose Wheel Lift-Off	Fwd	Max fwd loading + Nominal Fuel
Trim at Stall	Fwd	OEW
Stall Recovery	Aft	OEW

The mass case for the nose wheel lift-off is a special loading condition to achieve the forward-most CG position. The CG positions are defined by the weights group and are presented on a loading diagram. For the configuration to work, these CG positions must fall within the limits imposed by aerodynamic control and maneuvering requirements. That is to say, you cannot have a loading condition which results in a CG location outside the range of controllable positions.

For this configuration, the CG limits determined by the trim at stall and stall recovery conditions fall generally near the CG positions traced out on the loading diagrams, which is a good indication. However, more accurate assessment than that is not possible due to the uncertainties in the aerodynamic data. Also, the nose wheel lift-off solution did not converge, likely due to the gear positioning and the accuracy of the aerodynamic data.

The calculations for determining the CG limit positions require, in addition to the mass properties, aerodynamic data at the flight conditions pertaining to the case. If the configuration has not been at least wind tunnel tested, it is difficult to acquire quality low speed aerodynamic characteristics. The parameters of interest are usually in the non-linear regions such as full deflection of control surfaces or C_{Lmax}. Or they are complex and time consuming to model in CFD such as gear and ground effect increments.

For this configuration, CFD data were used for determining the baseline aerodynamic characteristics and included the effect of the drooped leading edge. For the control surface effectiveness, gear, and ground effects, increments from wind tunnel based data for the BWB-450-1L were taken and scaled for this configuration. The scale factors accounted for mostly planform effects like size, control surface volumes, and quarter-chord sweep lines. What could not be easily accounted for were the airfoil effects like thickness or camber.

And while the 450-1L data are wind tunnel based, it is not without its own complications. Conventional configurations are easier to install in wind tunnels in ways that minimize interference between the model and the support system. Furthermore, large databases exist from flight testing with which the deficiencies in the wind tunnel data may be countered. However, with a new and unconventional configuration which has not been extensively wind tunnel and flight tested, the uncertainties in the data cannot be easily addressed. And while wind tunnel testing is an important step in getting quality data, certain further limitations are imposed because of the flying wing design itself. Since there is nothing other than a lifting body to which the support system can be attached, this class of airplanes is subject to higher levels of interference. The first consequence of this is the greater difficulty in predicting or determining the correct pitching moments. Secondary, but still of vital importance, is the control surface effectiveness.

The experience on the BWB program was that despite a great deal of care and effort, it was very difficult to get conclusive baseline pitching moment data. However, wind tunnel data can be very useful for other important parameters like C_{Lmax} (even at the low Reynolds numbers), gear and ground effects, and control surface effectiveness. It is therefore recommended that the planned low speed wind tunnel test make provisions for testing for these effects. A higher quality database would enable a more accurate assessment of the overall viability of the aircraft from the standpoint of controllability through a practical range of CG locations.

The lift and pitching moment data is shown in Figure 46 and Figure 47 below.

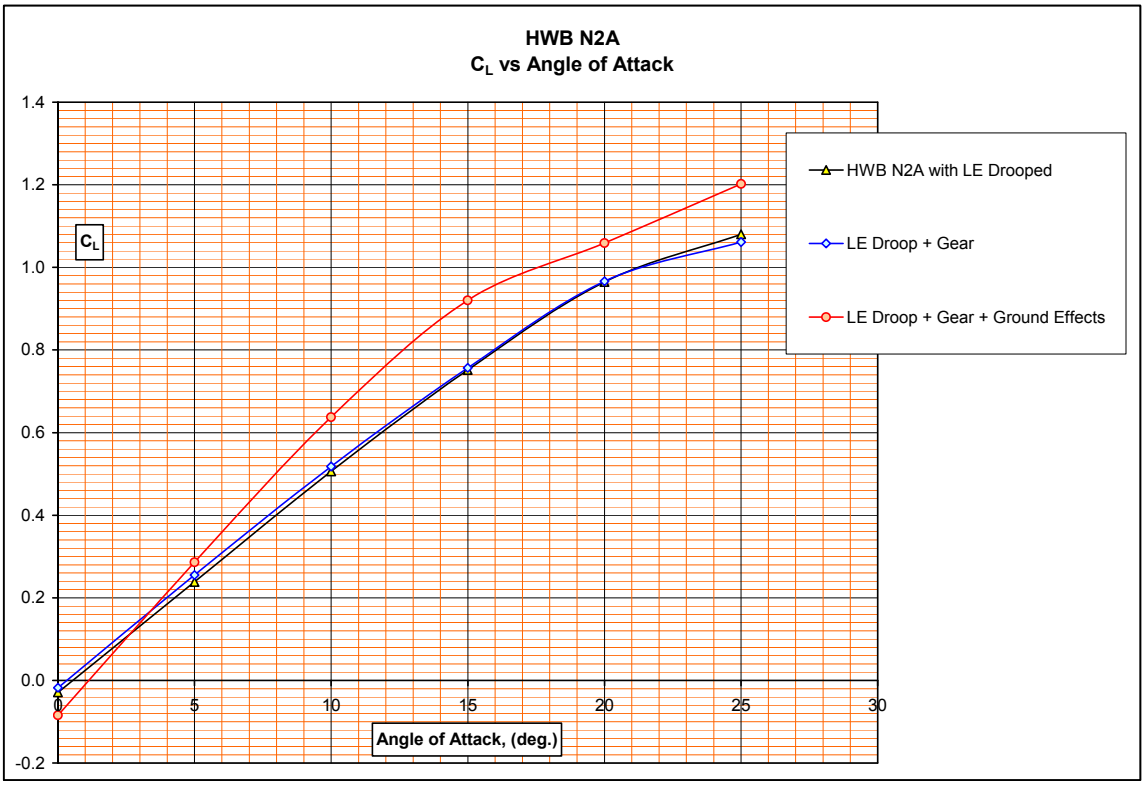

Figure 46 C_L vs. Angle of Attack for N2A Configuration

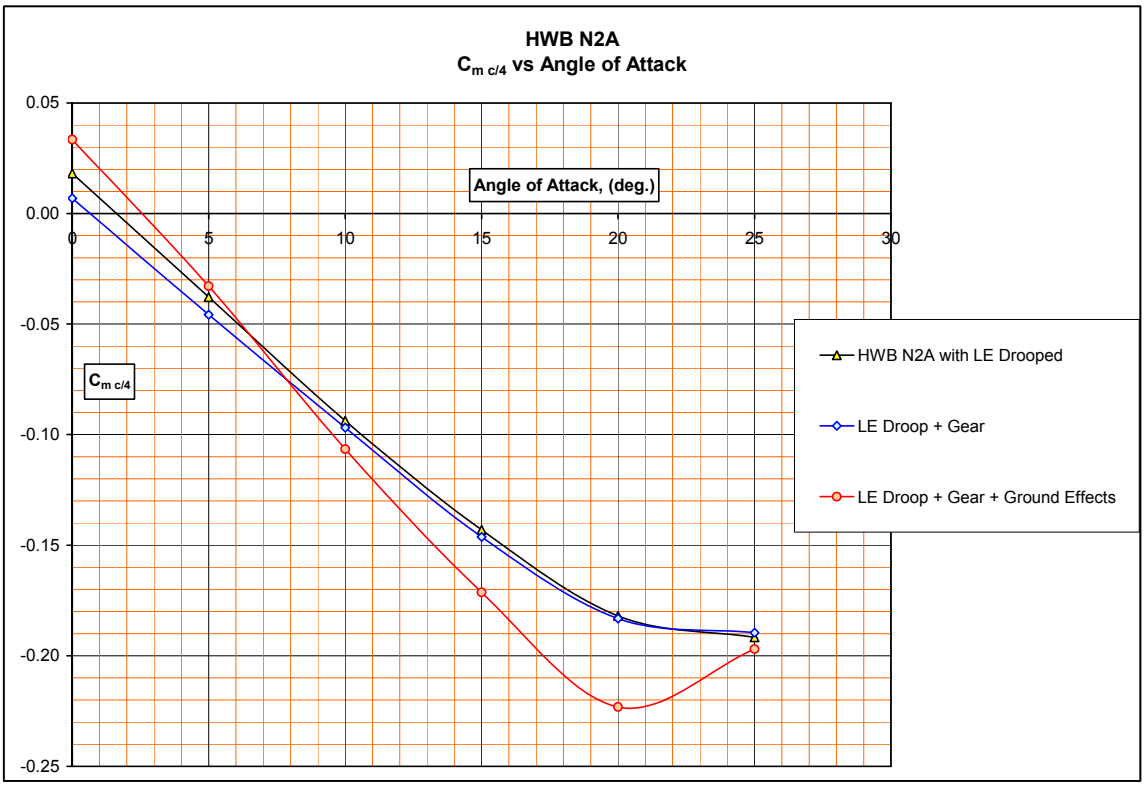

Figure 47 $C_{m\ c/4}$ vs. Angle of Attack for N2A Configuration

2.3.5.3.2 N2B CG Control Limits Analysis

The N2B configuration with embedded engines was not analyzed because of lack of a suitable data base. However, with the loss of the centerbody elevons, which are the most effective devices in the pitch axis, and the shift in the weight to the rear, it is expected that this configuration will be worse from the standpoint of acceptable CG positions

To cycle a configuration meant that the concept aircraft in question was weighed, a drag increment was established, the propulsion sizing was confirmed, the aero characteristics was confirmed, and preliminary stability and control issues were addressed. Using the above mentioned BIVDS system, all of this data was compiled, cross-checked, and preliminary performance was derived. The performance was required to comply with the stated mission requirements, including payload/range, cruise altitude and speed, fuel burn, and take-off and landing fields criteria.

3.0 PHASE I RESULTS

Phase I resulted in a HWB configuration with the potential to meet the NASA SFW fuel burn and noise goals using improved noise prediction methods as described below.

3.1 Vehicle Characteristics

A summary of vehicle characteristics and performance parameters for the Hybrid Wing Body podded engine (N2A) and embedded engine (N2B) configurations is shown in Table 4.

Table 4 Sized N2A and N2B Performance Parameters

Configuration	N2A	N2B
MTOGW (lb)	461,500	477,400
OEW (lb)	218,600	227,600
Payload (lb)	103,000	103,000
Fuel @ Max PL (lb)	139,900	146,800
Range (nm)	6,000	6,000
Fuel Burn (lb)	125,000	130,300
nm/lb	0.04799	0.04604
nm*PL/lb	4,943	4,742
Ton-nm/lb	2.47	2.37
Reference Wing Area (ft^2)	9,246	9,106
TO Ref FN @ SL Static +27°F (lbf)	69,757	48,320
Number of Engines	2	3
Time to Climb 31,000 ft (hr)	0.29	0.29
Distance to Climb 31,000 ft (nm)	109.6	115.9
Time to Climb 35,000 ft (hr)	0.43	0.41
Distance to Climb 35,000 ft (nm)	168.7	167.9
R/C at 35,000 ft (fpm)	388	367
Initial Cruise Altitude (ft)	35,000	35,000
Initial Cruise Mach	0.789	0.796
Initial Cruise L/D	21.61	21.55
Initial Cruise SFC	0.496	0.516
Initial Cruise Thrust & Drag (lbf)	20,919	21,704
Initial Cruise Power Setting	0.846	0.854
Final Cruise Altitude (ft)	43,000	43,000
Final Cruise Mach	0.791	0.796
Final Cruise L/D	21.48	21.35
Final Cruise SFC	0.497	0.499
Final Cruise Thrust & Drag (lbf)	15,754	16,357
Final Cruise Power Setting	0.935	0.944
Engine Out Field Length (ft)	6,196	5,436
All Engine Field Length (ft)	5,945	5,683

Note that the engine out field length for the N2B is shorter than the all engine out because it is a trijet. The second segment climb gradient requirement, per FAR-25, is 2.4% for 2-engine and 2.7% for 3-engine airplanes. Obstacle height is 35 ft for both Critical Field Length (ie. Engine Out Takeoff), and for All Engine Field Length. All Engine Field Length is 1.15 x All Engine Takeoff Distance. The Engine Out Field Length is typically more critical on a 2-engine configuration because loosing 1 engine out of 2 is more critical than loosing 1 out of 3.

3.2 Mission Fuel Burned

Fuel burned analyses results for the design mission are shown in Figure 48.

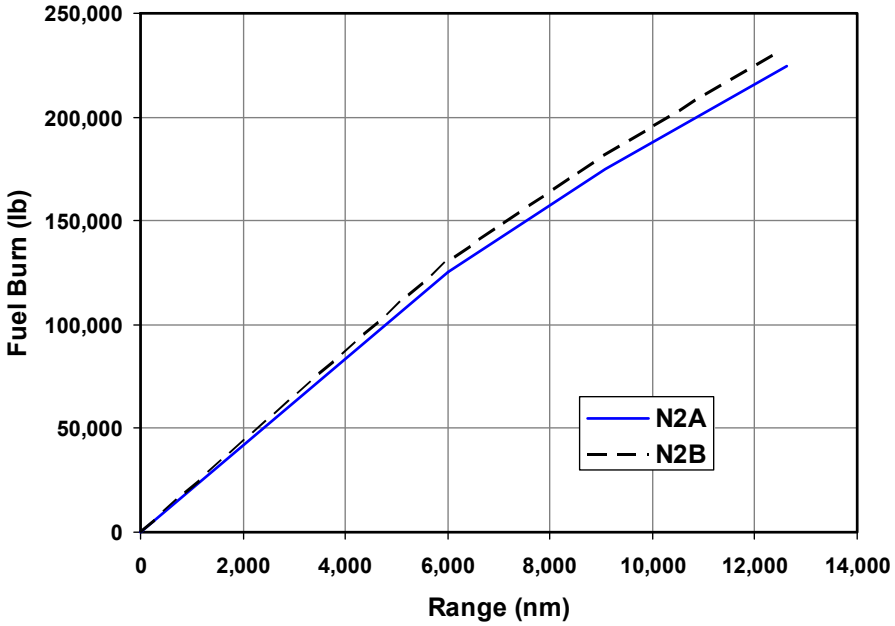

Figure 48 Fuel Burn Comparison of Podded and Embedded Engine Configurations

3.3 Noise

3.3.1 Noise Sources

The FAR 36 noise levels were estimated by MIT with documentation in Reference 5 in 0. The noise sources evaluated and the prediction methods used are listed in Table 5. Most airframe noise estimation methods used in this assessment were derived empirically on data from conventional aircraft configurations using the Aircraft Noise Prediction Program (ANOPP). The noise assessment methods below draw from many sources and previous research to present the most applicable methods for each component. Minor modifications were made to the base methods in several cases that are noted.

These analyses conducted by MIT were logarithmically summed for the FAR 36 points in EPNdB units at the lateral (sideline), flyover and approach noise certification conditions. The noise prediction base was ANOPP supplemented where judged to be necessary for the configuration under investigation. As described in Appendix C of Reference 5 the Beranek and Maekawa insertion loss method in ANOPP was determined to not properly represent shielding for jet noise. Model test data taken by UCI was therefore used. The UCI Phase I results are documented in Reference 5 in Appendix B. The N2B embedded configuration employs a tri-fan flow mixer nozzle for which data from the SAX 40 analyses were scaled.

Table 5 Summary of noise sources and estimation methods

Noise Source	Estimation Method
Fan Forward	ANOPP Heidmann Fan Module *- GE large turbofan method* TREAT acoustic inlet liner increments *- GE large turbofan method* SAI-based ray-tracing shielding increments
Fan Rearward	ANOPP Heidmann Fan Module *- GE large turbofan method* TREAT acoustic fan duct liner increments *- GE large turbofan method* Beranek & Maekawa barrier shielding increments (N2A)
Core	ANOPP GE Core Module Beranek & Maekawa barrier shielding increments (N2A)
Jet (N2A)	ANOPP Stone 2 Jet Module UCI jet noise shielding increments with perforated wedge
Jet (N2B)	Scaled Granta (SAI) jet hemisphere
Undercarriage	Modified ANOPP Boeing Airframe Module Faired landing gear noise reduction increments
Elevon	ANOPP Boeing Airframe Module (modeled as aileron)
Leading Edge Droop	Droop effect on BL properties included in FW-Hall method Contribution of side edge not modeled
Airfoil (Wing)	Physics-based airfoil self-noise method (FW-Hall)
Wing Tip (N2A) Winglet (N2B)	Tip vortex noise model from Brooks and Marcolini
Vertical Tail (N2A)	ANOPP Fink Airframe Module

3.3.2 Propulsion System Noise Sources

The propulsion system noise estimates were provided by NASA GRC. Engine cycle data at several different flight conditions and throttle settings are required as inputs to generate the engine source noise hemispheres in ANOPP. This cycle data was generated with a NASA NPSS web based tool. The N2A uses two FPR 1.6 direct-drive turbo fan engines with a 1.021 size scale factor to match static thrust. The N2B is calculated with three engines and a 0.9238 size scale factor to match static thrust.

3.3.3 Airframe Noise Sources

The estimated magnitude of airframe noise sources is shown in Figures 49 and 50.

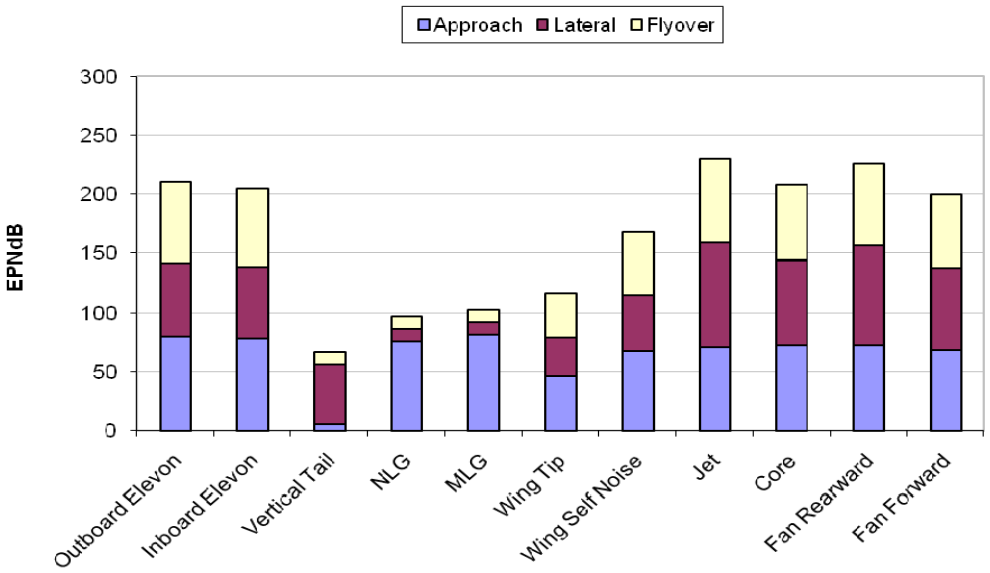

Figure 49 N2A Noise Sources

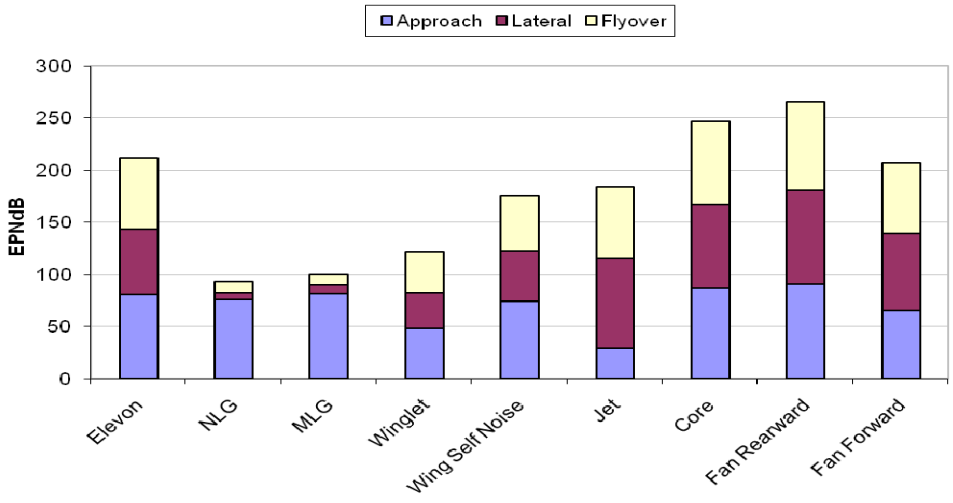

Figure 50 N2B Noise Source Breakdown for N2B.

3.3.4 FAR 36 Noise

The following outlines the reference conditions & ground rules used during the FAR Part 36 noise assessment of the N2A and N2B configurations. The noise certification analyses were performed for the following FAR Part 36 reference day conditions:

- ISA+10ºC
- 70% Relative Humidity
- Zero Wind
- Sea level

The noise certification measurement locations are shown in Figure 51.

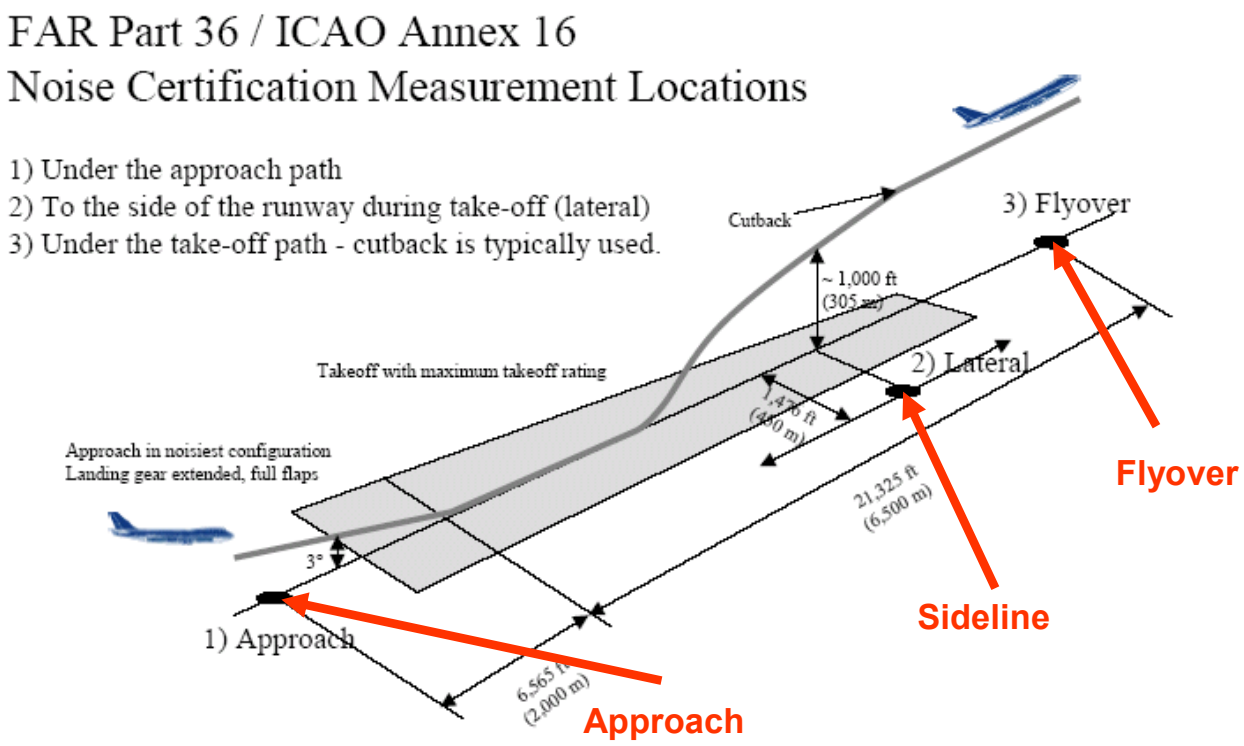

Figure 51 FAR 36 Noise Certification Measurement Locations

The flyover noise is calculated for the greater the following: the thrust to maintain level flight with one-engine inoperative or an all engine climb gradient of 4%. For the lateral condition it is assumed that peak lateral noise occurs when the aircraft altitude opposite the measurement location is at 984 feet. On Approach the noise is predicted for an aircraft height of 394 feet.

Flyover Conditions - Ground Rules

The following ground rules were used to estimate the flyover noise:

- MTOW
- Monitor point at 21325 ft from brakes release
- Maximum takeoff power from brakes release
- V2+10 TAS climb-out speed
- Thrust cutback performed at 3000-4000 feet before monitor
- Assume an instantaneous cutback flight profile

Lateral Conditions - Ground Rules

The following ground rules were used to estimate the lateral noise:

- MTOW
- Maximum Takeoff power
- V2+10 TAS climb-out speed
- Noise monitor at 1476 feet to the side of the runway extended centerline
- Assume initially peak lateral noise occurs at 1000 feet AGL (This will depend on the size and location of the two verticals during N2A configuration development)
- This represents an angle of elevation from monitor to aircraft of 34.1º
- No impact of cutback procedure on peak lateral noise allowed

Approach Conditions Ground Rules

The following ground rules were used to estimate the approach noise:

- MLW
- Approach monitor at 6565 ft from runway threshold (394 feet)
- Aircraft to maintain -3 degree glide-slope
- Define noisiest configuration (usually dirtiest aerodynamic - highest drag condition)
- Vref+ 10 TAS approach speed

The aircraft/engine flight parameters for lateral (sideline), flyover and approach FAR Part 36 reference conditions are shown in Table 6 for N2A and Table 7 for N2B.

Table 6 N2A FAR 36 Flight Conditions

Parameter	Lateral	Flyover	Approach
Flight Path Angle (º)	9.5	2.3	-3.0
Angle of Attack (º)	13.4	13.9	10.7
INB Elevon Angle (º)	-10	-10	-10
Mean OTB Elevon Angle (º)	-10	-10	-10
Fn/δ per Engine (lbs)	68,056	28,612	4,434
N1/√θ (rpm)	3,018	2,320	1,335
Altitude (feet)	1,000	2,104	394
TAS (kts)	145	147	146

Table 7 N2B Aircraft/Engine Performance Data

Parameter	Lateral	Flyover	Approach
Flight Path Angle (º)	9.0	2.3	-3.0
Angle of Attack (º)	13.4	14.0	10.7
INB Elevon Angle (º)	-10	-10	-10
Mean OTB Elevon Angle (º)	-10	-10	-10
Fn/δ (lbs)	38,664	19,729	2937
N1/√θ (rpm)			
Altitude (feet)	1000	2178	394
TAS (kts)	148	151	147

The Phase I noise assessment compared to the N+2 goal of -52dB relative to Far 36 Stage 3 is shown in Table 8. A detailed description of the Phase I noise assessment is in Reference 5 Appendix C.

Table 8 FAR 36 Noise

Noise Certification Conditions	N2A EPNdB	N2B EPNdB
Lateral	90.1	94.1
Flyover	76.9	87.0
Approach	86.8	93.6
Cumulative	253.8	274.7

3.4 Configuration Risk Assessment

A comparative risk assessment between the N2A and N2B relative to meeting the SFW EIS 2020 date was made. A risk assessment was made by NASA in Reference 7 for the SAX 40 in Reference 4 and reviewed for assessing the N2 configuration.

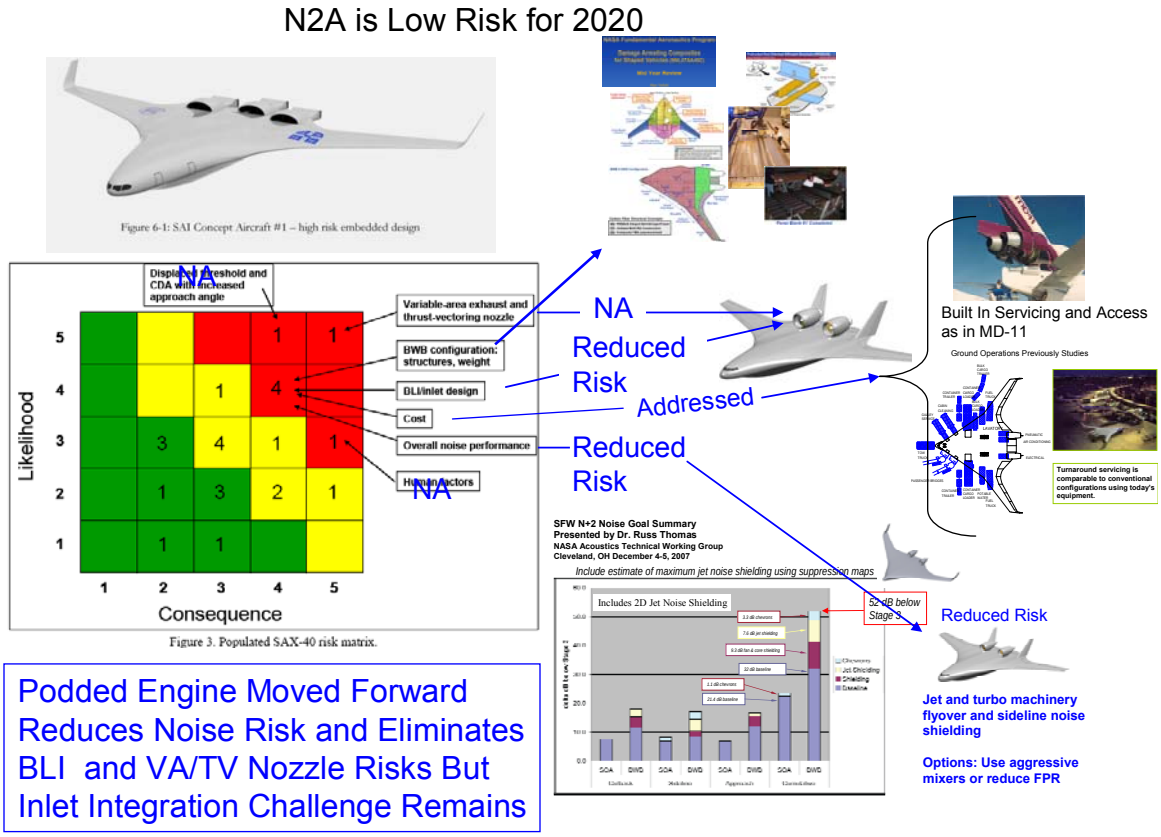

Figure 3. Populated SAX-40 risk matrix.

Figure 52 N2A Risk Assessment

The N2 configuration base as described below is a cargo freighter that eliminates the risks associated with passengers appeal. . Further, using podded engines eliminates the risk associated with the variable area vectoring nozzles. Locating the engine pods in a forward position to achieve shielding of aft propulsive noise moves the inlet into an area where the local onset Mach number is higher and there remains a challenge to minimize adverse propulsion/airframe aerodynamic integrations effects. Addressing this issue was proposed as a part of Phase II.

The N2 Hybrid wing body configurations have been specifically designed for low noise. The starting point SAX-40 employed forward inlet noise shielding from the airplane forebody, aft turbo machinery and combustor internal noise reduction from long acoustically treated nozzle ducts and low aft jet noise reduction from a low pressure ratio fan with mixed flow exhaust. The concept was envisioned as a 2025 technology advanced concept air vehicle. For this investigation, the time frame is 2020 for initial service operation and the technology level was constrained by assuming the development schedule would be similar to the current most recent developments, i.e.

the A380 and B787. Accounting for the need to be at TRL 7 before the sales campaign starts would require TRL 6 in about the 2011-2012 time frame. With this constraint, several features for achieving the very low noise levels in the Silent Aircraft Initiative from which the SAX-40 evolved were not employed. This included the variable take off cycle to minimize sideline noise and using a steep approach. The approach noise metric for FAR 36 specifies a 3 degree glide slope. For a consistent technology comparison between the N2A podded engine installation and the N2B embedded (SAX-40 type) propulsion systems, all the engine and engine internal source noise data was then estimated by NASA GRC. For risk reduction in the 2020 time frame, the podded engine configuration, N2A was created. In this configuration, forward inlet noise shielding is retained. Aft noise reduction is achieved by moving the engine pods forward such that there is aft noise shielding by the airframe trailing surfaces, and sideline noise shielding with vertical tails. . The internal aft radiated noise is thus shielded. Jet noise is created from the flow shear turbulence between the engine exhaust flow and ambient air as a distributed downstream source. With conventional conical nozzles the peak noise is generated where the exhaust flow potential core has dissipated and commonly 5 to 10 nozzle diameters downstream, with the highest frequencies near the nozzle exit and the noise wavelength increasing in the downstream direction. A concept investigated to increase jet noise shielding was to employ geometry that could accelerate flow mixing while shifting the source towards higher frequencies. The intent is to increase the geometric shielding, reduce diffraction from the reduced wave length to shielded length, and increase atmospheric attenuation from the increased noise absorption with frequency. This is depicted pictorially in Figure 53.

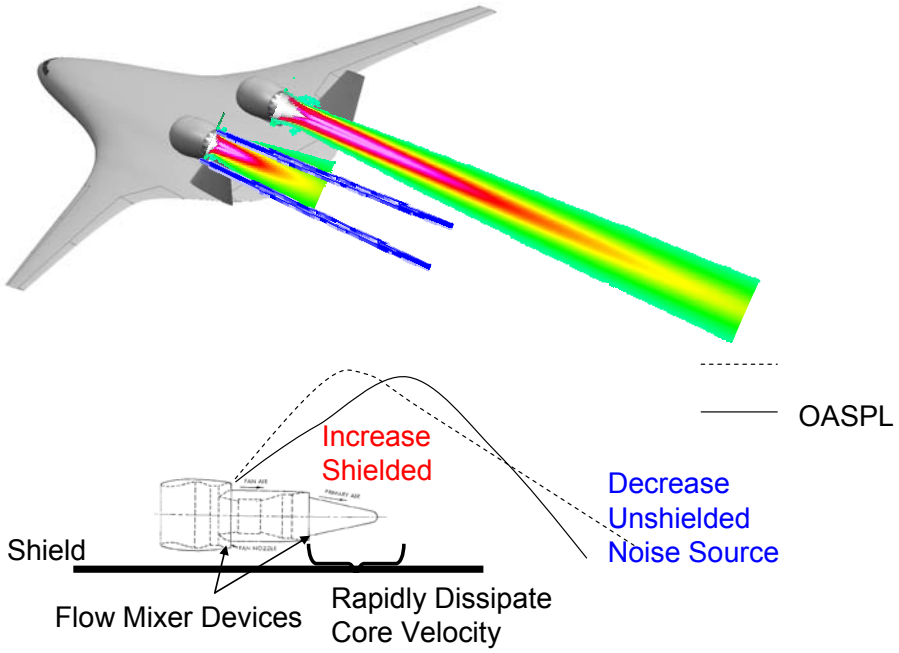

Figure 53 Noise Shielding

Development of concepts to improve jet noise shielding was conducted by Boeing via CFD analyses of mixer nozzle concepts to accelerate the turbulent mixing, and UCI

conducting small scale experiments in the UCI Aeroacoustics Facility. CFD analyses of the rate of mixing and turbulent intensity analyses presented in Figure 54 shows promise for greatly accelerating the downstream jet mixing process.

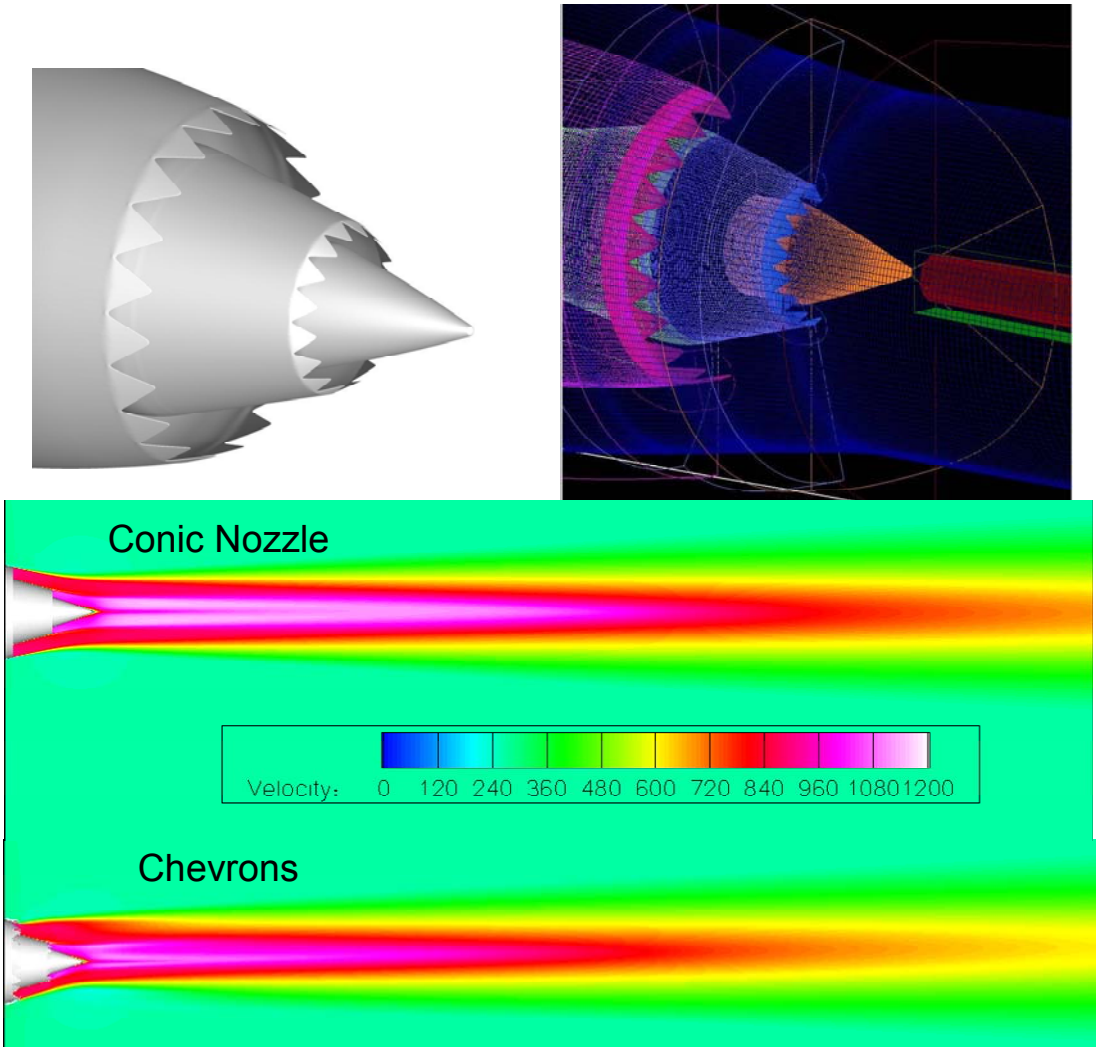

Figure 54 CFD Analysis of Flow Mixing

Small scale static experiments by UCI show promise using a chevron with a porous wedge which could significantly improve jet noise shielding. The concepts are envisioned as variable geometry devices which would be deployed after lift off and then retract for higher altitude climb and cruise. This jet noise compression concept is used in N2A with the shielded noise based on the UCI tests. Further larger scale testing would be required because there is an issue whether the very high frequencies beyond the measurable range are significant.

The N2B configuration was derived maintaining the Granta type propulsion system with some of the higher risk elements changed as noted in Figure 55.

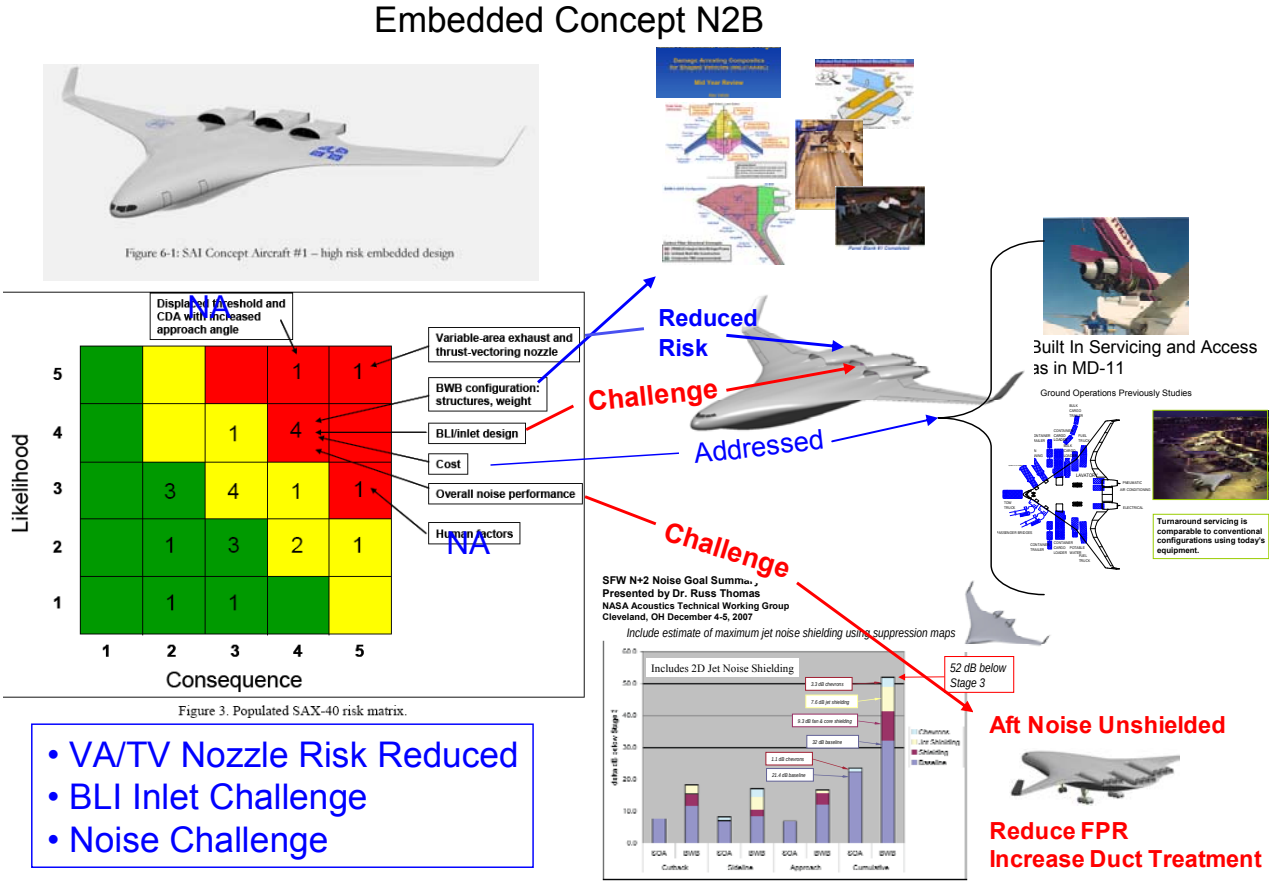

Figure 3. Populated SAX-40 risk matrix.

Figure 55 N2B Risk Assessment

N2B then still has a significant challenge for engine operability with boundary layer ingestion inlets and the need for one per rev blade integrity from circumferential distortion. The ability to achieve a high efficiency with single stage fans in high by pass ratio engines employing boundary layer ingestion inlets is yet to be proven. Further a preliminary assessment of controllability identifies the N2B at risk for meeting certification requirements because of a low pitch control surface volume, such as for upset protection during descent when engines are at idle and for all engines out flight control. Continuing investigation to reduce N2B noise is continuing in Phase II.

3.5 Phase I Metrics

The fuel burned was compared to current technology wide body wing and tube cargo freighters of equivalent capability at the time this contract was started. As previously discussed this was agreed to with NASA as the likely first opportunity for an ELNHWB with very low noise in the 2020 time frame. As previously noted, air cargo is growing

faster than passenger traffic and a freighter would not have the initial resistance relative to displays replacing windows and demonstrating ride quality. Very low noise can also be of greater benefit to freighters for expanding night operations. Conventional wing and tube configurations do not benefit from propulsive noise shielding by airframe surfaces, but have the opposite effect wherein the wings and flaps reflect noise downward increasing flyover noise. To determine the capabilities of the CMI SAX-40 starting base an interior layout was reviewed and assessed as capable of accommodating 262 passengers using Boeing's 3-class rule set compared to the 215 passengers and 5000 nmi range used in the SAX 40 as shown in Figure 56. As further shown in Figure 56, a current airplane of this passenger size is then the B767-400ER, with the B767-300ER and the A330-200 also being similar size class and design range. These three airplanes formed the basis for measuring progress on achieving a 25% fuel burn improvement wherein the B767-400ER range was extended for comparison purposes.

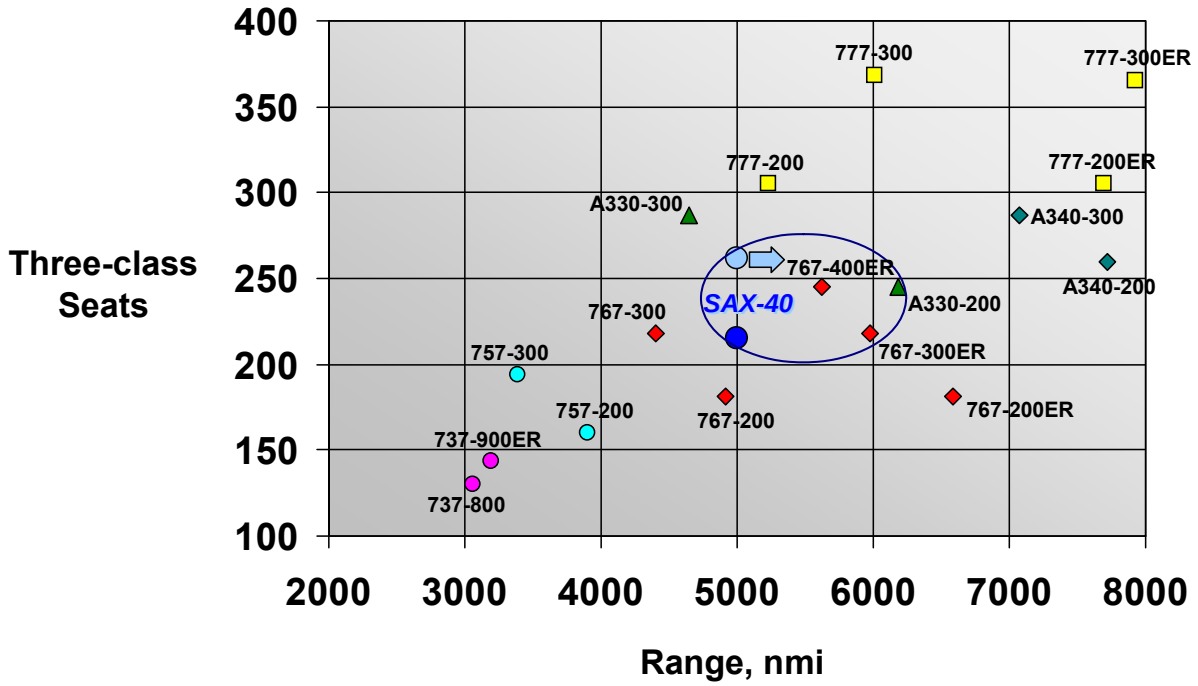

Figure 56 Nearest Comparison Aircraft to N2

The fuel burned efficiency metric is based on the fuel efficiency of doing work at the same range as a conventional cargo aircraft with a similar class payload (in this case the B767/A330 freighters). The efficiency metric used for this analysis was (Payload x Range) / (Fuel Burned) = payload work done per pound of fuel burned, for which the units are lbs x nautical miles / lbs.

Also, in order to see the benefit from the configuration with respect to technology level, a comparison is made for a conventional tube-and-wing with the same advanced technology levels in the engines and structures as was incorporated in the Hybrid Wing Body vehicles.

The A330-200FX was selected as the current conventional wing and tube freighter for fuel burn comparison to the Hybrid Wing Body vehicles. The results are shown in Figure 57.

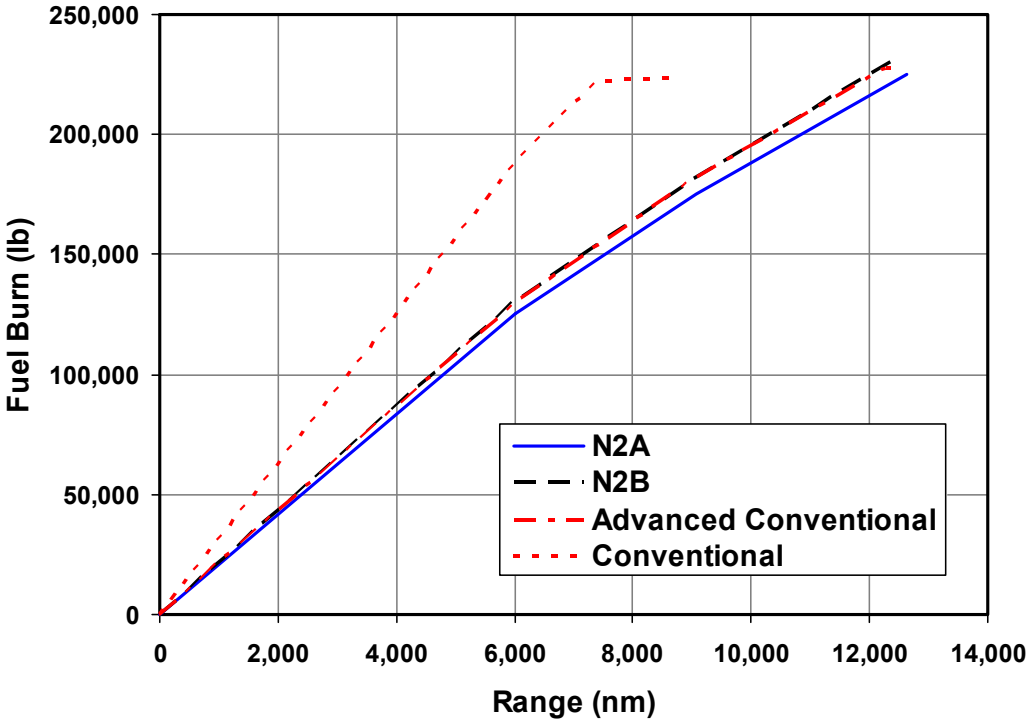

Figure 57 Fuel Burn Comparison of Hybrid Wing Body and Conventional Freighters

A review of the N2A compared to other studies shows that the payload packaging from the SAX 40 airfoil stack results in large unused internal volume and a much larger fuel tank volume than needed for 6,000 nmi ranges. While the N2 is an efficient configuration the OEW and fuel burn could be improved if the external aero mold lines were optimized for a cargo freighter carrying standard containers. Figure 58 shows a comparison between a previous Boeing BWB freighter study that had a higher efficiency with the N2A. The BWB 450-1U has proprietary mold lines and was not available for use in this project.

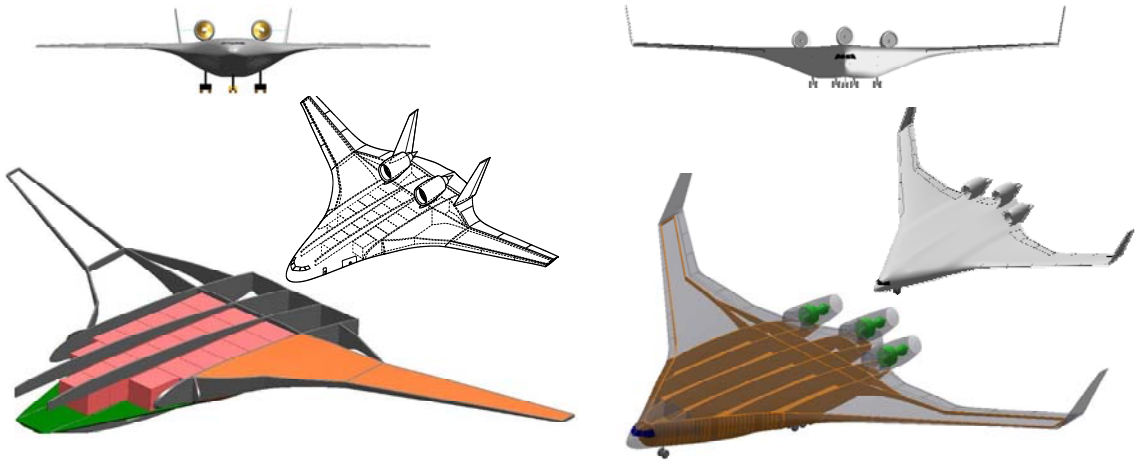

N2A Freighter

BWB 450-1U Freighter

N2 cargo freighter derived from passenger SAX 40

Meets -25% fuel burned
- Carries large unused volume for container cargo freighter
- Total available fuel tank volume not needed

450-1U mold lines are proprietary

Figure 58 Cargo Inboard Profile Comparison

The SAX 40 base was an available non-proprietary hybrid wing body configuration developed by extensive analysis that could be used to be within the scope of this investigation. The SAX 40 evolved by the Cambridge MIT Institute UK sponsored Silent Aircraft Initiative (Reference 4) through a progression of configurations starting with a WINGMOD SAX 12 to the SAX 40 by 35 researchers over 3 years. The configuration evolved with a high L/D and thus provided a good starting point.

However for acoustic testing to validate very low noise predictions, the configuration is representative and improved payload work efficiency is probable with configuration refinements. Different efficiency results would probably occur for passenger aircraft.

For acoustic purposes where shielding is limited by diffraction, the differences from relatively small changes in shielding surfaces area should not be significant. This is apparent in Figure 59 showing an overlay of a BWB 450 type scaled to the same size as the N2A. The increase in useful payload volume for the more efficient 450 configuration would have minimal affect on the noise shielding.

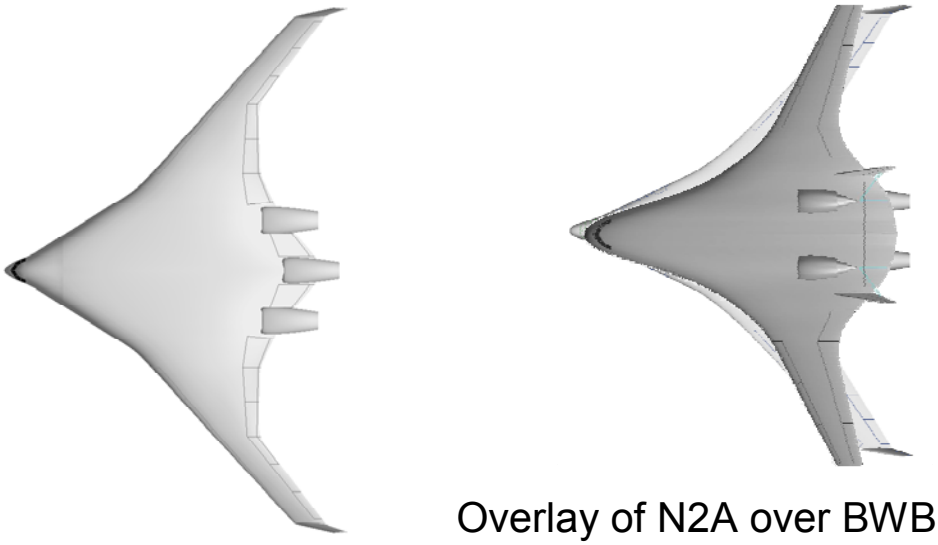

Figure 59 Overlay N2A on Scaled BWB 450

It should be noted that it is doubtful that a wing and tube can come close to meeting N+2 goals of a cum -52 dB noise with a -25% fuel burn, and neither could the BWB 450 with the aft engines although the later should be lower noise than a tube and wing because of the forward inlet noise shielding and lack of adverse downward noise reflections from wings and flaps that conventional wing and tube configurations have. The wing and tube configuration would be expected to need very high by-pass ratio fans with large acoustically treated inlets and exhausts for comparable noise levels. This would incur large weight and drag penalties that are compounded when integration considerations for extremely high bypass ratio engines are included. The most recent new transports such as the B787 and A380 have a by-pass ratio less than 12 for best economics. A past study on a wing and tube configuration shows that integration penalties result in by-pass ratios less than 12 for minimum fuel burned. The study from Reference 8 showed that min fuel burned and economics deteriorates and a noise floor at about -30 dB still occurs with conventional wing and tube configurations.

3.5.1 Fuel Burn Compared to -25% Goal

The N2A and N2B are shown relative to the trend band for current cargo freighters in Figure 60. It could be argued that then comparison be made for the middle of the band. Even using the highest efficiency top line, the N2B meets the -25% SFW goal while the N2A exceeds the goal at – 29%.

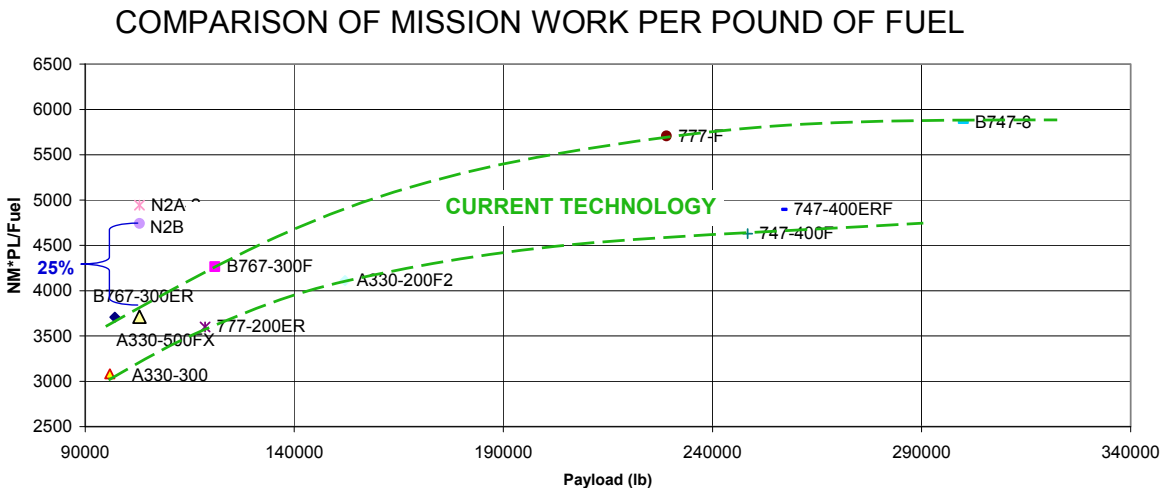

Figure 60 Fuel Efficiency Compared to N+2 Goal

3.5.2 Noise Compared to -52dB Goal

The HWB provides a very high level of noise shielding without the downward reflections on a tube and wing. Table 9 shows the noise shielding increments at peak directivity angles.

Table 9 Noise Shielding Increments At Peak Directivity Angles.

	N2A ΔdB at Peak			N2B ΔdB at Peak		
	Flyover	Lateral	Approach	Flyover	Lateral	Approach
Fan Fwd	24.4	22.6	23.5	27.1	23.5	25.0
Fan Rwd	19.6	14.9	19.6	--	--	--
Core	19.4	12.0	19.2	--	--	--
Jet	3.8	3.6	5.1	--	--	--

The Noise relative to the FAR 36 Stage 3 goal is shown in Table 10.

Table 10 FAR36 Noise Compared to N+2 Goal

Noise Certification Conditions	N2A EPNdB	N2B EPNdB
Lateral	90.1	94.1
Flyover	76.9	87.0
Approach	86.8	93.6
Cumulative	253.8	274.7
Delta from N+2 Goal	-5.3	-26.2

3.5.3 Phase I Compared to N+2 Goals

The summation of metrics at the end of Phase I based on the N2A is shown in Figure 61.

This Phase I effort resulted in predicting the N2A could meet the SFW fuel burn metric by refinements for propulsion airframe integration to avoid integration drag. The noise goal was approached with the expectation of meeting the goal in Phase II.

	"N+2" Generation Hybrid Wing 2018-2020	N2A Status Efficient Low Noise Hybrid Wing Body 2020
Noise (cum below Stage 3)	- 52 dB	- 46.7 dB
Performance: Aircraft Fuel Burn (relative to current technology	- 25%	- 29%

Figure 61 ELNHWB Phase I Relative to Goals

This Phase I investigation has thus resulted in the assessment that the N+2 fuel burned and noise goals may be achievable with continuing R&T on HWB types of air vehicles. As noted above, the fuel burn goal will require refinements to minimize the transonic interference drag that can result from integration of nacelles in a forward location needed to provide aft noise shielding.

A part of the continuing R&T is the need to further improve noise prediction methodologies with a wind tunnel test program to validate these improvements in a relevant environment.

Purposes of Phase II were to improve then HWB configuration towards meeting N+2 goals and design and build a wind tunnel model based on the configuration for acoustic and low speed aerodynamic testing for a configuration representative of meeting the goals for EIS 2020. The N2A had better fuel efficiency and lower noise than the N2B. The N2A was also assessed as low risk for EIS 2020. The N2B was assessed as high risk for EIS 2020 for using of boundary layer ingestion inlets that would need to be at TRL 6 in the 2011-2012 time frame. The configuration also has certification challenges related to flight control with all engines out. Based on the results from Phase I, it was proposed and agreed by NASA for Phase II to continue focused primarily on the N2A podded configuration and to develop a wind tunnel model for this. Work on the N2B is continuing by MIT and results will be published as an amendment to this final report in June 2011

4.0 PHASE II RESULTS

4.1 Transonic Configuration Refinement

The configuration development in Phase I was, as noted above, a Level 1 conceptual development to determine potential and was thus RANS CFD limited to the clean wing. That is, the CFD analyses were for the wing body without the interference effects of the nacelle/pylon or the effects of flow spillage that occurs with an inlet mass flow ratio less than unity. A RANS CFD analyses showing the IsoMachs above the clean wing using OVERFLOW is shown in Figure 62. The location of the podded nacelle is superimposed on the IsoMachs. The local Mach number at the inlet location is seen to be above 0.90.

Embed engine in wing-only flowfield
Engine "sees" M ~ 0.9

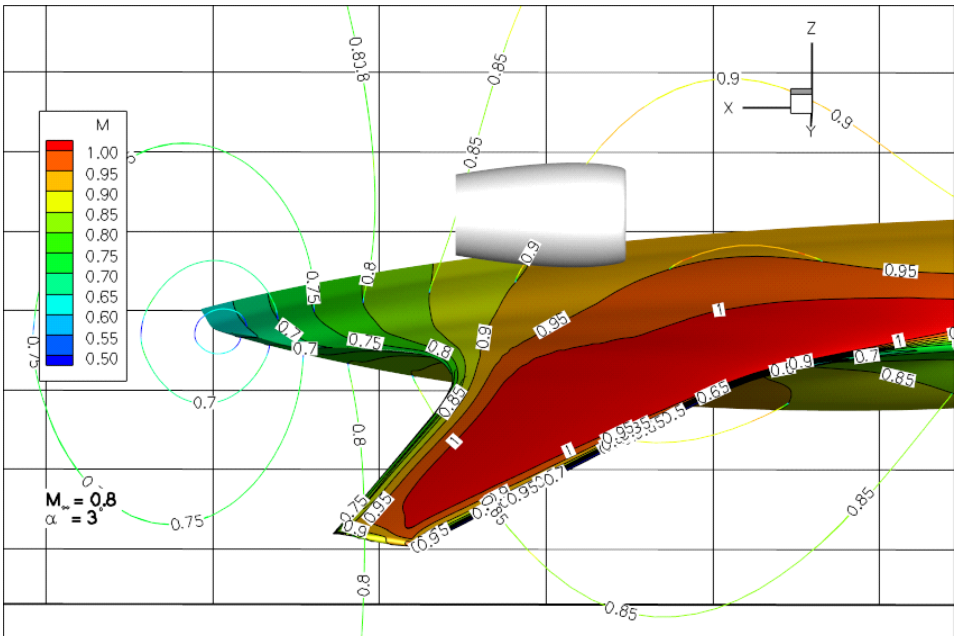

Figure 62 CFD Analysis of N2A Baseline

The inlet outer cowling lines where developed using design methods for conventional wing mounted engines with nacelles in freestream onset flow. The over wing flow into the inlet is at a Mach number greater than the flight speed. Mach number effect on the inlet cowling is apparent in Figure 63 where strong shocks occur around the outer cowling because the onset Mach number is greater than the cowl design speed.

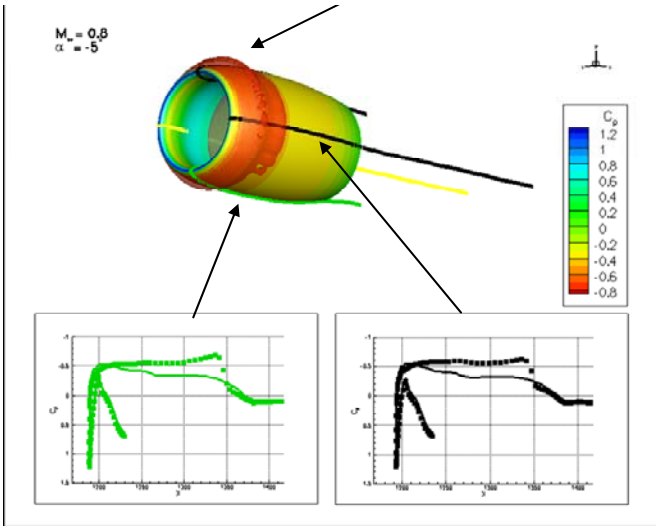

Symbols – M_∞ = 0.9
Lines -- M_∞ = 0.8

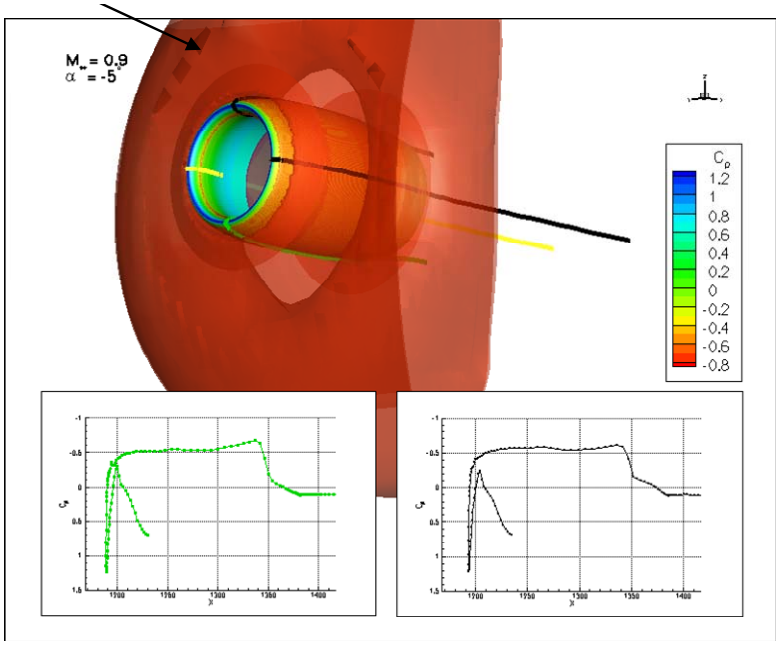

Figure 63 N2A Inlet CFD Analysis – Isolated Engine Cowl Lines

Further CFD analyses were conducted with a flow through nacelle at an inlet mass flow ratio of 0.6 representing an end of a constant altitude climb-cruise segment. The effect of the nacelle on the surface with a mass flow ratio less than unity is shown in a side-by-side comparison in Figure 64. The gray shading is the surface envelope for supersonic flow. There is a significant loss in lift because the inlet spillage disrupts the lift creating flow circulation over the wing body. Also apparent are the strong shocks from then sudden drop in flow velocities on the nacelles. Based on past experience, much of

performance degradation could be recovered by reshaping mold lines to account for the presence of the nacelles. The nacelle cowls also need to be redesigned for the higher onset Mach number with flow spillage.

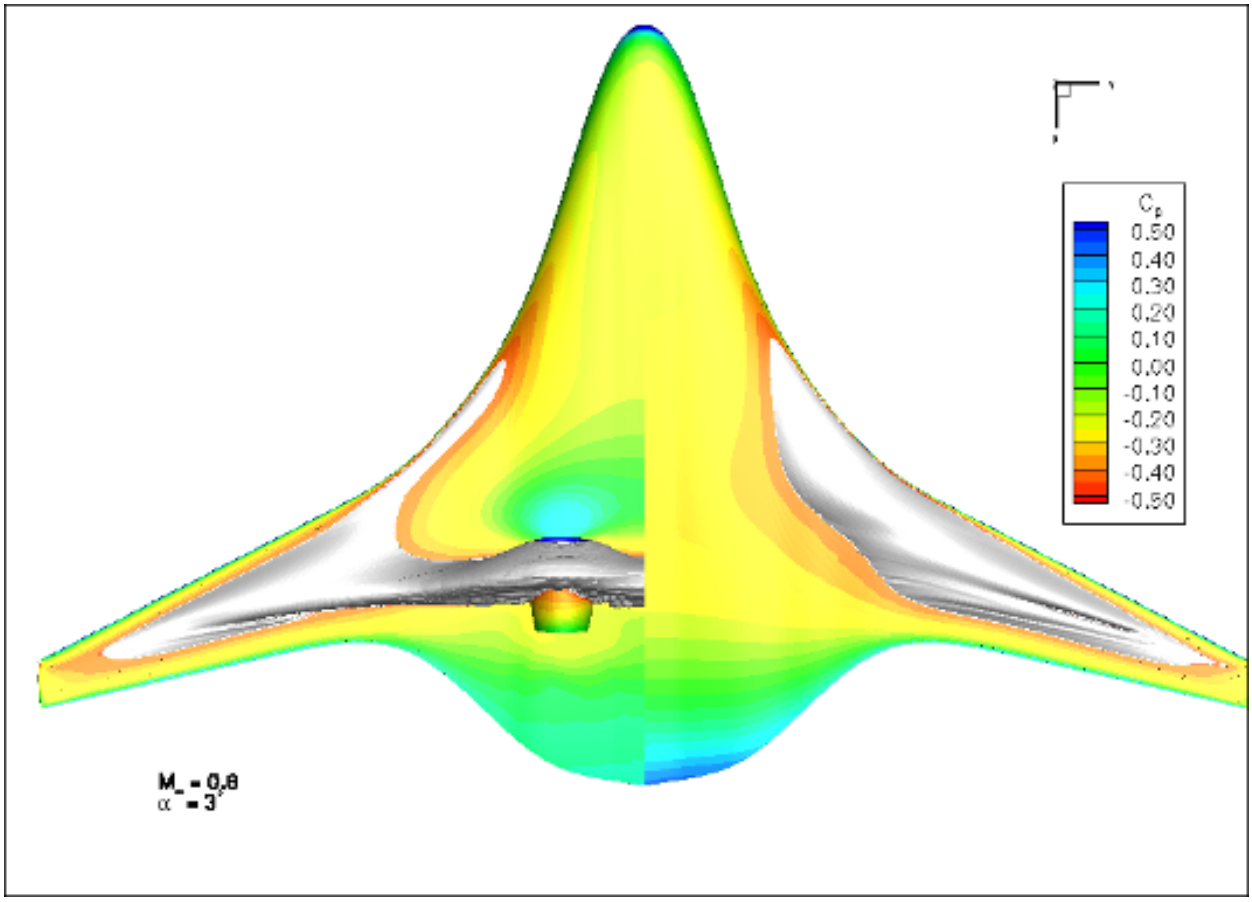

Figure 64 Effect of Nacelle on Surface

Diagnostic analyses were conducted to determine refinements needed. Some results are shown in Figure 65. There are areas where the flow is highly supersonic resulting in shock induced flow separations.

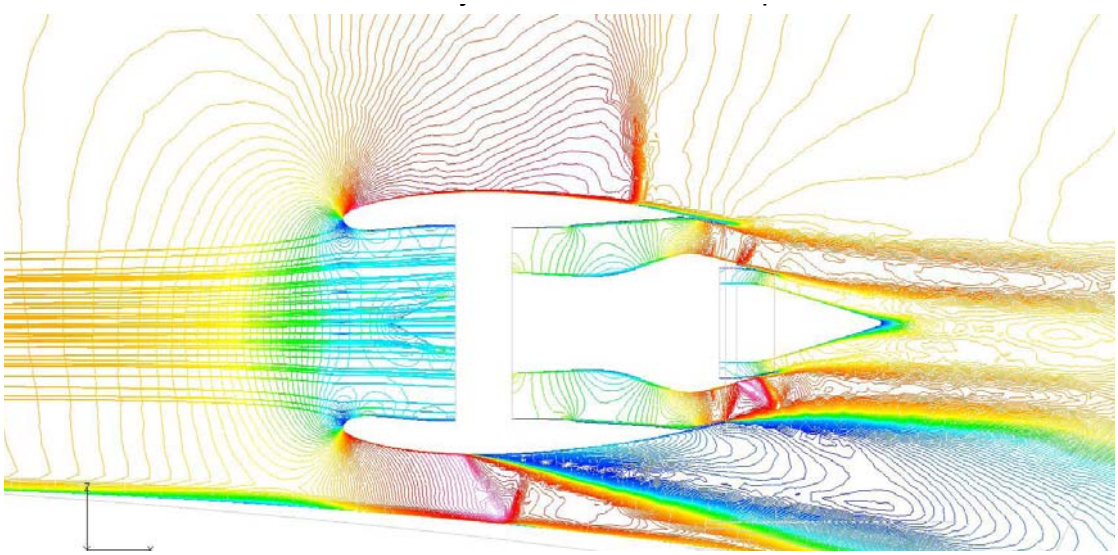

Problems are strong shocks with induced flow separations

Figure 65 Integrated Power-On CFD Analysis

An initial assessment was to determine whether a change in nacelle axial location, height above the wing/body surface, or increasing inlet mass flow ratio to reduce flow spillage around the inlet cowl could be a remedy. The results were negative as depicted in Figure 66, because relocating the engine was not sufficient and re-design of the wing and cowl were needed.

Nacelle position and inlet mass flow ratio were varied.

L/D still at from 10 to 14

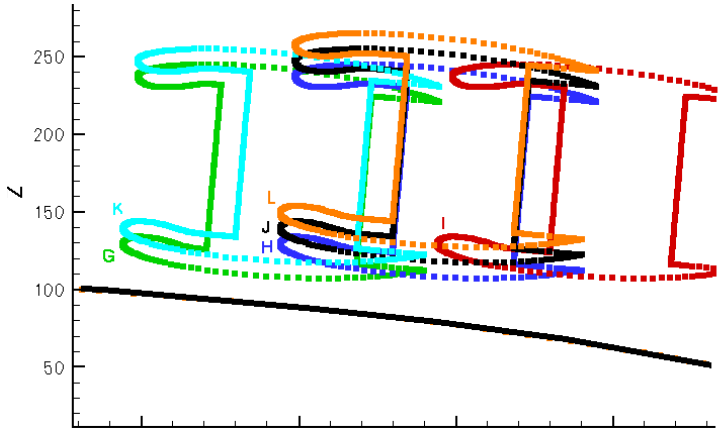

Figure 66 Engine Position and Mass Flow Ratio Study

It was believed achieving significant aft noise shielding needed to have about 2 nozzle exit diameters of shielding. Retaining this while reducing the local inlet onset Mach number would require increasing the centerbody chord length.

The original N2A planform was modified with a trailing edge extension (TEX) to address several potential issues with the original configuration. The reasons that drove the incorporation of the extended trailing edge include:

- engine nacelle is located in a lower Mach number region
- increased engine forward shielding for reduced noise
- increased longitudinal control power with the incorporation of an elevon on the extension
- Maintain engine rearward shielding for reduced noise
- simplified vertical tail integration

The impacts on the configuration are illustrated in Figure 67.

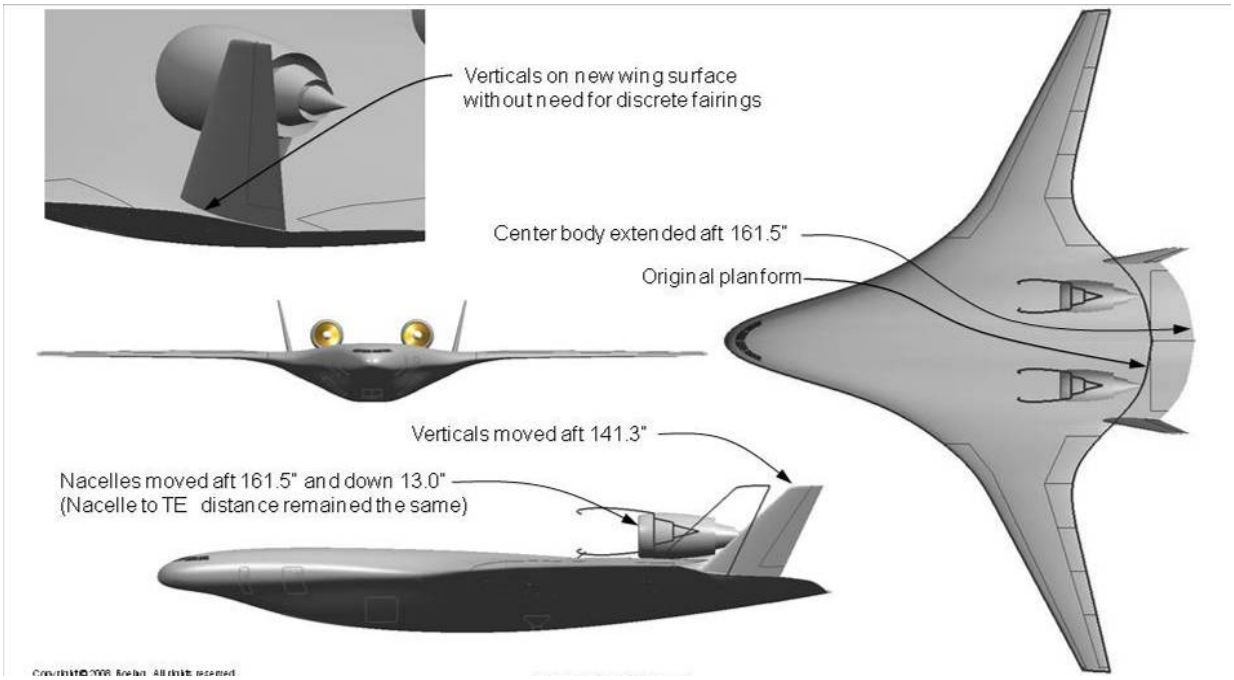

Figure 67 Extended Trailing Edge Configuration Modifications

The TEX is defined by a 10% chord extension on the centerline (161.4”) with constant extension out to y=293.48” on the wing. The original airfoil is modified starting at 60% chord and projected aft from that point to the new trailing edge location such that curvature continuity is maintained at 60% chord. No changes are made to the airfoil forward of 60%. A typical airfoil comparison is shown in Figure 68.

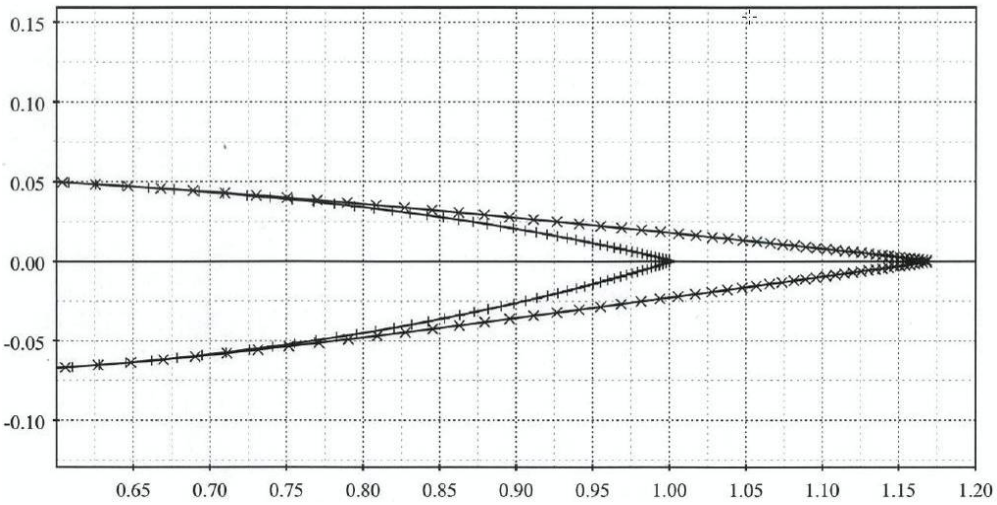

Figure 68 Typical Extended Airfoil Section

The camber of the extended portion of the airfoil was designed such that the TEX has an insignificant effect on aircraft performance, i.e., L/D, spanload and pitching moment. Figure 69 shows the overall effect of the TEX on wing pressures and aerodynamic performance at M=0.80 at a typical cruise C_L.

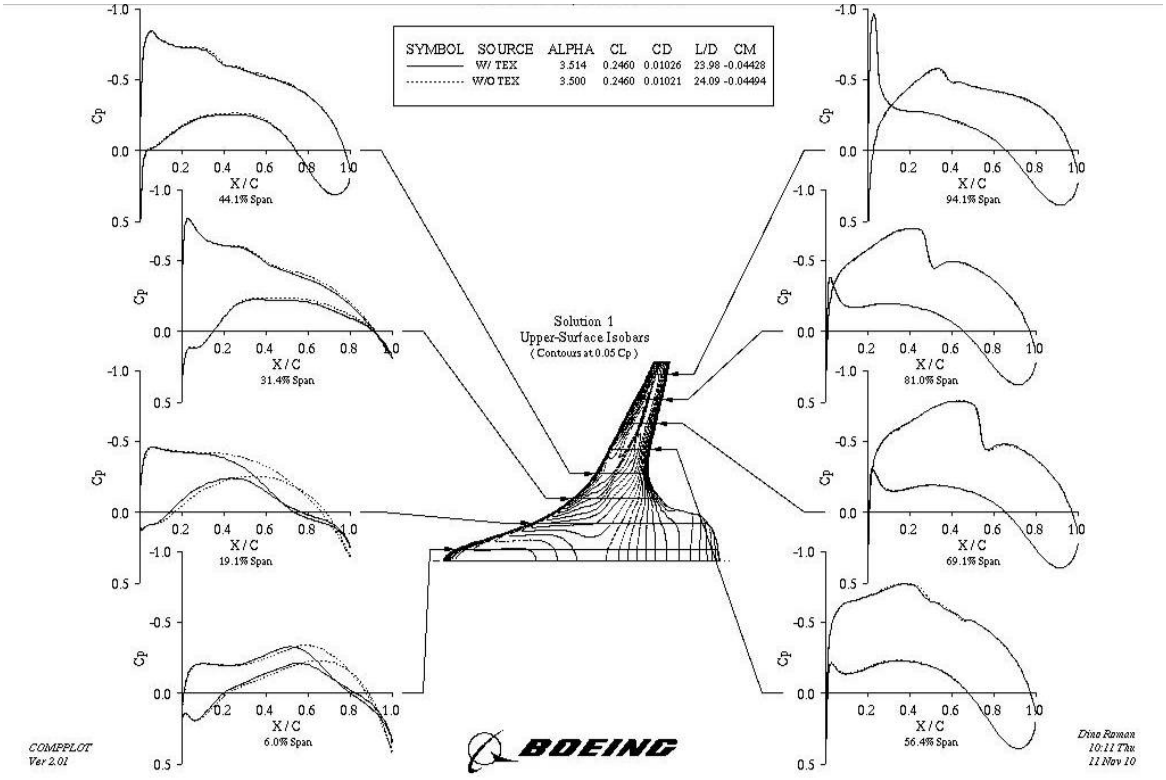

Figure 69 Pressure Distributions and Aero Performance w/ and w/o the TEX

The Mach number at the inlet location was successfully reduced from 0.951 to 0.863 as shown in Figure 70.

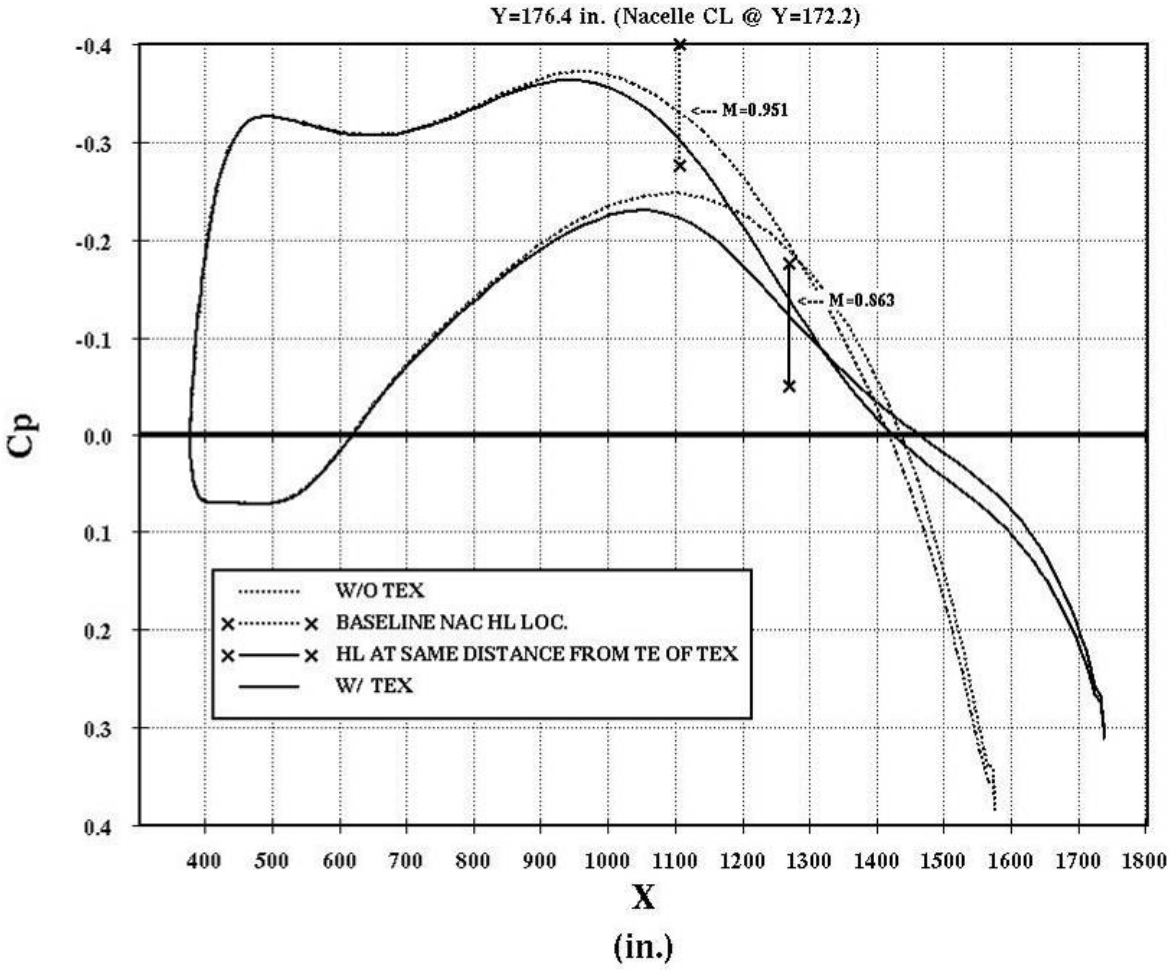

Figure 70 Mach Number Reduction at Inlet Location

With the reduced inlet onset Mach number, it was also decided to reflect using a mission profile that should be enabled by NGATS allowing a continuous climb cruise as to a step climb to constant altitude cruise segments currently used. With higher by-pass ratio engines, the sfc vs thrust as seen in Figure 27 is very flat at high power settings. The N2A with a min fuel burn step climb cruise at 35K/39K/43K ft altitude segments is at a CL starting at 0.255 and down to 0.216 in the 39K segment. The L/D vs CL is shown in Figure 71. This indicates the cruise range for the N2A is on the left or rising slope. For best Breguet factor of M x L/D / SFC, the best efficiency is a continuous climb cruise at the high power setting that has the highest corrected mass flow. This then also increases the cruise average inlet mass flow ratio reducing the inlet flow spillage. Reducing inlet flow spillage allows for a thinner cowl, reducing the nacelle/pylon/centerbody channel flow velocities, and making the transonic propulsion/aero integration easier. This was accounted for in refinement process.

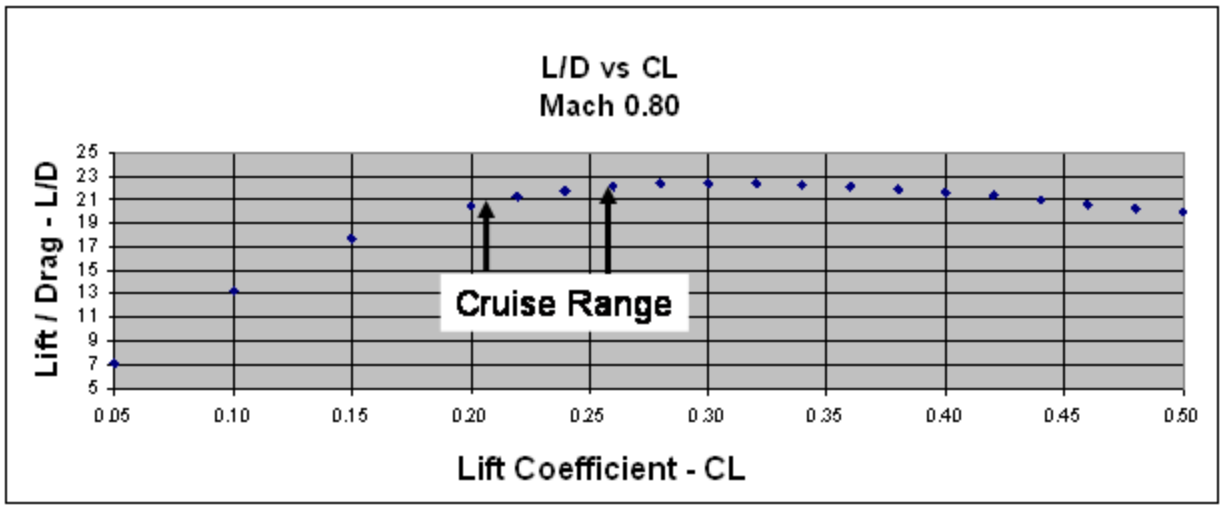

Figure 71 L/D Range for Step Climb-Cruise

The nacelle outer cowl lines were redesigned for the onset flow conditions using CDISC. The improvement is seen in Figure 72.

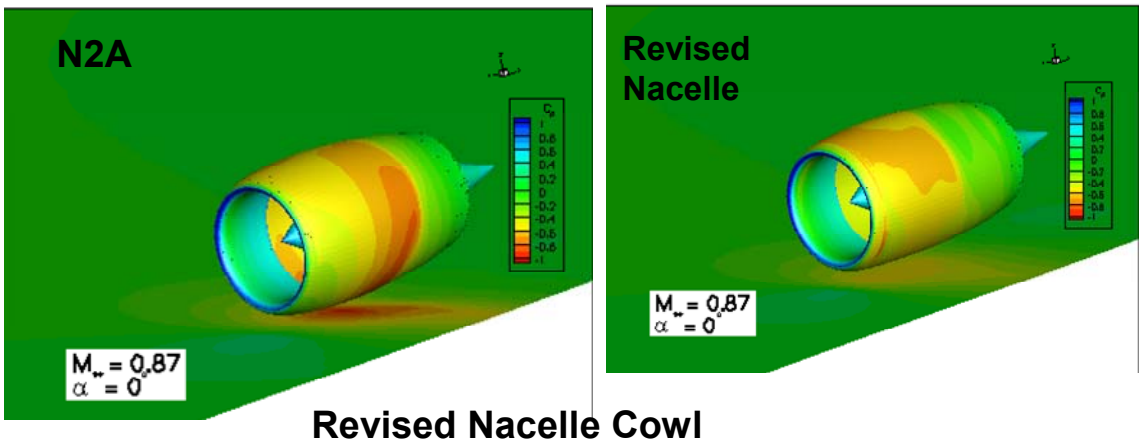

Revised Nacelle Cowl

Figure 72

RANS CFD refinements were then continued with the nacelle integrated on the wing body with pylons and vertical tails. Figure 73 depicts some of the progress.

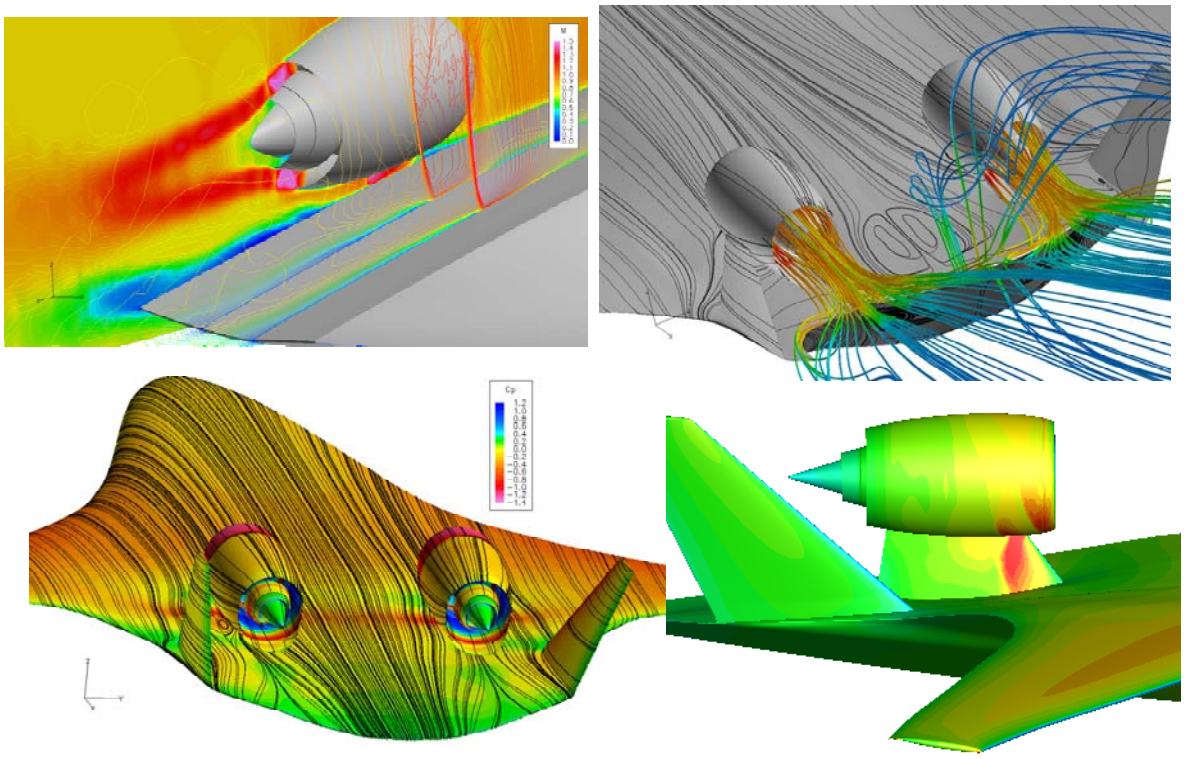

Figure 73 CFD Based Configuration Refinements

The end results were revised mold lines void of large area of flow separation as shown in Figure 74. The verticals were then aligned with the flow.

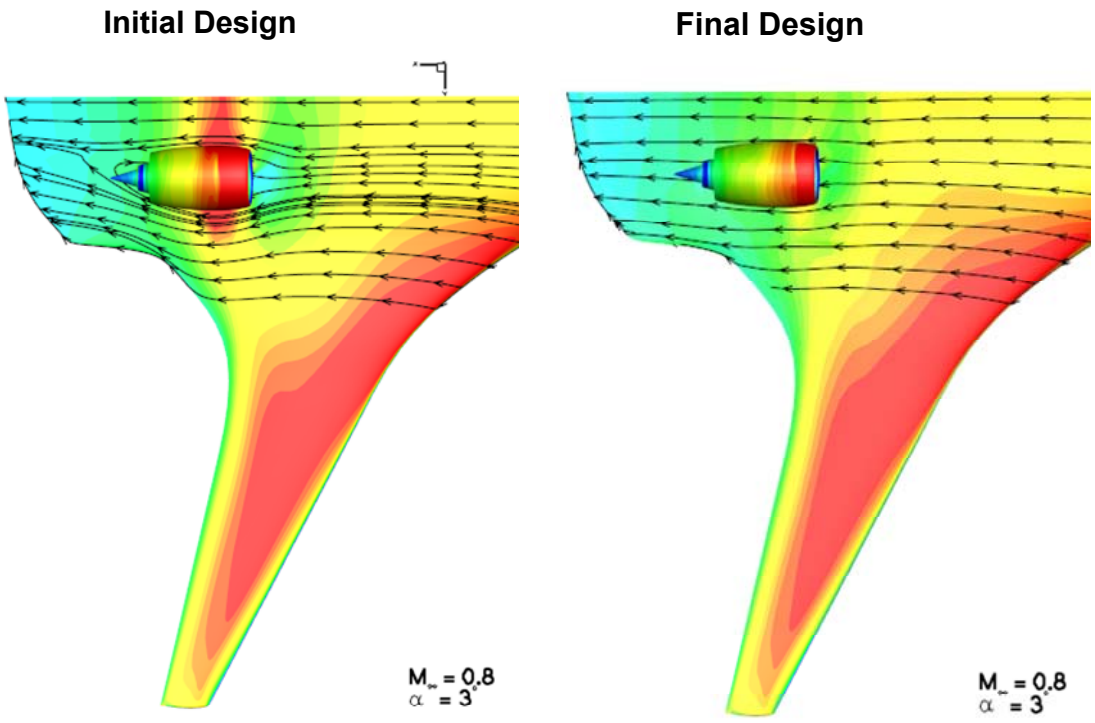

Figure 74 Evolved Design Showing Planform Surface Streamlines

Integrated RANS CFD analyses including propulsive power on were conducted and the evolution history is shown in Figure 75. Note that the comparisons are for relative values because the L/D was calculated from the pressure area integral that used the engine fan face and fan frame exit planes as boundaries. Thus internal duct viscous losses are in the drag. Configuration A is for the clean wing with verticals but without nacelles and pylons. B was with revised nacelle lines developed using CDISC to design the nacelle outer mold lines for the local onset Mach number without strong shocks. C modified the centerbody lines with “dishing” to reduce the converging-diverging channel cross sectional area between the nacelle/centerbody that was resulting in supersonic flow with strong shocks, but did not include the pylon since strong shocks result flow separation that increases drag and reduces lift. D was a further refinement to the lines including the pylon. Further attempts at improvements in E and F, including elevating the nacelle did not improve from D. Since the L/D was restored to close to the clean wing if the clean wing L/D is reduced for nacelle and pylon parasite drag, configuration D is judged to be representative of an efficient transonic configuration that was the objective for defining the wind tunnel model.

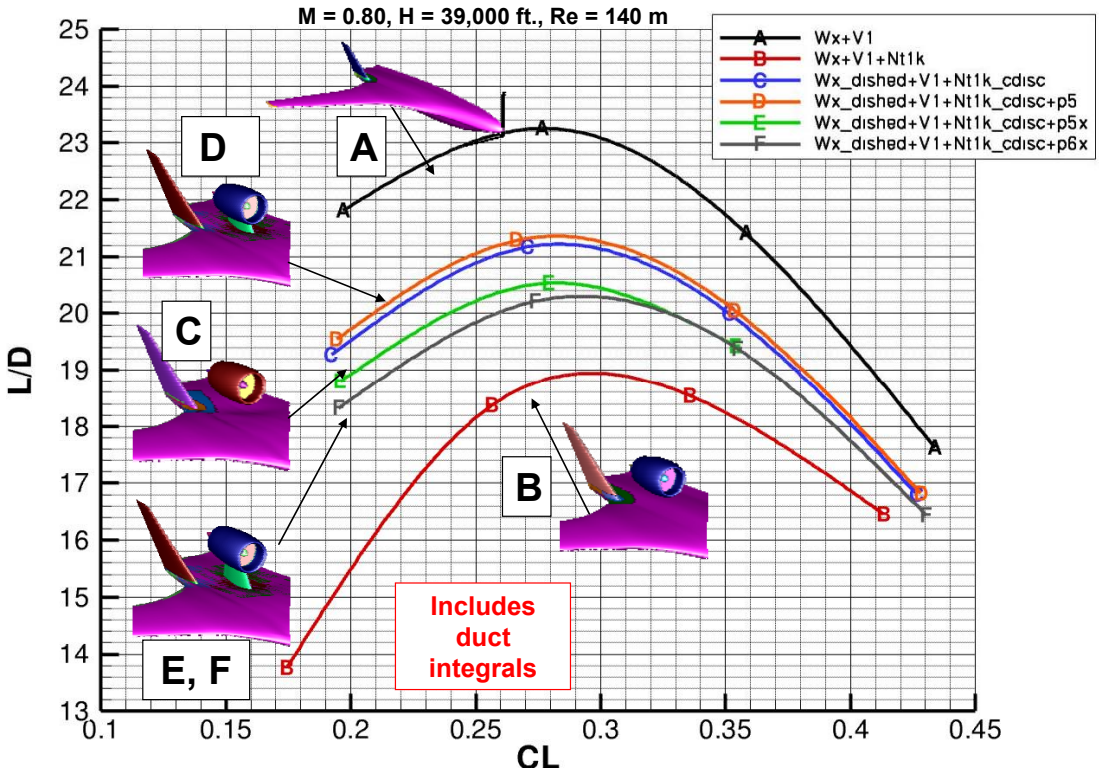

Figure 75 Evolution of Efficient Transonic Performance

4.2 Evolved Configuration N2A-EXTE

Phase II evolved the configuration to improve transonic cruise efficiency. Figure 76 shows the approach in which the lower nacelle mold lines where changed to eliminate the converging-diverging flow channel that was resulting in supersonic flow causing strong shocks.

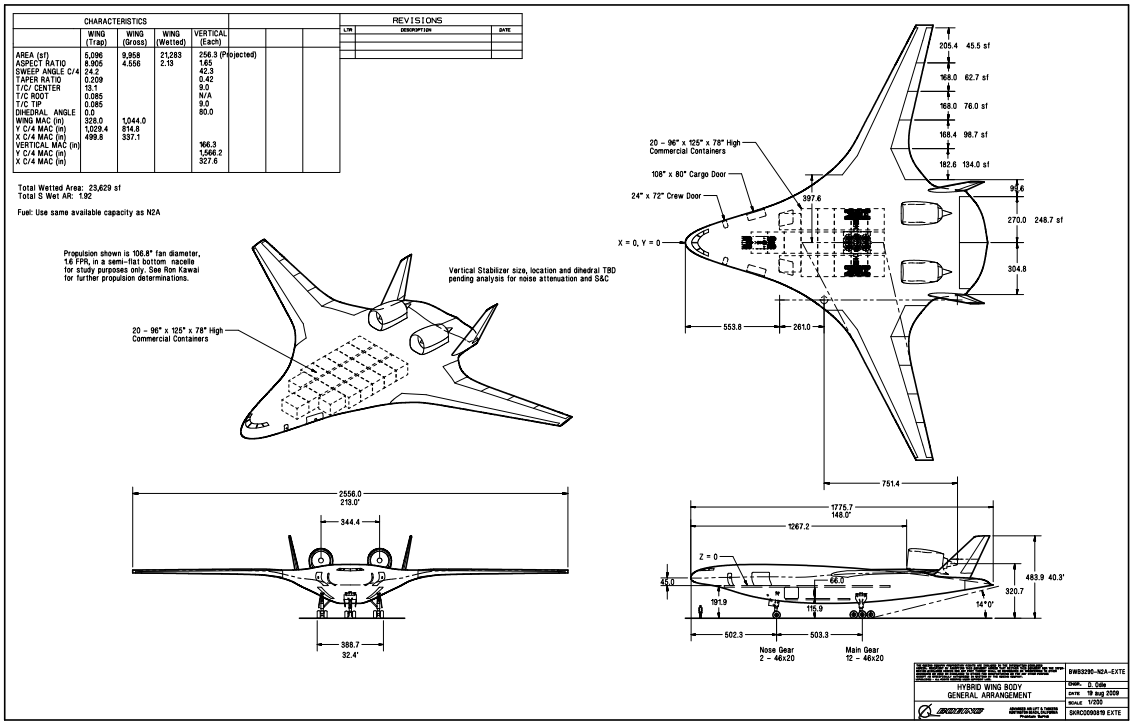

Figure 76 Extended Trailing Edge with Flat Bottom Nacelle

Alternatively, Figure 77 shows the versions wherein the transonic efficiency was improved by changing the mold lines in the channel between the nacelle and centerbody. The former configuration employs a “sugar scoop” nozzle to eliminate a diverging flow channel between the nozzle and centerbody. This configuration requires further refinements to the nozzle since the as drawn lines results in poor internal nozzle performance. The fuel efficiency and noise assessments were therefore made for the configuration with the mold line changes to the centerbody.

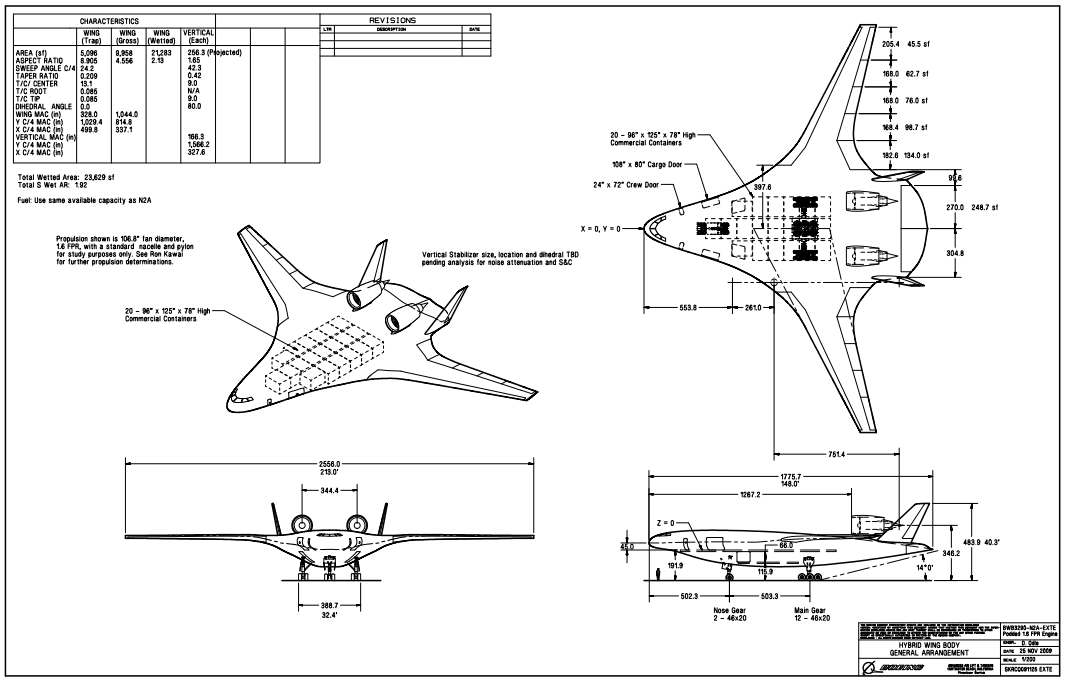

Figure 77 Extended Trailing Edge with Scalloped Centerbody

The N2A-EXTE was developed that extended the trailing edge to allow moving the engines aft while maintaining the aft propulsion noise shielding. While this increased surface area and thus viscous drag, this reduced the t/c (thickness/chord ratio) that reduced compressibility drag such that the L/D of the N2A analysis level was recovered. However, the increased surface area did increase weight as well as absolute drag so there was an increase in fuel burn compared to the Phase I analyses.

4.2.1 Drag

The CFD analysis is used to develop an efficient configuration at the cruise design point. The integrated CFD analyses shows the relative drag improvement void of strong shock flow separation. However, it is difficult to separate the propulsion forces from aero forces in the integrated CFD analyses for defining absolute drag without propulsive forces. Thus the drag polar was developed from the CFL3D clean wing with and then the nacelle, pylon and vertical tail drag are added. The N2A-EXTE drag polar is shown in Figure 78.

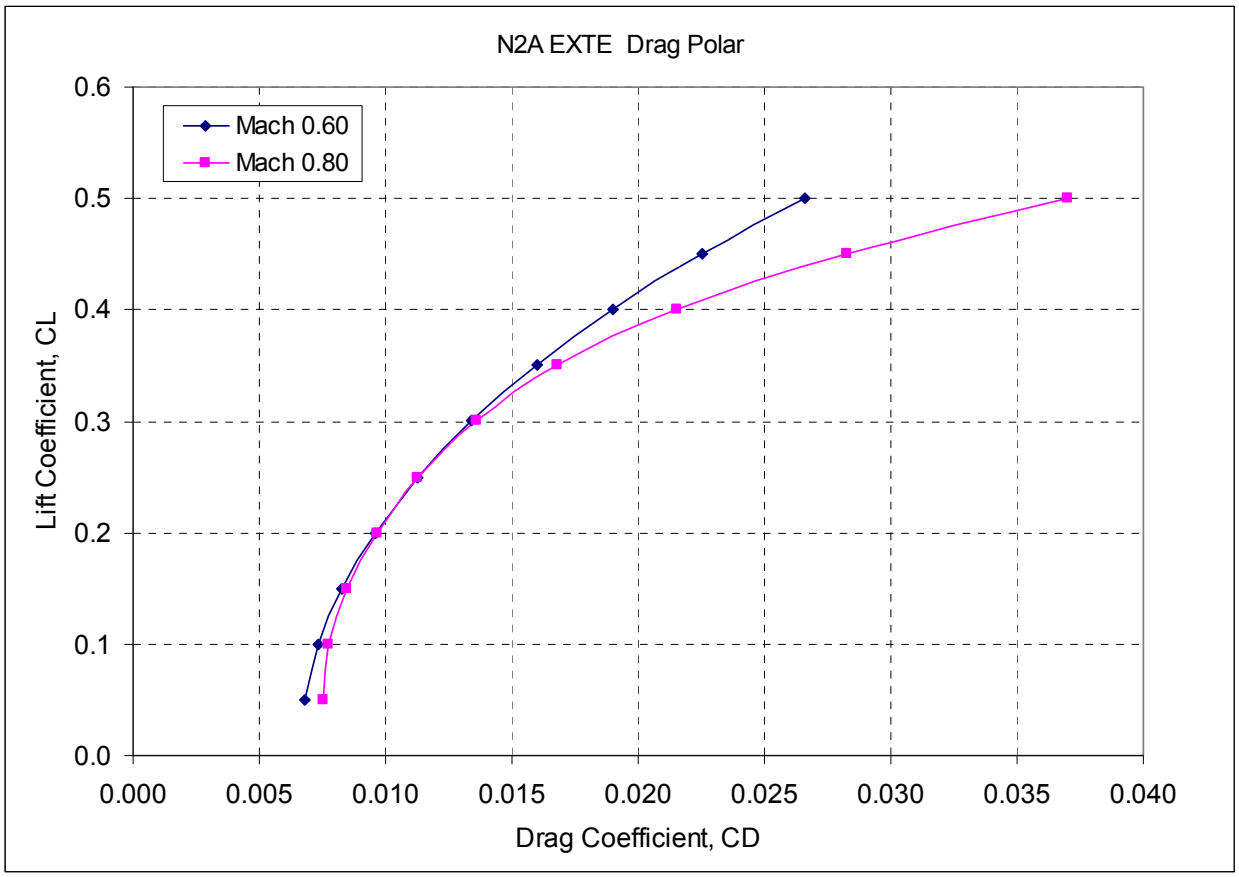

Figure 78 Drag Polar for N2A-EXTE

4.2.2 Weights

The weight changes for the N2A-EXTE are shown in Table 11. N2A-EXTE weight increases due to the afterbody extension that also increases thrust required landing gear loads with some reduction from a thicker outer wing.

Table 11 Weight Changes for N2A-EXTE

	N2A		N2A-EXTE		
	WEIGHT (LB)		WEIGHT (LB)		Δ Weight (LB)
WING-BODY	112,417		113,711		1,294
Outerwing Box, LE & TE		37,586		37,029	-558
Centerbody		55,104		55,255	151
Afterbody		10,875		12,575	1,700
LANDING GEAR	21,083		21,520		436
Propulsion Pod	26,320		28,952		2,632
Pylons	3,369		3,706		337
FLIGHT CONTROLS	10,437		11,115		678
HYDRAULICS	2,452		2,613		162
ANTI-ICING	555		597		43
Non-Cbdy Exterior Paint, Primer & Sealant	1,795		1,998		203
MANUFACTURERS EMPTY WEIGHT	215,605		221,390		5,785
OPERATIONAL ITEMS	3,048		3,074		26
OPERATIONAL EMPTY WEIGHT	218,653		224,463		5,811
USABLE FUEL	139,873		144,388		4,514
PAYLOAD	103,000		103,000		0
MAXIMUM TAKEOFF WEIGHT	461,526		471,851		10,325

4.2.3 N2A-EXTE Performance

The take off performance is based on using drooped leading edges. The trimmed CL is shown in Figure 79.

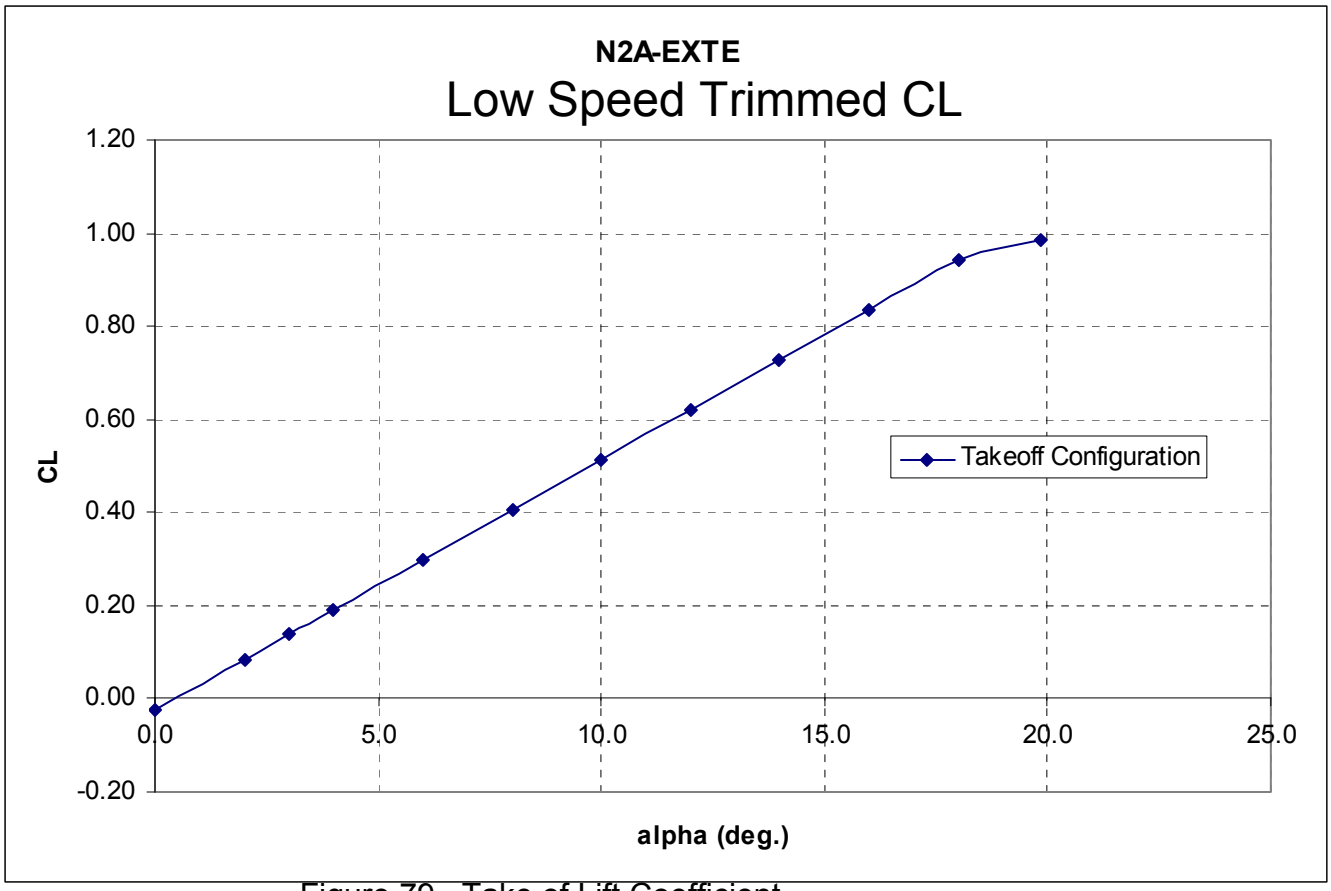

Figure 79 Take of Lift Coefficient

The comparative field length comparison is shown in Figure 79. The field length was reduced because thrust was increased to increase the cutback altitude to reduce flyover noise.

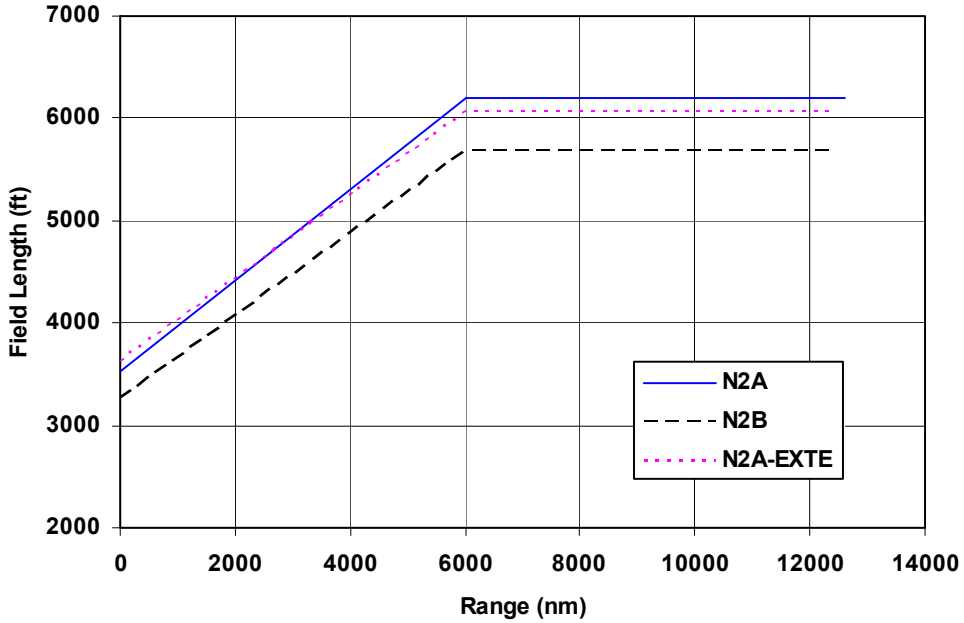

Figure 80 N2 Field Length Comparison

The payload range developed using BIVDS is presented in Figure 81.

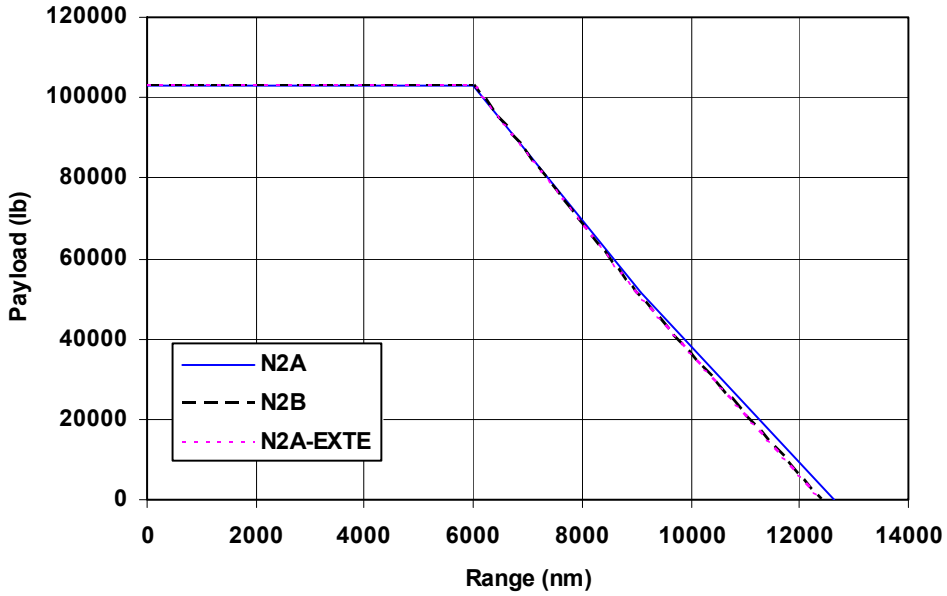

Figure 81 Payload Range

Table 12 shows the performance parameters with sizing for the payload-range mission.

Table 12 Sized N2A, N2B, and N2A-EXTE Performance Parameters

Configuration	N2A	N2B	N2A-EXTE
MTOGW (lb)	461,500	477,400	471,600
OEW (lb)	218,600	227,600	224,300
Payload (lb)	103,000	103,000	103,000
Fuel @ Max PL (lb)	139,900	146,800	144,300
Range (nm)	6,000	6,000	6,000
Fuel Burn (lb)	125,000	130,300	128,600
nm/lb	0.04799	0.04604	0.04665
nm*PL/lb	4,943	4,742	4,805
Ton-nm/lb	2.47	2.37	2.40
Reference Wing Area (ft^2)	9,246	9,106	9,958
TO Ref FN @ SL Static +27°F (lbf)	69,757	48,320	76,733
Number of Engines	2	3	2
Time to Climb 31,000 ft (hr)	0.29	0.29	0.28
Distance to Climb 31,000 ft (nm)	109.6	115.9	98.7
Time to Climb 35,000 ft (hr)	0.43	0.41	0.39
Distance to Climb 35,000 ft (nm)	168.7	167.9	149.2
R/C at 35,000 ft (fpm)	388	369	533
Cruise Type	Step-Cruise	Step-Cruise	Climb-Cruise
Initial Cruise Altitude (ft)	35,000	35,000	38,739
Initial Cruise Mach	0.789	0.796	0.810
Initial Cruise L/D	21.61	21.55	21.42
Initial Cruise SFC	0.496	0.501	0.503
Initial Cruise Thrust & Drag (lbf)	20,919	21,704	21,591
Initial Cruise Power Setting	0.846	0.854	0.941
Final Cruise Altitude (ft)	43,000	43,000	44,633
Final Cruise Mach	0.791	0.797	0.810
Final Cruise L/D	21.48	21.35	20.93
Final Cruise SFC	0.497	0.499	0.505
Final Cruise Thrust & Drag (lbf)	15,754	16,357	16,545
Final Cruise Power Setting	0.935	0.944	0.958
Engine Out Field Length (ft)	6,196	5,436	6,071
All Engine Field Length (ft)	5,945	5,683	5,824

The resulting fuel burn for the N2A-EXTE compared to the Phase I N2A and N2B is shown in Figure 82.

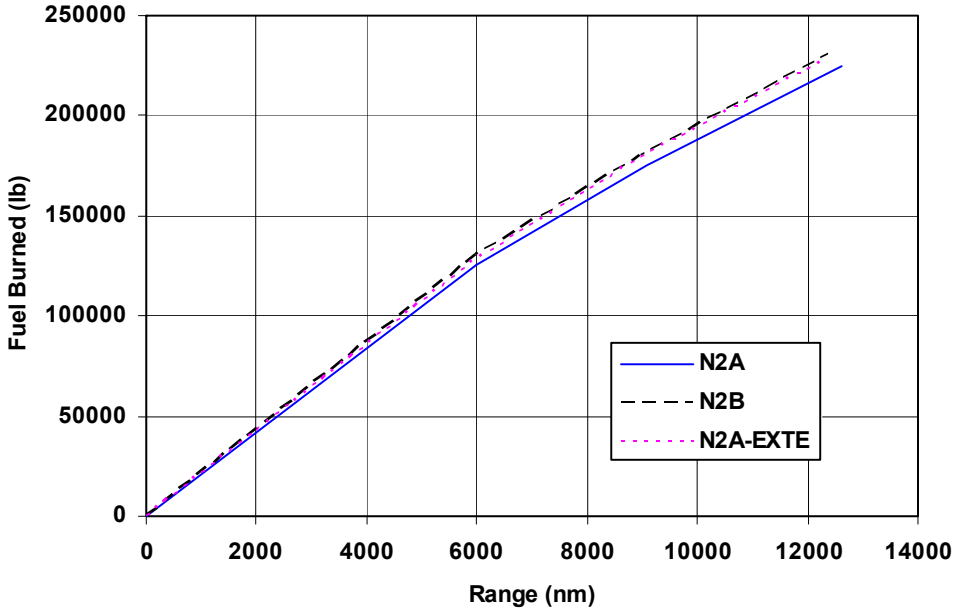

Figure 82: Fuel Burn Comparison of N2A, N2B, and N2A-EXTE

4.2.4 N2A-EXTE Noise

4.2.4.1 UCI Improvements

UCI continued improvements to improve noise shielding. The results are shown in Figure 83.

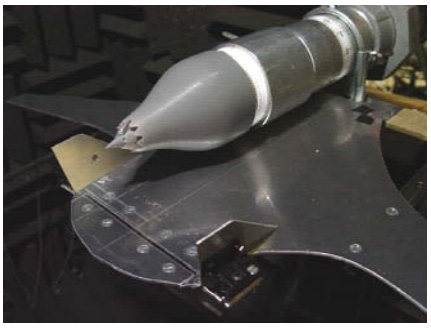

Chevrons with Porous Wedge

SHIELDING: EPNL REDUCTIONS RELATIVE TO UNSHIELDED PLAIN NOZZLE Nominal engine location Nominal Verticals			
Nozzle	**ΔEPNL (dB) Downward**	**ΔEPNL (dB) Sideline**	**ΔEPNL (dB) Cum**
Baseline (Plain)	**1.04**	**0.92**	**2.0**
Porous wedge W18x3	**4.57**	**3.41**	**8.0**
Aggressive Chevrons	**4.96**	**4.13**	**9.1**
Aggressive Chevrons + Wedge	**5.71**	**4.00**	**9.7**

Figure 83 UCI Phase II Results

Details of the UCI results are presented in Appendix A. These small scale test results were projected to full scale based on the Strouhal number and then shielded noise on 150 ft spheres where provided to MIT to logarithmically sum the EPNdB at the FAR 36 points.

The FAR 36 noise flight profiles for the N2A-EXTE is shown in Table 13.

Table 13 N2A-EXTE Aircraft/Engine Performance Data

Parameter	Lateral	Flyover	Approach
Flight Path Angle (º)	10.1	2.3	-3.0
Angle of Attack (º)	11.6	12.1	10.8
INB Elevon Angle (º)	-10	-10	-10
Mean OTB Elevon Angle (º)	-10	-10	-10
Fn/δ (lbs)	61,669	28,719	4180
N1/√θ (rpm)			
Altitude (feet)	1000	2207	394
TAS (kts)	152	155	137

N2A & N2B Acoustic Technology Assumptions

The acoustic technology assumptions assumed to identify the standard for acoustic analysis:

- Technology Readiness for 2020 Transport
- TRL6 acoustic technology readiness by about 2012 timeframe
- Followed by full scale flight noise demonstration validation before commitment to 2020 product design

4.2.4.2 MIT Phase II Results

Figure 84 gives an overview of the improved turbomachinery noise shielding method, DIM v2.0. There is an offline and an online part. The offline part is comprised of three main modules two of which were newly developed.

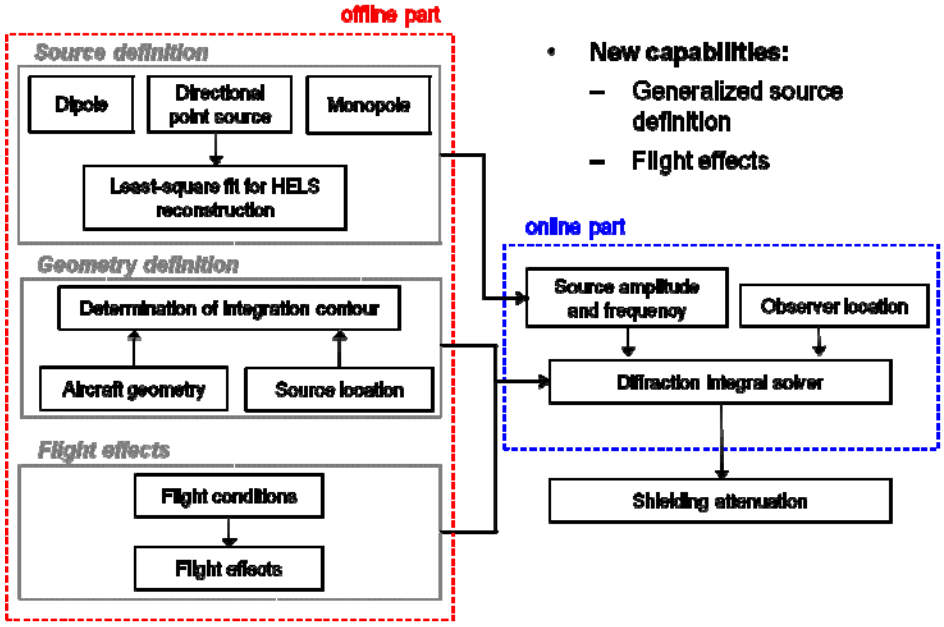

Figure 84 Overview of new diffraction integral shielding method, version v2.0

In the source definition part either a monopole, or dipole, or a directional point source can be specified. For the directional point source a least squares method is used to reconstruct the near field source definition using directivity information in the far field. The module that defines the shielding geometry and source location is unchanged from v1.0. Based on the aircraft flight conditions, flight effects can be included in the shielding assessment. This information together with the location of observers is used in the diffraction integral solver to compute the shielding attenuation. The theoretical development of the shielding method is presented in Appendix B.

4.2.4.3 N2A-EXTE Aircraft Noise

The FAR36 noise assessment of the N2A-EXTE powered by two podded turbofan engines with fan pressure ratio 1.6 is discussed first. The potential noise benefit of different fan pressure ratio propulsion systems was also investigated and is presented at the end. In addition, a comparison of the final noise audit at fan pressure ratio 1.6 is given relative to the previous noise audit. In the final assessment, the turbomachinery shielding model based on the HELS directional point source and experimentally measured jet shielding results including chevrons and an external wedge are also included. With this, the N2A-EXTE configuration is estimated to meet the NASA N+2 noise goal with margin. The details are discussed in this section.

ANOPP-L28vMIT version was used for the final analysis and a summary of the noise source and shielding estimation methods is given in Table 14 below.

Table 14 Summary of Noise Source and Shielding Methods

Noise Source	Estimation Method
Fan Forward	ANOPP Heidmann Fan Module *- GE large turbofan method* TREAT acoustic inlet liner increments *- GE large turbofan method* SAI-based ray-tracing shielding increments
Fan Rearward	ANOPP Heidmann Fan Module *- GE large turbofan method* TREAT acoustic fan duct liner increments *- GE large turbofan method* Beranek & Maekawa barrier shielding increments (N2A)
Core	ANOPP GE Core Module Beranek & Maekawa barrier shielding increments (N2A)
Jet (N2A)	ANOPP Stone 2 Jet Module UCI jet noise shielding increments with perforated wedge
Jet (N2B)	Scaled Granta (SAI) jet hemisphere
Undercarriage	Modified ANOPP Boeing Airframe Module Faired landing gear noise reduction increments
Elevon	ANOPP Boeing Airframe Module (modeled as aileron)
Leading Edge Droop	Droop effect on BL properties included in FW-Hall method Contribution of side edge not modeled
Airfoil (Wing)	Physics-based airfoil self-noise method (FW-Hall)
Wing Tip (N2A) Winglet (N2B)	Tip vortex noise model from Brooks and Marcolini
Vertical Tail (N2A)	ANOPP Fink Airframe Module

The landing gear noise estimate of the N2A-EXTE was updated using CFD flow field results available from Boeing to estimate the local flow Mach number around the nose and the main landing gear. The outboard aileron module from the Reference 9 NASA Contractor Informal Report of January 2000 was used to model elevon noise of the hybrid-wing body aircraft, since an update of the aileron module in ANOPP is not yet available. This model is currently being assessed and compared against conventional aircraft noise data. Due to this uncertainty and in order to give an upper and a lower bound on the overall FAR36 noise, the report includes results from audits conducted both with and without elevon noise. Jet noise shielding was included based on the N2A-EXTE experimental studies carried out by UCI. The nozzle was equipped with

aggressive devices such as chevrons and a wedge that were essential in reducing the jet noise. Turbomachinery fan and core noise shielding was implemented through the diffraction integral shielding method (DIM) using the HELS representation of the Heidmann fan noise directivity. In addition, flight effects were included. This method was documented in the first section of this report.

The FAR 36 noise certification analysis was performed at International Standard Atmosphere (ISA) reference conditions +18F, 70% relative humidity, zero wind and at sea level.

The noise certification measurement locations are sideline, flyover and approach. For sideline noise estimation, the observer is located at 450 m at sideline and at the point from brake release where peak sideline noise is encountered. For flyover noise estimation, the observer is located at 6,500 m from brake release on the runway centerline. For approach noise estimation, the observer is located 2,000 m from the runway threshold. See Figure 51 for an illustration of these locations.

The overall noise level is measured in Effective Perceived Noise Level decibels (EPNdB) capturing the sound pressure level and accounting for tonal and duration effects on human perception of noisiness.

The flight conditions at the FAR 36 Sideline, Flyover and Approach points are shown in Table 15.

Table 15 FAR 36 Flight Conditions

Parameter	Lateral	Flyover	Approach
Flight Path Angle (º)	10.1	2.3	-3.0
Angle of Attack (º)	11.6	12.1	10.8
INB Elevon Angle (º)	-10	-10	-10
Mean OTB Elevon Angle (º)	-10	-10	-10
Fn/δ (lbs)	61,669	28,719	4180
N1/√θ (rpm)			
Altitude (feet)	1000	2207	394
TAS (kts)	152	155	137

The noise audit was first carried out for the N2A-EXTE aircraft configuration powered by two podded engines with fan pressure ratio1.6. The following assumptions and methods were used in the assessment:

- Turbomachinery noise shielding based on DIM HELS directional point source definition using Heidmann fan directivity; flight effects included
- Local Mach suppression of main and nose landing gear per Boeing CFD
- Outboard aileron noise model by an internal method for elevon noise
- Sideline noise determined at peak noise location
- Updated N2A-EXTE airframe aerodynamics for noise assessment purposes
- Jet noise shielding data from UCI experimental studies on N2A-EXTE planform; nozzles equipped with aggressive chevrons and a wedge
- Ground effects

Figures 85, 86 and 87 show the estimated noise histories for observers at sideline, flyover and approach conditions.

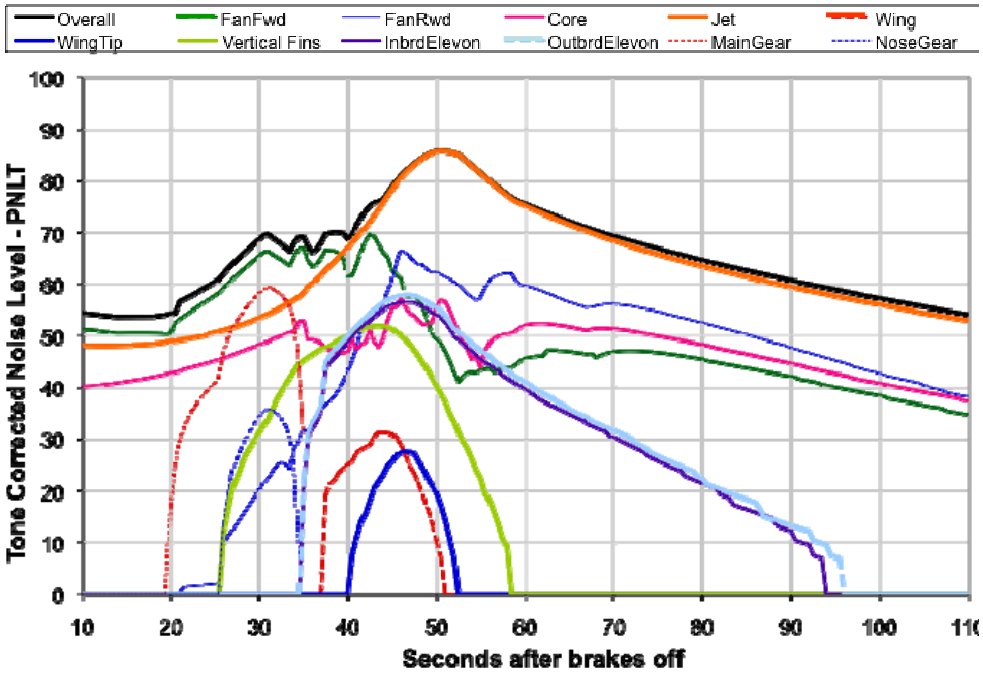

Figure 85 N2A-EXTE FAR36 Sideline Noise

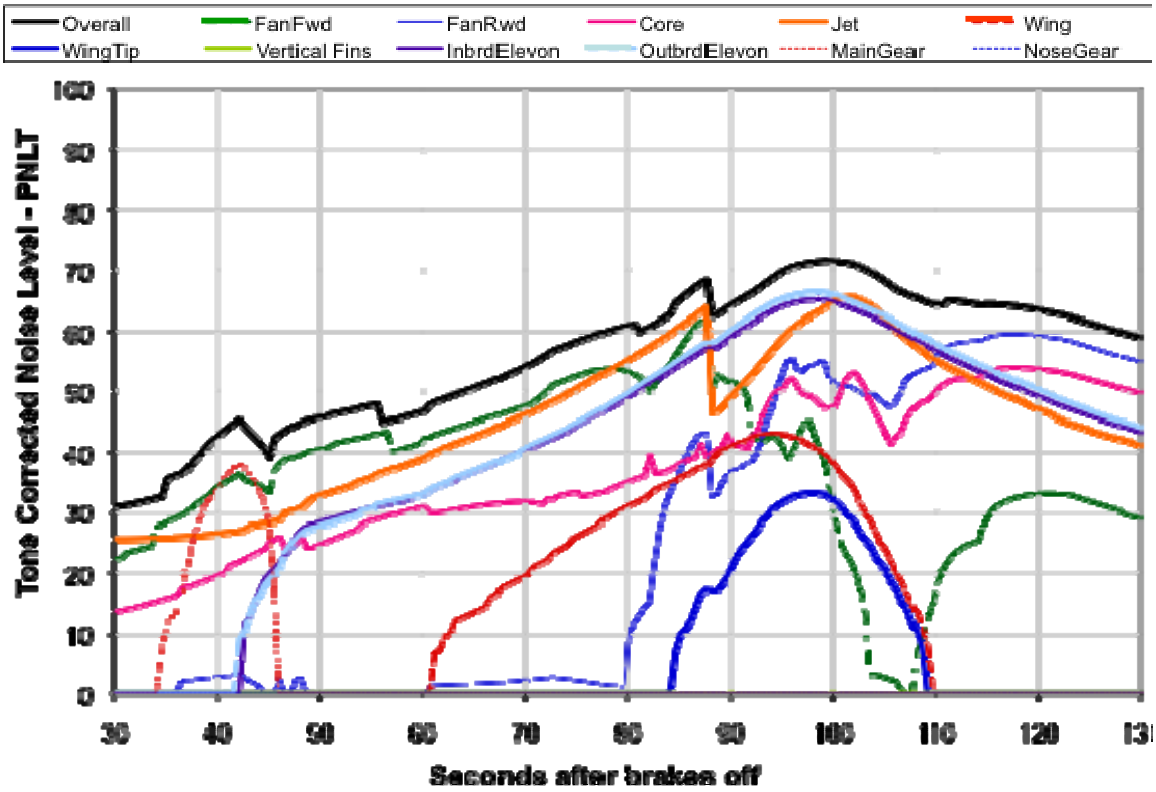

Figure 86 N2A-EXTE FAR36 Flyover Noise

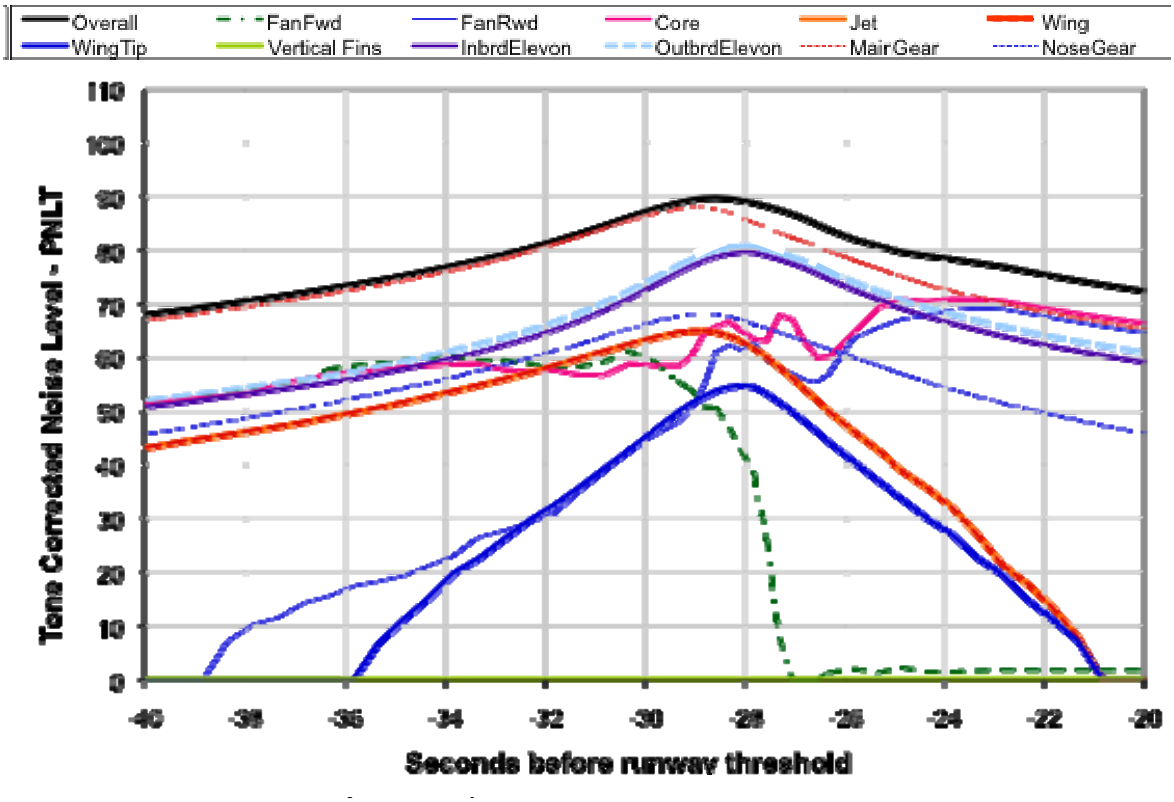

Figure 87 N2A-EXTE FAR 36 Approach Noise

Figure 88 summarizes the source noise breakdown for each certification location. For the case investigated the peak noise at sideline occurs for an aircraft altitude of 394 feet over the runway. At sideline, engine noise sources, mainly jet noise, are dominant. Based on this, sideline noise is expected to decrease when reducing the engine fan pressure ratio. The noise estimates for different fan pressure ratios are presented in a following section. At flyover both engine and airframe noise sources are dominant, especially jet noise and elevon noise. On approach airframe noise is the main noise contributor, mainly landing gear noise and elevon noise. The noise estimates at flyover and approach are considered an upper bound given the limitations and possible overestimation of the elevon noise model.

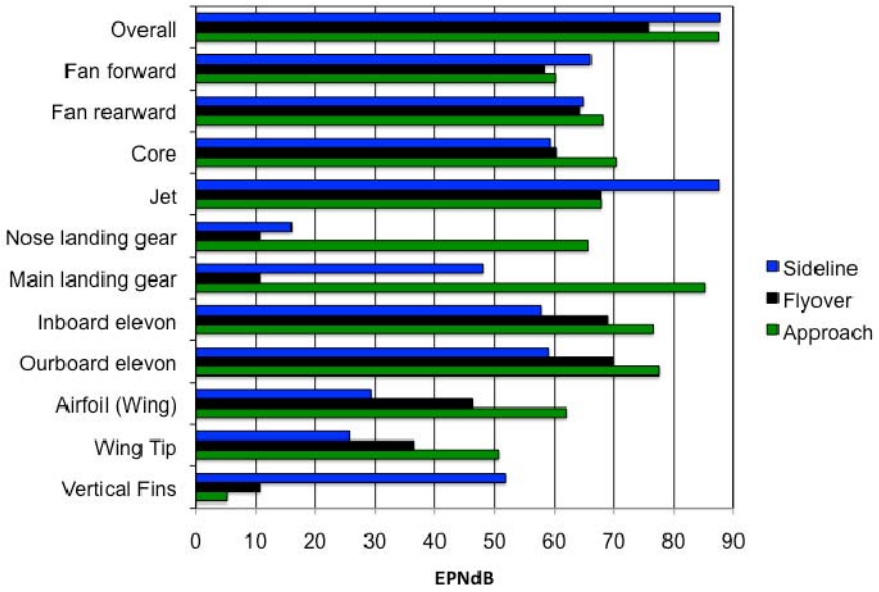

Figure 88 Source noise breakdown for sideline, flyover and approach.

Table 16 summarizes the EPNL results, the cumulative noise and the N+2 noise goal. Given the uncertainties in the elevon noise model, the noise estimates are conducted for both cases, with and without elevon noise. This yields an upper and lower bound on the overall aircraft noise assessment with a difference of -6.7 EPNdB between the two cases.

Table 16. Summary of N2A-EXTE FAR-36 noise assessment

Cumulative EPNdB with elevon noise (EPNdB)	251.0
Cumulative EPNdB without elevon noise (EPNdB)	244.3
N+2 Goal (EPNdB)	250.4
EPNdB Margin with elevon noise (EPNdB)	+0.6
EPNdB Margin without elevon noise (EPNdB)	-6.1

Table 17 summarizes the EPNL results, the cumulative noise and the N+2 noise goal. Given the uncertainties in the elevon noise model, the noise estimates are conducted for both cases, with and without elevon noise. This yields an upper and lower bound on the overall aircraft noise assessment with a difference of -6.7 EPNdB between the two cases.

Table 17 Phase I N2A and Phase II N2A EXTE noise results

	Phase I – N2A	***Phase II – N2A-EXTE***
Sideline (EPNdB)	90.1	87.7
Flyover (EPNdB)	76.8	75.8
Approach (EPNdB)	86.8	87.5
Cumulative (EPNdB)	**253.8**	**251.0**
N+2 Noise Goal	**248.5**	**250.4**
EPNdB Margin	**-5.3**	**-0.6**

Note that the noise goal of -42 dB below Stage 4 has slightly changed because of changes to the aircraft configuration. In summary, the fidelity of the noise assessment has been improved in the following key areas: (1) turbomachinery shielding method, (2) local Mach number effect of main and nose landing gear, (3) observer position for peak sideline noise estimation, and (4) jet noise shielding and nozzle design. These improvements are discussed in more detail below.

4.2.4.4 Landing Gear Noise

The landing gear noise method in version ANOPP-v28MIT was used for the N2A-EXTE noise estimation. The model was updated using CFD flow field results available from Boeing to estimate the local flow Mach number around the nose and the main landing gear. The CFD results are shown in Figure 89. The nose landing gear Mach number is estimated to be around 0.9 of free stream Mach number while there is practically no Mach number suppression near the main landing gear. The results of the elevon and the nose and main landing gear noise for the N2A-EXTE configuration were compared to the experimental data reported by Rackl et al. [Appendix B, Reference 14] for a B767. This is shown in Figure 89. In general the trends are similar with the exception of the nose landing gear noise being quieter for the hybrid-wing body aircraft. This is conjectured to be due to the above mentioned local Mach number suppression.

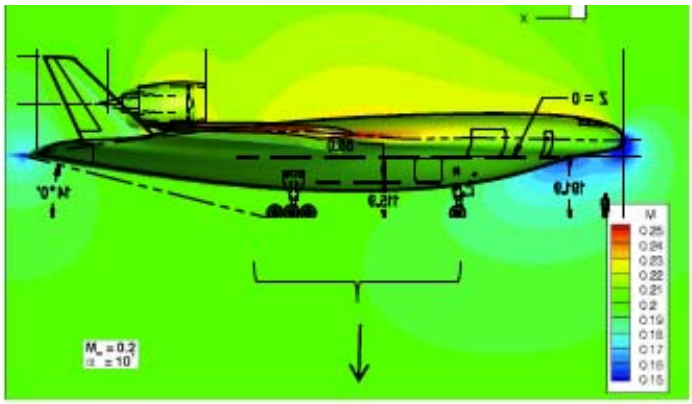

Figure 89. Local flow Mach number results from CFD around N2A-EXTE.

The airframe component noise comparison at approach with ground effects, including local Mach suppression on landing gear is shown in Figure 90. The basis of the B767 data is from Appendix B, Reference 14.

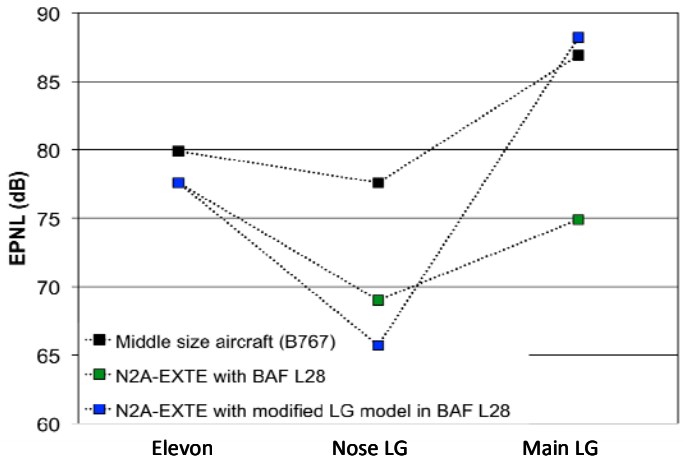

Figure 90 Airframe component noise comparison at approach

4.3 Fan Pressure Ratio Study

25K to 30K lb thrust class geared turbofans (GTF) are now being developed for short range transports. It is therefore reasonable to consider large thrust class geared turbofans for a later time frame for which the wind tunnel model and planned testing could be useful. As previously discussed, an EIS 2020 requires TRL 7 in the 2012 to 2013 time frame and a 70K lb thrust class GTF was not reasonable expectation for this investigation N+2 in EIS 2020. However, for future planning leading also towards a 2025 EIS the GTF should be considered. Therefore an assessment for lower fan pressure ratios with the GTF was assessed for consideration when the wind tunnel tests are conducted.

4.3.1 Fuel Efficiency vs FPR

The mission fuel burned for the fan pressure ratio sweep using the Phase I engine performance data from NASA GRC was determined for the N2A-EXTE again using BIVDS. The Fan Pressure Ratio (FPR) 1.4 and 1.5 are geared fans while the FPR 1.6 and 1.7 are direct drive fans. This assessment was a first order analysis using substitution of the base FPR1.6 propulsion system performance with isolated nacelle and pylon drags and weights. The results are shown in Table 18.

Table 18 Fuel Burn with FPR 1.4 thru 1.7

	N2A	N2A EXTE	N2A EXTE	N2A EXTE	N2A EXTE
	FPR 1.6	FPR 1.4	FPR 1.5	FPR 1.6	FPR 1.7
	Phase I	Geared	Geared	Direct-drive	Direct-drive
Payload (lbs)	103000	103000	103000	103000	103000
Reference Wing Area (sqft)	9246	9958	9958	9958	9958
Cruise type	Step-cruise	Climb-cruise	Climb-cruise	Climb-cruise	Climb-cruise
TO Ref FN @ SLS +27F (lb/eng)	69757	84950	78630	76733	76270
Takeoff thrust @ M=0.25 (lb/eng)	54001	61276	59107	59401	60338
Time to climb to 31000 ft (min)	17.634	16.62	16.92	16.746	16.35
Dist. to climb to 31000 ft (nm)	109.6	96.6	98.9	98.7	96.9
Initial cruise altitude (ft)	35000	38666	38835	38739	38519
Balanced field length @ SLS+27F (ft)	6196	6071	6071	6071	6071
All engine field length @ SLS+27F (ft)	5945	5789	5815	5824	5828
All engine liftoff velocity (ktas)	147.12	153.27	151.47	151.36	151.71
OEW (lbs)	218652	237927	228518	224319	222111
MTOGW (lbs)	461517	481783	472401	471648	473722
Block Fuel Burned (lbs)	125032	125763	125702	128614	132283
nm/lb	0.047988	0.047709	0.047732	0.046651	0.045357
NM*PL/LBf	4942.735	4914.005	4916.39	4805.076	4671.802

The payload-range efficiency in Figure 91 shows the potential to improve fuel efficiency with lower fan pressure ratios if the efficiency prediction based on supposition of nacelle weight and drag is not significantly offset by propulsion airframe integration penalties. Note that the N2A-EXTE fuel efficiency is somewhat poorer than the N2A but the N2A from Phase I did not include the aero integration penalties that CFD analyses showed were very large and eliminated in the N2A-EXTE.

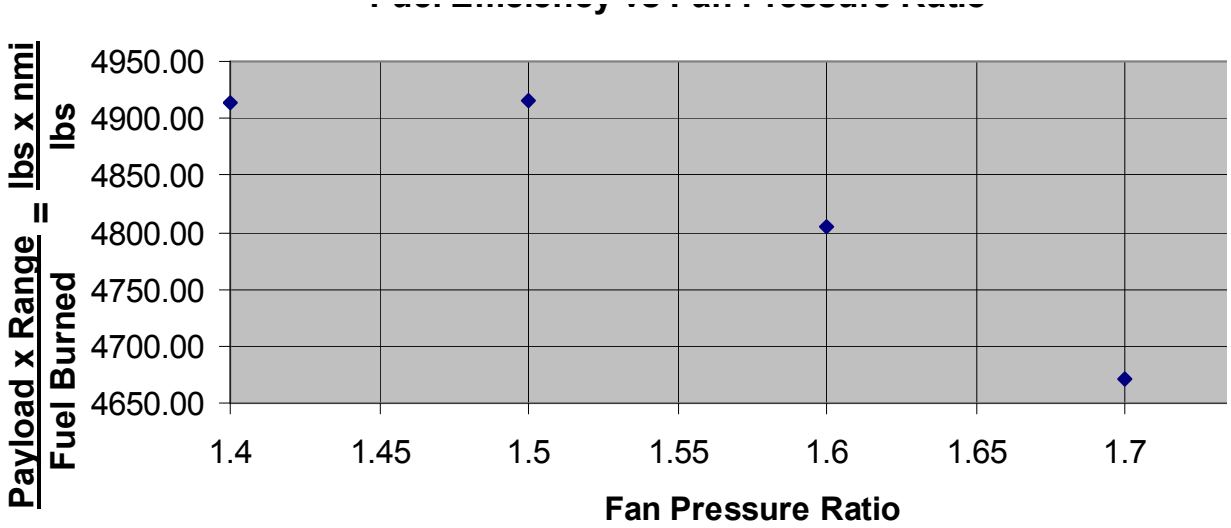

Figure 91 Fuel Efficiency vs Fan Pressure Ratio

The study shows the fuel burned goal for this investigation is met with a FPR of 1.6. As noted above, the integration effects on drag with larger diameter nacelles with the lower fan pressure ratios were not evaluated. For the FPR 1.6 base configuration, extensive analyses using RANS CFD codes were conducted, including the effect of the thrust pitching moment at cruise. The FPR sweep results, in combination with the noise assessment made by MIT shows further in-depth studies are warranted, particularly for the current NASA ERA N+2 goals shown in Reference 10 that are for an EIS in 2025 compared to the SFW goals used herein. For this current study, the EIS date is 2020 and a gearbox for a 70K lbs thrust engine in this time 2020 EIS time frame would require a development starting very soon to be at a TRL 6 by 2015 for an EIS in 2020.

The noise goal with a FPR 1.6 is predicted with jet noise compression nozzles and reductions in elevon noise. The base FPR 1.6 is the configuration for which the RANS CFD analyses were conducted to define the high speed lines. The results show the improvement potentials but similar PAI effort is required.

N2A-EXTE model will provide excellent data for noise prediction validations as well as low speed aero data that can be used to evaluate lower fan pressure ratios.

4.3.2 Noise vs FPR

A fan pressure ratio sensitivity study was carried out to investigate the potential noise reductions for lower fan pressure ratio propulsion systems.

Table 19 summarizes the key engine parameters. Turbomachinery noise shielding using DIM HELS directional point source definition is based on Heidmann fan directivity; flight effects are included.

Table 19 . *N2A-EXTE engine parameters for four different fan pressure ratio cases*

	FPR=1.4	*FPR=1.5*	*FPR=1.6*	*FPR=1.7*
BPR at Aerodynamic Design Point	20.5	15.5	12.3	10.1
OPR at Aerodynamic Design Point	36.6	29.1	27.8	26.8
Sea Level Static Thrust (klbs)	84.95	78.6	76.73	76.27
Cutback thrust (klbs)	27.30	26.67	26.57	26.65

Figure 92 depicts the flight trajectories for the four fan pressure ratio cases investigated. The bypass ratio increases when decreasing the fan pressure ratio, as expected. The flight trajectories do not show significant differences between the four cases. The estimates include:

1. Local Mach suppression of main and nose landing gear
2. Outboard aileron noise model by Sen et al. [Appendix B, Reference 13] for elevon noise
3. Sideline noise determined at peak noise conditions
4. Updated N2A-EXTE airframe aerodynamics for noise assessment purposes
5. Jet noise shielding data from UCI experimental studies on N2A-EXTE; nozzles equipped with aggressive chevrons and a wedge
6. Ground effects

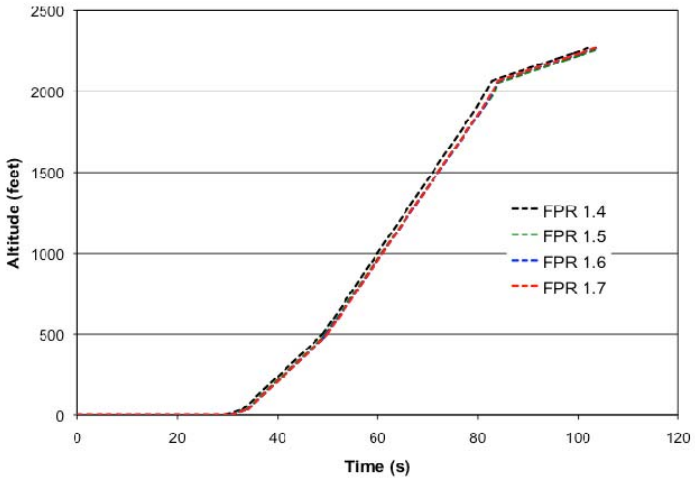

Figure 92 Flight trajectory

Figures 93, 94 and 95 show the breakdown of the noise sources for the three certification points and the four fan pressure ratios investigated.

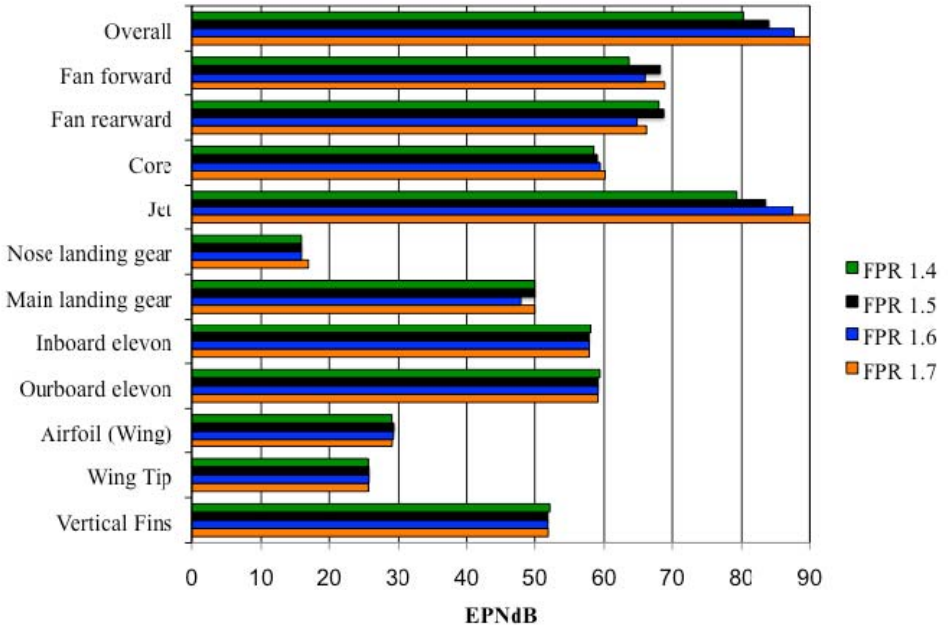

Figure 93 Noise source breakdown at sideline

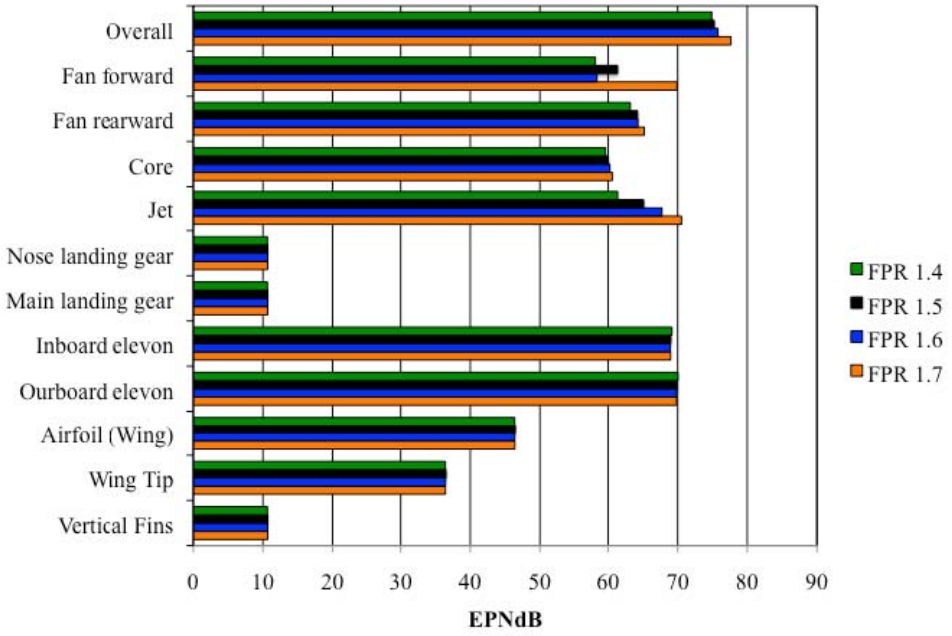

Figure 94**.** Noise source breakdown at flyover

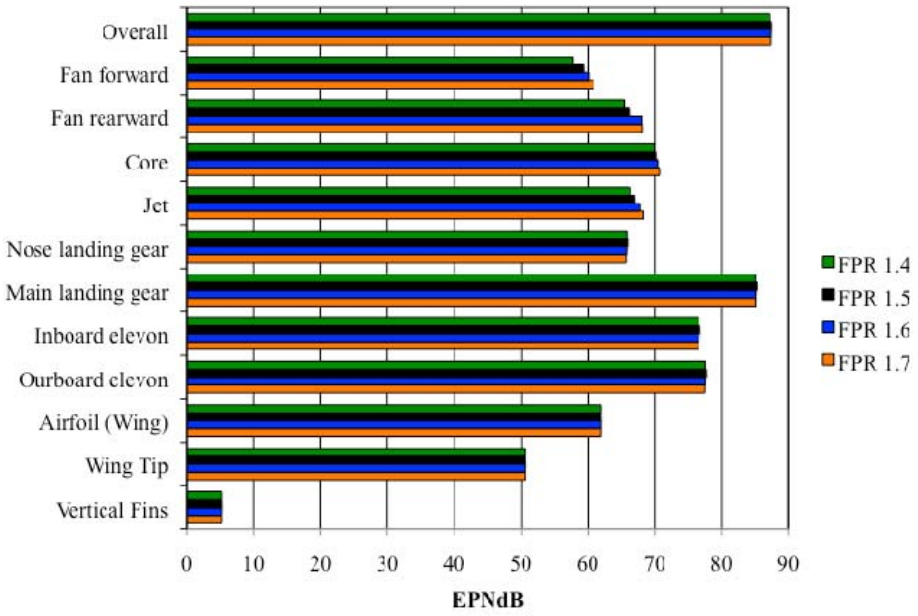

Figure 95. Noise source breakdown at approach

Figure 96 shows the peak noise assessment at sideline observer location. The peak noise occurs at an aircraft altitude different from 1,000 ft. The 1,000 ft altitude, marked by the yellow dots, was used in previous noise audits based on a recommendation by Boeing guided by experience with conventional aircraft. The change in altitude is due to the change in aircraft configuration, changes in fan pressure ratio and in the flight trajectory.

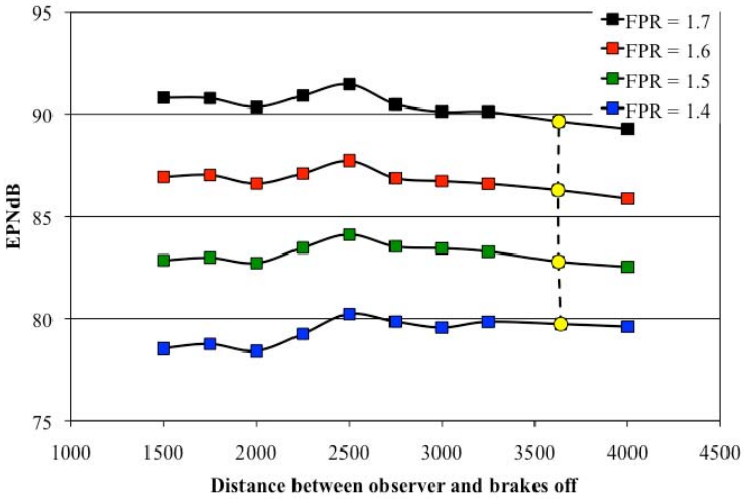

Figure 96 Peak noise assessment at sideline observer locations.

Table 20 shows a comparison of the sideline noise levels as well as the change in altitude. There is a difference of up to 2 EPNdB in sideline noise between peak noise and the previously used noise level at an altitude of 1,000 feet.

Table 20 *Comparison of sideline noise levels for different fan pressure ratios*

	FPR=1.4	*FPR=1.5*	*FPR=1.6*	*FPR=1.7*
Sideline noise at 1000 feet altitude	79.7	82.8	86.3	89.6
Sideline peak noise	80.2	84.1	87.7	91.4
Aircraft altitude at peak noise (ft)	393	395	394	392
Delta EPNdB	**+0.5**	**+1.3**	**+1.4**	**+1.8**

Figure 97 summarizes the FAR36 noise levels at the three observer locations for the case with and without elevon noise. At sideline, the noise reduces significantly when decreasing the fan pressure ratio. Also, there is no effect when the elevon noise is suppressed. This is because the jet noise is the dominant source as can be observed in Figure 92. At flyover, there is also a reduction of the overall noise when the fan pressure ratio is decreased as jet noise together with the elevon noise are the dominant sources, as observed in Figure 93. As expected, there is a significant effect on flyover noise when the elevon noise is removed. Since airframe noise is the dominant noise source at approach, there is no effect on the overall noise when changing the fan pressure ratio. However, there is a reduction on the overall noise when suppressing elevon noise.

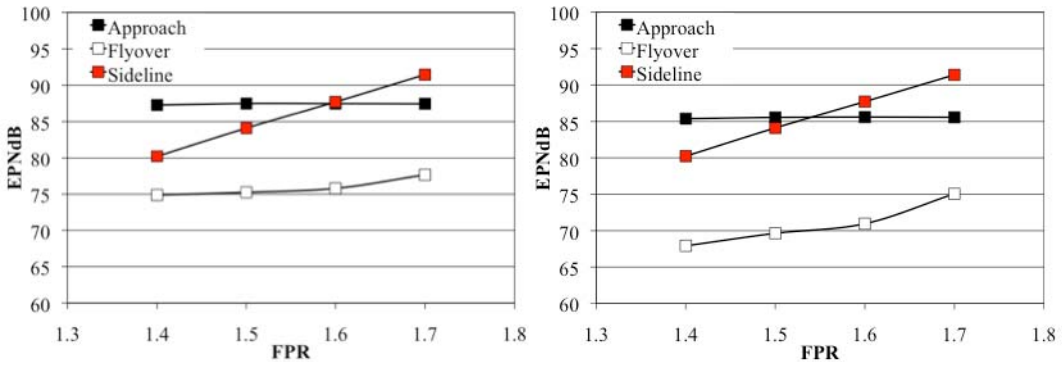

Figure 97. Fan pressure ratio study with elevon noise (left) and without elevon noise (right).

Table 21 summarizes the N2A-EXTE FAR-36 noise assessment for the four fan pressure ratio cases. The results suggest that, with a conservative estimate of elevon noise, the configurations with fan pressure ratio of 1.4 and 1.5 meet the N+2 noise goal, while a fan pressure ratio of 1.6 is just 0.6 EPNdB above the goal. For the optimistic scenario where elevon noise is below all other dominant noise source levels, the results suggest that all the configurations except the case for the fan pressure ratio of 1.7 can potentially meet the N+2 noise goal.

Table 21 *N2A-EXTE FAR-36 noise assessment.*

	FPR=1.4	*FPR=1.5*	*FPR=1.6*	*FPR=1.7*
Cumulative EPNdB with elevon noise	242.4	246.9	251.0	256.5
Cumulative EPNdB without elevon noise	233.5	239.3	244.3	252.0
N+2 Goal	250.7	250.4	250.4	250.4
EPNdB Margin with elevon noise	**-8.3**	**-3.5**	**+0.6**	**+6.1**
EPNdB Margin without elevon noise	**-17.2**	**-11.1**	**-6.1**	**+1.6**

5.0 WIND TUNNEL MODEL

The major end hardware product of this contract is a wind tunnel model representative of a HWB configuration capable of meeting the SFW N+2 goals. An artist's rendition of the model based on the N2A-EXTE is shown in Figure 98. This model is identified as the Quiet Ultra Integrated Efficient Test Research Aircraft #1, or QUIET-R.

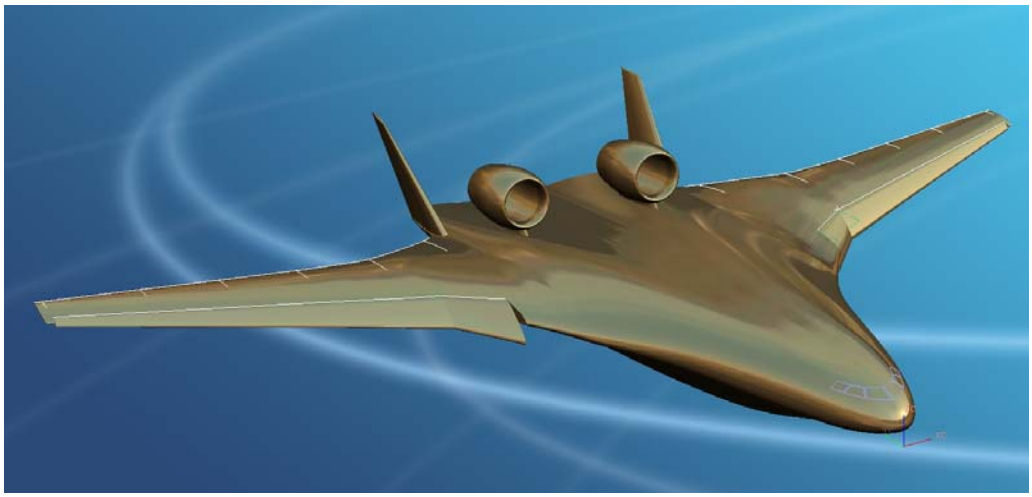

Figure 98 ELNHWB N2A-EXTE QUIET-R1

5.1 Test Facility

The wind tunnel model is for NASA to conduct noise testing and aero testing in the Langley 14 x 22 ft low speed wind tunnel. BR&T is supplying the N2A-EXTE model with changeable parts. The NASA plan is to acquire data on the effect of these changes on noise shielding as well as on airframe noise. The model also has removable flow through nacelles for low speed aero testing. The NASA test depiction is shown in Figure 99.

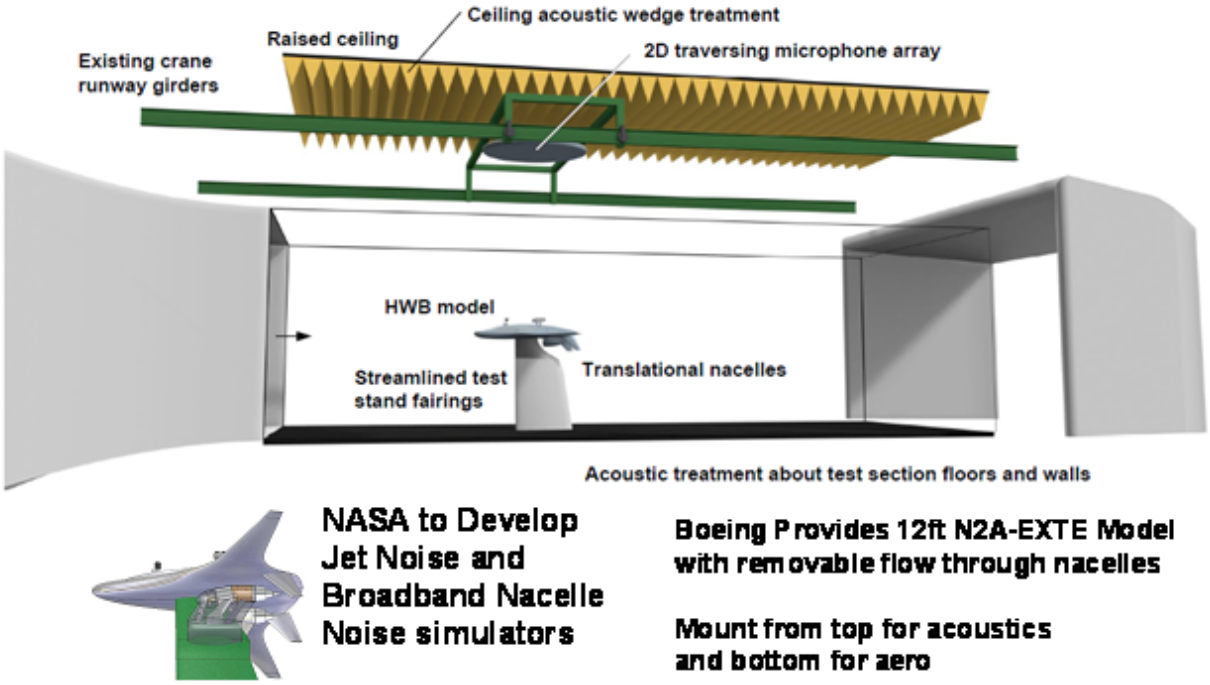

Figure 99 Test Arrangement in 14 x 22 Wind Tunnel

5.2 Model Sizing

The HWB type of configuration with the engines placed above the wing body provides a high degree of noise shielding. The shielding prediction methods used require validation in a relevant environment with geometry representative of future aircraft including forward flight and angle of attack effects. A NASA review of size requirements for validating prediction methods for a 213 ft span HWB concluded that a 5.8% model would be needed to measure model frequencies that could be scaled 1 kHz to 4 kHz SPL range that is highly weighted for PNdB while atmospheric attenuation becomes pronounced above 4 kHz for sideline and flyover distances which are greater than 1500 ft. The sizing basis is shown in Figure 100.

Need Large Tunnel with Array and DAMAS capability

Need to measure the full scale 1-5 khz range because of SPL weighting for PNdB and atmospheric attenuation effects

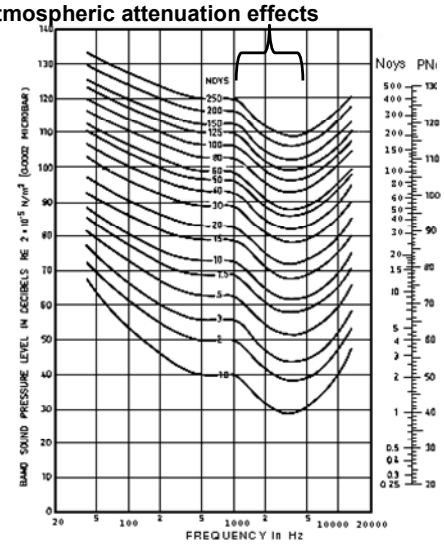

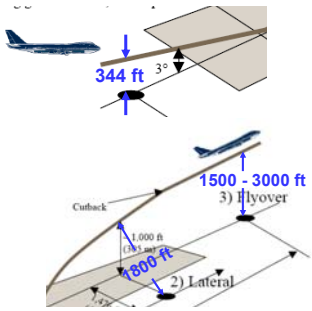

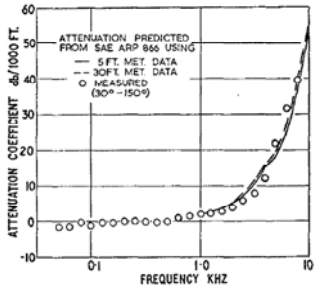

Approach high frequency noise will be shielded
Sideline and flyover 5+kHz atmospheric attenuation 30+dB

Need to measure FS 1- 4 kHz for EPNdB considering Atmospheric Attenuation

Strouhal Scaling

Span	% scale	FS - 1KHz	FS - 4KHz	Aero practicality	Noise Meas pract.
8'	3.78%	MS - 26.5KHz	MS - 106KHz	very easy	no
10'	4.73%	MS – 21.2KHz	MS – 84.8KHz	easy	tough - no guar
12'	5.67%	MS – 17.6KHz	MS – 70.4KHz	should be OK	should be OK mostly
14'	6.615%	MS – 15.1KHz	MS – 60.4KHz	OK with limitations	best

LaRC Assessment

Figure 100 Model Test Needs to Measure 1 to 4 KHz Full Scale Range for EPNdB

As shown in Figure 98, the nacelles are flow through for low speed aero testing but would be removed with pylon cover plates installed for acoustic testing. The model would be installed upright for aero testing and inverted for acoustic testing.

5.3 Wind Tunnel Model Design

5.3.1 Model Tolerances

The model main body and wings were designed for configuration changes. Fidelity and robustness are requirements in the model vendor SOW. The external model surfaces are geometrically scaled and will be fabricated to the tolerances detailed below. Tolerances for all internal surfaces shall be set to accommodate fabrication processes and to reduce costs. All model components shall be smooth and fair.

- Surface finish RMS 32 micro-inch
- Surface contours ± 0.010 in
- Steps-forward facing + 0.000 in

- Steps-aft facing - 0.002 in
- Linear dimensions ± 0.010 in
- Angular dimensions ± 0.10°
- Leveling plate alignment ± 0.01°

5.3.2 Modularity

The model design modularity is shown in Figure 101.

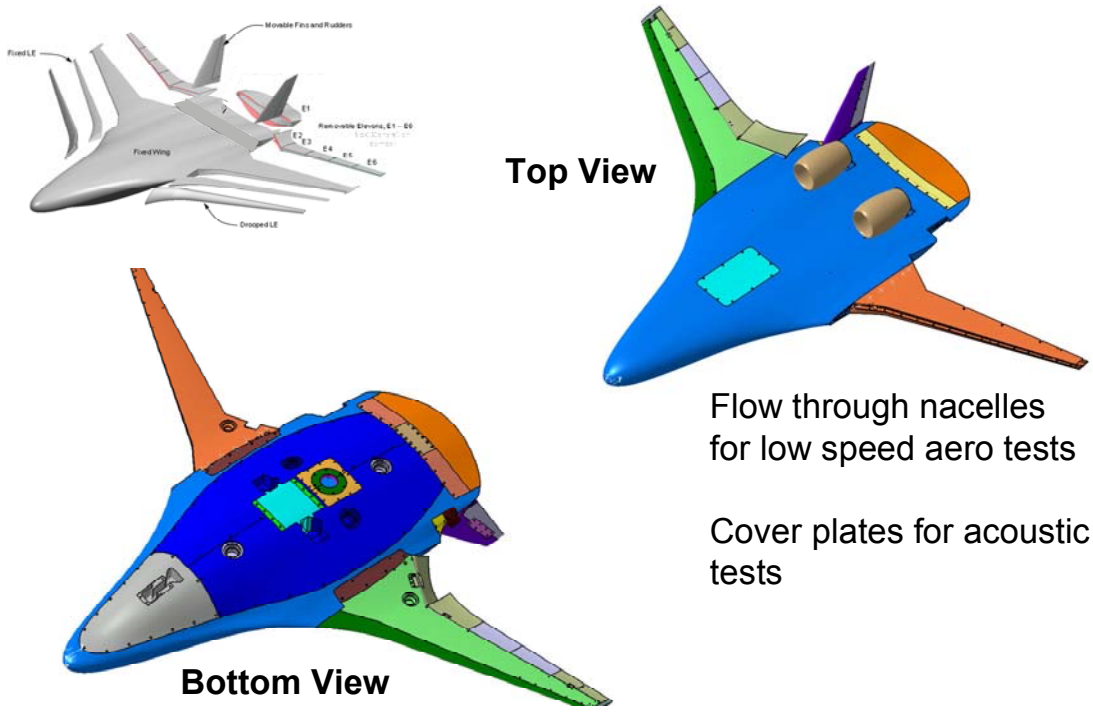

Figure 101 12 ft Model Modularity

Modularity includes support from the top for inverted noise testing, and support from the bottom with a force balance for aero testing and configuration change hardware as partially shown in Figure 102.

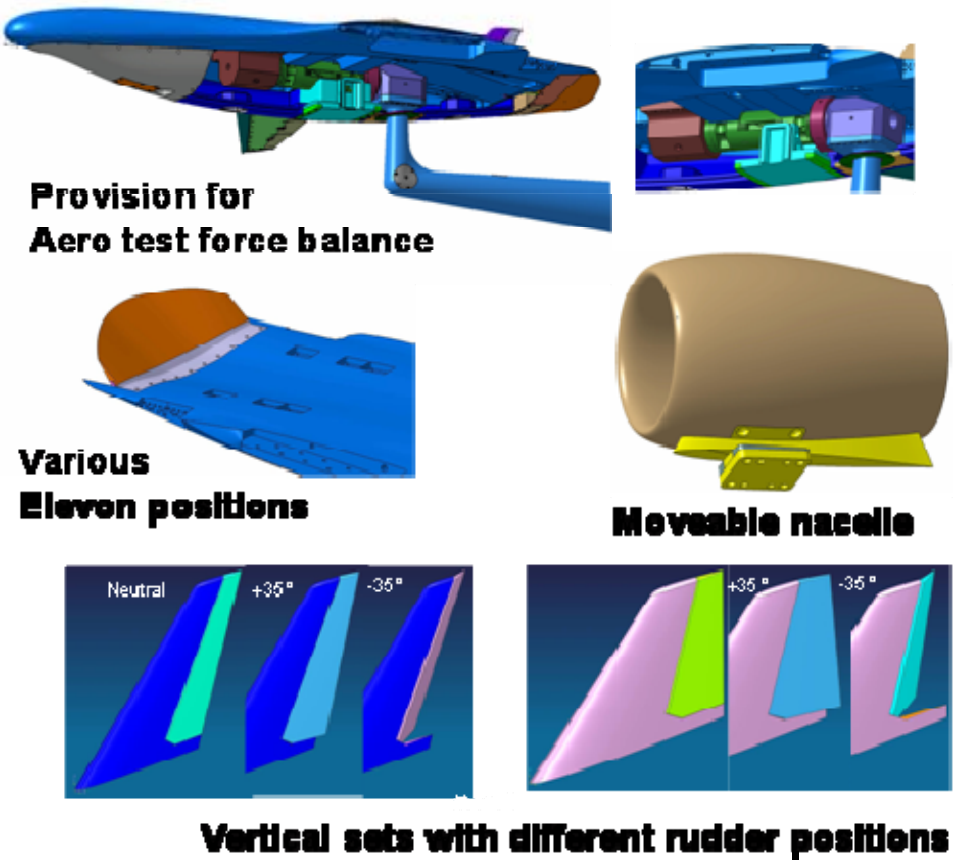

Figure 102 Partial Configuration Variable Model Parts

Ancillary hardware includes a drooped leading edge, different vertical cant angles that can be positioned fore and aft, different trailing edge elevon angles, flow through nacelle/pylons for low speed aero tests and detailed models of the nose and main landing gear as depicted in Figure 103.

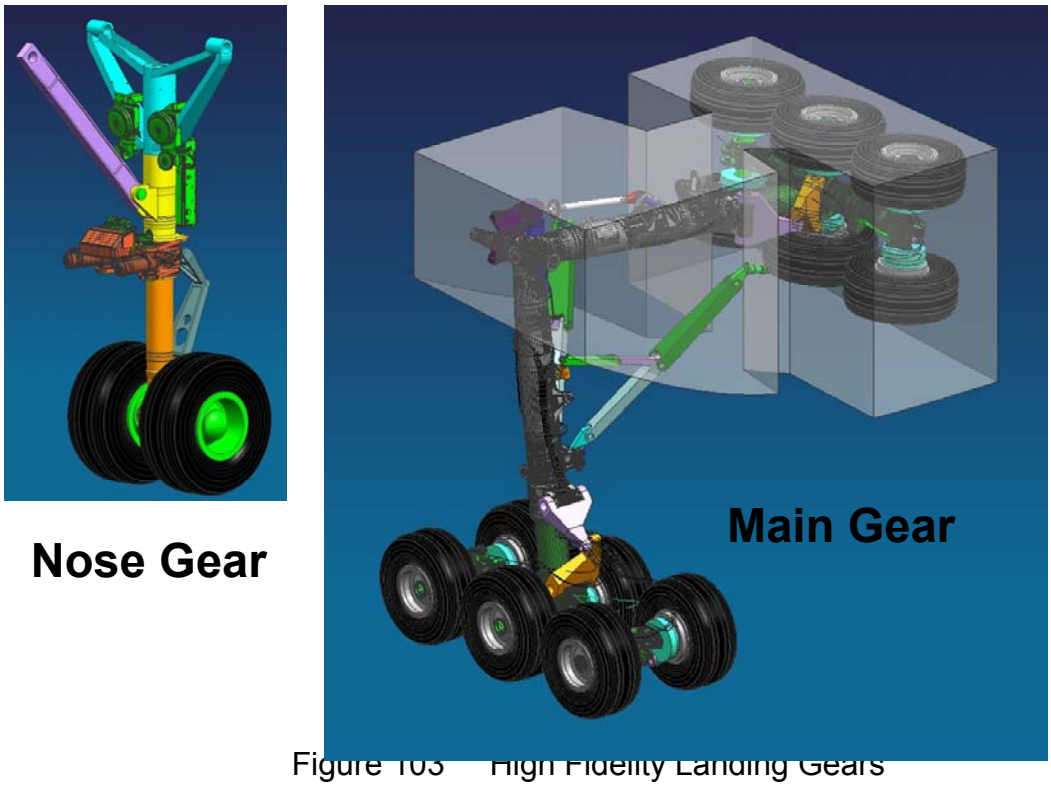

Figure 103 High Fidelity Landing Gears

The model is designed for static and dynamic pressure instrumentation and thermocouples for temperature measurements as shown in Figure 104.

Instrumentation Requirements for model:

- **Internal six component force & moment balance**
  - **NASA SR03 balance selected**
- **Static pressure taps**
  - **180 pressure taps on LH wing / body**
  - **52 pressure taps on RH wing**
  - **4 pressure taps in LH nacelle**
  - **2 pressure taps in balance cavity**
- **Acoustic point sources for calibration of test equipment**
  - **Requirement reduced to six devices because outboard wing cannot accommodate available noise sources**
- **Temperature sensors**
  - **Required to ensure model integrity during acoustic testing with engine exhaust simulators**
  - **Locations: inboard vertical tail & upper aft centerbody ahead of elevon hinge line**

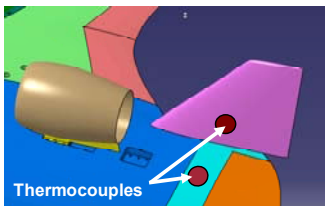

Figure 104 Instrumentation

The pressure tap locations are shown in Figure 104.

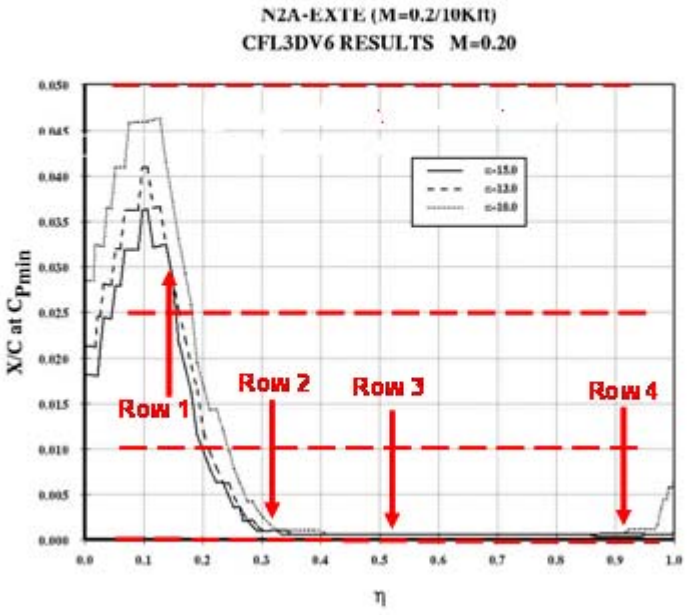

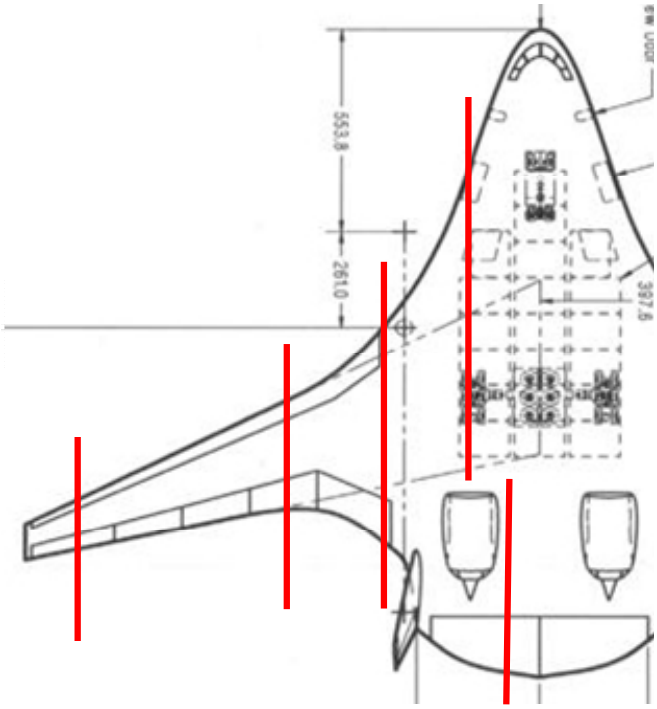

Locations of pressure rows (schematic)

Figure 105 Static pressure locations

5.3.3 Model Fab

The detailed design and fab of the model was completed and assembled at ATK in Tullahoma, TN. Figure 106 shows model major elements including the detailed landing gears for noise tests and flow through nacelles for low speed aero tests.

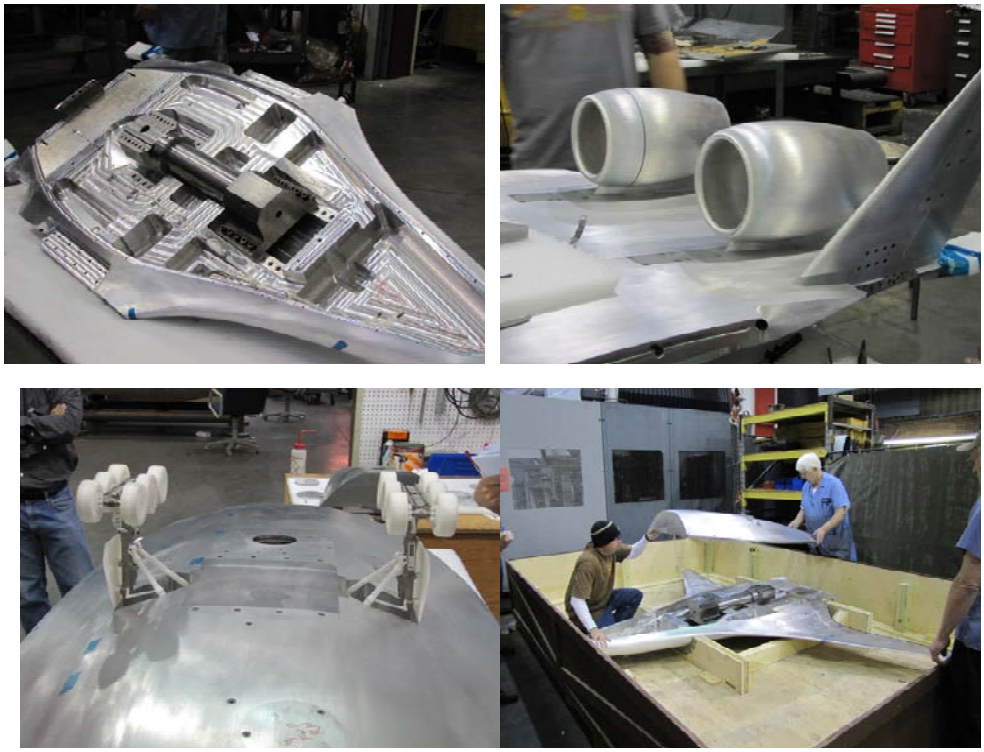

Figure 106 Model Fab

The completed main body in the inverted noise test attitude is shown in Figure 107 before shipping to NASA LaRC.

Figure 107 Assembled QUIET R-1 Wind Tunnel Model

5.3.4 Model Buy Off

The model was delivered to NASA LRC on Feb 16, 2011. Buy off will be subject to a detailed inspection. A detailed inspection will be conducted for:

- Cross-section versus station, particularly in the area of transitions and protuberance cross-section versus station, particularly in the area of transition
- Pressure tap location in both spanwise station and local x/c value. Final drawings must reflect as-built conditions.
- As required for the rest of the model.
- Balance bores relative to model reference (i.e., leveling plates).

6.0 CONCLUSIONS AND RECOMMENDATIONS

The N2A-EXTE will meet the SFW N+2 noise and fuel burn goals. This investigation meets the metrics for this contract as reported in Reference 11. Although the MIT noise results indicates then elevon noise may be a limiting factor, recent wind tunnel results from an internal BR&T review of the BWB model in the Boeing Low Speed Aeroacoustic Facility (Ref 12) showed the elevon noise may not be significant. The LSAF tests showed the need for jet noise suppression devices similar to the results herein. These results apply to a BPR 10 turbofan with a fan pressure ratio of 1.6. This was deemed appropriate for the EIS 2020 because of the technology readiness for 70K lb thrust class gearboxes needed for lower fan pressure ratio geared turbofans. The fan pressure ratio study results shows the potential for meeting a lower noise level, or meeting the noise without jet noise suppression devices, with a lower engine SFC. This should be further investigated for a 2025 EIS.

6.1 Conclusions

N2A-EXTE can meet N+2 goals.

Figure 108 summarizes the results for the N2A-EXTE.

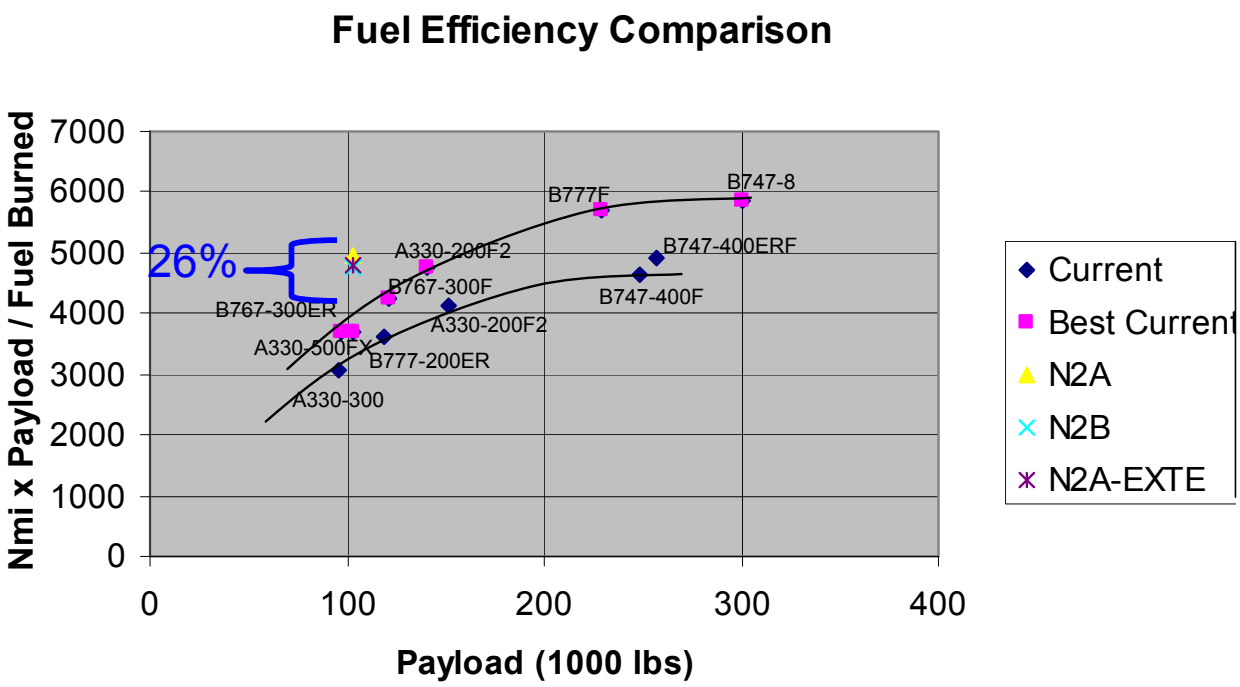

Noise Relative to FAR 36 Stage 3

	FPR=1.6
Cumulative EPNdB with elevon noise	251.0
Cumulative EPNdB without elevon noise	244.3
N+2 Goal	250.4
EPNdB Margin with elevon noise	**+0.6**
EPNdB Margin without elevon noise	**-6.1**

Figure 108 Fuel Efficiency and Noise Results

The elevon noise is expected to be low and the N2A-EXTE is expected to meet the NASA SFW N+2 noise goal. Figure 109 summarizes relative to the circa 2007 SFW N+2 goals for fuel efficiency and noise.

	"N+2" Generation Hybrid Wing 2018-2020	Phase I N2A Efficient Low Noise Hybrid Wing Body 2020	Phase II N2A-EXTE Efficient Low Noise Hybrid Wing Body 2020
Noise (cum below Stage 3)	- 52 dB	- 46.7 dB	- 51.6-57.3 dB**
Performance: Aircraft Fuel Burn (relative to current technology	- 25%	- 29%*	- 26%

* Did not include transonic PAI penalty

** Depends on elevon noise level

Figure 109 Goals Summary

The conclusions are summarized in Figure 110. The BR&T led team has developed a cruise efficient low noise HWB configuration starting from the MIT SAX 40 evolving into the N2A-EXTE powered by NASA GRC propulsors that employ noise compression nozzles from UCI. The N2A-EXTE is predicted to meet the SFW N+2 goals for a 2020 EIS.

CONCLUSIONS

The ELNHWB Team has successfully completed the major purpose of this contract investigation:

- UCI developed jet noise compression nozzle concepts to improve jet noise shield and developed for field noise prediction method for partial shielding of the distributed jet noise source
- MIT developed a rapid method for ANOPP to predict noise shielding applicable to turbomachinery noise as a point source
- BR&T developed an efficient low noise Hybrid-wing Body (N2A-EXTE) configuration predicted to meet the SFW N+2 fuel efficiency and noise goals
- BR&T and UTRC have developed recommended plans for testing
- BR&T has defined and commissioned ATK to build a 12.35 ft 5.8% model of the N2A-EXTE for NASA to test in the LaRC 14 x 22 ft low speed wind tunnel

Figure 110 Project Conclusions

A prediction method for a jet that has a distributed noise source with partial shielding has been developed by UCI. UCI has also developed jet noise compression nozzle concepts to increase shielding to reduce noise. The UCI activities are based on small scale tests and require validations with larger scale testing.

MIT has developed a rapid turbomachinery noise shielding prediction method suitable for ANOPP2.

ATK has designed and built a high fidelity 12 ft wind tunnel model for the 14x22 low speed wind tunnel.

6.2 Recommendations

The recommendations based on the progress and results are summarized in Figure 111.

RECOMMENDATIONS

- Conduct tests of the QUIET R-1 model and compare results with selected conditions to verify prediction noise methods
- Conduct tests for data that can be corrected to FAR 36 conditions to assess potential for the N2A-EXTE to meet the N+2 noise goal
- Conduct test to develop low speed aero S&C and loads for a HWB
- Consider spiraling up low speed aero model with powered models for power on effects on loads and pitching moments
- Consider follow on ERA acoustic and low speed aero tests with powered open rotor and geared turbofan simulators

Figure 111 Project Recommendations

Acoustic tests are recommended to validate the prediction methods to provide confidence for applications to other configurations and full scale. Test should also evaluate the ability for the N2A-EXTE to meet the N+2 noise goal.

Low speed aero tests should be conducted for stability and control and loads data.

Expansion of testing to include powered models for power effect benefits for pitch control on aircraft with no empennage.

The QUIET R-1 model is versatile and should be considered for ERA EIS 2025 acoustic and aero tests with a geared turbofan and open rotor propulsion simulators. Tests should be with twin engines to expand the acoustic data base beyond LSAF tests for multiple engine effects and higher angle of attack.

7.0 REFERENCES

1. NASA Aeronautics Research Mission Directorate, Fundamental Aeronautics Program, Subsonic Fixed Wing Project NRA NNH06ZEA001N Amendment 4, Appendix A.2 Topic A.2.4-Hybrid wing/body Technologies released March 2007.

2. The Boeing Company, *Current Market Outlook 2008 – 2027*; Retrieved August 18th, 2008 from: http://www.boeing.com/commercial/cmo/growth.html

3. Airbus Global Market Forecast; *Air CargoForecast – Freighter Demand ;* Retrieved August 18th, 2008 from: http://www.airbus.com/en/corporate/gmf/air-cargo-forecast/freighter-demand/

4. "Silent Aircraft Conceptual Design", the Cambridge – MIT Institute, 6 November 2006

5. Phase I Acoustic Prediction Methodology and Test Validation for an Efficient Low-Noise Hybrid Wing Body Subsonic Transport, NASA Contract Number NNL07AA54C Final Report, October 30, 2008

6. Kawai, R.T., Friedman, D.M., Serrano, L., "Blended Wing Body (BWB) Boundary Layer Ingestion (BLI) Inlet Configuration and System Studies", NASA/CR-2006-214534, Dec. 2006

7. Nickol, Craig L. "Silent Aircraft Initiative Concept Risk Assessment" NASA/TM-2008-215112, February 2008

8. Daggett, D.L., Brown, S.T., Kawai, R.T., "Ultra-Efficient Engine Diameter Study",

NASA/CR-2003-212309, May 2003

9. Sen, R., Hardy, B., Yamamoto, K., Guo, Y. and Miller, G., "Airframe Noise Sub-Component Definition and Model," NASA Contractor Report, NASA CR-2004-213255, 2004.

10. Collier, Fayette, "NASA's Recent Progress Toward Quiet and Efficient Subsonic Air Transport", AIAA Applied Aerodynamics Meeting, Chicago, Illinois, June 28, 2010.

11. NASA ARMD Subsonic Fixed Wing Project, Acoustic Prediction Methodology and Test Validation for an Efficient Low-Noise Hybrid Wing Body Subsonic Transport, NASA Contract Number NNL07AA54C Revised Modification 6, Phase II Metrics Report, December 2010

12. Czech, Thomas, and Elkoby, Propulsion Airframe Aeroacoustics LSAF Experimental Overview" September 19, 2009, NASA Fundamental Aerodynamics Program Annual Meeting

APPENDIX A

Methodology for the Prediction of Jet Noise Shielding

Final Report
Project period: January 2008-December 2010

Dimitri Papamoschou
Department of Mechanical and Aerospace Engineering
University of California, Irvine

December 27, 2010

1. INTRODUCTION

University of California, Irvine (UCI) conducted computational, theoretical, and experimental work on jet noise shielding for the Hybrid Wing Body (HWB) planform, with emphasis on development of methodology for predictive models for jet noise scattering. The research was funded by Boeing Subcontract No. 208547 in support of NASA contract NNL07AA54C "Acoustic Prediction Methodology and Test Validation for an Efficient Low-Noise Hybrid Wing Body Subsonic Transport."

This report emphasizes the documentation of a predictive computational model for jet noise scattering, with a brief overview of recent acoustic experiments on the extended trailing edge N2AEXTE version of the HWB. Additional information is provided in the following conference publications, available from http://supersonic.eng.uci.edu/articles.htm:

- Huang, C., and Papamoschou, D., "Numerical Study of Noise Shielding by Airframe Surfaces," AIAA-2008-2999, 14th Annual AIAA/CEAS Aeroacoustics Conference, Vancouver, Canada, May 2008.
- Papamoschou, D., and Mayoral, S., "Experiments on Shielding of Jet Noise by Airframe Surfaces", AIAA-2009-3326, 15th Annual AIAA/CEAS Aeroacoustics Conference, May 10-12, 2009, Miami, FL.
- Mayoral, S., and Papamoschou, D., "Effects of Source Redistribution on Jet Noise Shielding," AIAA-2010-0652, 48th AIAA Aerospace Sciences Meeting and Exhibit, Jan.4-7, 2010, Orlando, FL.
- Papamoschou, D., "Prediction of Jet Noise Shielding," AIAA-2010-0653, 48th AIAA Aerospace Sciences Meeting and Exhibit, Jan.4-7, 2010, Orlando, FL.
- Papamoschou, D., and Mayoral, S., "Jet Noise Shielding for Advanced Hybrid Wing-Body Configurations," AIAA-2011-0912, 49th AIAA Aerospace Sciences Meeting and Exhibit, Jan.4-7, 2011, Orlando, FL.

Additionally, extensive documentation of the Jet Noise Diffraction Code (JNDC) is available in the software package delivered to NASA.

1.1 Background

This study is motivated by the development of ultra-quiet advanced aircraft that will meet NASA's N+2

and eventually N+3 noise goals of 42 and 71 dB, respectively, relative to the Stage 4 baseline. Whether the aircraft are powered by turbofan or open-rotor engines, the noise reduction goals are unlikely to be met without exploiting the propulsion-airframe integration that will reduce the noise emitted towards the community. The advent of the Hybrid Wing-Body (HWB) airplane[1], with the engines mounted over the wing, has reinvigorated the engine over-the-wing (OTW) concept for noise shielding, an area of active research in the 1970s[2-4]. The HWB design allows sufficient planform area for shielding of both the forward-emitting turbomachinery sources and the aft-emitting jet noise sources.

To properly integrate the engine with the airframe for jet noise shielding, physics-based predictive tools must be developed. The challenge is that jet noise is a distributed and directive source, whose exact nature remains under investigation. The previous state of the art in empirical prediction of jet noise shielding involves approximating the noise source as a small number of discrete sources[5] combined with insertion loss formulas developed for barrier insertion losses of sound from point sources. The insertion loss formula is based on Maekawa's experiments[6] and involves only the Fresnel number. The current state of the art is thus inadequate because jet noise is a distributed directive source while the barrier-insertion relations were developed for omnidirectional point sources. Development of reliable, physics-based predictive tools for jet noise shielding is inextricably connected to properly describing the jet noise source. Given the complexity of sound generation by turbulent mixing, one must resort to simplified models that retain some of the essential physics - such as the wavepacket model for noise generation from large-scale structures. The intent is to develop predictive methodologies that will be used in the next-generation ANOPP tools for aircraft noise. The tools must be *useful* in the sense that they should not require tremendous amount of computational resources.

To appreciate the nature of jet noise diffraction, it is helpful to examine some acoustic data involving simple jets and shields from tests conducted at UCI. Figure 1.1.1 shows a canonical setup for experiments and computations reported here. Figure 1.1.2 shows narrowband sound pressure level spectra for one of the configurations tested. The spectra are plotted against Strouhal number $Sr=fD_j/U_j$. With increasing polar angle θ from the jet axis shielding becomes more pronounced for $Sr\geq 0.5$ but there is substantial noise excess for $Sr<0.5$. This is consistent with trends observed in previous works[2], which attributed the excess noise to jet scrubbing the shielding surface. However for the experiment shown in Fig.1.1.2 it was verified, using Pitot surveys, that the jet did not contact the shielding plate. The excess noise therefore is not necessarily connected to scrubbing and may also be caused by the jet noise source and its interaction with the surface. Any physical model should be able to predict not only the noise suppression but also the noise excess created by the boundary.

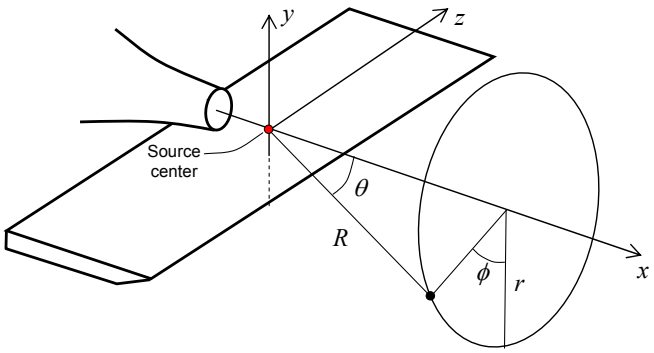

Fig. 1.1.1 Canonical jet shielding configuration.

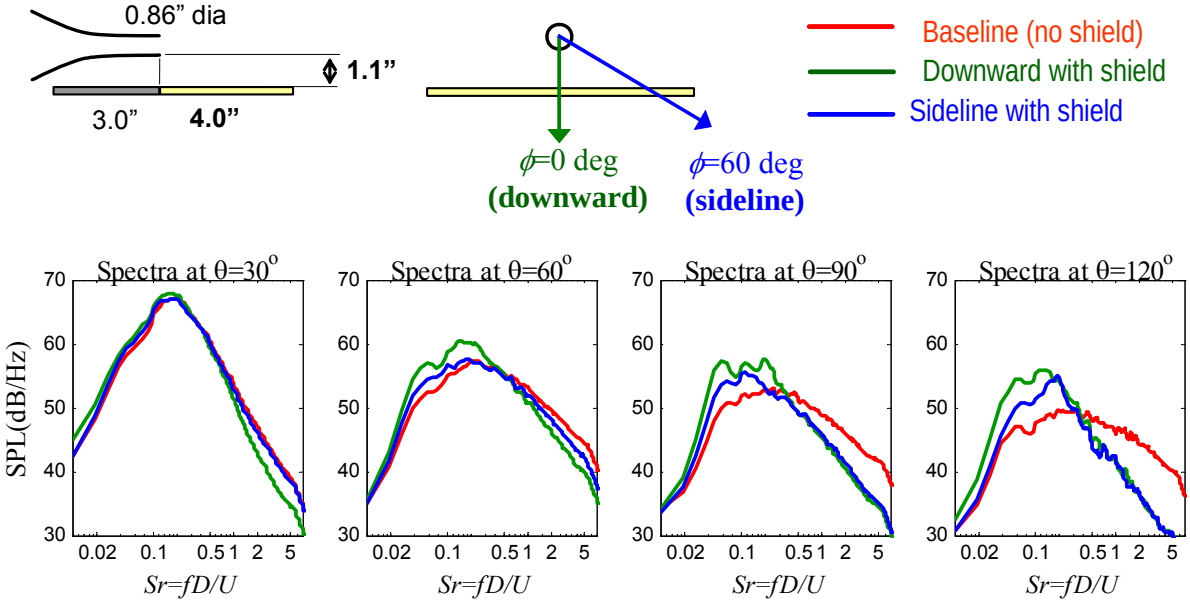

Fig. 1.1.2 Experimental spectra of noise shielding from a Mach 0.9 cold jet. The span of the rectangular shield was 24 inches. The polar angle θ is defined from the downstream jet axis.

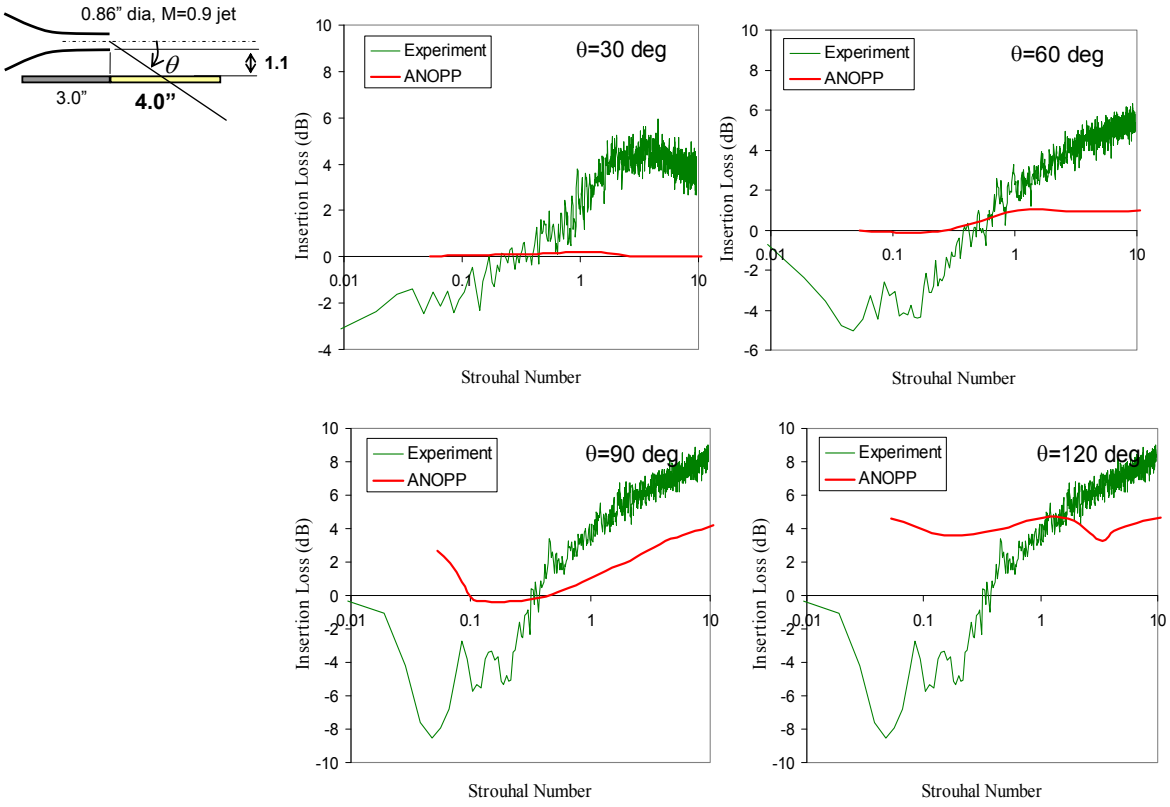

Fig. 1.1.3 Insertion loss for configuration shown on top left. Experimental measurements and ANOPP-based predictions are compared at difference polar angles.

1.2 Assessment of Point Source Approximation for Jet Noise

The first step in our investigation was to assess the accuracy with which existing tools in ANOPP could predict jet noise shielding. The tools are the ST2JET module[5] and Maekawa's insertion-loss formula[6] used in the WING module. The Maekawa relation is based on geometric acoustics from omni-directional point sources. The ST2JET module simplifies the jet noise source a number of independent point sources. The results of the ANOPP-based shielding prediction were compared to experimental data from past works[2-4] and from subscale tests in the UCI lab. The comparisons were not encouraging. As shown in Fig. 1.1.3, ANOPP-based predictions of insertion loss are in strong disagreement with experiments. The basic reasons for the disagreement are that (a) the noise source is much more complex than a collection of independent point sources and (b) the shielding tool used (Maekawa's formula) is inappropriate for a complex source like the jet.

Let us consider the effect of the directivity of the jet noise. Here we are concerned with the *acoustic near field* of the jet, because diffraction occurs in the near field. Can we make the approximation that, in the near field, sound of a directional source comes from a point? To answer this question, we note that an acoustic pressure with directivity in polar angle θ can be reconstructed in terms of Legendre polynomials:

$$p(R,\theta,t) = \sum^{\infty} A_m P_m(\cos\theta) h_m(kR) e^{i\omega t} \qquad (1.2.1)$$

where P_m are the Legendre polynomials, h_m are spherical Hankel functions, and $k=\omega/a_\infty$ is the

wavenumber. As $kr \to \infty$, the spherical Hankel function is approximated by

$$h_m(kR) = i^{-(m+1)} \frac{e^{ikR}}{kR}$$

and the acoustic pressure takes the form

$$p(R,\theta,t) = \sum_{m=0}^{\infty} A_m P_m(\cos\theta) i^{-(m+1)} \frac{e^{ikR}}{kR} e^{i\omega t} = \frac{e^{i(kR-\omega t)}}{R} \sum_{m=0}^{\infty} \frac{A_m}{k} P_m(\cos\theta) i^{-(m+1)} \tag{1.2.2}$$

Equation (1.2.2) represents a directive pressure field that comes from a point and can be written as

$$p(R,\theta,t) = \frac{e^{i(kR-\omega t)}}{R} \Psi(\theta) \tag{1.2.3}$$

The first term on the right-hand side is sound emission from a monopole, and the second term $\Psi(\theta)$ is the polar directivity of the far acoustic field. In the far-field formulation of Eq.3, the directivity Ψ is a real function. If we apply the formulation of Eq.3 in the near field, we realize that Ψ becomes complex and its distribution is different from that in the far-field. This will be illustrated by examples to follow. Comparing Eqs. 1.2.1 and 1.2.2 it becomes evident that the validity of the point-source approximation depends on how close the function

$$g_m(kR) = i^{m+1} \frac{kr}{e^{ikr}} h_m(kR)$$

approaches unity on the complex plane, i.e., how close it is to $1+0i$. To quantify the error in the point-source approximation, we look at the departure of g_m from unity:

$$\text{Departure} = \sqrt{(\text{Re}\{g_m\}-1)^2 + (\text{Im}\{g_m\})^2}$$

To accurately reconstruct a typical jet noise field using Eq.1.2.1, our experience indicates that we need at least five Legendre terms. Figure 1.2.1 plots the departure from unity of the function g_5 versus distance and frequency for a full-scale application. This figure illustrates the error in the point-source approximation for a directional acoustic field. For frequencies of relevance to aircraft certification, the error is unacceptably high (more than 50%) for typical distances associated with shielding (a few meters). This addresses only one complexity of the jet noise source. The other major complication is that the source has a finite spatial coherence.

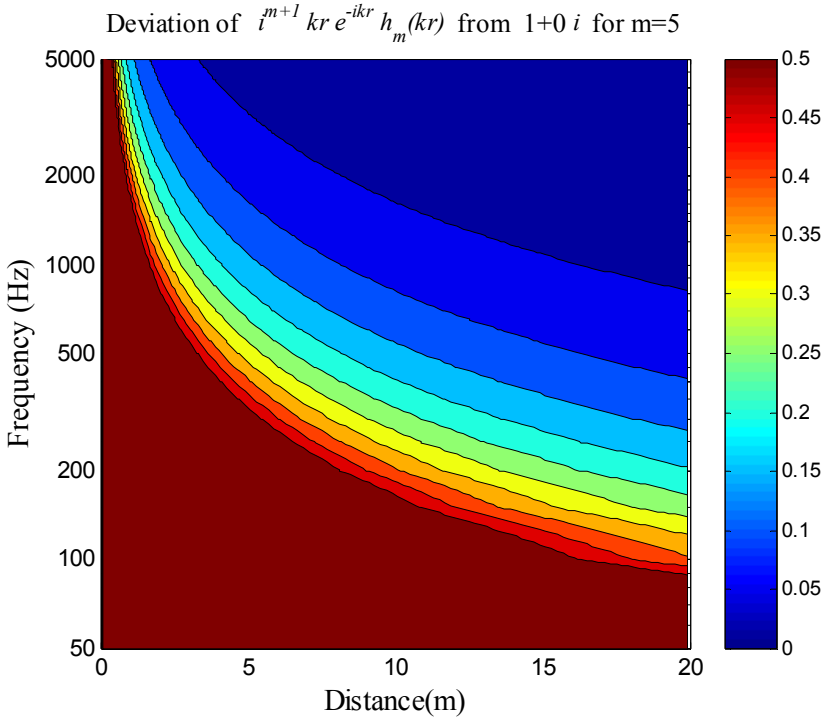

Fig. 1.2.1 Error in approximating a directional acoustic field as coming from a point. Brown region indicates more than 50% error.

2. DEVELOPMENT OF THE JET NOISE DIFFRACTION CODE

The failure of the point source model for the jet noise source motivated the development of a more advanced, computational approach for the prediction of jet noise shielding. The methodology proposed here combines an instability-wave model of the jet noise source with the Boundary Element Method for predictions of diffraction. The noise source modeling is generic enough that it can be applied with other diffraction methods, such as the Fast Scattering Code (FSC).

It should be kept in mind that the jet noise source is an extremely complex phenomenon that remains under intense investigation by the aeroacoustics community. From a fundamental standpoint, our ability to predict the diffraction on jet noise depends on how well we know the noise source. The Boundary Element Method is used widely for diffraction problems but its ability to solve efficiently high-frequency problems remains an area of development. Although the BEM is intrinsically an exact method, its application to complex problems requires approximations such as the multipole expansion. The validities of those approximations have not been demonstrated in a robust fashion by the code developers. The user should thus be mindful that both the knowledge of the jet noise source and the development of practical diffraction tools are evolving areas of research.

This section provides the fundamental background and documentation for the Jet Noise Diffraction Code developed under this effort. The software package (JNDC Version 1.3) has been provided to

NASA.

2.1 Code Structure and Contents

The overall computational approach is illustrated in Fig.2.1.1. The main tasks are as follows:

1. Build a simple model for jet noise that produces sound with far-field directivity comparable to the experimental one. This model gives the *incident field*, which is evaluated on the boundary surface and at the field points.
2. Define the boundary surface and mesh it according to the requirements of the Boundary Element Method (BEM.)
3. Solve the diffraction problem using BEM. The output is the *scattered field* on the boundary and at the field points. The *total field* is the summation of the incident field and the scattered field. Keep in mind that these fields are complex.
4. Provide a code structure and user interface that facilitates the processing of a large number of cases and simplifies the organization of the results.

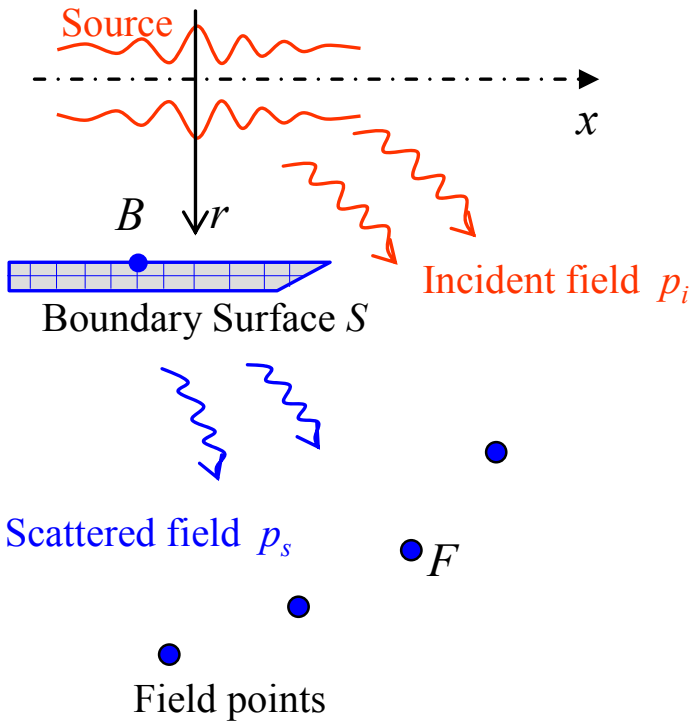

Fig. 2.1.1 Setup of boundary element method (BEM) for diffraction of wavepacket noise.

The code is arranged in the following directories:

WORK. This is the working directory from which the wavepacket parameterization and diffraction programs are called. The principal files are:

BEM.FOR	Fortran code for diffraction calculation using either regular BEM or fast monopole BEM (FastBEM). To compile, run B.BAT on the command prompt
WPARAM.FOR	Standard source parameterization. The compile, run W.BAT on the command prompt
WPARAMX.FOR	Global source parameterization. The compile, run WX.BAT on the command prompt
SHIELD.XLS	Spreadsheet with source, shield, and field point information, read by BEM.FOR
WPARAM.XLS	Spreadsheet for standard wavepacket parameterization, read by WPARAM.FOR
WPARAMX.XLS	Spreadsheet for global wavepacket parameterization, read by WPARAM.FOR
FASTBEM_ACOUSTICS_64.EXE	Executable code for FastBEM. Needs license file *.LIC to run.

In addition the directory includes Matlab files for plotting, explained in Chapter 9.

SOURCE\HELM3D. Collection of fortran subroutines used in the regular BEM computation. Matrices up to 7K × 7K.

SOURCE\HELM3D_12K. Same as HELM3D but with matrices up to 12K× 12K. Requires large RAM.

SOURCE\INCIDENT. Subroutines used for the computation of the incident field.

WPINC.FOR	Exact solution for wavepacket incident pressure field. Called by BEM.FOR.
WPINC_FBEM.FOR	Computational solution of wavepacket incident field using FastBEM. Called by BEM.FOR
WPINC_RBEM.FOR	Computational solution of wavepacket incident field using Regular BEM. Called by BEM.FOR
WPVINC.FOR	Exact solution for wavepacket incident pressure and velocity fields. Called by BEM.FOR.
PPINC.FOR	Incident field for a monopole source. Called by BEM.FOR
ENVELOPE.FOR	Amplitude modulation function of wavepacket. Called by BEM.FOR and by WPARAM.FOR.
SUMGH.FOR	Computation of Hankel summation term
WPFAR.FOR	Far-field approximation of incident field for a given frequency. Called by WPARAM.FOR

CALCFG.FOR	Calculates function and its gradient. Called by CONMIN.FOR
CONMIN.FOR	Minimization using conjugate gradient method. Called by WPARAM.FOR
WPFARX.FOR	Far-field approximation of incident field for a set of frequencies. Called by WPARAMX.FOR
CALCFGX.FOR	Calculates function and its gradient. Called by CONMINX.FOR
CONMINXFOR	Minimization using conjugate gradient method, applied to global parameterization. Called by WPARAMX.FOR

SOURCE\MESH. Subroutines used for mesh generation and refinement. All are callable by BEM.FOR

PLATE3MESH.FOR	Triangular mesh for rectangular plate
PLATE4MESH.FOR	Quadrilateral mesh for rectangular plate
WING3MESH.FOR	Triangular mesh for wing-shaped boundary
FOIL.FOR	NACA 00xx airfoil shape, called by WING3MESH.
ANSYS3MESH.FOR	Conversion of ANSYS triangular grid to format used by BEM.
SPLIT3MESH.FOR	Local refinement for triangular mesh
OUT2TECB.FOR	Tecplot output for solution on boundary
OUT2TECF.FOR	Tecplot output for solution at field points (meshed sphere or hemisphere only)
OUT2TECW.FOR	Tecplot output for solution on cigar-shaped wavepacket surface (for computational solution of incident field)

SOURCE\MATH. Mathematical and geometric relations, used by multiple programs.

HANKEL.FOR	Hankel function of the first kind and order m. Argument can be real or imaginary.
FOUR1.FOR	Fast Fourier Transform
SAGOX.FOR	Savitzky-Golay smoothing.
INTERP.FOR	Linear interpolation
GEOMETRY.FOR	Several geometric relations.
FCSERIES.FOR	Complex Fourier series for Gaussian distribution or square window.

INCIDENT. Storage of incident fields and wavepacket shapes used in wavepacket parameterization and diffraction computation.

*.FAR	Far-field approximation to wavepacket incident field, generated by WPARAM.FOR
*.PARAM	Source parameters generated by WPARAM.FOR or WPARAMX.FOR
*.WPK	Wavepacket shape, generated by WPARAM.FOR

MESH. Storage of meshes used in diffraction computation.

*.MS3 are triangular meshes generated by the code
*.MS4 are quadrilateral meshes generated by the code (rectangular plate only)
*.MSF are sphere or hemisphere grids used for Tecplot field point solution.

*.IN are ANSYS files generated by outside software

EXPDATA. Experimental far-field sound pressure level (*.SPL) files used for wavepacket parameterization and for comparing with results of diffraction codes. Each file is an ASCII matrix of SPL versus frequency and polar angle. Read by WPARAM.FOR.

ANOPPDATA. Output files of ANOPP for single- and dual-stream jets.

RESULTS. Diffraction results from regular or Fast BEM.

*.FIE	Solution at field points. Header includes all the problem parameters.
*.BOU	Solution on boundary. Header states 'F' for FastBEM, 'R' for Regular BEM.
*.PLT	Tecplot output of solution on boundary and field points. See Chapter 10 for details.

DOCUMENTATION. This document, FastBEM user guide, and PPT on mesh generation for wing-shaped boundary.

2.2 Noise Source Model

2.2.1 Wavepacket Model

It is generally agreed that sound emission in the aft direction, at shallow angles to the jet axis, is caused by large-scale turbulent structures while noise emitted at large angles to the jet axis is caused by fine-scale turbulent motions. The former is highly directional, while the latter radiates uniformly. The large-scale structures can be modeled as instability waves that grow and then decay with axial distance. This is model based on the foundational works by Tam and Burton[7], Crighton and Huerre[8], Avital *et al.*[9], and Morris[10]. In this section we describe the wavepacket analysis, starting from a simple formulation and progressing to more complex treatments. The generic wavepacket model is depicted in Fig.2.2.1 and the coordinate systems used in the analysis that follows are shown in Fig.2.2.2.

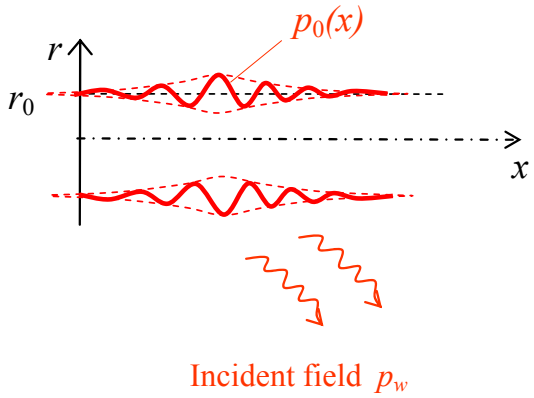

FIG. 2.2.1 WAVEPACKET MODEL OF JET NOISE

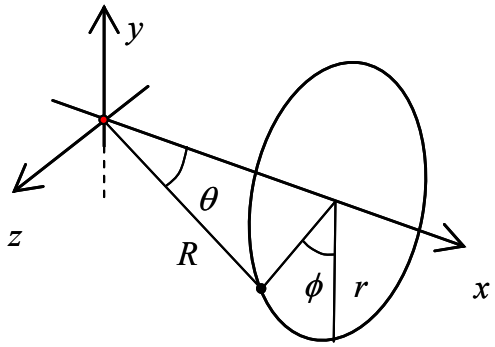

FIG. 2.2.2 CARTESIAN (*X, Y, Z*) , POLAR (*X ,R, ϕ*), AND SPHERICAL (*R,θ, ϕ*) COORDINATE SYSTEMS.

2.2.1.1 Elementary Model

The jet is replaced by a cylinder $r=r_0$ on which we prescribe the pressure perturbation

$$p_w(n,r_0,x,\varphi,t) = p_0(x)e^{-i\omega t+in\phi} \tag{2.2.1}$$

where n denotes the azimuthal mode and ϕ is the azimuthal angle. The shape $p_0(x)$ is expected to be of the form $p_0(x) = A(x)e^{i\alpha x}$, with $A(x)$ an amplification-decay envelope that represents the axial coherence length scale, and α the wavenumber. The precise form for $p_0(x)$ does not come into play until we examine specific implementations of the wavepacket mode. Denoting the spatial Fourier transform of $p_0(x)$ as $\hat{p}_0(k)$, the solution for $r \geq r_0$ is[10]

$$p_w(n,r,x,\varphi,t) = \frac{1}{2\pi}e^{-i\omega t+in\phi}\int_{-\infty}^{\infty}\hat{p}_0(k)\frac{H_n^{(1)}(\lambda r)}{H_n^{(1)}(\lambda r_0)}e^{ikx}dk \tag{2.2.2}$$

$$\lambda = \left[\left(\frac{\omega}{a_\infty}\right)^2 - k^2\right]^{1/2}, \quad -\frac{\pi}{2} < \arg(\lambda) < \frac{\pi}{2}$$

Equation 2.2.2 is the exact solution to the linearized problem, valid everywhere for $r \geq r_0$. Once the wavepacket shape $p_0(x)$ is determined (through the minimization scheme explained in the next section), Eq. 2.2.2 yields the incident field p_i on the object surface and at the field points. The actual computation of Eq.2.2.2 involves taking the forward FFT of $p_0(x)$ to obtain $\hat{p}_0(k)$, then the inverse FFT of $\hat{p}_0(k)$ multiplied by the Hankel functions. An important aspect of the pressure field generated by the wavepacket is that it has radiative (supersonic) and decaying (subsonic) components. It is useful to separate the two in order to gain insights into the mechanisms of diffraction. The decaying component involves phase speeds that are subsonic, $|\omega/k|<a_\infty$ or $|k|> \omega/a_\infty$:

$$p_{w,sub}(n,r,x,\varphi,t) = \frac{1}{2\pi}e^{-i\omega t+in\phi}\int_{|k|>\omega/a_\infty}\hat{p}_0(k)\frac{H_m^{(1)}(\lambda r)}{H_m^{(1)}(\lambda r_0)}e^{ikx}dk \tag{2.2.3a}$$

The radiating component involves phase speeds that are sonic or supersonic, $|k|\leq \omega/a_\infty$:

$$p_{w,\sup}(n,r,x,\varphi,t) = \frac{1}{2\pi} e^{-i\omega t + in\phi} \int_{-\omega/a_\infty}^{\omega/a_\infty} \hat{p}_0(k) \frac{H_n^{(1)}(\lambda r)}{H_n^{(1)}(\lambda r_0)} e^{ikx} dk \qquad (2.2.3b)$$

From Eq.2.2.3b, using the convolution property of the Fourier transform, we obtain an expression for the part of $p_0(x)$ that radiates to the far field:

$$p_{0,\sup}(x) = \frac{1}{\pi} \int_{-\infty}^{\infty} \frac{p_0(\xi)}{x-\xi} \sin\left[\frac{\omega}{a_\infty}(x-\xi)\right] d\xi \qquad (2.2.4)$$

This is relevant to the axial alignment of the wavepacket based on far-field noise source location measurements, discussed in the next section (subroutine **P0RAD.FOR**).

The far-field approximation of Eq.2.2.2 is[10]

$$p_{w,far}(n,R,\theta,\varphi,t) = -\frac{i}{\pi R} \frac{\hat{p}_0\left(\frac{\omega}{a_\infty}\cos\theta\right)}{H_n^{(1)}\left(\frac{\omega}{a_\infty} r_0 \sin\theta\right)} e^{i\omega R/a_\infty} e^{-i\omega t + in\phi} \qquad (2.2.5)$$

where R is the distance of the observer from the origin and θ is the polar angle from the downstream wavepacket (jet) axis. The modulus squared of Eq.2.2.5 yields the modeled autospectrum of the far-field pressure:

$$S_{w,far}(n,R,\theta,\omega) = \frac{1}{(\pi R)^2} \left| \frac{\hat{p}_0\left(\frac{\omega}{a_\infty}\cos\theta\right)}{H_n^{(1)}\left(\frac{\omega}{a_\infty} r_0 \sin\theta\right)} \right|^2 \qquad (2.2.6)$$

For fixed frequency ω, Eq.2.2.6 gives the polar intensity distribution. The simplicity of the far-field solution lends itself to the minimization process for determining the wavepacket shape, wherein Eq.2.2.6 (and its versions discussed later) needs to be evaluated hundreds of times.

2.2.1.2 Model with azimuthal amplitude variation

We can generalize the approach of Eq.2.2.1 to prescribe an arbitrary azimuthal variation that can include the helical mode term $e^{in\phi}$ as well as an azimuthal amplitude variation. This approach is relevant to jets with non-axisymmetric noise source distribution and allows the development of a stochastic noise source model with a noise source having limited azimuthal coherence. We revise the formulation of Eq.2.2.1 as follows:

$$p_w(r_0, x, \varphi, t) = p_0(x) G(\varphi) e^{-i\omega t} \qquad (2.2.7)$$

where $G(\phi)$ is an azimuthal variation that can include helical modes and/or non-uniformities due to asymmetric flows. Expressing $G(\phi)$ in terms of its complex Fourier series

$$G(\varphi)=\sum_{-\infty}^{\infty} g_m e^{im\varphi}$$
$$g_m=\frac{1}{2\pi}\int_{-\pi}^{\pi} G(\varphi)e^{-im\varphi}d\varphi \qquad (2.2.8)$$

and denoting the spatial Fourier transform of $p_0(x)$ as $\hat{p}_0(k)$, the solution for $r \geq r_0$ is

$$p_w(r,x,\varphi,t)=\frac{1}{2\pi}e^{-i\omega t}\sum_{-\infty}^{\infty} g_m e^{im\varphi}\int_{-\infty}^{\infty}\hat{p}_0(k)\frac{H_{|m|}^{(1)}(\lambda r)}{H_{|m|}^{(1)}(\lambda r_0)}e^{ikx}dk$$
$$\lambda=\left[\left(\frac{\omega}{a_\infty}\right)^2-k^2\right]^{1/2}, \quad -\frac{\pi}{2}<\arg(\lambda)<\frac{\pi}{2} \qquad (2.2.9)$$

where $H_m^{(1)}$ is the Hankel function of the first kind of order m and the property $H_{-m}^{(1)}=(-1)^m H_m^{(1)}$ has been used. Equation 2.2.9 is the exact solution to the linearized problem, valid everywhere for $r \geq r_0$, and gives the incident field p_i on the object surface and at the field points (subroutine **WPINC.FOR**). The same distinctions of radiative and decaying pressure fields hold as for the simple formulation. The supersonic part of the wavepacket is still given by Eq.2.2.4.

The azimuthal variation function $G(\phi)$ used in JNDC v.1.3 can take the forms of a Gaussian distribution or a square window function, both centered at ϕ_0, with width $\Delta\phi$ and helical mode of order n:

$$G(\varphi)=\exp\left[-18.42\left(\frac{\varphi-\varphi_0}{\Delta\varphi}\right)^2\right]e^{in\varphi}$$
$$G(\varphi)=\begin{Bmatrix}1, & |\varphi-\varphi_0|\leq\Delta\varphi/2\\ 0, & |\varphi-\varphi_0|>\Delta\varphi/2\end{Bmatrix}e^{in\varphi} \qquad (2.2.10)$$

For the Gaussian distribution, $\Delta\phi$ represents the 1% width. The Fourier coefficients $g(-M{:}M)$ are computed by subroutine **FCSERIES.FOR** up to an order M that gives an error of about 3%. Widths as small as $\Delta\phi$=10° are possible (they require M~50). Setting $\Delta\phi$=0° is interpreted by the code as an azimuthally uniform intensity with helical mode n.

Using the asymptotic form of the Hankel function

$$H_m^{(1)}(\zeta)\to\sqrt{\frac{2}{\pi\zeta}}\exp\left[i\left(\zeta-\frac{\pi}{4}-m\frac{\pi}{2}\right)\right], \quad |\zeta|\to\infty$$

the method of stationary phase gives the following result for the pressure in the far field

$$p_{w,far}(R,\theta,\varphi,t)=-\frac{i}{\pi R}e^{i\omega R/a_\infty}e^{-i\omega t}\hat{p}_0\left(\frac{\omega}{a_\infty}\cos\theta\right)\sum_{m=-\infty}^{\infty}\frac{g_m e^{-i|m|\frac{\pi}{2}}}{H_{|m|}^{(1)}\left(\frac{\omega}{a_\infty}r_0\sin\theta\right)}e^{im\phi} \qquad (2.2.11)$$

where R is the distance of the observer from the origin and θ is the polar angle from the downstream wavepacket (jet) axis. The modulus squared of Eq.2.2.11 yields the modeled autospectrum of the far-field pressure:

$$S_{w,far}(R,\theta,\varphi,\omega)=\frac{1}{(\pi R)^2}\left|\hat{p}_0\left(\frac{\omega}{a_\infty}\cos\theta\right)\right|^2\left|\sum_{m=-\infty}^{\infty}\frac{g_m e^{-i|m|\frac{\pi}{2}}}{H^{(1)}_{|m|}\left(\frac{\omega}{a_\infty}r_0\sin\theta\right)}e^{im\phi}\right|^2 \qquad (2.2.12)$$

Equation Eq.2.2.12 is the analogue of Eq.2.2.6 for a wavepacket with generalized azimuthal variation. It is evident that azimuthal directivity (summation term on the right hand side) is independent of the wavepacket shape $p_0(x)$. It only needs to be evaluated once. This is done by subroutine **SUMGH.FOR** and the resulting intensity is saved and used in the parameterization process.

2.2.1.2 Superposition of uncorrelated azimuthal disturbances

There is significant evidence that at high frequency the jet turbulence is weakly correlated in the azimuth angle, hence the interest in treating azimuthally-incoherent disturbances. Here we are interested in obtaining the far-field solution (used in the parameterization) for a superposition of azimuthally-uncorrelated disturbances. Figure 2.2.3 helps illustrate the physics of this problem. A single, isolated azimuthal disturbance of extent $\Delta\phi$ creates a far-field intensity distribution (in a given polar direction) that has a certain directivity in ϕ, with extent much wider than $\Delta\phi$. The superposition of isolated azimuthal disturbances, spaced apart by $\Delta\phi$ and covering the whole circle, will lead to a far-field intensity distribution that is the summation of the intensities from each isolated disturbance. Even though the far-field intensity distribution will be uniform in ϕ, the solution to this problem is very different from the uniform intensity distribution resulting from the coherent wavepacket of Eq. 3.6.

Considering a wavepacket with azimuthal extent $\Delta\phi$ (either a Gaussian or a square-window distribution, as given by Eq. 3.10) and oriented at azimuth angle ϕ_k, the far-field intensity (Eq.2.2.12) can be expressed as

$$S_{w,far}(R,\theta,\varphi,\omega)=\frac{1}{(\pi R)^2}\left|\hat{p}_0\left(\frac{\omega}{a_\infty}\cos\theta\right)\right|^2\Phi(\varphi-\varphi_k,\Delta\varphi,\theta)$$

$$\Phi(\varphi-\varphi_k,\Delta\varphi,\theta)=\left|\sum_{m=-\infty}^{\infty}\frac{g_m e^{-i|m|\frac{\pi}{2}}}{H^{(1)}_{|m|}\left(\frac{\omega}{a_\infty}r_0\sin\theta\right)}e^{im(\varphi-\varphi_k)}\right|^2 \qquad (2.2.13)$$

Consider now a number of azimuthally-uncorrelated wavepackets according to the middle drawing of Fig. 2.2.3. The resulting far-field intensity distribution is

$$S_{w,far}(R,\theta,\varphi,\omega)=\frac{1}{(\pi R)^2}\left|\hat{p}_0\left(\frac{\omega}{a_\infty}\cos\theta\right)\right|^2\sum_{k=0}^{K}\Phi(\varphi-\varphi_k,\Delta\varphi,\theta)$$

$$\varphi_k=k\Delta\varphi \qquad (2.2.14)$$

$$K=\frac{2\pi}{\Delta\varphi}-1$$

Considering the azimuthal direction ϕ=0, the modeled intensity distribution becomes:

$$S_{\mathrm{mod}}(R,\theta,0,\omega)=\frac{1}{(\pi R)^2}\left|\hat{p}_0\left(\frac{\omega}{a_\infty}\cos\theta\right)\right|^2\sum_{k=0}^{K}\Phi(-\varphi_k,\Delta\varphi,\theta)$$

$$\varphi_k=k\Delta\varphi \qquad (2.2.15)$$

$$K=\frac{2\pi}{\Delta\varphi}-1$$

This is the modeled intensity used in the parameterization of a jet with limited azimuthal coherence. The function Φ and its summation are evaluated by subroutine **SUMGH.FOR.**

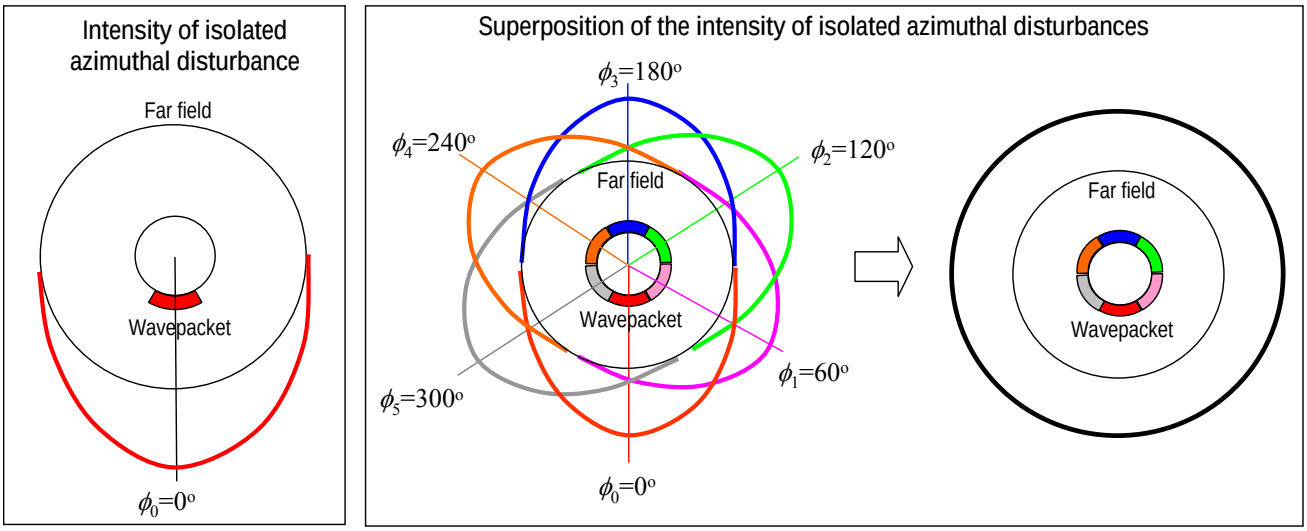

Fig. 2.2.3 Illustration of the treatment of azimuthally-uncorrelated wavepackets. In this example the azimuthal spacing is $\Delta\phi$=60°.

2.2.1.3 Computational solution for the wavepacket incident field

For azimuthal distributions requiring a large number of modes m, and hence evaluation of large-order Hankel functions, the solution of Eq.2.2.11 becomes extremely laborious. An alternative is to compute the wavepacket incident field using the Boundary Element Method, applying the packages described in Chapter 6. The initial perturbation, Eq.2.2.7, is prescribed on a cylindrical grid that represents the jet. The ends of the cylinder are rounded up, so the mesh has a cigar-like appearance. The mesh generation is described in Section 2.1.4. An example mesh is shown in Fig. 2.2.4.

The BEM is then used in radiation mode wherein we impose a pressure boundary condition on the cigar surface according to Eq.2.2.7. In particular, the efficiencies of the fast-multipole BEM (FastBEM) allow rapid computation of the incident field, so this approach may be used for simple and complex wavepackets. Subroutine WPINC_FBEM.FOR computes the incident field using FastBEM and subroutine WPINC_RBEM.FOR computes the incident field using Regular BEM.

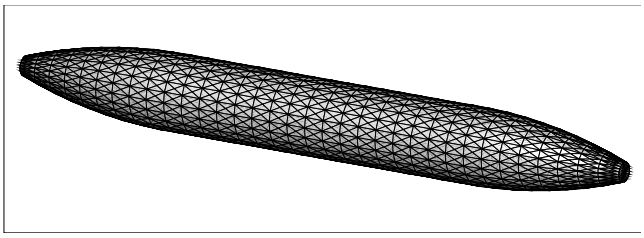

Fig. 2.2.4 Example mesh for computation of wavepacket incident field using BEM.

2.2.1.4 Wavepacket velocity field

The incident velocity field is not used in this particular code, but is used in other diffraction codes. For this reason, it is useful to have a tool for computing the incident velocity field of the wavepacket (the monopole velocity is very simple and probably already included in those codes). Starting from the linearized momentum equation

$$\rho \frac{\partial \mathbf{u}}{\partial t} = -\nabla p \qquad (2.2.16)$$

and assuming that both **u** and p fluctuate in time harmonically according to $e^{-i\omega t}$, we solve for the velocity field

$$\mathbf{u} = -\frac{i}{\rho\omega}\nabla p \qquad (2.2.17)$$

Now we use the simple-wavepacket solution for the pressure field, Eq.2.2.2. Letting

$$P(r,x) = \frac{1}{2\pi}\int_{-\infty}^{\infty} \hat{p}_0(k)\frac{H_n^{(1)}(\lambda r)}{H_n^{(1)}(\lambda r_0)}e^{ikx}dk$$

the velocity field takes the form

$$\mathbf{u}(x,r,\phi,t) = -\frac{i}{\rho\omega}e^{-i\omega t}\nabla\left[e^{in\phi}\,P(x,r)\right] \qquad (2.2.18)$$

and the resulting velocity components in the polar coordinate system (axial, radial, and azimuthal - see Fig. 2.2.2) are:

$$\begin{aligned}
u_x(x,r,\phi,t) &= \frac{1}{\rho\omega}e^{-i\omega t+in\varphi}\frac{1}{2\pi}\int_{-\infty}^{\infty} k\hat{p}_0(k)\frac{H_n^{(1)}(\lambda r)}{H_n^{(1)}(\lambda r_0)}e^{ikx}dk \\
u_r(x,r,\phi,t) &= -\frac{i}{\rho\omega}e^{-i\omega t+in\varphi}\left[\frac{n}{r}P(x,r) - \frac{1}{2\pi}\int_{-\infty}^{\infty}\lambda\,\hat{p}_0(k)\frac{H_{n+1}^{(1)}(\lambda r)}{H_n^{(1)}(\lambda r_0)}e^{ikx}dk\right] \qquad (2.2.19) \\
u_\phi(x,r,\phi,t) &= \frac{1}{\rho\omega}e^{-i\omega t+in\varphi}\frac{n}{r}P(x,r)
\end{aligned}$$

Rotational transformation gives the Cartesian velocity components:

$$u_y = -u_r \cos\phi + u_\phi \sin\varphi$$
$$u_z = u_r \sin\phi + u_\phi \cos\varphi \qquad (2.2.20)$$

The velocity field (along with the pressure field) is computed by subroutine **WPVINC.FOR.** The resulting file name *.INC has the following structure:

x, y, z, p_{real}, p_{imag}, $u_{x,\text{ real}}$, $u_{x,\text{ imag}}$, $u_{y,\text{ real}}$, $u_{y,\text{ imag}}$, $u_{z,\text{ real}}$, $u_{z,\text{ imag}}$

2.2.2 Combination with Monopole

The wavepacket model by itself may be unable to capture the directivity of jet noise at large polar angles from the jet axis. It is therefore necessary to combine it with an additional noise source that has omnidirectional character. Here we use a simple point source (monopole) whose incident field is given by

$$p_p(R,t) = \frac{Q}{R} e^{-i\omega t + ikR} \qquad (2.2.21)$$

WHERE Q DENOTES THE MONOPOLE STRENGTH (SUBROUTINE **PPINC.FOR**). THE WAVEPACKET AND MONOPOLE SOURCES ARE ASSUMED TO BE UNCORRELATED TO EACH OTHER, SO THE AUTOSPECTRUM OF THE COMBINED FIELD IS THE SUMMATION OF THE INDIVIDUAL AUTOSPECTRA. FOR THE THREE WAVEPACKET FORMULATIONS PRESENTED, THE MODELED INTENSITY IN THE FAR FIELD TAKES THE FORMS:

Simple Formulation

$$S_{\mathrm{mod}}(n,R,\theta,\omega)=\frac{1}{(\pi R)^2}\left|\frac{\hat{p}_0\left(\frac{\omega}{a_\infty}\cos\theta\right)}{H_n^{(1)}\left(\frac{\omega}{a_\infty}r_0\sin\theta\right)}\right|^2+\frac{Q^2}{R^2}$$

Formulation with arbitrary azimuthal variation

$$S_{\mathrm{mod}}(R,\theta,\varphi,\omega)=\frac{1}{(\pi R)^2}\left|\hat{p}_0\left(\frac{\omega}{a_\infty}\cos\theta\right)\right|^2\left|\sum_{m=-\infty}^{\infty}\frac{g_m e^{-i|m|\frac{\pi}{2}}}{H_{|m|}^{(1)}\left(\frac{\omega}{a_\infty}r_0\sin\theta\right)}e^{im\phi}\right|^2+\frac{Q^2}{R^2} \qquad (2.2.22)$$

Stochastic formulation

$$S_{\mathrm{mod}}(R,\theta,0,\omega)=\frac{1}{(\pi R)^2}\left|\hat{p}_0\left(\frac{\omega}{a_\infty}\cos\theta\right)\right|^2\sum_{k=0}^{K}\Phi(-\varphi_k,\Delta\varphi,\theta)\ +\ \frac{Q^2}{R^2}$$

$$\Phi(\varphi-\varphi_k,\Delta\varphi,\theta)=\left|\sum_{m=-\infty}^{\infty}\frac{g_m e^{-i|m|\frac{\pi}{2}}}{H_{|m|}^{(1)}\left(\frac{\omega}{a_\infty}r_0\sin\theta\right)}e^{im(\varphi-\varphi_k)}\right|^2$$

$$\varphi_k=k\Delta\varphi$$

$$K=\frac{2\pi}{\Delta\varphi}-1$$

The modeled intensity in the far field is computed by subroutine **WPFAR.FOR**, in conjunction with subroutine **SUMGH.FOR**

2.2.3 Self-Similar Wavepacket

This is a special implementation of the wavepacket model, applicable to the shear layer surrounding the potential core of the jet where we expect a constant convective velocity U_c and some aspects of self-similar behavior. In particular, we expect that the axial extent of the wavepacket envelope (or coherence length scale) will be inversely proportional to the frequency ω. Equivalently, we are saying that the axial extent of the wavepacket envelope scales inversely with wavenumber $\alpha=\omega/U_c$. Whereas in the original formulation of $p_0(x)$ in Eq.1 we imply a variation

$$p_0(x) = A(x)e^{i\alpha x}$$

now we are stating

$$p_0(x) = A(\alpha x)e^{i\alpha x}$$

In other words, we replace $p_0(x)$ by the self-similar form $P_0(\alpha x) = P_0(\omega x/U_c)$. The advantage of this formulation is that it leads to a process for identifying the dominant azimuthal mode n as a function of frequency ω. At this point it is applicable to the simple wavepacket analysis of Eq.3.1, but it can be extended to the more complex forms.

In the simple wavepacket analysis of Section 2.1.1, the pressure on the cylinder $r=r_0$ was prescribed as

$$p_w(n, r_0, x, \varphi, t) = p_0(x)e^{-i\omega t + in\phi} \tag{2.2.1}$$

We now revise this formulation as follows:

$$p_w(r_0, x, \varphi, t) = \varepsilon(\omega)P_0(\omega x / U_c)e^{-i\omega t + in(\omega)\phi} \tag{2.2.23}$$

where $\varepsilon(\omega)$ is an empirically-determined amplitude, and the azimuthal mode is assumed to follow a given relationship with frequency, $n=n(\omega)$. The function $P_0(\omega x/U_c)$ is implied to be a universal function for a given jet. It is easy to show that

$$\hat{p}_0(k) = U_c \frac{\varepsilon(\omega)}{\omega} \hat{P}_0(kU_c / \omega) \tag{2.2.24}$$

and thus the far-field solution for the simple wavepacket (Eq.3.6) takes the form

$$S_{w,far}(R, \theta, \omega) = U_c^2 \frac{\varepsilon^2(\omega)}{(\pi R \omega)^2} \left| \frac{\hat{P}_0(M_c \cos\theta)}{H^{(1)}_{n(\omega)}\left(\frac{\omega}{a_\infty} r_0 \sin\theta\right)} \right|^2 \tag{2.2.25}$$

where $M_c = U_c / a_\infty$ is the convective Mach number, which is a constant for the shear layers surrounding the potential core of the jet. In Eq.2.2.25, the only coupling between frequency and polar angle comes from the Hankel-function term. This is relevant to the procedure covered in Section 2.3.8 wherein in the azimuthal mode - versus - frequency relation, $n(\omega)$, is estimated by the directivity of the sound pressure level spectrum.

2.3. Noise Source Parameterization

2.3.1 General Approach

The current philosophy of the wavepacket parameterization is determination of the noise source using experimental data that are either already available or not too difficult to obtain. It is noted that highly sophisticated experiments, using elaborate near-field microphone arrays, have been applied to the study of jet noise and specifically the detection of wavepackets. These experiments have yielded valuable insight into the physics of jet noise; however, were done on a limited set of nozzle configurations. It is not reasonable to expect that such elaborate data will be widely available for the type of predictive tools being developed here. In this study the parameterization is based on the availability of experimental far-field sound pressure level (SPL) spectra, and knowledge of the peak noise source location versus frequency.

2.3.2 Mathematical Procedure

There are infinite choices for the wavepacket shape $p_0(x)$ in Eq.2.2.7, so one needs to narrow down the scope to a set of generic functions that can be described in terms of a finite number of parameters. Upon selecting a functional form, the wavepacket shape for given frequency ω and azimuthal mode m can be expressed as

$$p_0(x, A_k)$$

where A_k, k=1,..,K-1, is a vector consisting of K-1 parameters that define the wavepacket shape. The K^{th} parameter is reserved for the monopole strength Q. The parameterization is conducted for a fixed frequency ω and distance R. Given a functional form for $p_0(x)$ and a parameter A_k, we obtain the modeled intensity distribution $S_{\text{mod}}(\theta, m, A_k)$ from Eq. 2.2.22. The idea is then to select the parameter vector A_k in a way that minimizes the difference between the modeled intensity distribution $S_{\text{mod}}(\theta, m, A_k)$ and the experimental intensity distribution $S_{\text{exp}}(\theta)$. Realizing that we are interested in matching the *shape* (directivity) of the polar intensity distribution, and not so much its absolute value, we deal with the normalized values of the modeled and experimental intensities:

$$S^*_{\text{mod}}(\theta, m, A_k) = \frac{S_{\text{mod}}(\theta, m, A_k)}{S_{\text{mod,max}}(m, A_k)}$$
$$S^*_{\text{exp}}(\theta) = \frac{S_{\text{exp}}(\theta)}{S_{\text{exp,max}}} \qquad (2.3.1)$$

where max denotes the peak value of the polar distribution. The above normalization eliminates the amplitude constant from the minimization process. Once the shape is matched, the absolute levels can be matched through a trivial adjustment of the amplitude. Figure 2.3.1 illustrates the minimization process.

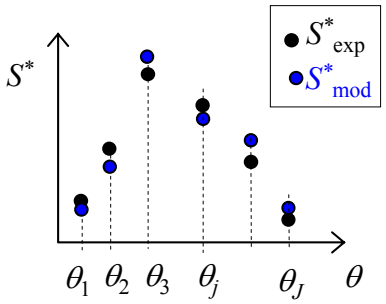

Fig. 2.3.1 Illustration of the minimization scheme between modeled and experimental intensity distributions.

For a given jet flow, the experimental intensity distribution (autospectrum) is known at discrete polar angles θ_j, j=1,..,J. We construct a cost function based on the relative difference between the modeled and experimental intensity distributions at all the measurement polar angles,

$$F(A_k) = \frac{1}{J}\sum_{j=1}^{J}\left|\frac{S^*_{\exp}(\theta_j) - S^*_{\mathrm{mod}}(m, A_k, \theta_j)}{S^*_{\exp}(\theta_j)}\right|^2 \qquad (2.3.2)$$

We then seek determination of A_k that minimizes the cost function. However, indiscriminate use of Eq.2.3.2 can easily lead to non-physical outcomes for A_k. It is typically necessary to constraint key parameters of the problem to ranges that are physically meaningful. Supposing that we want to constraint the parameters A_k to be near a target value $A_{k,\,\mathrm{target}}$, we add a corresponding penalty to the cost function:

$$F(A_k) = \frac{1}{J}\sum_{j=1}^{J}\left|\frac{S^*_{\exp}(\theta_j) - S^*_{\mathrm{mod}}(m, A_k, \theta_j)}{S^*_{\exp}(\theta_j)}\right|^2 + \sum_{k=1}^{K} C_k\left(A_k - A_{k,\mathrm{target}}\right)^2 \qquad (2.3.3)$$

where C_k is a vector of appropriately chosen penalty coefficients. Using the interface described in Section 2.3.6, the user can constraint any parameters of the problem.

2.3.3 Wavepacket Shapes and Source Parameters

Four functional forms for $p_0(x)$ are available:

(a) tanh-tanh

$$p_0(x) = \tanh(x/b_1)^{p_1}\left\{1 - \tanh(x/b_2)^{p_2}\right\}e^{i\alpha x} \qquad (2.3.4a)$$

(b) x-exp

$$p_0(x) = (x/b_1)^{p_1} e^{-(x/b_2)^{p_2}} e^{i\alpha x} \qquad (2.3.4b)$$

(c) sin(tanh)

$$p_0(x) = \sin^{p_2}[\pi \tanh(x/b_1)^{p_1}]e^{i\alpha x} \qquad (2.3.4c)$$

(d) asymmetric "Gaussian"

$$p_0(x) = \left\{ \begin{array}{ll} \exp\left(-\left| \frac{x-b_1}{b_1} \right|^{p_1} \right), & x \le b_1 \\ \exp\left(-\left| \frac{x-b_1}{b_2} \right|^{p_2} \right), & x > b_1 \end{array} \right\} e^{i\alpha x} \qquad (2.3.4d)$$

All four functions involve an amplifying part and a decaying part. In (a), (c), and (d), the amplification is controlled by the length scale b_1 and power p_1, and the decay is controlled by length scale b_2 and power p_2. For function (c) the amplification-decay is governed by the sine term and the parameters b_1 and p_1 control the shape of the envelope. The first three functions start at x=0, which appears physically sensible given that no flow exists for x<0, while the last function (d) does not have a specific origin. Best functions so far are deemed (a) and (d), with some preference for (a) because it gives more independent control over the amplification and decay parts.

The noise source parameter vector is defined as:

$$\begin{aligned} A_1 &= \frac{U_c}{U_j} = \frac{\omega/\alpha}{U_j} \\ A_2 &= b_1 \\ A_3 &= b_2 \\ A_4 &= p_1 \\ A_5 &= p_2 \\ A_6 &= Q \end{aligned} \qquad (2.3.5)$$

Constraints are placed on A_1 so that the convective velocity U_c is close to a target value of about $0.6U_j$ for jets associated with a subsonic engine cycle. The wavenumber α is thus determined from the parameter A_1. For functions not using all the parameters (e.g., function (c)) the vector can still be defined as above with the unused parameters not participating in the minimization scheme. The computation of the above functions is done by subroutine **ENVELOPE.FOR**. This subroutine is used both in the wavepacket parameterization (called by WPFAR.FOR or WPFARX.FOR) and in the computation of the exact incident field (called by WPINC.FOR).

2.3.4 Treatment of Coaxial Jets

The near field of the coaxial jet is significantly different from that of the single-stream jet, necessitating a two-source approach for the parameterization. The approach follows the breakdown of the coaxial jet into initial, intermediate, and fully-mixed regions by Fisher et. al[11], as demonstrated in Fig.2.3.2b. For secondary-to-primary velocity ratios of 0.7 or higher (typical for turbofan engines), noise from the initial region is dominated by the secondary shear layer. Noise from the downstream regions is dominated by the primary shear layer. The two-source nature of the coaxial jet is supported by beamforming data on a BPR10 jet (Fig. 2.3.2a) showing an abrupt transition of the location o peak noise from $x/D_s \ge 4$ for $Sr \le 5$ to $x/D_s \approx 0$ for $Sr > 5$, with Sr the Strouhal number based on secondary (fan) conditions. With the transition Strouhal number Sr_{trans}=5.0 (as example), the approach for the parameterization of the coaxial jet is as follows:

- For $Sr \leq 5$, parameterization is based on primary velocity U_p and effective (thrust-equivalent) diameter D_{eff}.
- For $Sr > 5$, parameterization is based on primary velocity U_s and secondary effective (thrust-equivalent) diameter D_{eff}.

a) **b)**

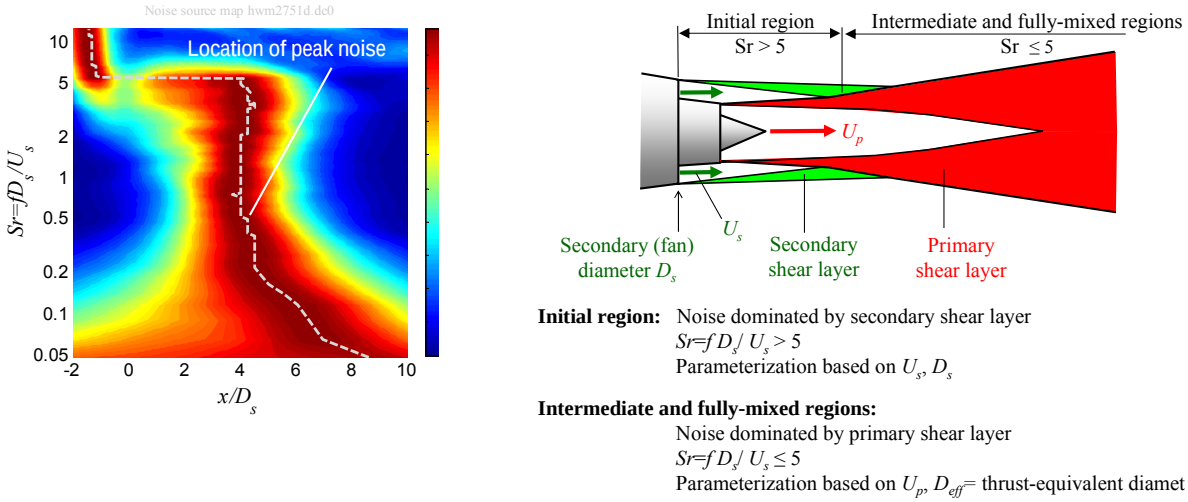

Fig. 2.3.2 Parameterization approach for baseline BPR10 coaxial jet. a) Noise source map; b) two-source model.

No distinction is made between intermediate and fully-mixed regions as noise from the latter is accounted for simply with a lower ratio U_c/U_p. The approach described is specific to high bypass ratios of around 8 to 12.

2.3.5 Minimization Process

The minimization process of Eq.2.3.3 uses the *Restarted Conjugate Gradient* method of Shanno and Phua[12](ACM TOM Algorithm 500). The related subroutines are **CONMIN.FOR** (Algorithm 500 with slight modifications) and **CALCFG.FOR** (calculates $F(A_k)$ in Eq. 7 and its gradient G). All the subroutines involved in the wavepacket parameterization (ENVELOPE.FOR, WPFAR.FOR, CALCFG.FOR, CONMIN.FOR) are called by main program **WPARAM.FOR**, which reads the input data and generates the output files containing the vector A_k and comparing experimental and modeled intensity distributions. The code structure is illustrated in Fig.2.3.3.

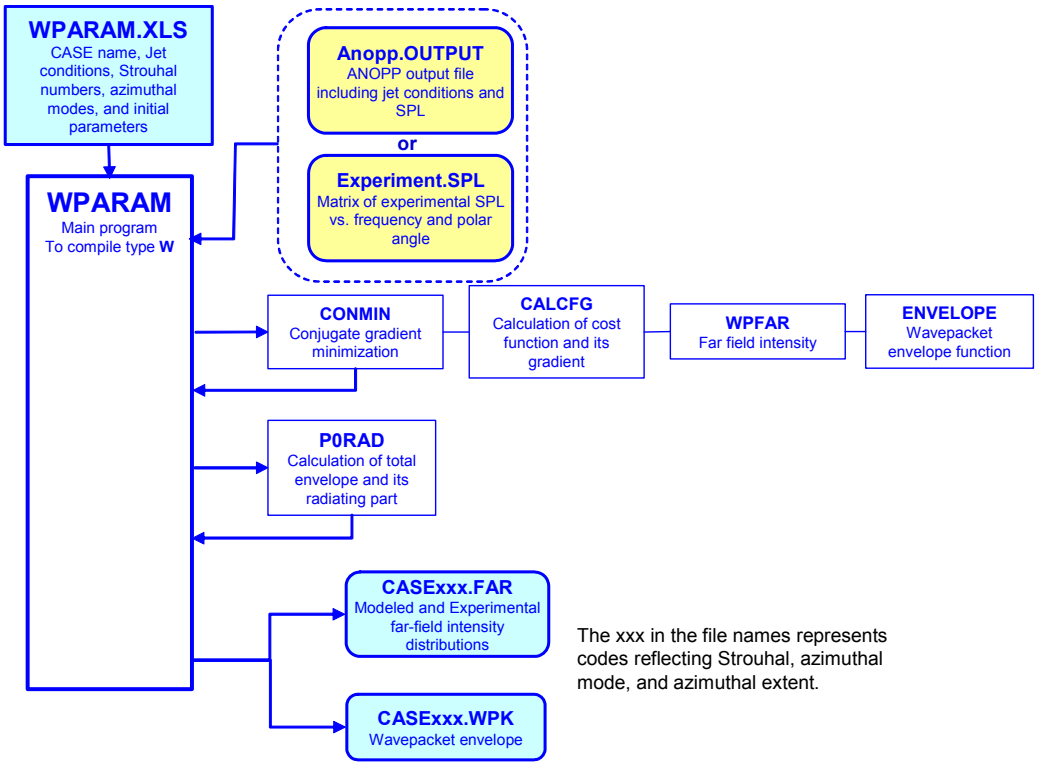

Fig. 2.3.3 Structure of wavepacket parameterization code.

2.3.6 User Interface For Wavepacket Parameterization.

The user interface for wavepacket parameterization is the Excel spreadsheet WPARAM.XLS, shown in Fig.2.3.4. The user inputs the experimental jet conditions, Strouhal numbers to be covered, corresponding envelope shapes and azimuthal modes, and initial wavepacket parameters for a given Strouhal number/azimuthal mode/shape combination. In addition, the range of polar angles for each simulation is prescribed. Below are explanations for each entry:

NAME = Prefix for the output files.

ANOPP = File prefix for the ANOPP output file, located in the ANOPPDATA folder. This entry supersedes any later entries regarding the jet conditions and spectra.

EXP = Experiment name for which SPL spectra are available. For example, if the spectrum file is JNS001.SPL (located in the EXPDATA folder), the experiment name is JNS001.

Dp = Primary jet equivalent diameter (m).

Up = Primary jet velocity (m/s).

Ds = Secondary jet diameter (fan exit diameter) (m).

Us = Secondary jet velocity (m/s).

Srtrans = Transition Strouhal number, relevant to coaxial jets. Below this value, jet reference conditions are Up, Deff; above this value, jet reference conditions are Us, Ds.

Do = 1 to do a certain case, 0 to skip it.

Sr = Strouhal number.

Shape = Index of envelope shape. 1,2,3,4 correspond to a,b,c,d in Section 2.3.2.

Param = Maximum number of parameters used in the parameterization.

Mode = Helical mode number

Dphi = Azimuthal extent of disturbance, $\Delta\phi$

$\Delta\phi = 0$: Fully-coherent wavepacket.

$\Delta\phi < 0$: Azimuthal coherence = $|\Delta\phi|$, isolated azimuthal disturbance only.

$\Delta\phi > 0$: Azimuthal coherence = $\Delta\phi$, superposition of all azimuthal disturbances.

UcUj = U_c/U_j (Parameter A_1).

b1 = normalized width b_1/D (Parameter A_2).

b2 = normalized width b_2/D (Parameter A_3).

p1 = exponent 1 (Parameter A_4).

p2 = exponent 2 (Parameter A_5).

Q = monopole strength (Parameter A_6).

θ_{min} = smallest polar angle (from jet axis)

θ_{max} = smallest polar angle (from jet axis)

MXFUN = maximum number of function calls in CONMIN.FOR. To skip minimization, enter 0.

To constrain a source parameter, enter it as a positive number. Unconstrained parameters should be entered as negative numbers.

The spreadsheet allows entries for up to 12 combinations of Strouhal numbers, azimuthal modes, envelope shapes, etc. Typically one would try several parameters at a given Strouhal number, then move on to the next Strouhal number. The naming of each output file is illustrated by an example:

M090S05A02D030 means the following:

M090: Case name
S05: Strouhal number = 0.5
A02: Envelope shape "A" at azimuthal mode 2.
D030: $\Delta\phi = 30^o$

For negative $\Delta\phi$, the 'D' becomes an 'X'.

NAME=	M090											
ANOPP=	UCI_SINGLE_SAE											
EXP=	JNS001											
Dp=	0.0218											
Up=	389											
Ds=	0.031											
Us=	279											
Srtrans=	1.0											
Do=	0	0	0	1	0	0	0	0	0	0	0	0
Sr	**0.20**	**0.50**	**1.00**	**2.00**	**3.00**	**5.00**	**7.00**	**9.00**	**1.00**	**0.21**	**0.50**	**1.00**
Shape	1	1	1	1	1	1	1	1	1	1	1	1
Param	6	6	6	6	6	6	6	6	6	6	6	6
Mode	0	1	2	3	7	10	14	18	0	1	2	2
Dphi	0.0	0.0	0.0	0.0	0.0	0.0	0.0	0.0	30.0	30.0	30.0	0.0
UcUj	**0.450**	**0.500**	**0.520**	**0.570**	**0.600**	**0.600**	**0.600**	**0.600**	**0.600**	**0.507**	**0.518**	**0.586**
b1	-5.000	-2.000	-1.000	-0.500	-0.333	-0.200	-0.143	-0.111	-2.000	**4.715**	**1.500**	**3.345**
b2	-5.000	-2.000	-1.000	-0.500	-0.333	-0.200	-0.143	-0.111	-2.000	**7.289**	**2.569**	**1.693**
p1	-1.500	-1.500	-1.500	-1.500	-1.500	-1.500	-1.500	-1.500	-2.000	**2.251**	**1.854**	**0.911**
p2	-2.000	-2.000	-2.000	-2.000	-2.000	-2.000	-2.000	-2.000	-2.000	**3.408**	**2.841**	**2.883**
Q	-1.000	-1.000	-1.000	-1.000	-1.000	-1.000	-1.000	-1.000	-0.500	**1.421**	**1.254**	**2.546**
θ_{min}	20.0	20.0	20.0	20.0	20.0	20.0	20.0	20.0	15.0	15.0	15.0	15.0
θ_{max}	160.0	160.0	160.0	160.0	160.0	160.0	160.0	160.0	165.0	180.0	180.0	180.0
MXFUN	500	500	500	50	100	500	500	300	200	200	200	0

Save as TXT then XLS

NOTES
- For ANOPP or EXP, enter "none" (lowercase) if no file exists
- For coaxial jets, Strouhal number is based on Ds and Us
- Reference jet velocity and diameter: Deff, Up for Sr < Srtrans; Ds, Us for Sr >= Srtrans
- b1 and b2 are normalized by jet diameter
- Constrained parameters should be entered positive
- Unconstrained parameters should be entered negative
- Dphi=0: Fully-coherent wavepacket
- Dphi<0: Azimuthal coherence = |Dphi|, isolated azimuthal disturbance only
- Dphi>0: Azimuthal coherence = Dphi, superposition of all azimuthal disturbances

Fig. 2.3.4 User interface for wavepacket parameterization (WPARAM.XLS)

2.3.7 Example Problem

We consider a cold single-stream air jet with Mach number M_j=0.9, velocity U_j=285 m/s, and diameter D_j=21.8 mm. Parameterization of the wavepacket requires judicious choices for the azimuthal mode and a reasonable constraint for the convective velocity ratio U_c/U_j. Experimentation with the minimization process of Eq.2.3.3 shows that, for given frequency, there are one or two azimuthal modes that can fit the experimental results very well, while for other modes it is impossible to get a good fit regardless of the parameter values. For example, for Sr=0.2 modes m=0 and 1 work best; for Sr=0.5, m=2; and for Sr=1.0, m=2. The other constraint is the convective velocity ratio U_c/U_j, which here is set to range between 0.45 (low frequency) to 0.6 (high frequency). Figure 2.3.5 shows parameterizations results for Strouhal numbers Sr=0.2, 0.5, and 1.0. The "tanh-tanh" wavepacket function of Eq. 2.3.4a was used. Plotted are the full wavepacket shape $p_0(x)$, the supersonic portion of $p_0(x)$, and the modeled and experimental intensity distributions. Note that the amplitude of the $p_{0,sup}(x)$ is about two orders of magnitude less than $p_0(x)$, underscoring how small a fraction of the initial perturbation radiates to the far field. There are significant differences between the shapes of $p_0(x)$ and $p_{0,sup}(x)$ owing to the truncation of the Fourier transform in Eq. 2.2.3b, manifested by the sinc convolution of Eq. 2.2.4. Figure 2.3.5 demonstrates that good fits can be obtained between the modeled and experimental intensity polar distributions, with errors of less then 3% in the cost function of Eq. 2.3.3.

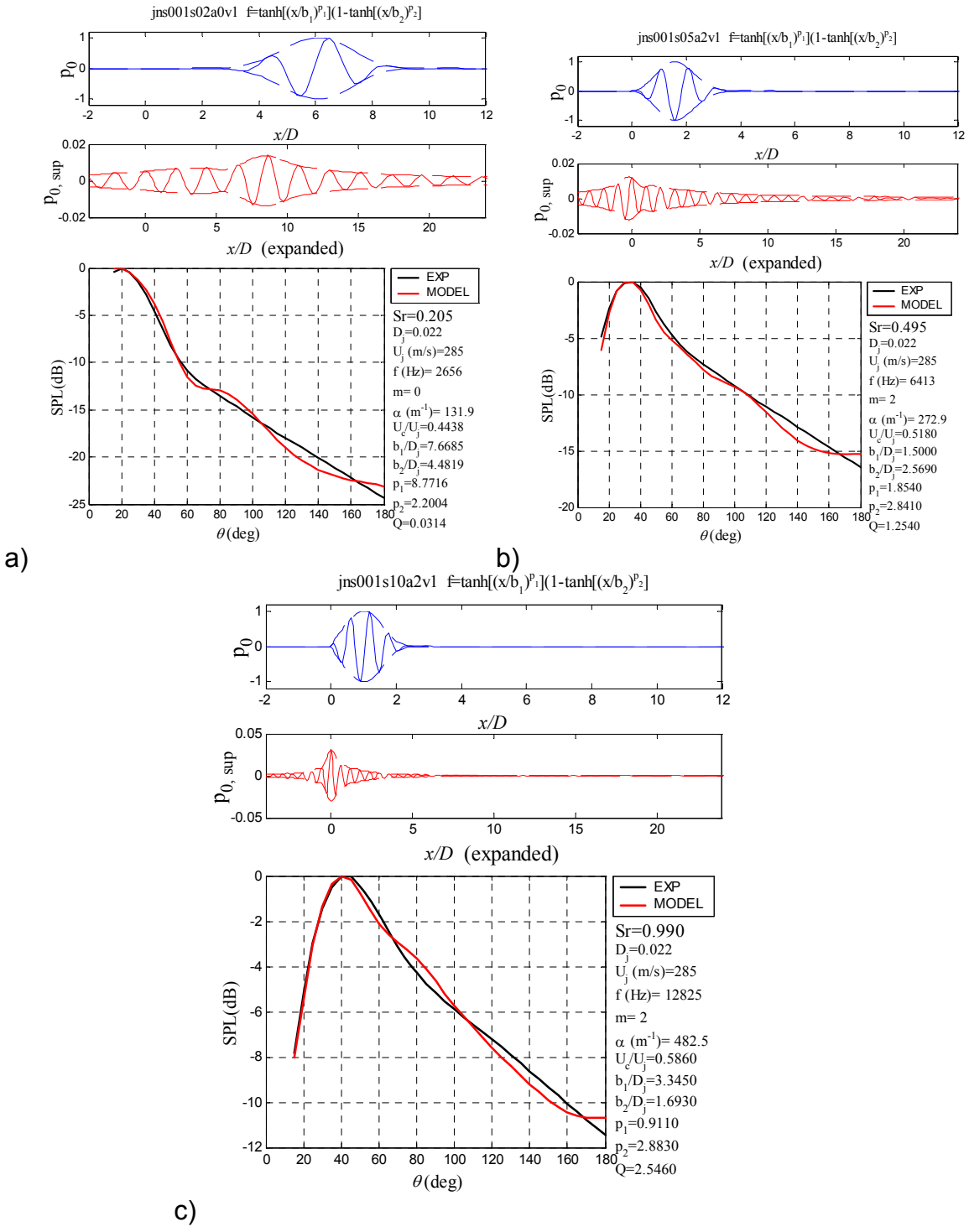

Fig. 2.3.5 Results of parameterization for (a) Sr=0.2; (b) Sr=0.5, and (c) Sr=1.0

2.3.8. Global Parameterization

2.3.8. General concept and formulation

The preceding approaches deal with determination of the noise source parameters for a given frequency. The global parameterization procedure pertains to estimating the source parameters for all frequencies of interest using a single minimization scheme. It is based on prescription of general trends versus frequency for the wavepacket and monopole parameters. This currently applicable only to the elementary wavepacket model (Section 2.2.1.1) and should be considered as being in a "beta" mode of evaluation. Central to this scheme is the *self-similar* wavepacket formulation of Section 2.2.3.

The source parameters A_k remain as defined in Eq.2.3.5. Now, however, they are given as functions of frequency ω, using the functional relations below and the parameter vector B_k

$$A_1 = \frac{U_c}{U_j} = B_1 \tanh(B_2 \omega^{0.5})$$

$$A_2 = \frac{\omega/\alpha}{D_j} = \frac{B_3}{\omega}$$

$$A_3 = \frac{\sigma_1}{D_j} = \frac{B_4}{\omega} \tag{2.3.6}$$

$$A_4 = p_1 = B_5 + \frac{B_6}{\omega}$$

$$A_5 = p_2 = B_7 + \frac{B_8}{\omega} \approx \text{constant}$$

$$A_6 = Q = B_9 \tanh(B_{10}\omega) S_{w,\max}$$

The tanh trend for the convective velocity (A_1) comes from the expectation that at low frequency (typically Strouhal numbers less than 0.1) noise comes from the region past the potential core where the velocity (and consequently the ratio U_c/U_j) decays. As the frequency increases, the noise source location tends toward the potential-core region where the $U_c/U_j \approx$ constant. The expressions for the wavepacket widths (A_2, A_3) are consistent with the self-similar concept of the wavepacket where the width is inversely proportional to frequency. The exponents (A_4, A_5) depend on frequency only for low frequencies where we are dealing with flow past the potential core. Finally, the monopole strength (A_6) displays a tanh trend with frequency when normalized by the peak wavepacket intensity $S_{w,\max}$. In the actual implementation of Eq.2.3.6, the frequency takes the non-dimensional form of the Strouhal number. The relevant subroutine is **WPFARX.FOR**

2.3.8.2 Cost function

We seek parameters B_k (10 parameters for the formulation of Eq. 2.3.6) that minimize the difference, in a least-squared sense, of the modeled and experimental autospectra for all the polar angles and frequencies (Strouhal numbers) of interest. The cost function becomes:

$$F(B_k) = \frac{1}{N_j N_q} \sum_{q=1}^{N_q} \sum_{j=1}^{N_j} \left| \frac{S^*_{\exp}(\theta_j, \omega_q) - S^*_{\mathrm{mod}}(n_q, B_k, \theta_j, \omega_q)}{S^*_{\exp}(\theta_j, \omega_q)} \right|^2 + \sum_{k=1}^{K} C_k \left(B_k - B_{k,\mathrm{target}} \right)^2 \tag{2.3.7}$$

where θ_j, j=1,..,N_j are the polar angles of interest and ω_q, q=1,.., N_q are the frequencies of interest. As with the standard cost function of Eq. 4.3, we constrain selected parameters to fall within a certain range through the second term in the cost function. A critical aspect of this minimization scheme is a reasonable prescription for the dominant azimuthal mode versus frequency, n_q. As with the standard parameterization, the Conjugate Gradient method is used, involving subroutines **CALCFGX.FOR** and **CONMINX.FOR**.

2.3.8.3 Azimuthal mode versus frequency

Refer to the solution for the autospectrum for the self-similar wavepacket, Eq. 2.2.25. The polar direction of peak emission (where $S_{w,\mathrm{far}}$ is maximixed at given frequency) is obtained by differentiating Eq.2.2.25 with respect to the polar angle θ, resulting in:

$$\frac{d}{d\theta}\frac{\left|\hat{P}_0\left(M_c\cos\theta\right)\right|}{\left|H^{(1)}_{n(\omega)}\left(\frac{\omega}{a_\infty}r_0\sin\theta\right)\right|}=0 \qquad (2.3.8)$$

For a given universal wavepacket funtion $P_0(\xi)$, Eq.2.3.8 gives the direction of peak emission θ_{peak} as a function of frequency ω and azimuthal mode $n(\omega)$. Figure 2.3.6 shows such as solution on the polar angle - Strouhal number plane. For each azimuthal mode n, the blue line describes the locus of θ_{peak} versus frequency. Overlayed on the diagram is the experimental direction of peak emission. The intersection of the theoretical curves with the experimental curve define the azimuthal mode number versus frequency. It is seen that as the frequency increases, progressively higher modes are needed to match the experimental directivity. Aside from its practical value, the process illustrated by Fig. 2.3.6 indicates a strong connection between azimuthal mode content and directivity of jet noise.

To apply the process of Eq. 2.3.8, we need a reasonable choice for the universal wavepacket shape $P_0(\xi)$. We determine this shape by applying Eq. 2.3.7 at a single frequency - essentially reducing it to Eq. 2.3.3. The frequency should be high enough that the self-similar assumption is valid -- typically Strouhal number above 0.5. We minimize the cost function for a variety of azimuthal modes, and select the azimuthal mode (and associated model parameters, B_1,..., B_{10}) that provide the best match between the modeled and experimental intensities for that frequency. Now that we have the desired wavepacket shape, we apply the azimuthal-mode-determination scheme of Eq. 2.3.8. Once the modes are determined, the global minimization process of Eq. 2.3.7 is applied for all frequencies of interest.

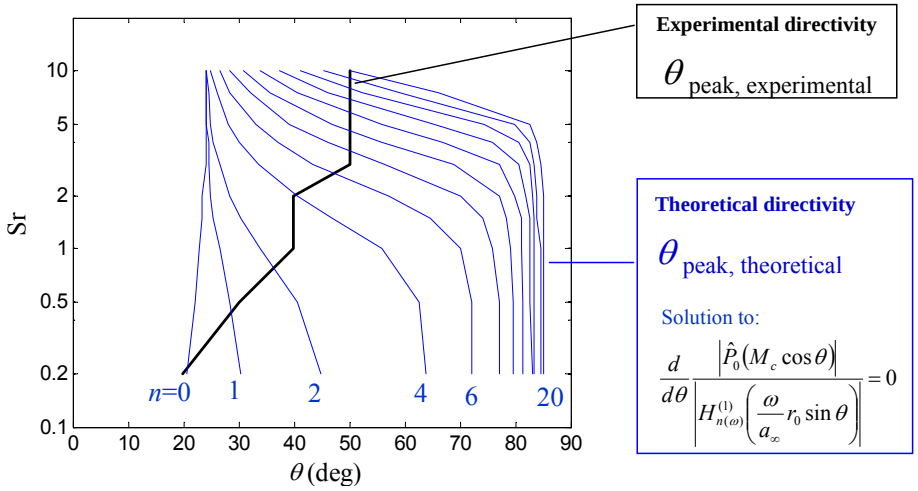

Fig. 2.3.6 Determination of azimuthal mode versus frequency.

2.3.8 Interface for Global Parameterization

The main program for the global parameterization is **WPARAMX.FOR**. The program structure and interface (Fig. 2.3.7) are similar to those for the standard parameterization, with the cost function as defined in Section 2.3.8.2 and with the additional steps outlined in Section 2.3.8.3. The user defines the Stouhal number and range of azimuthal modes to be used for the initial parameterization (highlighted

light blue in the spreadsheet), and the Strouhal numbers for which the global parameterization is applied.

Files and Jet Info			
NAME=	M090	Save as TXT then XLS	
ANOPP=	UCI_Single_SAE		
EXP=	JNS001		
Dp=	0.0218		
Up=	285		
Ds=	0.000		
Us=	0		
Srtrans=	10.0		
Jet Noise Source Parameters			
Shape	1		
Nb=	**10**		
B1=	**0.610**		
B2=	-3.000		
B3=	-2.000		
B4=	-2.000		
B5=	-2.000		
B6=	0.000		
B7=	-2.000		
B8=	0.000		
B9=	-1.000		
B10=	-1.000		
Minimization details			
θ_{min}=	20.0		
θ_{max}=	160.0		
MXFUN=	500		
Schedule of Strouhal numbers			
Do	Sr	n1	n2
1	**1.00**	**2**	**4**
1	**0.20**		
1	**0.50**		
1	**1.00**		
1	**1.50**		
1	**2.00**		
1	**3.00**		
1	**4.00**		
1	**5.00**		
1	**7.50**		
1	**9.00**		

Fig.2.3.7 User interface for global parameterization

2.3.9. Example Results for Global Parameterization

Figure 2.3.8 presents the parameterization results for a Mach 0.9 cold air jet. The contour plots illustrate the good match between the experimental and modeled spectra for all frequencies of interest. The line plots represent a "slice" of the contour plots at Sr=3.0, and demonstrate the good agreement at that frequency.

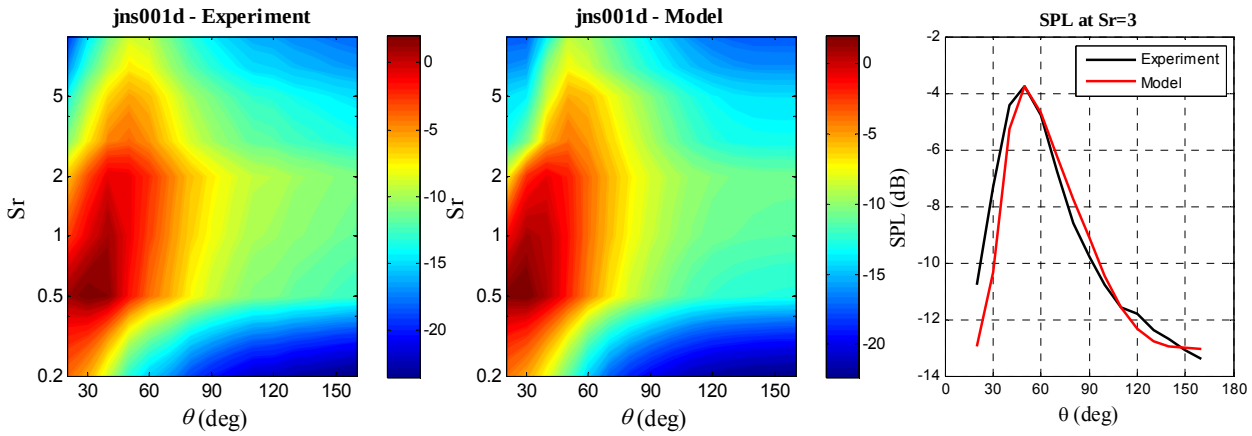

Fig. 2.3.8 Example results for global parameterization of a Mach 0.9 cold air jet.

2.3.10 Wavepacket Positioning

The wavepacket parameterization based on far-field autospectra does not provide sufficient information for locating the axial position of the wavepacket relative to the nozzle. In other words, the coordinate system used in the definition of the functions in Eqs. 2.3.4a-d may not coincide with the nozzle coordinate system. To locate the wavepacket, we use far-field phased array results that provide the distribution of the noise source on the axial distance-frequency plane, and specifically the axial location of the peak source versus frequency. It is important to realize that far-field phased array measurements detect only the radiating part of the noise source. Consequently, the wavepacket is aligned so that the peak of the supersonic envelope $p_{0,\mathrm{sup}}(x)$ coincides with the location of peak noise source as measured by the phased array. The alignment process is illustrated in Fig.2.3.9. For given frequency, the location of peak noise relative to the nozzle exit is X_0. The nozzle exit is located at distance X_{te} from the trailing edge of the shield. It is evident from the figure that the axial shield length, in the wavepacket frame of reference, is $x_s=X_{\mathrm{te}}-X_0+x_{peak}$. The vertical position of the shield, y_s, is defined relative to the wavepacket (jet) axis. Note that the Cartesian (x,y,z) system used in the diffraction computation is the wavepacket coordinate system. The monopole is added at the location of the peak of the supersonic envelope, $x=x_{\mathrm{peak}}$.

Some issues with this alignment procedure should be noted. First, conventional phased array imaging treats the noise source as a line of incoherent monopoles, which may be seen as incompatible with the current wavepacket modeling; second, refraction effects on the propagation of rays from the source to the microphone are typically not accounted for when processing phased array data. These limitations should be kept in mind as we refine our methods for properly positioning the wavepacket.

For pure monopole computations, the monopole is placed at distance $X_{\mathrm{te}}- X_0$ from the trailing edge, and the coordinate system (x, y, z) is referenced to the monopole location.

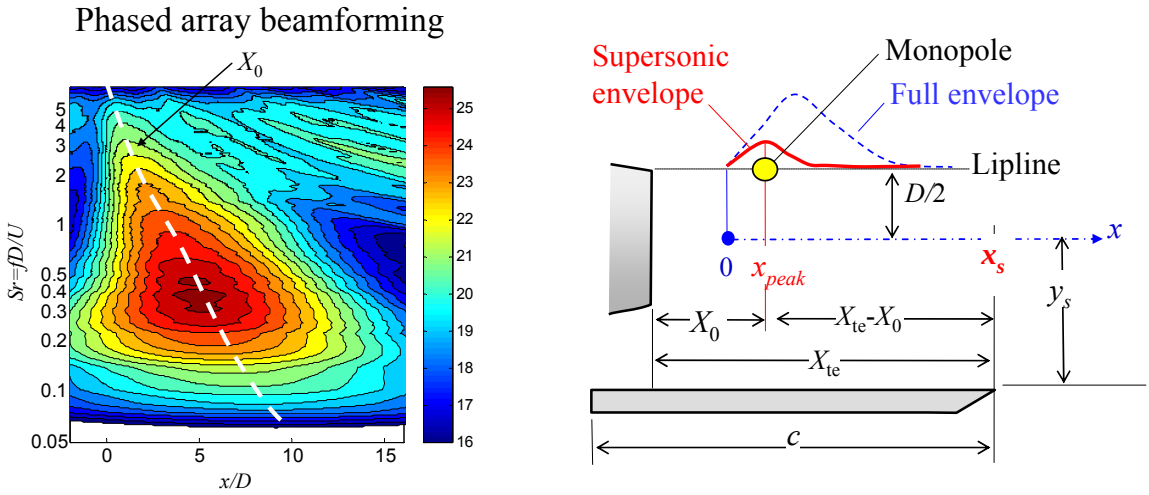

Fig. 2.3.9 Axial positioning of the wavepacket. Left: noise source map for M=0.9 cold jet; right: alignment of wavepacket based on peak of supersonic (radiating) envelope.

2.4 Mesh Generation for the Boundary

The Boundary Element Method has particular requirements for the mesh and the element connectivity. The code currently allows generation "from scratch" of meshes for a rectangular plate with angled trailing edge, and a canonical wing with symmetric or asymmetric NACA00xx airfoil and variable sweep and taper. In addition, the code allows conversion of externally-produced ANSYS files into the mesh format required by BEM.

2.4.1 Mesh Generation Subroutines

The plate mesh is generated by subroutines **PLATE3MESH.FOR** (triangular mesh) and **PLATE4MESH.FOR** (quadrilateral mesh). The subroutines for the wing mesh (triangular only) is **WING3MESH.FOR**. The mesh generation for the wing-shaped surface is explained in the document WING_MESH.PPT. For complex shapes, such as the HWB, subroutine **ANSYS3MESH.FOR** converts a properly configured ANSYS file to the format read by the BEM programs.

All the above subroutines generate mesh files having the same format: node coordinates followed by element connectivity. The files are named CASE.MS3 (triangular mesh) or CASE.MS4 (quadrilateral mesh), where CASE=case name. For the MS3 files, the element connectivity contains a repeated node so that they have exactly the same format as the MS4 files. The regular BEM program works with both MS3 and MS4 files, while the FastBEM program works only with MS3 files. With exception of the ANSYS-based mesh (whose resolution is set in the ANSYS software), the mesh resolution is set by the user interface SHIELD.XLS.

2.4.2 Mesh Refinement for the Boundary

The code allows the option of specifying a minimum grid density in two regions of the boundary surface: a region centered at the source, and the remaining region. The user specifies a fine mesh density for the

region near the source; and a coarse density for the remaining region. The reason for this capability is to reduce computational demands by concentrating the fine mesh near the source region where diffraction phenomena occur (this is particularly applicable to jet noise). The mesh density is based on a minimum value for the number of elements per wavelength specified for each region. For example, the user can specify 8 elements/wavelength (fine density) in the near-source region and 4 elements/wavelength (coarse density) in the remaining region. This defines the fine and coarse element lengths, Λ_f and Λ_c, that should not be exceeded in their respective regions. If the largest side of an element exceeds these criteria, it is divided according to the method below.

Referring to Fig. 2.4.1, the near-source region is defined as the surface contained within a sphere of radius R centered at the source center $\mathbf{P}=(0,0,Z_s)$ and whose unit normal $\mathbf{n}$ (defined by the element connectivity) is pointing away from source center (for an exterior acoustics problem, the element connectivity is such that the unit normal points *away* from the exterior medium). Letting $\mathbf{x}$ be a point on the surface, the near-source region is defined by the criterion

$$|\mathbf{x}-\mathbf{P}|<R \quad \text{and} \quad (\mathbf{x}-\mathbf{P})\bullet\mathbf{n}>0 \tag{2.4.1}$$

The element division process is illustrated by Fig.2.4.2. Within the near-source region, we check the maximum length $l_{\max}$ of all elements. If $l_{\max}>\Lambda_f$, the element is divided according to the process of Fig. 2.4.2. Every time an element is divided, we create one additional node and one additional element. After every element has been examined and, if necessary, divided, the process starts again for the new set of elements. The division cycles stop when every element satisfies $l_{\max}\leq\Lambda_f$. The analogous process is applied to the remaining region, using the coarse mesh criterion that all elements should satisfy $l_{\max}\leq\Lambda_c$.

The mesh division, using the above criteria, is handled by subroutine **SPLIT3MESH.FOR** (triangular mesh). The mesh resolutions (in terms of elements per wavelength) and the sphere radius that defines the near-source region are set by the user interface discussed in Chapter 9.

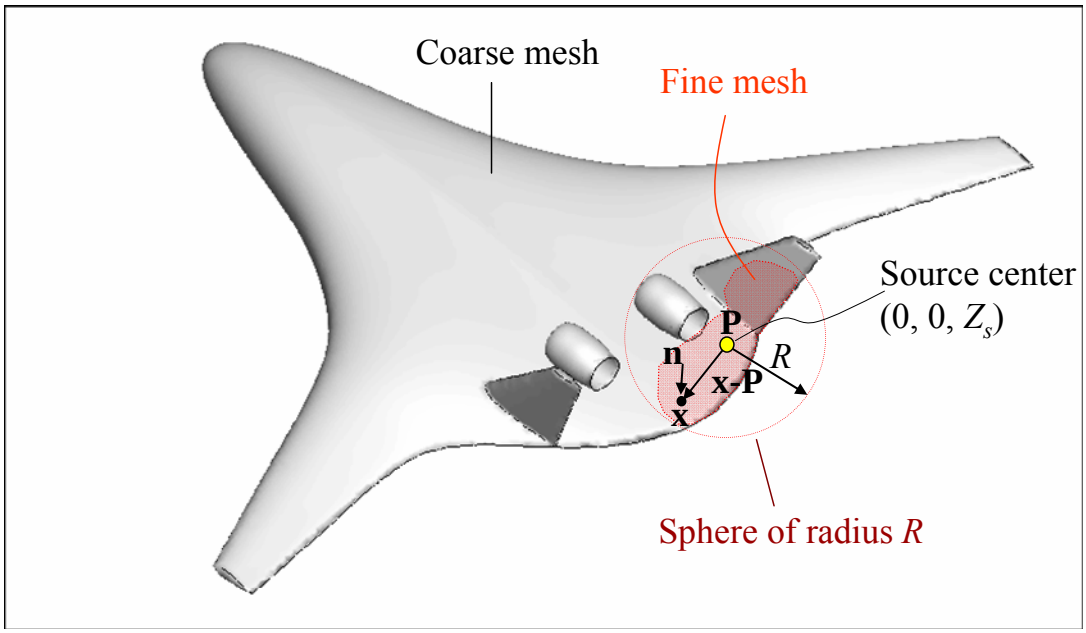

Fig. 2.4.1 Mesh refinement strategy.

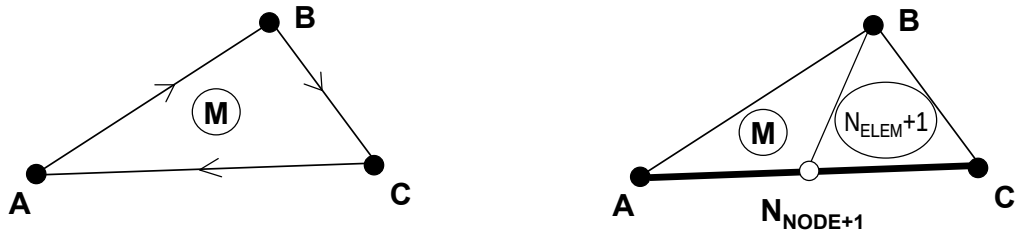

Original element of mesh with
N_{NODE} number of nodes and
N_{ELEM} number of elements

Element number: M
Nodes numbers: A, B, C
Connectivity A → B → C

ELEMENT DIVISION

1. Detect longest side
2. Define new node point N_{NODE}+1 midway between nodes defining longest side
3. Split element as shown:
   Element M: A → B→ N_{NODE}+1
   Element NELEM+1: NNODE+1 → B →C

g. 2.4.2 Element division for triangular mesh.

2.4.3 Wavepacket Mesh

The cigar-shaped mesh for computation of the wavepacket incident field (Fig. 2.2.4) is generated by subroutine **CIGARMESH.FOR.** It uses the same basic mesh generation algorithm as WINGMESH.FOR. The output file has the generic name CIGAR.MS3, so it gets overwritten every time the program is run. However, the mesh and the pressure field prescribed on it are saved as tecplot files.

2.4.4 Routines for Tecplot Outputs

Additional programs related to mesh generation are subroutines that convert the results into Tecplot data files. These comprise the subroutines **OUT2TECB.FOR** for the boundary data; **OUT2TECF.FOR** for field data on a prescribed sphere/hemisphere; and **OUT2TECW.FOR** for the data on the surface of the wavepacket (only when BEM is used to compute the incident field).

2.5 Diffraction Computation Using the Boundary Element Method

2.5.1 Fundamental Relations

Figure 2.1.1 shows the basic setup for the shielding prediction discussed here. The incident field p_i comes from the wavepacket solution, Eq.2. We seek the solution for the scattered field, p_s, at the field points F. The total field is then obtained by adding the incident and scattered fields. The BEM method solves the Helmholtz equation

$$\nabla^2 p + k^2 p = 0 \tag{2.5.1}$$

where $k = \omega/a_\infty$ is the wave number and $p = p(\mathbf{x},\omega)$ is the complex pressure in the frequency domain. The solution to the Helmholtz equation is the boundary integral equation[6],

$$C(F)\,p(F) = -\int_S \left(i\rho\omega\, u_n(B)\psi + p(B)\frac{\partial \psi}{\partial n} \right) dS + p_i \qquad (2.5.2)$$

where ψ is the solution of the Helmholtz equation in 3D free space,

$$\psi = \frac{1}{4\pi r} e^{-ikr} \qquad (2.5.3)$$

and r is the distance from the field point F to the surface point B. In Eq.2.5.2, the factor C takes different values depending on whether the field point F is located in the acoustic domain, or in the interior of the object, or on the object surface S,

$$C(F) = \begin{cases} 1, & F \text{ in acoustic domain} \\ 1 - \int_S \frac{\partial}{\partial n}\left(\frac{1}{4\pi r}\right) dS, & F \text{ on object surface} \\ 0, & F \text{ in object interior} \end{cases} \qquad (2.5.4)$$

2.5.2. Codes

The user has the option of using the following diffraction computational codes:

- "Regular BEM" code developed by T.W. Wu and available as CD-ROM from his book[13]. This package of fortran routines (HELM3D) has been modified by us to enable integration with the main program and specification of a user-defined incident field. Figure 2.5.1 shows the integration of the HELM3D package with the main program BEM.FOR. Figure 2.5.2 details the source programs within the HELM3D package.
- "FastBEM" (Fast Multipole BEM) code developed by Y. Liu[14] (University of Cincinnati) and sold commercially through CAE Research Lab. The FastBEM user manual is in a separate document. At our request, the software was modified to accept a user-defined incident field. Only the executable file FASTBEM_ACOUSTICS.EXE is available. Figure 2.5.3 shows the integration of the FastBEM code with the main program BEM.FOR.

There are important differences between the Regular BEM and FastBEM implementations: Regular BEM generates an exact solution; however, the code is limited to matrices with up to 7000×7000 elements. This means that the boundary surface cannot have more than 7000 elements. Marginal expansion is possible by rewriting parts of the code with more advanced variable declarations.

FastBEM can handle much larger matrices (possibly up to 250,000 elements). It generates an approximate solution based on an iterative algorithm with a specified tolerance (e.g., 0.001). Further, the fast multipole solution is sensitive on the multipole expansion level (parameter *nexp*). This parameter depends on the non-dimensional wavenumber *kL*, where *L* is the largest size of the boundary (in our case usually the span of the wing). It is supposed to increase with *kL*, but increasing the expansion level slows down the computation considerably. In other words, the FastBEM solution involves "knobs" that need to be carefully adjusted for accurate and efficient solution.

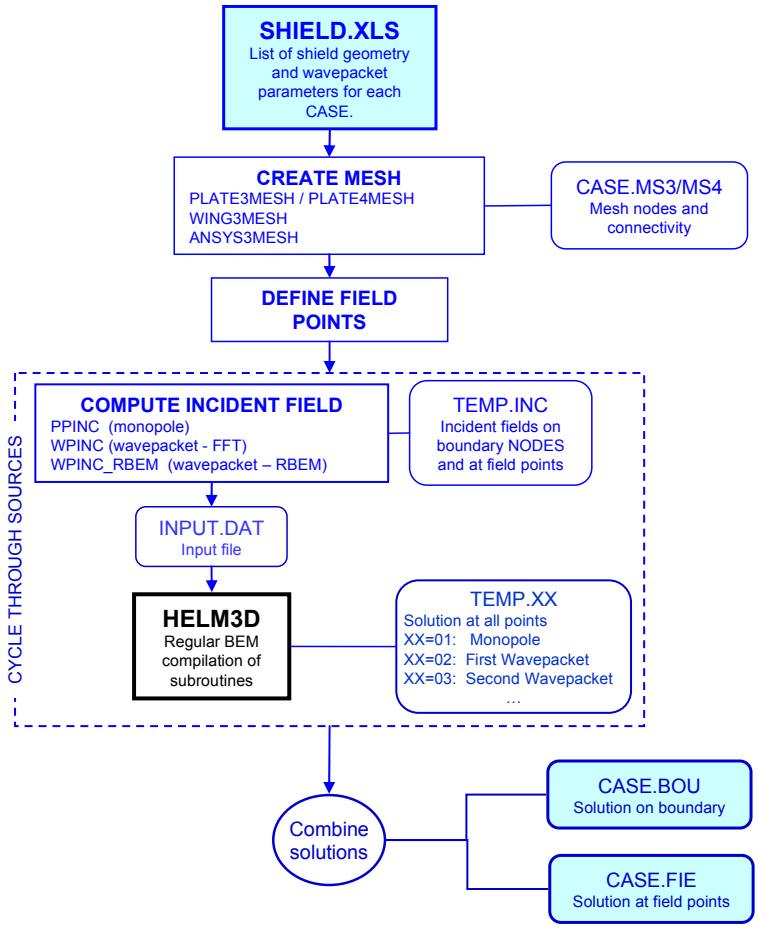

Fig. 2.5.1 Computational structure for Regular BEM, showing the main related elements of program BEM.FOR

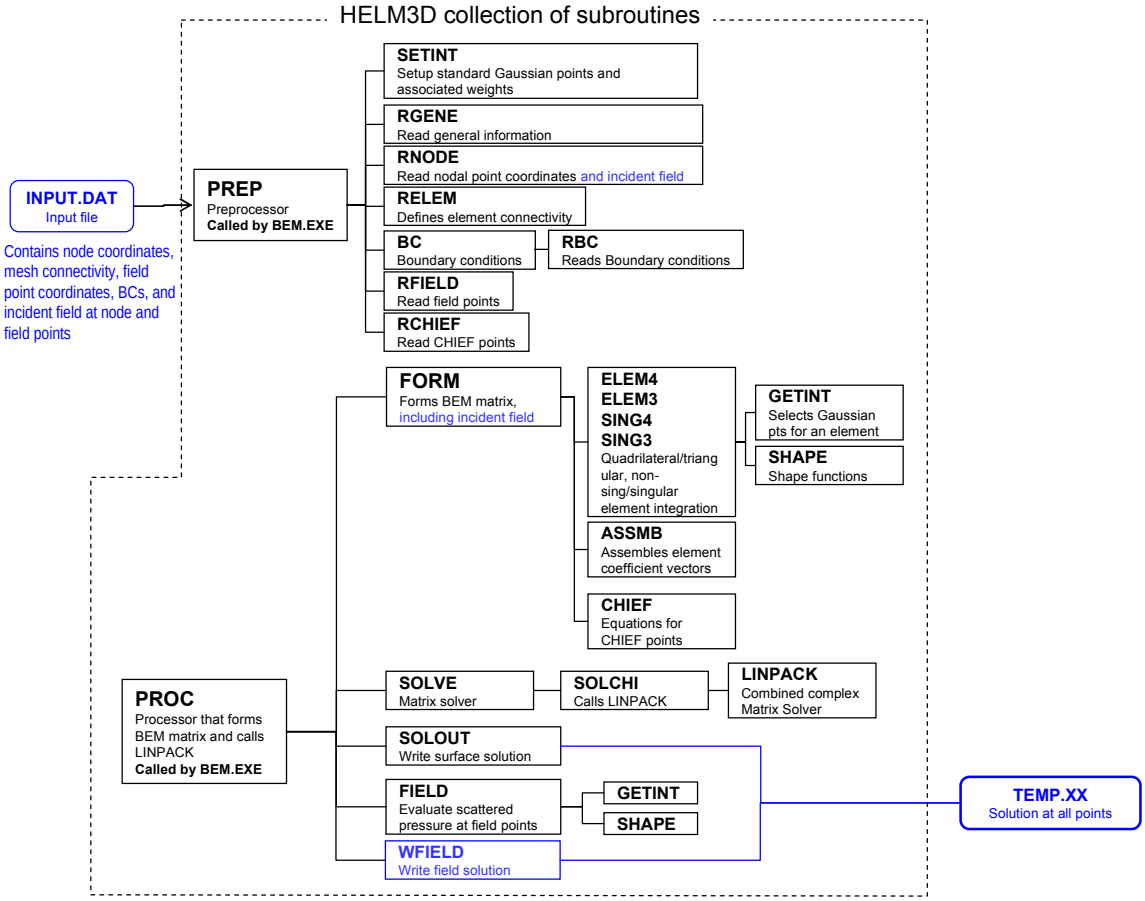

Fig. 2.5.2 Details of HELM3D collection of subroutines for Regular BEM. Blue fonts indicate changes relative to the original code by T.W. Wu [13].

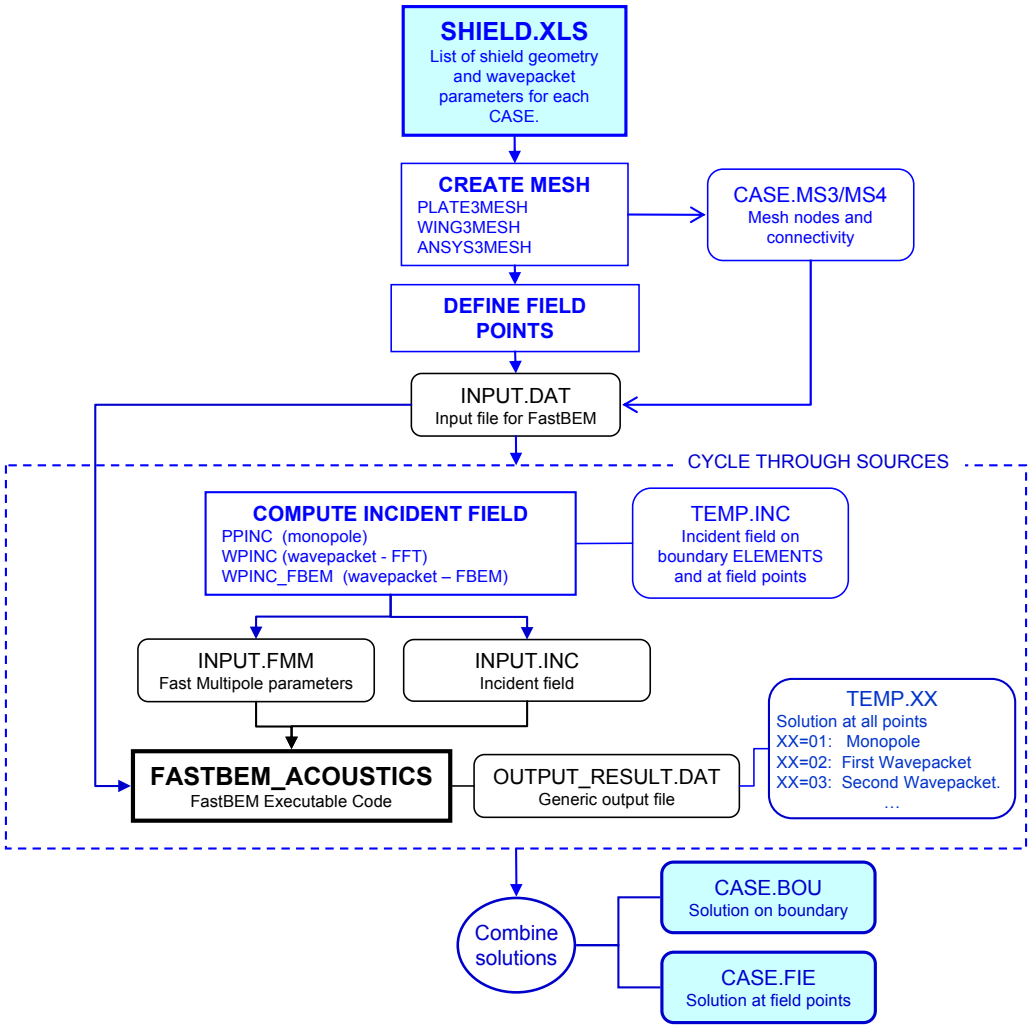

Fig. 2.5.3 Computational structure for FastBEM, showing the main related elements of program BEM.FOR. FastBEM code was developed by Y. Liu[14]

2.5.3 Integration of Results

As described in Section 2.2.1, the jet noise source model comprises several source components that are uncorrelated to each other: monopole and a variety of wavepackets. This section illustrates how individual solutions, corresponding to each source component, are integrated into a final prediction scheme.

Let us denote by $S_j(x,y,z)$ the intensity field created by source component j. This could be the incident, scattered, or total field. Since the source components are uncorrelated, the complete intensity field is the summation of the individual intensity fields:

$$S(x,y,z) = \sum_{j=1}^{N} S_j(x,y,z) \tag{2.5.5}$$

where N is the total number of source components. We now discuss how many source components N are needed to obtain physically correct results for the complete intensity field. We consider a boundary

surface (airframe) that is symmetric around the plane z=0 and single- or twin-engine arrangements (Figs. 2.5.4 and 2.5.5, respectively).

2.5.3.1 Simple wavepacket

Consider the simple wavepacket formulation of Eq. 2.2.1 with azimuthal mode n, with optional incoherent addition of a monopole. For $n \neq 0$ the wavepacket pressure field is asymmetric around the centerline of the source. Let us first look at a single-engine arrangement of Fig.2.5.4. The intensity field is:

$$\widetilde{S}(x,y,z) = S_q(x,y,z) + S_{w,n}(x,y,z) \tag{2.5.6}$$

where S_q is intensity associated with the monopole and $S_{w,n}$ the intensity associated with wavepacket having mode n. Because of the asymmetry of the wavepacket, the intensities of the resulting scattered and total fields will not be symmetric around z=0. Clearly this is not a physical result, given the symmetry of the airframe-engine configuration. We need to add (incoherently) the azimuthal mode $-n$ to obtain a symmetric diffraction field. The complete intensity field would then given by

$$S(x,y,z) = S_q(x,y,z) + S_{w,n}(x,y,z) + S_{w,-n}(x,y,z) \tag{2.5.7}$$

There is a more elegant approach, however. We realize that $S_{w,-n}(x,y,z)$ is equivalent to $S_{w,n}(x,y,-z)$. This means that we only have to solve intensity field for one mode, then add its mirror image around the symmetry plane z=0.. More generally, and consistent with the parameterization approach, we obtain the complete intensity field by adding to Eq. 2.5.6 to its mirror image:

$$S(x,y,z) = \widetilde{S}(x,y,z) + \widetilde{S}(x,y,-z) \tag{2.5.8}$$

Now examine the dual-engine arrangement of Fig. 2.5.5. For each engine, the azimuthal modes n and $-n$ produce results that are not mirror images. So we cannot get away with computing the field of only one mode, we need to include both. For the left engine, for example, the complete intensity field is

$$S_{left}(x,y,z) = S_q(x,y,z) + S_{w,n}(x,y,z) + S_{w,-n}(x,y,z) \tag{2.5.9}$$

The right engine produces a field that is the mirror-image of S_{left}, so the complete field is

$$S(x,y,z) = S_{left}(x,y,z) + S_{left}(x,y,-z) \tag{2.5.10}$$

So for both single- and twin-engine configurations, the integration process involves adding the intensities of the elemental source components, then adding the mirror image of the resulting intensity field. Table 2.5.1 outlines the number of sources needed for the simple-wavepacket formulation

Table 2.5.1. Source components involving simple wavepacket

SINGLE ENGINE		TWIN ENGINE	
Number of source components	**Component**	**Number of source components**	**Component**
1	Monopole	1	Monopole

2	Wavepacket with mode *n*	2	Wavepacket with mode *n*
Summation of resulting intensity field with its mirror image		3	Wavepacket with mode -*n*
		Summation of resulting intensity field with its mirror image	

2.5.3.2 Complex wavepacket

Extension to complex wavepackets, involving the superposition of azimuthally-limited disturbances, is straight forward. As with the simple wavepacket, asymmetries arise from helical azimuthal modes and/or the engine placement in a twin-engine configuration. Table 2.5.2 lists the source component for an example wavepacket having azimuthal coherence of 90 deg. and azimuthal mode *n*.

Table 2.5.2. Source components involving wavepacket with azimuthal coherence of 90 deg.

SINGLE ENGINE		TWIN ENGINE	
Number of source components	**Component**	**Number of source components**	**Component**
1	Monopole	1	Monopole
2	Wavepacket with mode *n* emitting at ϕ=0 deg	2	Wavepacket with mode *n* emitting at ϕ=0 deg
3	Wavepacket with mode *n* emitting at ϕ=90 deg	3	Wavepacket with mode *n* emitting at ϕ=90 deg
4	Wavepacket with mode *n* emitting at ϕ=180 deg	4	Wavepacket with mode *n* emitting at ϕ=180 deg
5	Wavepacket with mode *n* emitting at ϕ=270 deg	5	Wavepacket with mode *n* emitting at ϕ=270 deg
Summation of resulting intensity field with its mirror image		6	Wavepacket with mode -*n* emitting at ϕ=0 deg
		7	Wavepacket with mode -*n* emitting at ϕ=90 deg
		8	Wavepacket with mode -*n* emitting at ϕ=180 deg
		9	Wavepacket with mode -*n* emitting at ϕ=270 deg
		Summation of resulting intensity field with its mirror image	

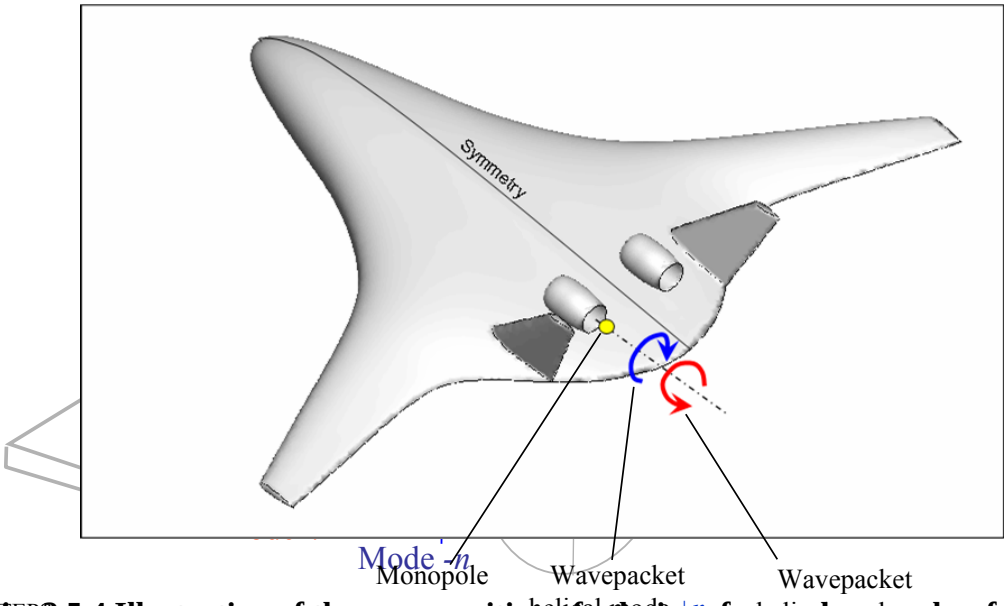

Fig. 2.5.4 Illustration of the superposition of solutions for modes *n* and *-n* for a single-engine configuration.

STEPS:

- Diffraction computation for three uncorrelated sources: monopole, wavepacket with mode *n*, wavepacket with mode *–n*.
- Summation of intensity fields for the three sources.
- Addition of resulting intensity field with its mirror image (around symmetry plane) .

Fig. 2.5.5 Steps for the treatment of a dual-engine configuration.

2.5.3.3 Half-space problems

The code allows for the solution of half-space problems (by setting the span to negative value). Half-space problems are appropriate only for configurations symmetric around z=0 and for incident fields symmetric around z=0: wavepacket with mode n=0 and/or monopole.

2.5.3.4 Structure of output file

For a given case, the field-point solutions for all the source components are contained in the file *.FIE. It has the following structure:

Header (4 lines) containing problem parameters

x y z $PI_r\ PI_i\ PS_r\ PS_i\ PT_r\ PT_i$ $PI_r\ PI_i\ PS_r\ PS_i\ PT_r\ PT_i$ $PI_r\ PI_i\ PS_r\ PS_i\ PT_r\ PT_i$ ...

Coordinates

Incident, Scattered, Total fields for first source (monopole)

Incident, Scattered, Total fields for second source (wavepacket)

Incident, Scattered, Total fields for third source (wavepacket), etc

The monopole field is always the first field, even when no monopole is used (in which case all 6 entries are zero). Integration of the pressures into intensities, per above procedures, are performed by the Matlab and Tecplot programs included in the JNDC software package.

2.5.3.5 Example Predictions

The first set of results considers the Mach 0.9 cold jet (parameterized in Section 2.3.7) and the canonical geometry of Fig.1.1.1 with the following boundary dimensions: chord lenth c=178 mm; span s=600 mm; thickness t=15 mm; trailing edge angle = 30°; and distance between nozzle exit and trailing edge X_{te}=102 mm. These are the boundary dimensions used in the experiments, except that the plate thickness in the experiments was 3.2 mm. The BEM cannot handle very thin plates, so the plate is thicker for the computations. Trials with different thicknesses showed insensitivity of the results for $0.05 < t/c < 0.2$. The same holds true for trailing edge angles above 20°. The parameters listed in Fig. 2.3.5 were used to model the noise source.

We begin the presentation of results with plots of the intensity distributions on a downward polar arc (ϕ=0°) and a sideline polar arc (ϕ=60°), both arcs having a radius R=1 m. The distributions are plotted versus polar angle θ for a given Strouhal number and are compared to the experimental data. Note that the experimental data are limited to θ=120°. Figures 2.5.6, 2.5.7, and 2.5.8 present such plots for Strouhal numbers Sr=0.2, 0.5, and 1.0, respectively. For Sr=0.2 the computations capture the noise excess created by the boundary, as seen in the experimental spectra of Fig.1. For Sr=0.5 and 1.0, the boundary reduces noise and the model captures the experimental trends reasonably well, with some overprediction of the reduction at Sr=1.0. At large polar angles we observe oscillations of the modeled intensity, particularly at Sr=1.0. This is the result of interference caused by the deterministic nature of the noise source model used. More detailed discussion of these results can be found in Ref. 16.

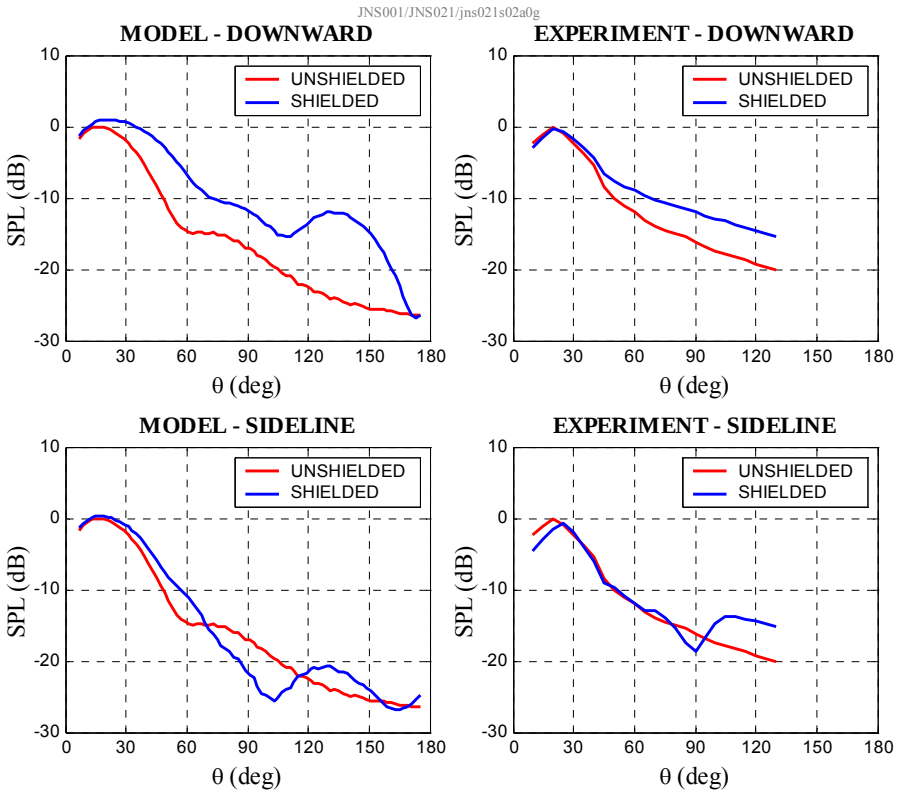

Fig. 2.5.6 Intensity distributions on downward and sideline arcs for Sr=0.2.

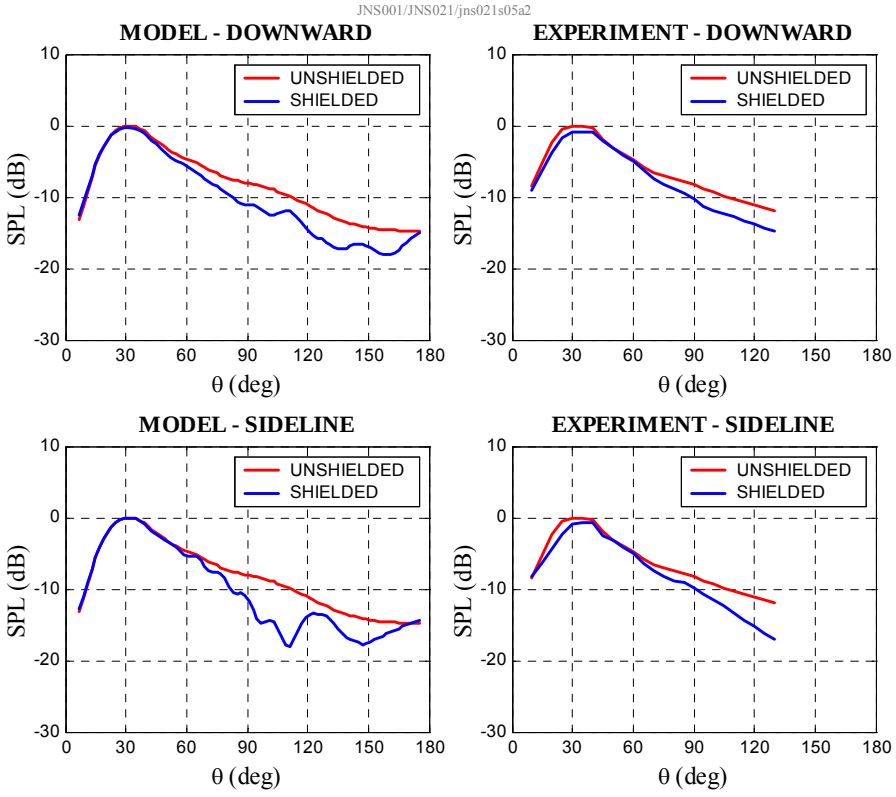

Fig. 2.5.7 Intensity distributions on downward and sideline arcs for *Sr*=0.5

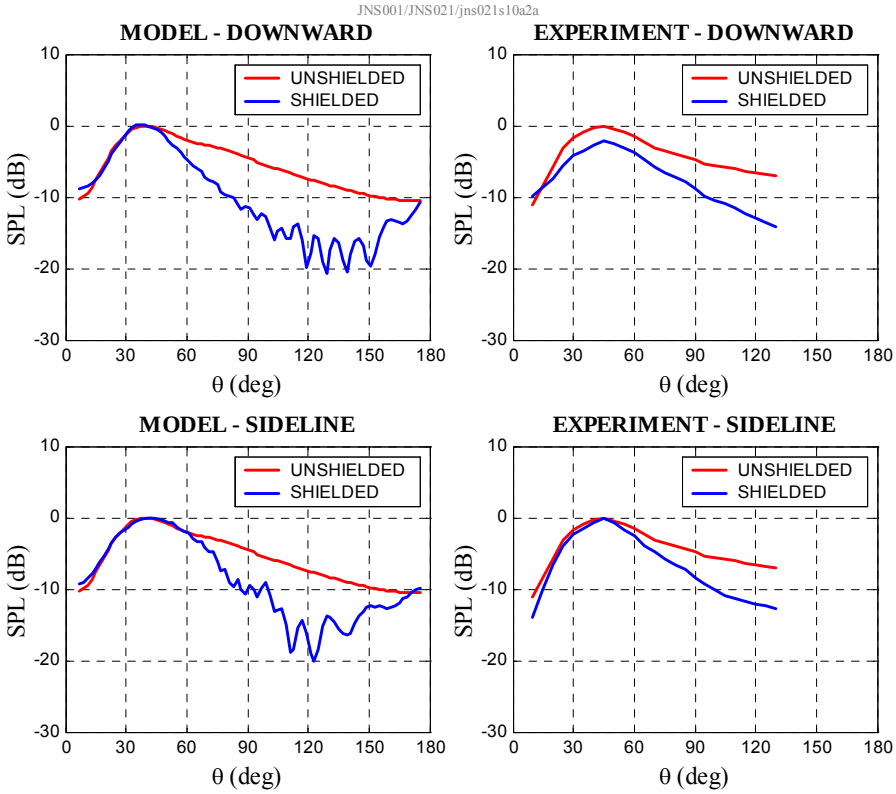

Fig. 2.5.8 Intensity distributions on downward and sideline arcs for *Sr*=1.0

Figure 2.5.9 shows the relative contributions of the wavepacket and monopole to the diffraction problem for Sr=0.5. The insertion loss for the monopole is much greater than that of the wavepacket. As a result, the total (incident plus scattered) intensity field for the combined source is practically equal to that of the wavepacket alone, except near θ=180 deg. For aircraft noise, only angles up to θ=150 deg are important. Therefore, acceptable solutions may be generated by computing only the diffraction of the wavepacket (thus saving 50% of the computational cost), and using the incident field based on the combination of the wavepacket and monopole for computing the insertion loss.

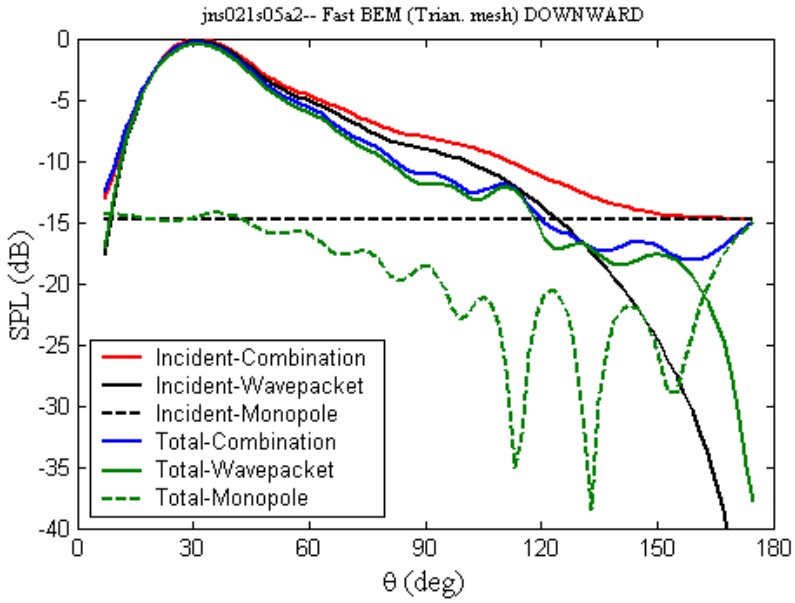

Fig. 2.5.9 Relative contributions of wavepacket and monopole sources to the incident and total fields for *Sr*=0.5

Further insight into the physics of diffraction is gained by examining contours of the incident and total intensity fields on the symmetry plane z=0 in the near field. These are presented in Figs. 2.5.10, 2.5.11, and 2.5.12 for *Sr*=0.2, 0.5, and 1.0, respectively. White dots indicate the nodes of the boundary on the symmetry plane. For *Sr*=0.2, the generation of the excess noise is evident in the contour plots showing strong diffraction of sound towards large polar angles as the shield penetrates more into the acoustic field created by the wavepacket. For *Sr*=0.5 and 1.0, there is clear attenuation of the total intensity field as the polar angle increases.

Finally, Fig. 2.5.13 presents contours of the insertion loss on the "ground" plane y=–1 m for *Sr*=0.5. The source center is indicated at the red circle, and the white region represents the boundary. It is seen that the insertion loss peaks in the general direction of maximum distance between source and edge of the boundary.

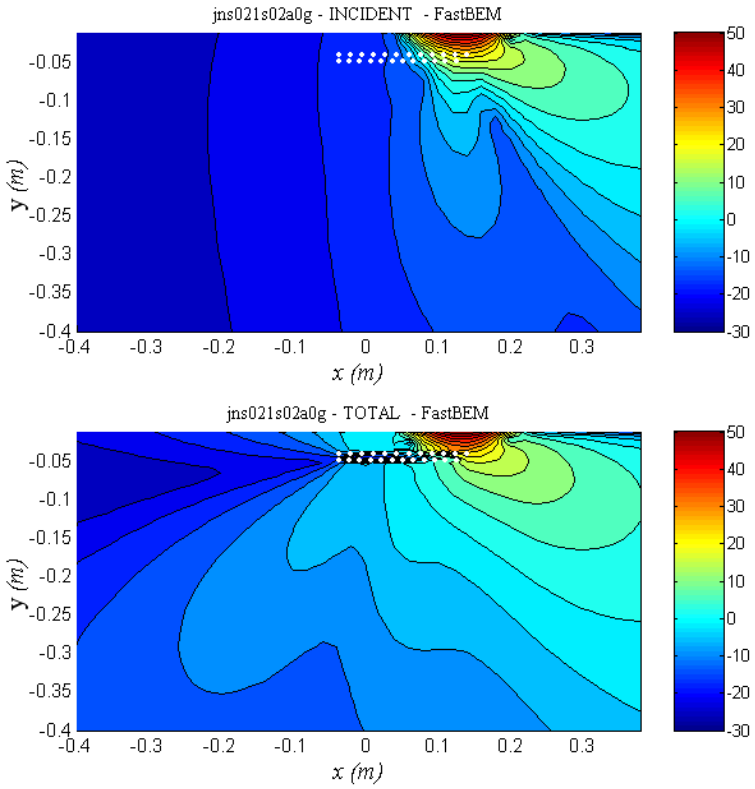

Fig. 2.5.10 Decibel contours of incident (top) and total (bottom) pressure fields on symmetry plane for *Sr*=0.2.

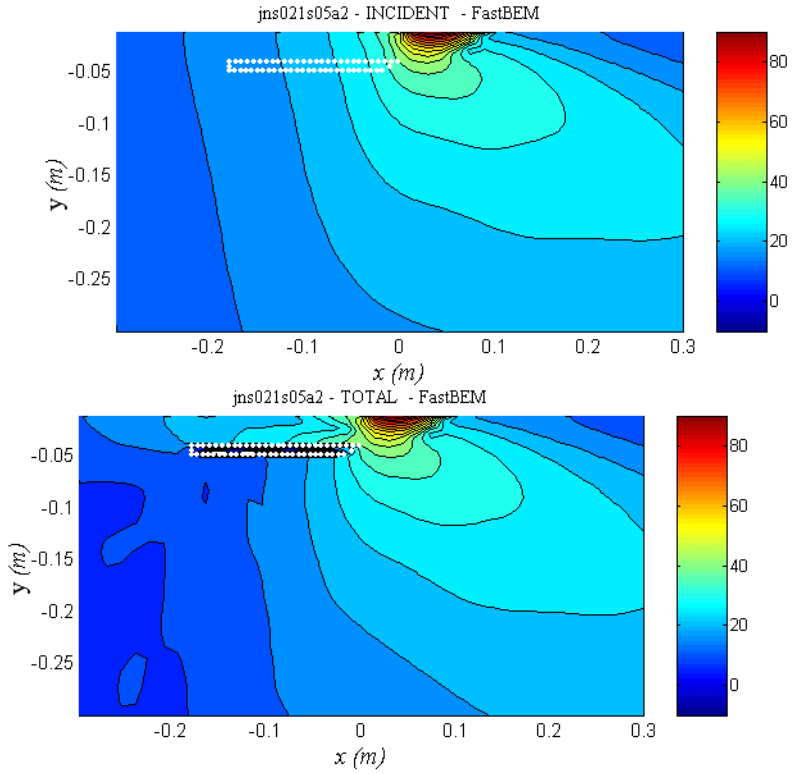

Fig. 2.5.11 Decibel contours of incident (top) and total (bottom) pressure fields on symmetry plane for *Sr*=0.5.

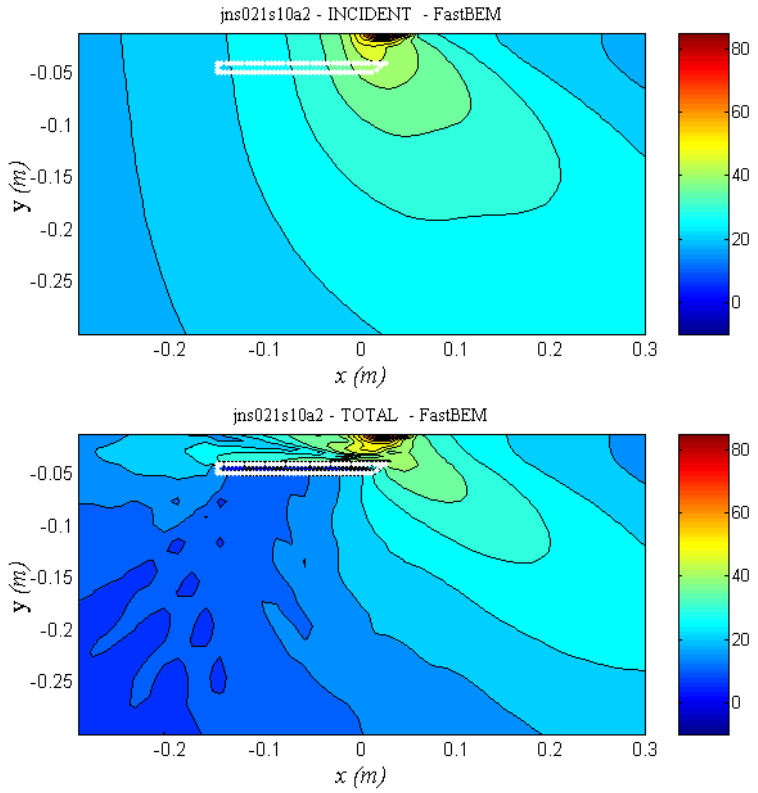

Fig. 2.5.12 Decibel contours of incident (top) and total (bottom) pressure fields on symmetry plane for *Sr*=1.0.

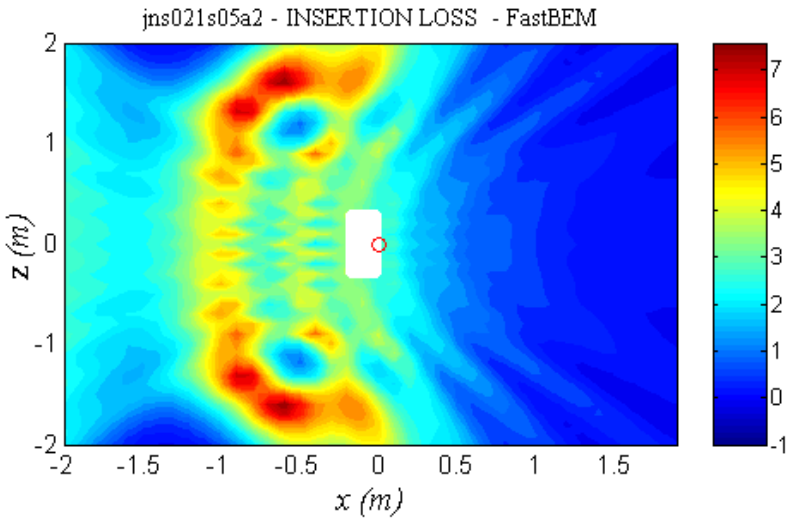

Fig. 2.5.13 Contours of insertion loss (dB) on the plane y = – 1 m for *Sr*=0.5.

Considering now more complex arrangements, Fig. 2.5.14 plots various pressure fields predicted for the N2AEXTE version of the HWB. The plot serves to illustrate the capability of the code in solving for complex configurations. Figure 2.5.15 shows the effects of inboard verticals on the insertion loss on the ground plane. It is seen that the verticals make a significant impact on the sideline insertion loss, an aspect confirmed by the experiments of Section 3.

Diffraction results for N2AEXTE+BPR10+chevrons+Nacelles+Verticals

Strouhal number =1.5; full-scale frequency = 170 Hz

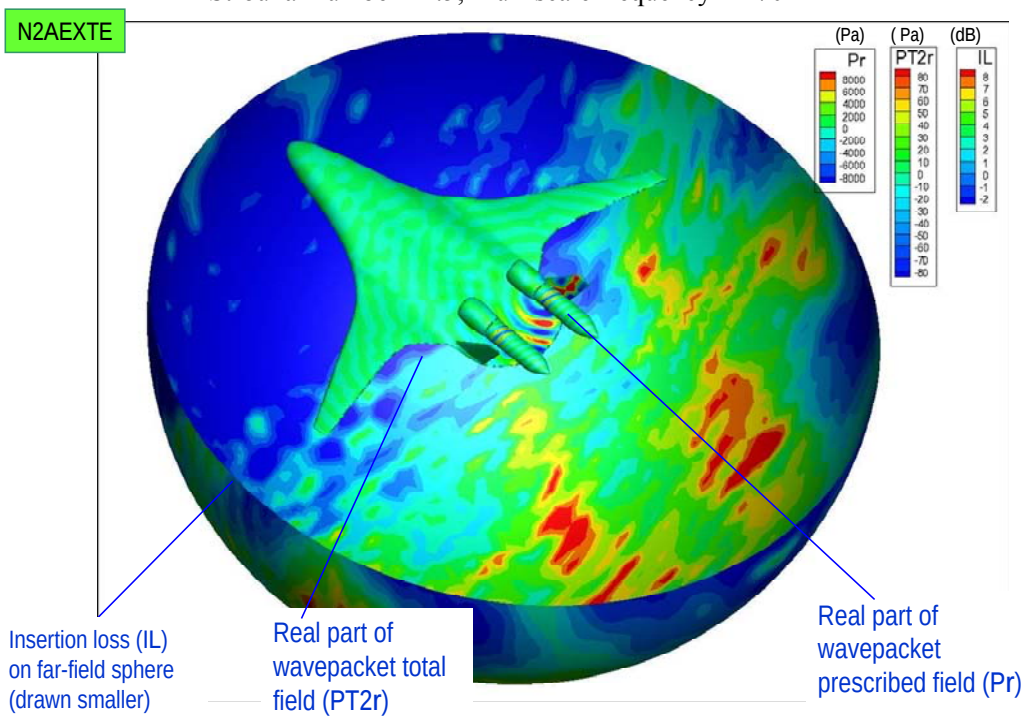

Fig. 2.5.14 Example pressure fields for N2AEXTE model.

WITHOUT VERTICALS

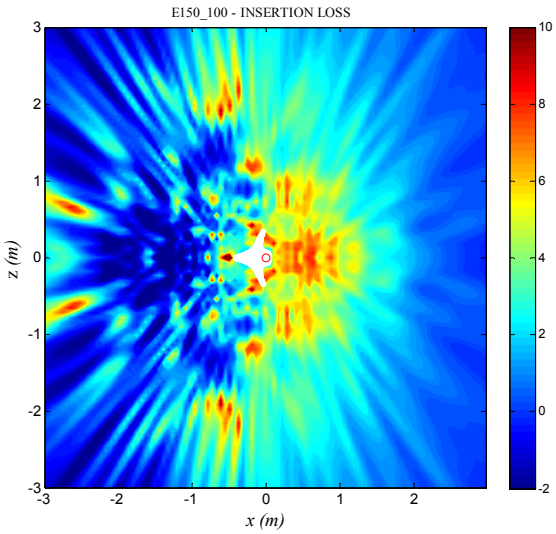

WITH VERTICALS

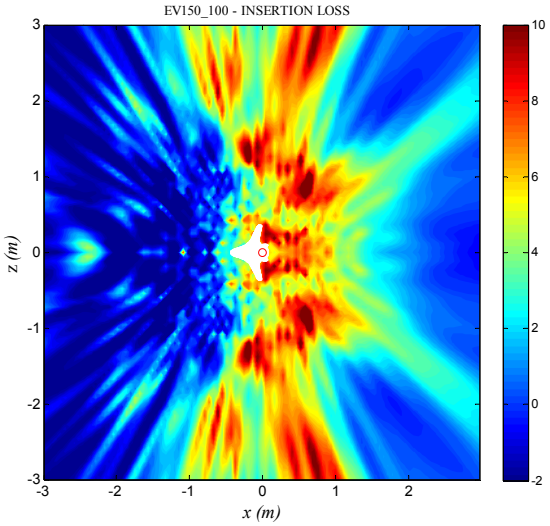

Fig. 2.5.15 Contours of insertion loss (dB) on the plane y = – 1 m for *Sr*=1.5. Configuration of Fig. 2.5.14.

2.6 Effect of Forward Flight

Forward flight affects the jet noise source as well as the acoustic propagation and diffraction. Both impacts are addressed here at a basic level

2.6.1 Effect on Acoustic Propagation

The Helmholtz equation for sound propagation in a uniform stream with Mach number M in the *x*-direction has the form

$$\nabla^2 p + k^2 p - 2ikM\frac{\partial p}{\partial x} - M^2\frac{\partial^2 p}{\partial x^2} = 0 \tag{2.6.1}$$

It has been shown[15] that above equation can be reduced to the static form using the "Prandtl-Glauert" coordinate transformations

$$\tilde{x} = \frac{x}{\sqrt{1-M^2}}$$
$$\tilde{y} = y \tag{2.6.2}$$
$$\tilde{z} = z$$

in combination with the variable transformation

$$\tilde{p} = pe^{-i\kappa\tilde{x}}, \quad \kappa = k\frac{M}{\sqrt{1-M^2}} \tag{2.6.3}$$

Eq. 2.6.1 then takes the form

$$\tilde{\nabla}^2\tilde{p} + \tilde{k}^2\tilde{p} = 0, \quad \tilde{k} = \frac{k}{\sqrt{1-M^2}} \tag{2.6.4}$$

and is solved subject to the boundary condition in the transformed domain

$$\frac{\partial\tilde{p}}{\partial\tilde{n}} = e^{-i\kappa\tilde{x}}\left(\frac{\partial p}{\partial\tilde{n}} - i\kappa p\,\tilde{n}_{\tilde{x}}\right) \tag{2.6.5}$$

For problems with near-horizontal, rigid surfaces, Eq.2.6.5 reduces to

$$\frac{\partial\tilde{p}}{\partial\tilde{n}} \approx 0 \tag{2.6.6}$$

which is identical to the zero-transverse velocity boundary condition in the original domain for static problems. In this version of the JNDC, we make the assumption of near-horizontal surfaces, thus we use the simplified boundary condition of Eq. 2.6.6. All the computations of incident field and its diffraction are done in the transformed domain. Once the solution in the transformed domain has been obtained, the solution in the physical domain is obtained by reversing the transformations. The coordinate transformation and solution steps are shown in Fig. 2.6.1. For low Mach numbers, the coordinate stretching is very small and the main effect comes from the variable transformation of Eq. 2.6.3. Figure 2.6.2 shows that a flight Mach number of 0.3 causes minor impacts on the insertion loss of the canonical configuration treated in Section 2.5.3.5.

2.6.2 Effect on the Jet Noise Source

The forward velocity reduces shear between the jet and the ambient and thus elongates the mean flow of the jet, as illustrated in Fig. 2.6.3. As far as the modeling is concerned, the effect is on the location of the source, X_0 in Fig. 2.3.9. We adopt a simple, incompressible model based on the classical relation for the shear layer growth rate:

$$\frac{d\delta}{dx} = C\frac{U_j - U_\infty}{U_j + U_\infty} \tag{2.6.7}$$

where U_j is the jet velocity and U_∞ is the freestream (flight) velocity. The flow elongation is inversely proportional to the growth rate; accordingly, the peak noise source location shifts according to

$$\frac{X_{0,\text{flight}}}{X_0} = \frac{U_j + U_\infty}{U_j - U_\infty} \tag{2.6.8}$$

The jet velocity U_j is selected according to the critical Strouhal number criterion of Fig. 2.3.2, again summarized in Fig.2.6.3. An illustrative depiction of the elongation of X_0 is shown in Fig.2.6.4. Specifically for the high-bypass nozzle, we expect significant stretching of the jet noise source for sub-transitional Strouhal numbers, but no stretching for super-transitional Strouhal numbers since $X_0 \approx 0$.

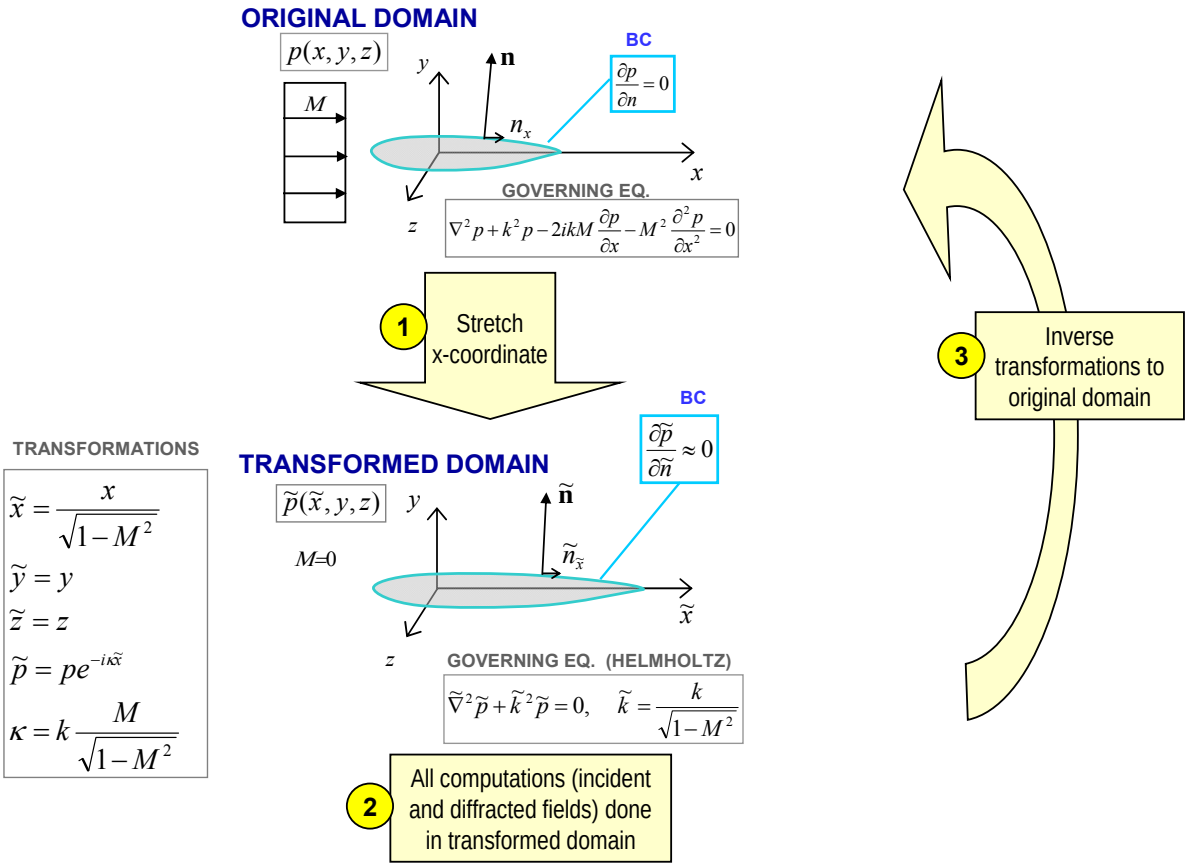

Fig. 2.6.1 Schematic of coordinate and variable transformations for including the effect of forward flight.

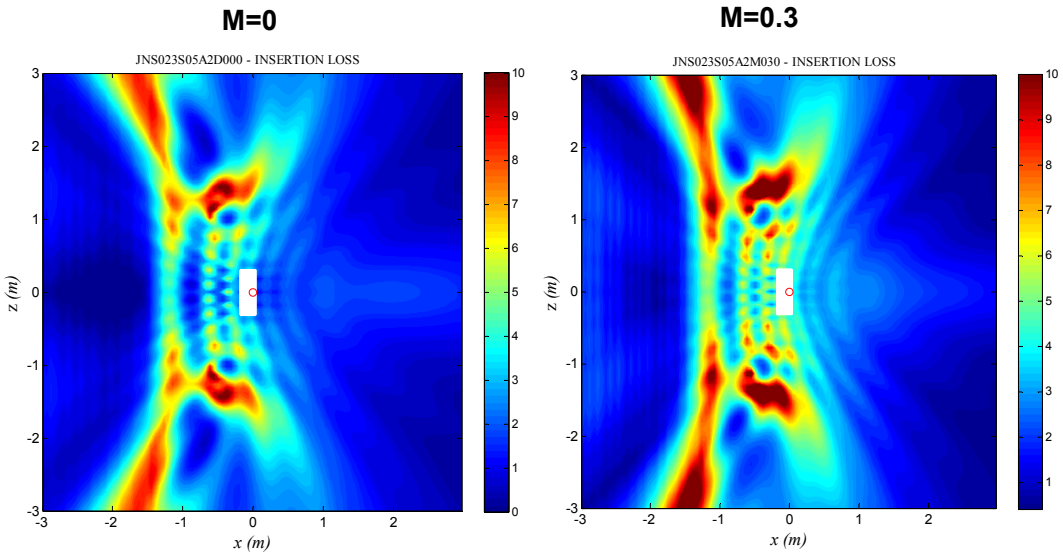

Fig. 2.6.2 Effect of flight Mach number on insertion loss on ground plane.

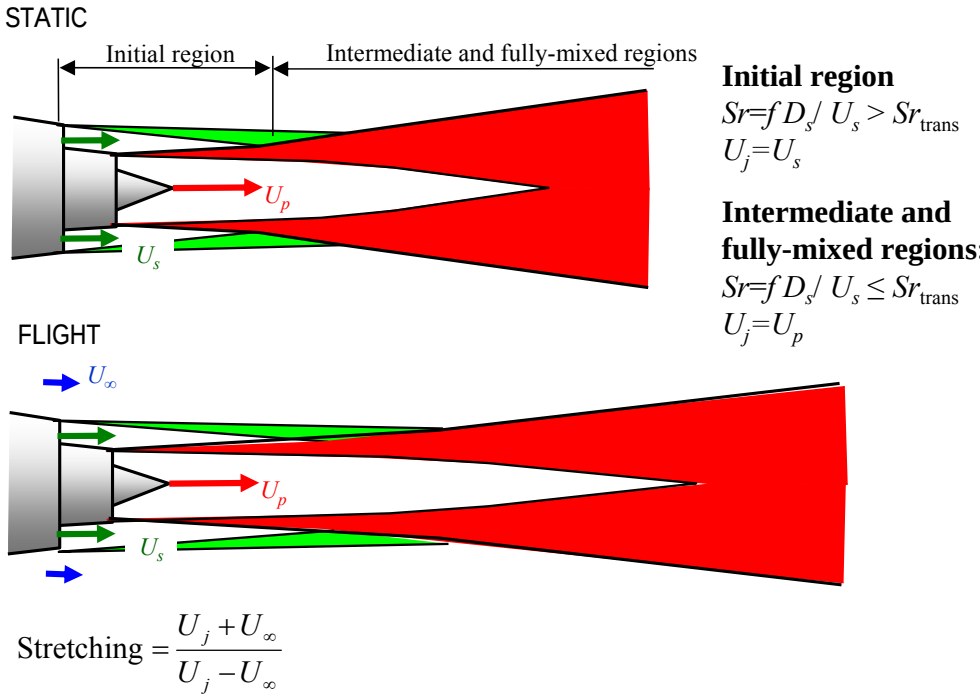

Fig. 2.6.3 Treatment of the elongation of the jet noise source with flight velocity

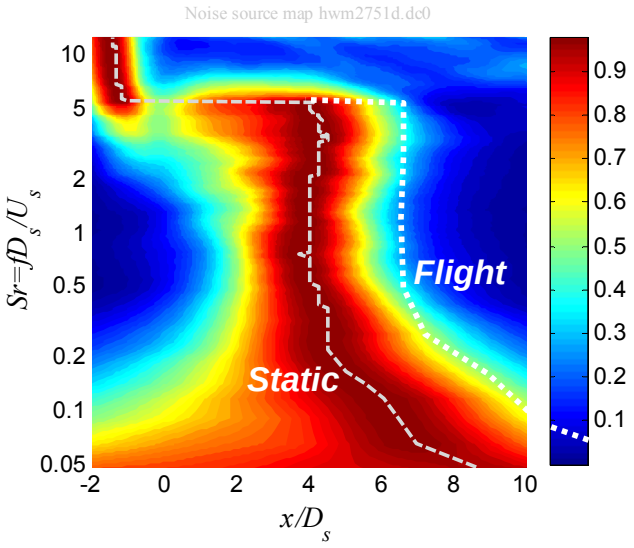

Fig. 2.6.4 Illustration of the alteration of the peak noise source location with forward flight.

2.7 User Interface for Diffraction Computation

As illustrated in Figs. 2.5.1 and 2.5.3, the diffraction user interface is an Excel spreadsheet (SHIELD.XLS) that contains the parameters of the diffraction problem. An example is included in the code package. Once the spreadsheet is filled, it is converted to a text file (SHIELD.TXT) through the use of a macro button on the spreadsheet. Then the executable BEM.EXE is run and the output files are generated. Through the spreadsheet, the user can specify Regular BEM or FastBEM for the diffraction computation.

	BEM METHOD AND SURFACE DEFINITION								
	Freq	Method				Mesh			
CASE	Hz	F/D	Direct	Acc	Type	ANSYS	Fine	Coarse	Radius
JNS001S05R4	6413	R4	1.E-02	P	none	4.0	4.0	0.100	
JNS001S05R3	6413	R3	1.E-02	P	none	4.0	4.0	0.100	
JNS001S05F	6413	F	1.E-02	P	none	4.0	4.0	0.100	
JNS001S05I	6413	I	1.E-02	P	none	4.0	4.0	0.100	
JNS001S05RR4	6413	RR4	1.E-02	P	none	4.0	4.0	0.100	
JNS001S05RR3	6413	RR3	1.E-02	P	none	4.0	4.0	0.100	
JNS001S05FF	6413	FF	1.E-02	P	none	6.0	6.0	0.100	
JNS001S05FFW	6413	FF	1.E-02	W	none	6.0	6.0	0.100	
B150_100	13500	FF	1.E-02	A	B100	8.0	4.0	0.100	
BV150_100	13500	FF	1.E-02	A	BV100	8.0	4.0	0.100	
BVN150_100	13500	FF	1.E-02	A	BV100+N100	8.0	4.0	0.100	

A view of all the spreadsheet entries is shown blow. The entries for each section are explained next.

2.7.1 BEM Method and Surface Definition

Hz = Frequency (Hz).

F/R= F: FastBEM for diffraction
R3: Regular BEM for diffraction (triangular mesh)
R4: Regular BEM for diffraction (quadrilateral mesh)
FF: FastBEM for diffraction *and* incident field
RR: Regular BEM for diffraction *and* incident field (triangular mesh)
RR4: Regular BEM for diffraction *and* incident field (quadrilateral mesh)

I : Incident pressure and velocity fields only (subroutine WPVINC)

Acc = Solution tolerance (only for FastBEM). Typically 1E-4 for low frequency, 1E-3 for high frequency

Type= P for rectangular plate
W for wing
A for Ansys file

ANSYS Ansys file name prefix. To add nacelle Ansys file, use + sign (no spaces)

Fine Elements/wavelength for fine mesh

Coarse Elements/wavelength for coarse mesh

Radius Radius of sphere centered at source that defines region of fine mesh

Note: Mesh refinement is disabled using the following settings:
Fine=Coarse=0 for surface type=A
Fine = Coarse for surface types = P or W.

2.7.2 Surface Dimensions and Source Location

SURFACE DIMENSIONS AND SOURCE LOCATION (units=meters,degrees)											
SPAN	LE sweep	ROOT			TIP			Source Location			
S	SWLE	Chord	t/c-up	t/c-lo	Chord	t/c-up	t/c-lo	Xte	X0	YS	Zs
0.70	30.0	0.203	0.050	0.050	0.203	0.050	0.050	0.071	0.016	0.050	0.060
0.70	30.0	0.203	0.050	0.050	0.203	0.050	0.050	0.071	0.016	0.050	0.060
0.70	30.0	0.203	0.050	0.050	0.203	0.050	0.050	0.071	0.016	0.050	0.060
0.70	30.0	0.203	0.050	0.050	0.203	0.050	0.050	0.071	0.016	0.050	0.060
0.70	30.0	0.203	0.050	0.050	0.203	0.050	0.050	0.071	0.016	0.050	0.060

S = Model span. Negative value indicates half-space problem.

SWLE = Sweep angle of leading edge for W surface; Trailing-edge angle for P surface.
Chord = Chord length.

t/c-up= thickness-to-chord ratio of upper section.

t/c-lo = thickness –to-chord ratio of lower airfoil.

Xte = distance of nozzle from shield trailing edge.

X0 = location of peak noise (as measured by phased array) relative to nozzle exit.

Ys = elevation of noise source above shield. For wing, reference plane is mid-plane.

Zs = Engine centerline distance from plane of symmetry (for twin-engine configurations)

Notes:

- For surface P (rectangular plate) chord takes value at root, and thickness = (t/c-up+ t/c-lo)*Chord. Tip values are not used.

- For surface A (ANSYS file) coordinates will be scaled so that the span = S. Root and tip parameters are not relevant.

2.7.3 Jet Conditions and Source Parameters

Flow and Jet Conditions				Source Parameters								
Ma	Dj	Uj	dphi	ishape	Uc/Uj	b1/Dj	b2/Dj	p1	p2	Q	n	sub
0.00	0.0310	279	0.0	1	0.556	0.929	0.748	2.027	1.463	0.464	3	1.00
0.00	0.0310	279	0.0	1	0.556	0.929	0.748	2.027	1.463	0.464	3	1.00
0.00	0.0310	279	0.0	1	0.556	0.929	0.748	2.027	1.463	0.464	3	1.00
0.00	0.0310	279	0.0	1	0.000	0.929	0.748	2.027	1.463	0.464	3	1.00
0.00	0.0310	279	0.0	1	0.000	0.929	0.748	2.027	1.463	0.464	3	1.00

Ma= Flight Mach number

Dj = jet reference diameter (m)

Uj = jet reference velocity (m/s)

dphi = Azimuthal extent of disturbance, $\Delta\phi$

$\Delta\phi = 0$: Fully-coherent wavepacket.

$\Delta\phi < 0$: Azimuthal coherence = $|\Delta\phi|$, isolated azimuthal disturbance only.

$\Delta\phi > 0$: Azimuthal coherence = $\Delta\phi$, superposition of all azimuthal disturbances.

ishape = index of function describing wavepacket shape (1,2,3,4 correspond to a,b,c,d in Section 2.3.2)

Uc/Uj = ratio of convective speed to jet speed.

b1/Dj = width 1 of wavepacket function, normalized by jet diameter.

b2/Dj = width 2 of wavepacket function, normalized by jet diameter.

p1 = exponent 1 of wavepacket function.

p2 = exponent 2 of wavepacket function.

Q = monopole strength.

n = azimuthal mode.

sub = 1.0 to include subsonic solution (full solution); 0.0 for supersonic solution only; -1.0 for subsonic solution only.

Important note: Setting Uc/Uj=0 instructs the program to compute only the monopole field. Setting Q=0 instructs the program to compute only the wavepacket field.

2.7.4 Field Points

Z	A	B	C	D	E	Ecode
0.00	3.0	0.2	0.5	2.0	1.0	1
0.00	1.0	0.2	0.5	2.0	1.0	1
0.00	1.0	0.2	0.5	2.0	1.0	1
0.00	1.0	0.2	0.0	3.0	1.0	2
0.00	1.0	0.2	0.0	1.0	1.0	2

The selection of field points is illustrated in Fig.2.7.1. Keep in mind that the coordinate system is centered at the source:

Z = value of z-plane for boxes B and C

A = radius of 180-deg arcs centered at source. The planes of the arcs are ϕ=0°, 60°, and -60°

B, **C** = dimensions of *xy*-planes that slice the boundary at *z*=**Z**.

D = dimension of ground plane *y*= –**A.** If **A**=0, Box D is located at *y*= –1.0 m.

E = radius of meshed sphere or hemisphere centered at origin. Program will read sphere/hemisphere coordinates and mesh connectivity for unit-radius sphere or hemisphere Coordinates will be scaled according to **E**. Tecplot output only (subroutine OUT2TECF.FOR). **Ecode** selects the following meshes:

Ecode = 1 : Coarse sphere (sphere_coarse.ms3)

Ecode = 2 : Coarse hemisphere (hemi_coarse.ms3)

Ecode = 3 : Fine sphere (sphere_fine.ms3)

Ecode = 4 : Fine hemisphere (hemi_fine.ms3)

Entering 0 for any of A,B,C,D, or E will skip the calculation for this particular set of field points. The density of field points on boxes B, C and D is controlled by parameter qmax in BEM.FOR.

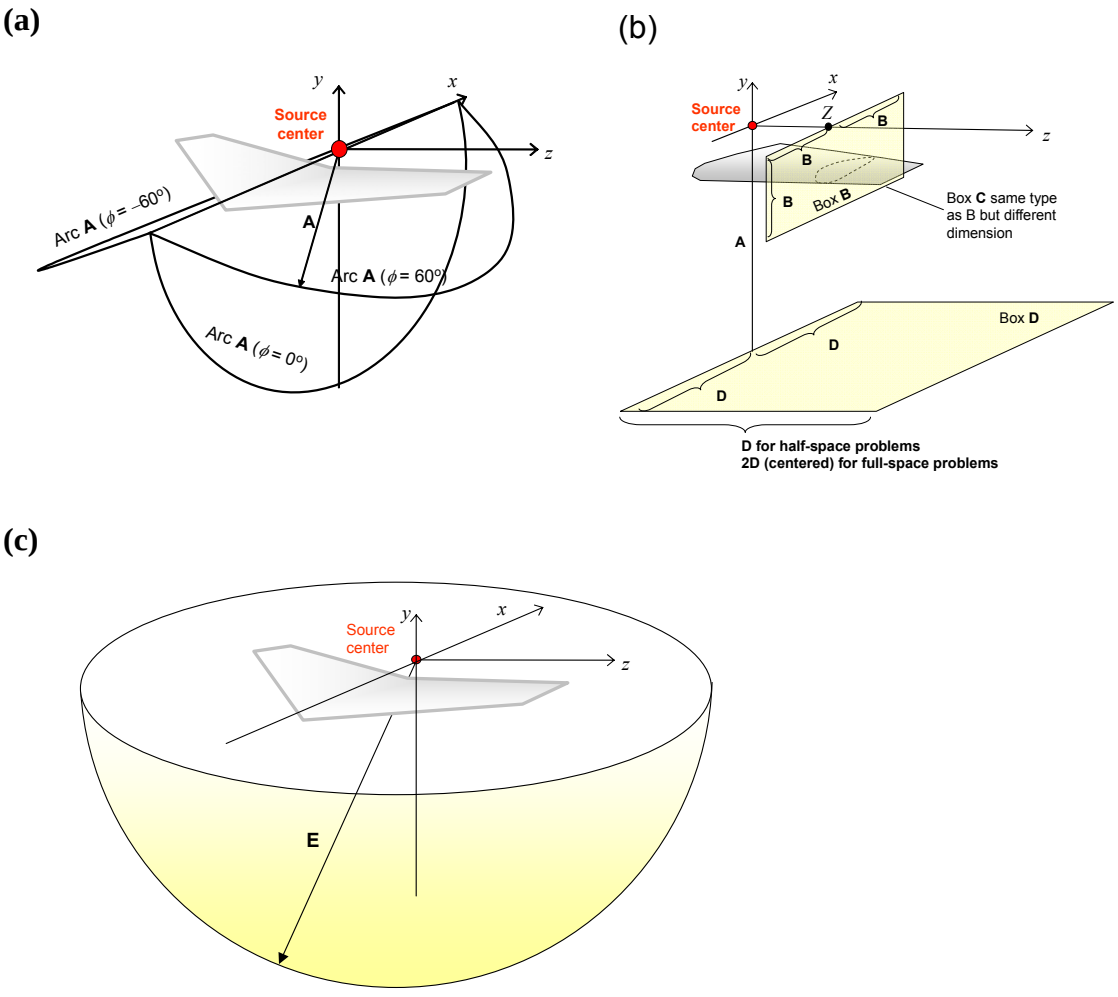

Fig. 2.7.1 Distribution of field points. (a) Arcs on planes ϕ=0, -60 and 60 deg; (b) rectangles on transverse and "ground" planes; (c) hemisphere (for Tecplot use).

3. SUBSCALE ACOUSTIC EXPERIMENTS ON N2AEXTE MODEL

3.1 Background

A large number of jet noise shielding experiments were conducted in the UCI Jet Aeracoustics Lab, comprising canonical and HWB configurations [17,18,20]. Here we review only the latest experiments using the extended trailing edge "N2AEXTE" version of the HWB. Using the initial "N2A" design of the HWB, we demonstrated cumulative EPNL reductions of up to 7.5 dB[17,18]. An important finding was that jet noise shielding was marginal unless the noise source was altered using devices such as chevrons or fan flow deflectors[18]. Large-scale tests at Boeing, using similar shield and nozzle arrangements, confirmed those noise reduction trends and included the element of forward flight[19]. However, the N2A configuration has inherent aerodynamic challenges when placing the engines sufficiently upstream to obtain

satisfactory jet noise shielding. Consequently, Boeing designed an advanced, extended-trailing-edge version of the N2A, called N2AEXTE. The extended trailing edge enables sufficient surface area between the nozzle exit and the trailing edge without exposing the engines to high-transonic Mach numbers that can seriously penalize its aerodynamic performance. The work presented here is a follow-up to our past study, using the N2AEXTE as the shielding planform. We investigate source compaction/redistribution devices, in association with varying designs for the vertical fins (for sideline noise suppression) and axial placement of the nozzle. The one-third octave spectra associated with the data presented in this section were provided to MIT for their overall assessment of aircraft noise. Further details can be found in Ref.20.

3.2 Experimental Details

3.2.1 Nozzle and Shield Configurations

Subscale jet noise shielding experiments were carried out with a nozzle–shield configuration composed of a dual-stream nozzle with an N2AEXTE-shaped shield, as depicted in Fig. 3.2.1. The scale factor was 90. The HWB shield has two types of vertical fins, shown in Fig.3.2.2. The baseline nozzle is designed for a bypass ratio 10 and has a secondary (fan) diameter D_s =31.2 mm and fan exit height of 4.0 mm. The nozzle exit coordinates are plotted in Fig.3.2.3. The nozzle and its chevron counterparts were rapid-prototyped using high-definition stereolithography with a tolerance (layer thickness) of 0.178 mm. The HWB planform was manufactured from a 3.2-mm thick aluminum sheet preserving the essential dimensions for shielding. It was mounted on a longitudinal traverse that permits the axial displacement of the shield relative to the nozzle.

For the experiments of this report, the following parameters were varied:

- *Nozzle axial location*. The fan exit plane was situated at normalized distances X/D_s=2.4, 3.3, and 4.3 upstream of the shield trailing edge, with X denoting the distance from the fan exit plane to the trailing edge on the vertical plane through the nozzle centerline.
- *Design of vertical fins*. The nominal and alternate designs depicted in Fig. 3.2.2 were tested. The idea of the alternate design is to increase the length of the shield (chord length of the fin) while maintaining its aerodynamic effectiveness. In addition, tests were done with the fins removed. The dihedral angle of all the verticals was 79°.
- *Nozzle devices*. Chevrons and a wedge-shaped fan flow deflector were integrated into the baseline nozzle to modify the noise source. Figure 3.2.4 displays the nozzle modifications. The chevrons, designed by Boeing, featured ten serrations with a 20° insertion angle along the lips of the fan and core nozzles, thus they are of the aggressive type. The wedge-shaped fan flow had a half angle of 18°, height of 5 mm, and length of 13 mm. The wedge apex was placed 3.0 mm downstream of the fan exit plane. The wedge was fabricated from a fine interwoven metal mesh with a mesh size of 0.223 mm and porosity of 49.6%. The basic function of the wedge is to reshape the mean flow such that velocity gradients are reduced in the downward and sideline directions, hence reducing turbulent kinetic energy and sound generation in those directions. A detailed investigation of porous wedge/flap fan flow deflectors can be found in Ref. 21. In addition a combination of chevrons and wedge were also tested.

Figure 3.2.5 shows pictures of some of the shield/nozzle configurations tested in this program. Table 3.2.2 presents all the configurations tested along with the reductions in Effective Perceived Noise Level (EPNL).

3.2.2 Aeroacoustic Testing

The nozzles were attached to a dual-stream apparatus that delivers cold mixtures of helium and air to the primary (core) and secondary (bypass) nozzles. Helium-air mixtures have been shown to accurately duplicate the acoustics of hot jets[22]. The exit flow conditions, listed in Table 3.2.1, matched the typical exit conditions of a turbofan engine with bypass ratio 10 at takeoff power. The Reynolds number of the jet, based on fan diameter, was 0.68×10^6.

Noise measurements were performed in the aeroacoustic facility shown in Fig.3.2.6. The microphone array consists of twenty four 3.2-mm condenser microphones (Bruel & Kjaer, Model 4138). For acoustic surveys, the microphones were arranged with twelve on a downward arm (azimuth angle ϕ=0°) and twelve on a sideline arm (azimuth angle ϕ=60°). Fig. 6a depicts the configuration of the downward arm; the sideline arm is practically identical. On each arm, the polar angles θ ranged approximately from 20 to 120 deg relative to the jet axis. This arrangement enabled simultaneous measurement of the downward and sideline noise at all the polar angles of interest. The sideline surveys were conducted in the half-space for which the nozzle is proximal to the vertical fin. For noise source mapping, the 24 microphones were aggregated on a dense linear array as shown in Fig. 6b. The polar aperture was 27.5 deg, with the first microphone at θ=47.5° and the last microphone at θ=73.0°.

The microphones were connected, in groups of four, to six conditioning amplifiers (Bruel & Kjaer, Model 2690-A-0S4). The 24 outputs of the amplifiers were sampled simultaneously, at 250 kHz per channel, by three eight-channel multi-function data acquisition boards (National Instruments PCI-6143). National Instruments LabView software was used to acquire the signals. The temperature and humidity inside the anechoic chamber were recorded to enable computation of the atmospheric absorption.

The narrowband sound pressure level spectra were corrected for actuator response, free-field correction, and atmospheric absorption. Overall sound pressure levels (OASPL) were obtained by integrating the corrected spectra. The conditions used for Perceived Noise Level (PNL) and Effective Perceived Noise Level (EPNL) calculations in the downward and sideline directions are shown in Fig.3.2.7 and reflect the typical takeoff profile for the HWB. The microphone measurements in the downward (ϕ=0°) and sideline (ϕ=60°) directions were used respectively to assess the downward and sideline EPNL. Details of the PNL and EPNL calculation procedure can be found in Ref. 21. Noise source maps of the jets were generated from the deconvolution of the delay-and-sum beamformed output of the microphone array (Fig. 3.2.6b), using the method of Ref. 22.

3.3 Aeroacoustic Testing.

3.3.1 Insertion Loss

The deconvolution procedure of Ref.22 yields high-resolution noise source distributions $q(Sr, x/D_s)$. They are presented here in the normalized form $q(Sr, x/D_s)/q_{max}(Sr)$ that helps identify the location of peak noise versus frequency. Figure 3.3.1 presents noise source distributions plain, chevron, and wedge nozzles. For the plain nozzle, the peak noise source location is practically constant at x/D_s=4.0 up to Sr=6, then it drops abruptly to x/D_s= −1 (it should be kept in mind that here x is defined relative to plug tip, so x/D_s= −1 denotes the fan exit plane). This sudden transition has been observed in the past in phased array measurements of full-scale high-bypass turbofan engines[23]. Application of the aggressive chevrons makes a

notable change in the noise source location, moving the transition Strouhal number to $Sr \approx 1.2$. In contrast to the abrupt transition in the peak noise source location with the chevrons, the wedge induces a more gradual trend of reduction in noise source length. These trends have direct consequences on the insertion loss, discussed next.

Insertion loss data are presented as contour maps of the difference in sound pressure level between a given nozzle in isolation and the same nozzle with shield, plotted against polar angle θ and Strouhal number Sr. Black lines represent insertion loss of 3 dB. In Fig. 3.3.2 we examine the insertion loss in the downward direction for the nominal shield configuration for different nozzle designs. For the plain nozzle, the insertion loss map shows very small values except at high polar angles. The larger insertion loss at high frequency is associated with the noise source moving upstream closer to the fan exit plane. Application of the aggressive chevrons makes a notable change in the noise source location, moving the transition Strouhal number to $Sr \approx 1.2$. The insertion loss map shows very significant levels starting at $Sr \approx 1.2$. The insertion loss for the wedge is more modest than for the chevrons. However, the wedge being quieter in isolation, the EPNL shielding benefits of the two devices are similar.

In Fig. 3.3.3 we assess the impact of the vertical fin, and its design variations, on sideline insertion loss, using the chevron nozzle. With the fins removed, the sideline insertion loss is minimal, consistent with the small sideline EPNL reductions noted in Table 2. The nominal fin design provides significant insertion loss (> 3 dB) for $50^o < \theta < 100^o$ and $Sr > 2$. The alternate fin design broadens this range of polar angle and increases the overall level of insertion loss. Thus the increased chord length of the alternate fin design has a measurable impact on sideline shielding, although the improvement in EPNL is modest.

3.3.2 EPNL Reduction Trends

To optimize the propulsion integration of the turbofan-powered HWB, the designer needs to know the relative benefits of nozzle devices versus axial placement of the engines, as well as the effects of the vertical fins on noise suppression. We attempt to provide this information in Figs. 3.3.4-3.3.6. In each figure, we plot the EPNL reduction (downward, sideline, and cumulative = downward+sideline) versus axial placement X/D_S of the fan exit plane relative to the trailing edge. Figures 3.3.4, 3.3.5, and 3.3.6 consider the shield configurations without verticals, with nominal verticals, and with alternate verticals, respectively. Focusing in the downward direction (left columns of all the figures), we note that the benefit of forward placement of the engine is connected to the aggressiveness of the nozzle device. For the plain nozzle, moving the engine upstream by two fan diameters we gain only 1 dB reduction in EPNL. This benefit goes up to 3 dB for the AC+W18 nozzle. In general, however, we note that modifying the nozzle is a much more effective way to suppress noise than moving the engine upstream. As far as downward reductions are concerned, the presence and designs of the vertical fins have very small impact.

On the other hand, sideline reductions (middle column) are affected strongly by the presence of the verticals, and to a lesser extent by their designs. Without verticals (Fig.3.3.4), the maximum sideline EPNL reduction is 2.2 dB using the wedge nozzle. The axial nozzle placement has practically no effect on the sideline reduction without the verticals. With the nominal verticals (Fig.3.3.5), nozzle configurations including the chevrons show a maximum sideline reduction at X/D_S=3.3 (i.e., the nozzle is moved forward by one fan diameter). This suggests an optimal integration of the vertical and the chevron nozzle at that location. Alternatively, if the engine were to stay at its nominal location, the optimal location of the fin would be one fan diameter aft of its present location. This trend is particularly noticeable for the alternate vertical (Fig. 3.3.6), with the optimization yielding an additional 1 dB in sideline

reduction, using either the chevron (AC) nozzle or the combination (AC+W18) nozzle. Examining the cumulative EPNL reductions in Figs. 3.3.4-3.3.6, we note diminishing returns for the engine moving forward past one fan diameter.

Looking at the general picture portrayed by the above figures, and Table 3.2.2, we see a very encouraging potential of reducing cumulative EPNL by up to 10 dB with the engines at nominal location and 13 dB with the engines moved forward. Nozzle devices (chevrons, wedge) and inboard fins are essential for achieving these reductions.

3.4 Overall Assessment

The advanced N2AEXTE design of the Hybrid Wing-Body airplane offers very promising potential for jet noise shielding. Our subscale static experiments show cumulative EPNL reductions of up to 10 dB with the nozzle at its nominal position and up to 13 dB with the nozzle moved forward by one fan diameter. These reductions are 2-3 dB better than with the basic N2A design. Redistribution/compaction of the jet noise source and incorporation of inboard vertical fins are essential elements for achieving those reductions. Devices used to alter the jet noise source comprised aggressive chevrons, a porous wedge fan flow deflector, and their combination. Two shapes for the vertical fins were tested - a nominal design and an alternate design featuring longer chord and shorter height. The alternate fin design offered slight noise benefits.

Our experiments underscore the importance of nozzle devices to compact and redistribute the noise source. Even though the resulting noise reductions are substantial, they come at a performance cost which this study did not address. The thrust penalty of the porous wedge deflector is estimated at 0.5% and, with a deployable wedge (flaps), it would be suffered for only the takeoff phase of the flight[21]. The aerodynamic penalty of the aggressive chevrons is unknown at this time, but it is probably not small; this penalty would be sustained over the entire flight unless the chevrons are deployable as well, a rather complex undertaking.

The effect of forward flight comes up often when one assesses acoustic performance based on static tests. Forward flight has aerodynamic effects on the jet flow field and acoustic propagation effects on the diffraction pattern. For the plain jet, the aerodynamic effect elongates the jet noise source. However, when using aggressive devices such as the chevrons and wedge of this study, the location of peak noise at high frequency is unlikely to be displaced significantly. With regards to changes in the diffraction pattern (for a fixed noise source), the low takeoff Mach number of around 0.2 is not expected to affect significantly the insertion loss. Indeed the canonical experiments of Von Glahn et al.[3] showed minimal impacts of forward flight on jet noise shielding, particularly when mixer devices were used. Nevertheless, the effect of forward flight on a complex airframe-propulsion system such as the HWB deserves further study.

Table 3.2.1 Cycle conditions for the BPR10 jet

Quantity	Core	Fan

NPR	1.376	1.550
NTR*	2.950	1.139
T_0 (°K)*	864	334
T (°K)*	781	291
M	0.691	0.817
U (m/s)	387	279

*Equivalent conditions using helium-air mixture jets

Table 3.2.2 Configurations tested and EPNL reductions relative to isolated plain nozzle

No Verticals

	PLAIN			W18			AC			AC+W18		
X/D_s	$\Delta EPNL_D$	$\Delta EPNL_S$	$\Delta EPNL_C$	$\Delta EPNL_D$	$\Delta EPNL_S$	$\Delta EPNL_C$	$\Delta EPNL_D$	$\Delta EPNL_S$	$\Delta EPNL_C$	$\Delta EPNL_D$	$\Delta EPNL_S$	$\Delta EPNL_C$
2.3	1.0	0.3	1.3	4.6	2.2	6.7	5.1	1.5	6.6	6.0	1.4	7.4
3.3	-	-	-	5.5	2.3	7.9	6.5	1.9	8.3	7.7	1.6	9.3
4.3	1.0	0.9	1.9	6.5	2.7	9.2	7.3	2.3	9.6	8.9	2.2	11.0

Nominal Verticals

	PLAIN			W18			AC			AC+W18		
X/D_s	$\Delta EPNL_D$	$\Delta EPNL_S$	$\Delta EPNL_C$	$\Delta EPNL_D$	$\Delta EPNL_S$	$\Delta EPNL_C$	$\Delta EPNL_D$	$\Delta EPNL_S$	$\Delta EPNL_C$	$\Delta EPNL_D$	$\Delta EPNL_S$	$\Delta EPNL_C$
2.3	1.0	0.9	1.9	4.5	3.4	8.0	4.9	4.2	9.1	5.7	4.0	9.7
3.3	-	-	-	5.3	3.6	8.9	6.1	4.4	10.5	7.5	4.3	11.8
4.3	2.2	1.4	3.6	6.4	4.0	10.4	7.1	3.9	11.0	9.1	3.9	13.0

Alternate Verticals

	PLAIN			W18			AC			AC+W18		
X/D_s	$\Delta EPNL_D$	$\Delta EPNL_S$	$\Delta EPNL_C$	$\Delta EPNL_D$	$\Delta EPNL_S$	$\Delta EPNL_C$	$\Delta EPNL_D$	$\Delta EPNL_S$	$\Delta EPNL_C$	$\Delta EPNL_D$	$\Delta EPNL_S$	$\Delta EPNL_C$
2.3	1.1	0.9	2.0	4.7	3.3	7.9	5.0	3.9	8.9	5.9	3.9	9.8
3.3	-	-	-	5.5	3.8	9.3	6.3	5.1	11.4	7.6	5.3	12.9
4.3	2.3	1.4	3.7	6.5	4.1	10.6	7.1	4.5	11.6	9.0	4.8	13.8

PLAIN = Plain BPR10 nozzle

W18 = BPR10 nozzle with 18-deg porous wedge

AC = BPR10 nozzle with aggressive chevrons

AC+W18 = BPR10 nozzle with aggressive chevrons and 18-deg wedge.

$\Delta EPNL_D$ = Reduction in downward EPNL

$\Delta EPNL_S$ = Reduction in sideline EPNL

$\Delta EPNL_C$ = Reduction in cumulative (downward+sideline) EPNL

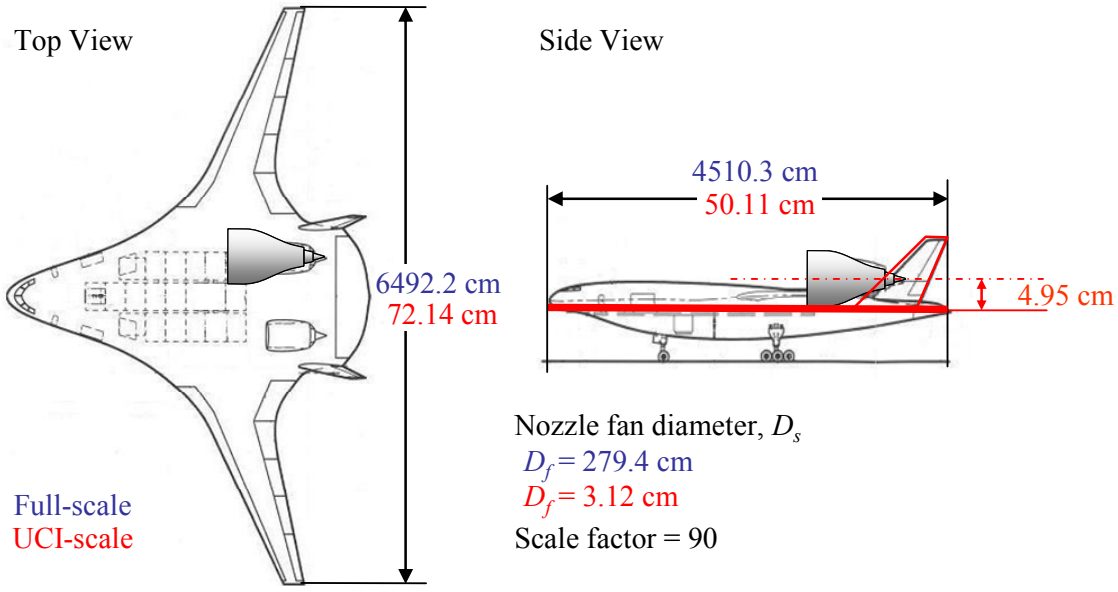

Fig. 3.2.1 Scaling of HWB planform to UCI dimensions and retention of critical dimensions for shielding (red lines).

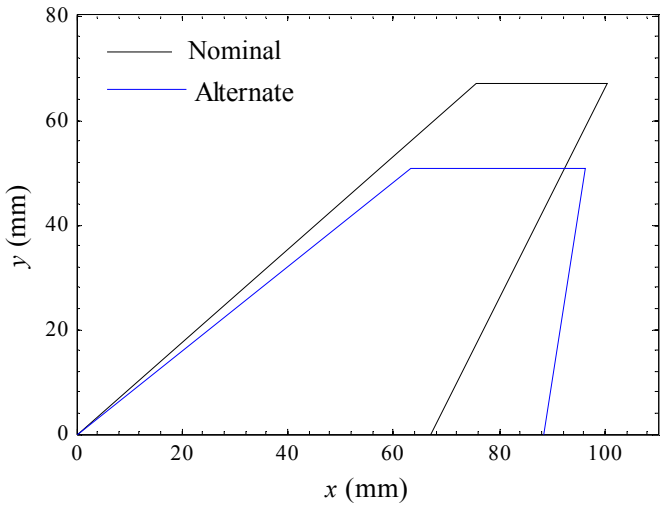

Fig.3.2 2 Designs of nominal and alternate vertical fins.

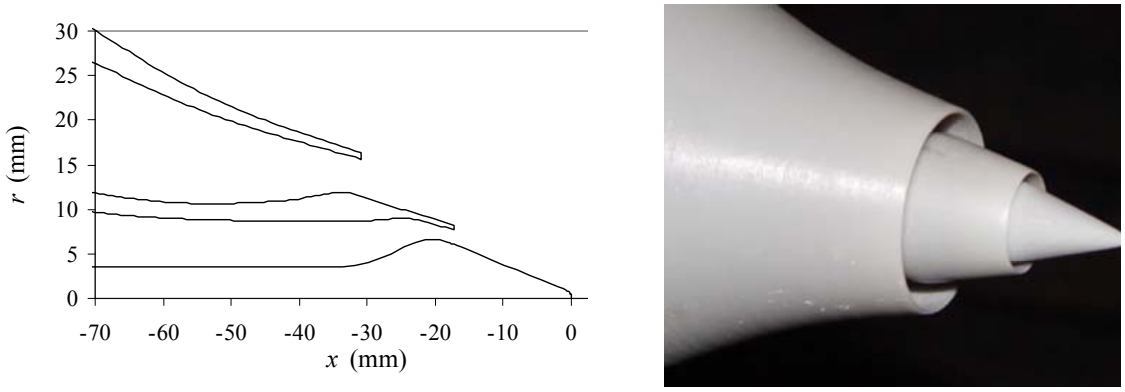

Fig. 3.2.3 Coordinates and picture of BPR10 nozzle

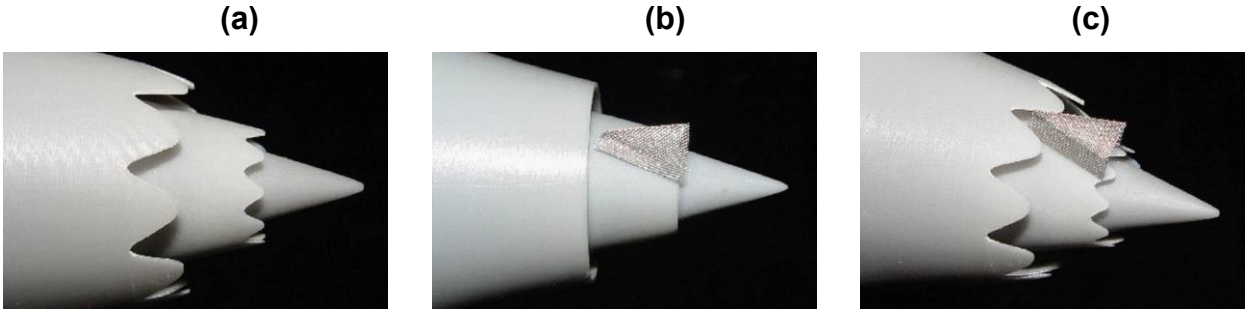

Fig. 3.2.4 Nozzle modifications. (a) Aggressive chevrons (AC); (b) porous wedge with 18-deg half angle (W18); and (c) combination (AC+W18).

(a)

(b)

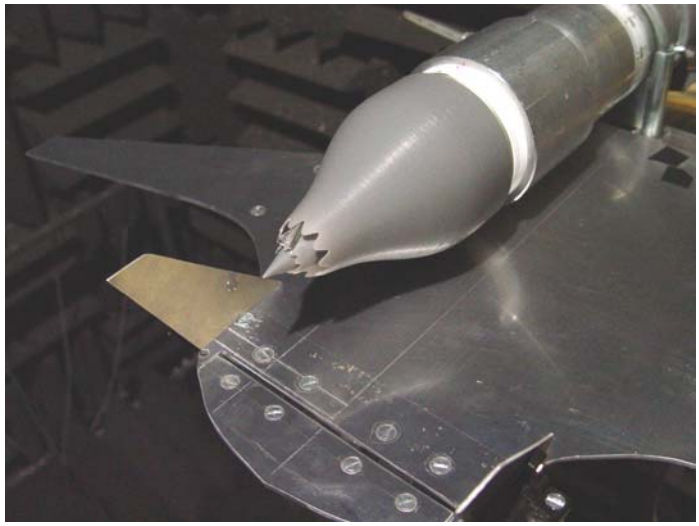

(c)

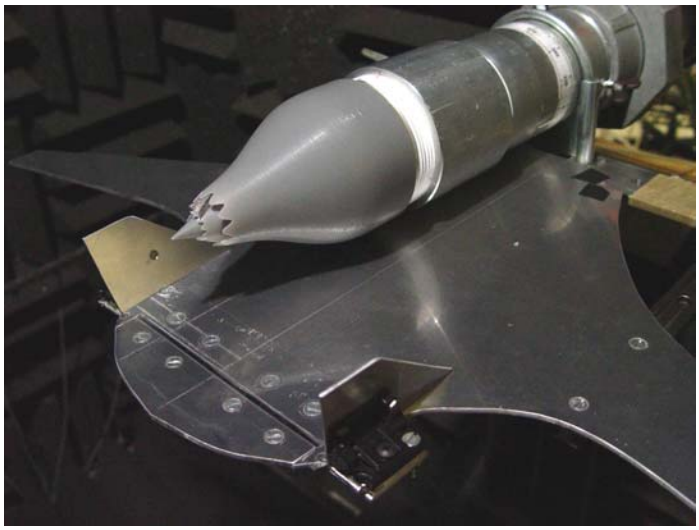

Fig. 3.2.5 Photos of experimental configurations with combination (AC+W18) nozzle. (a) No verticals; (b) nominal verticals; (c) alternate verticals.

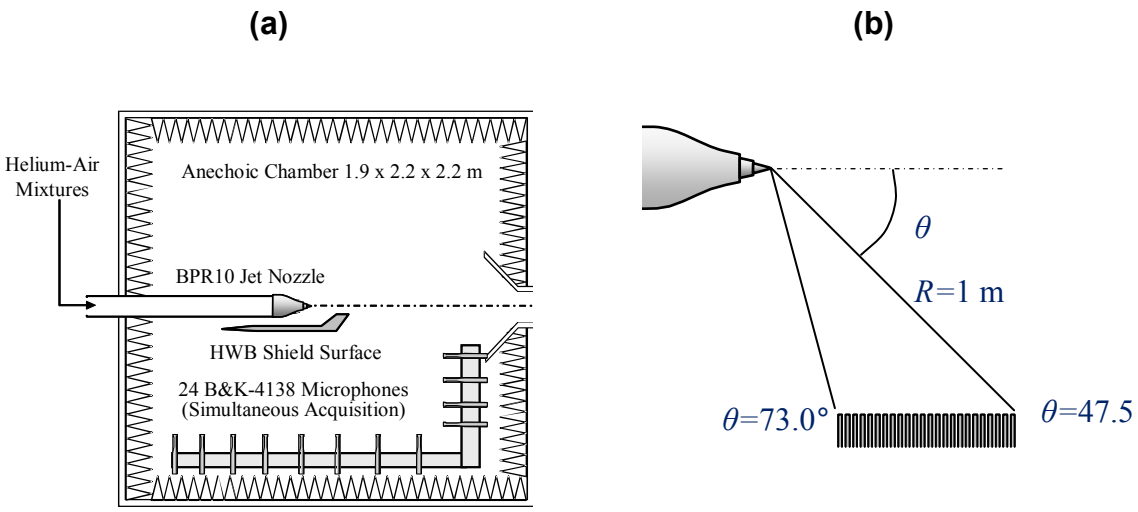

Fig. 3.2.6 Aeroacoustic measurement. (a) Setup for acoustic surveys; (b) setup for noise source imaging.

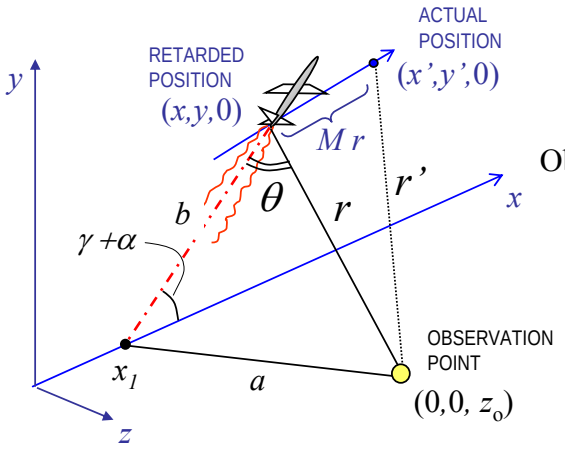

Aircraft flying with Mach number M, angle of attack α, and climb angle γ

Observation distance and polar emission angle

$$r' = \sqrt{x'^2 + y'^2 + z_0^2}$$

$$r = \sqrt{x^2 + y^2 + z_0^2}$$

$$\tan(\theta/2) = \sqrt{\frac{(p-b)(p-r)}{p(p-a)}}$$

where

$$x_1 = x - y/\tan(\gamma+\alpha)$$

$$a = \sqrt{x_1^2 + z_0^2}$$

$$b = y/\sin(\gamma+\alpha)$$

$$p = \frac{1}{2}(a+b+r)$$

CONDITIONS FOR EVALUATON OF PNL		
	SIDELINE	CUTBACK
Lateral distance, z_o=	1476 ft	0 ft
Altitude at x=0	1500 ft	2171 ft
Angle of attack, α=	13.35°	13.93°
Climb angle, γ=	9.46°	2.29°
Flight Mach, M=	0.220	0.224

Fig. 3.2.7 Geometric relations and conditions for assessment of perceived noise level.

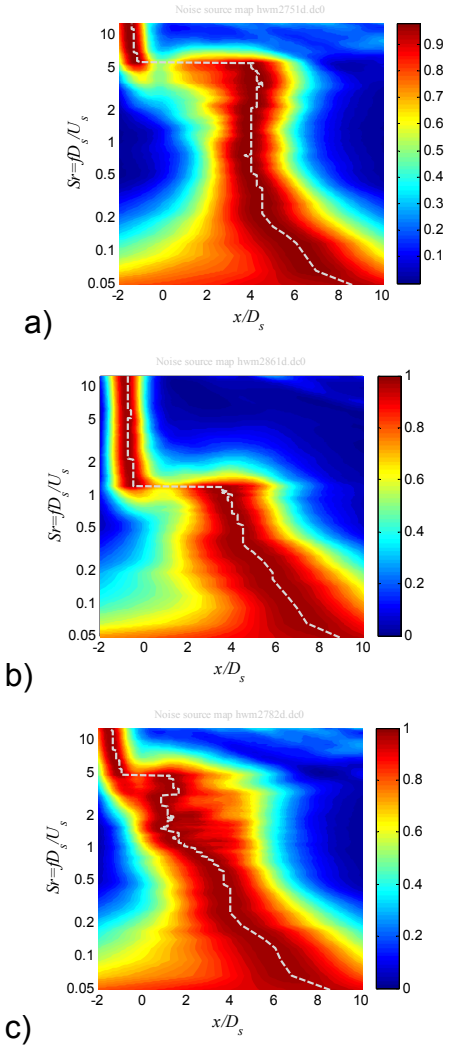

Fig. 3.3.1 Noise source distributions for isolated BPR10 jets, with dashed white lines indicating location of peak noise. (a) Plain nozze; (b) aggressive chevrons; (c) porous wedge.

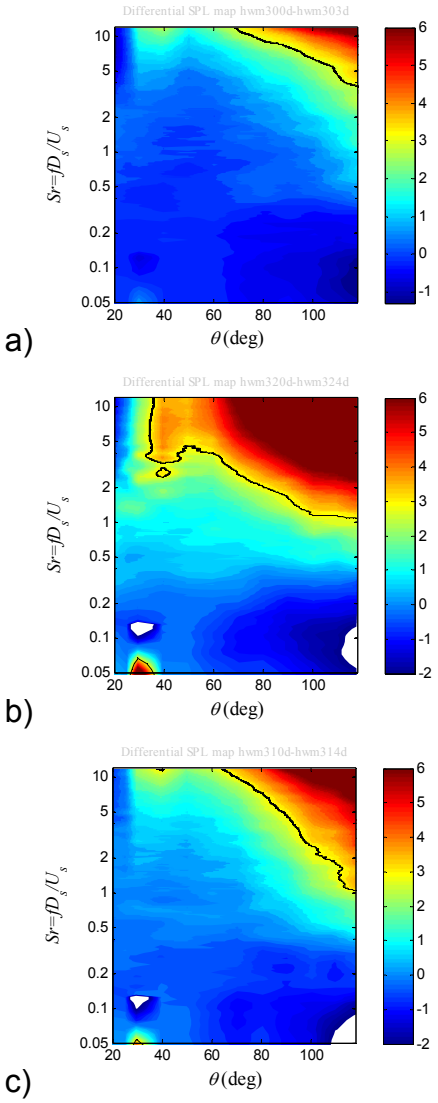

Fig. 3.3.2 Insertion loss (dB) for noise in the downward direction, using nominal verticals with nozzle at nominal location X/D_s=2.3. (a) Plain nozze; (b) aggressive chevrons; (c) porous wedge.

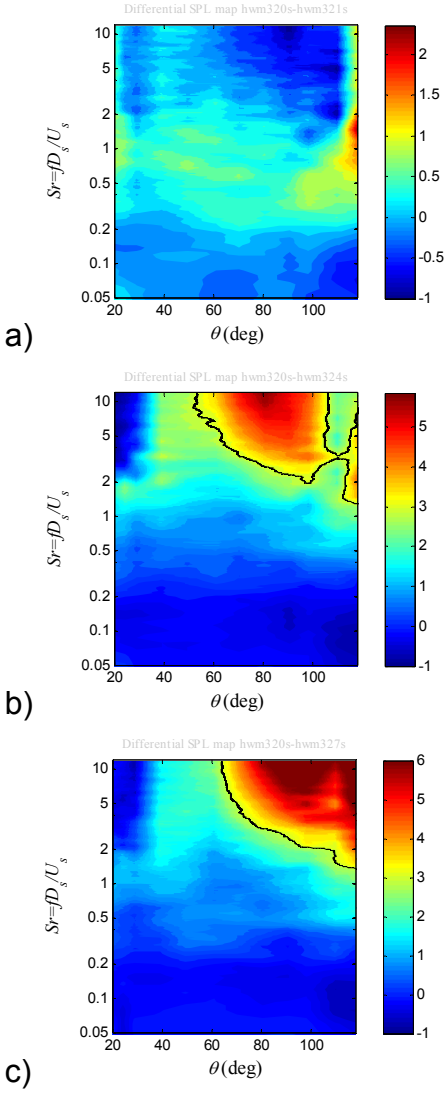

Fig. 3.3.3 Insertion loss (dB) for noise in the sideline direction, using aggressive chevron nozzle at nominal location X/D_s=2.3. (a) no verticals; (b) nominal verticals; (c) alternate verticals.

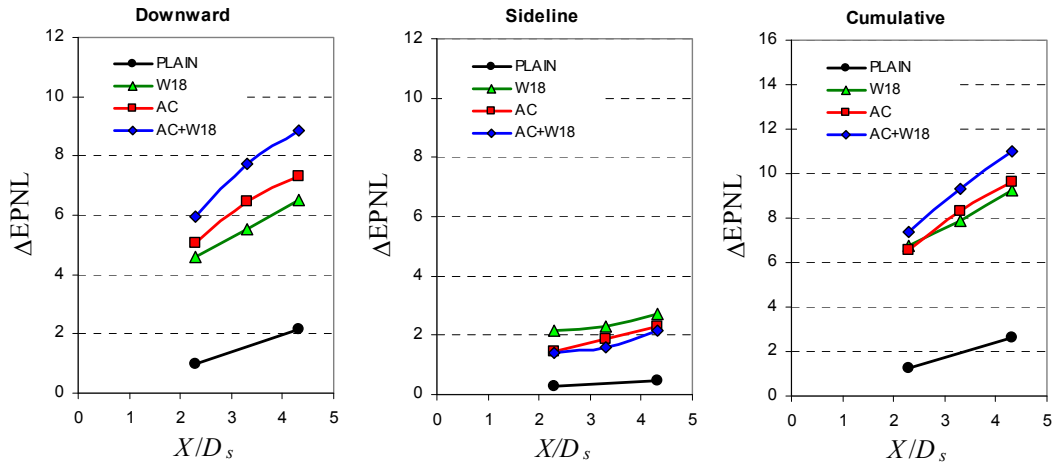

Fig. 3.3.4 EPNL reductions (relative to isolated plain nozzle) versus axial position of fan exit plane relative to trailing edge. Shield without verticals.

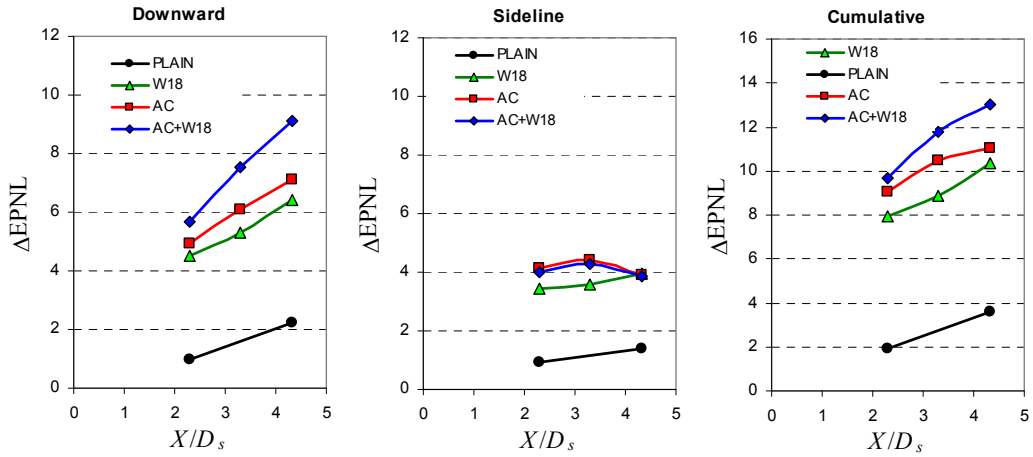

Fig. 3.3.5 EPNL reductions (relative to isolated plain nozzle) versus axial position of fan exit plane relative to trailing edge. Shield with nominal verticals.

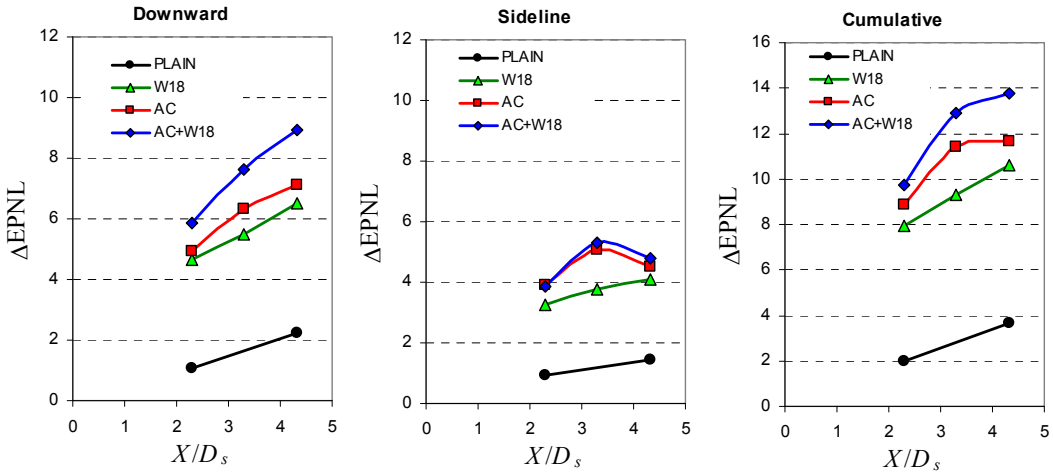

Fig. 3.3.6 EPNL reductions (relative to isolated plain nozzle) versus axial position of fan exit plane relative to trailing edge. Shield with alternate verticals.

REFERENCES

1. Liebeck, R.H., "Design of the Blended Wing Body Subsonic Transport," *Journal of Aircraft*, Vol. 41, No. 1, Jan.–Feb. 2004.
2. Von Glahn, U., Groesbeck, D., and Reshotko, M., "Geometry Considerations for Jet Noise Shielding with CTOL Engine-Over-The-Wing Concept," AIAA Paper 74-568, June 1974.
3. Von Glahn, U., Goodykoontz, J., and Wagner, J., "Nozzle geometry and forward velocity effects on noise for CTOL engine-over-the-wing concept," NASA TM-X-71453, Oct. 1973
4. Von Glahn, U., Groesbeck, and D. Wagner, J., "Wing shielding of high-velocity jet and shock-associated noise with cold and hot flow jets," AIAA Paper 76-547, July 1976.
5. Russell, J., and Berton, J., "Stone Jet Noise Module (ST2JET)", ANOPP Theoretical Manual, ver.25, NASA Langley Research Center, Hampton, VA, 2006.
6. Maekawa, Z. "Noise Reduction by Screens," *Applied Acoustics*, Vol.1, 1968, pp. 157–173.
7. Tam, C. K. W., and Burton, D. E., "Sound Generation by the Instability Waves of Supersonic Flows. Part 2. Axisymmetric Jets," *Journal of Fluid Mechanics*, Vol. 138, 1984, pp. 273-295.
8. Crighton, D.G. and Huerre, P., "Shear-Layer Pressure Fluctuations and Superdirective Acoustic Sources," *Journal of Fluid Mechanic*s, Vol. 220, 1990, pp. 355-368.
9. Avital, E.J., Sandham, N.D., and Luo, K.H., "Mach Wave Radiation by Mixing Layers. Part I: Analysis of the Sound Field," *Theoretical and Computational Fluid Dynamics*, Vol. 12, 1998, pp. 73-90.
10. Morris, P.J., "A Note on Noise Generation by Large Scale Turbulent Structures in Subsonic and Supersonic Jets," *International Journal of Aeroacoustics*, Vol. 8, No. 4, 2009, pp. 301-316.
11. Fisher, M.J., Preston, G.A., and Bryce, W.D., "A Modelling of the Noise from Simple Coaxial Jets, Part I: With Unheated Primary Flow," *Journal of Sound and Vibration*, Vol. 209, No.3, 1998, pp. 385-403.
12. Shanno, D.F., and Phua, K.H., "Minimization of Unconstrained Multivariate Functions," *ACM Transactions on Mathematical Software*, Vol. 6, pp. 618-622.
13. Wu, T. W., *Boundary Element Acoustics*, WIT Press, Boston, 2000.
14. Liu, Y.J., *Fast Multipole Boundary Element Method - Theory and Applications in Engineering*, Cambridge University Press, Cambridge (2009).
15. Wu, T.W., and Lee, L., "A Direct Boundary Integral Formulation for Acoustic Radiation in Subsonic Uniform Flow," *Journal of Sound and Vibration*, Vol. 175, No.1, 1994, pp. 51-63.
16. Papamoschou, D., "Prediction of Jet Noise Shielding," AIAA Paper 2010-0653, Jan. 2010.
17. Papamoschou, D., and Mayoral, S., "Experiments on Shielding of Jet Noise by Airframe Surfaces," AIAA Paper 2009-3326, May 2009.

18. Mayoral, S., and Papamoschou, D., “Effects of Source Redistribution on Jet Noise Shielding," AIAA Paper 2010-0652, Jan. 2010.

19. Czech, M.J., Thomas, R.H., and Elkoby, R., “Propulsion Airframe Aeroacoustic Integration Effects for a Hybrid Wing Body Aircraft Configuration,” AIAA-2010-3912, June 2010.

20. Papamoschou, D., and Mayoral, S., “Jet Noise Shielding for Advanced Hybrid Wing-Body Configurations,” AIAA Paper 2011-0912, Jan. 2011.

21. Papamoschou, D., “Pylon Based Jet Noise Suppressors,” *AIAA Journal*, Vol. 47, No. 6, 2009, pp. 1408-1420.

22. Papamoschou, D., “Acoustic Simulation of Coaxial Hot Air Jets Using Cold Helium-Air Mixture Jets,” *Journal of Propulsion and Power*, Vol. 23, No.2, 2007, pp. 375-381.

23. Papamoschou, D., “Imaging of Distributed Directional Noise Sources,” AIAA Paper 2008-2885, May 2008.

24. Brusniak, L., Underbrink, J.R., and Nesbitt, E., “Phased Array Measurements of Full-Scale Exhaust Noise,” AIAA Paper 2007-3612, May 2007.

APPENDIX B

Gas Turbine Laboratory
Department of Aeronautics and Astronautics
Massachusetts Institute of Technology

Final Report – Phase II

ACOUSTIC ASSESSMENT OF VERY QUIET HYBRID WING BODY SUBSONIC TRANSPORT

submitted to

Ron Kawai
The Boeing Company
5301 Bolsa Avenue
M/C H013-A319
Huntington Beach, CA

Principal Investigator: Zoltán S. Spakovszky
Director Gas Turbine Laboratory
Associate Professor of Aeronautics and Astronautics

Students: Elena de la Rosa Blanco
Research Engineer
Dorian Colas
Graduate Research Assistant

Kelly Strominger
Undergraduate Research Student
Gas Turbine Laboratory

Period of Investigation: January 26, 2009 – December 31, 2010

December 6, 2010

1. Executive Summary

MIT's major research efforts in phase II focused on Tasks 4.2.2 Turbomachinery Noise Scattering Prediction Method, 4.2.4 HWB Configuration Improvements, 4.2.5 Fan Pressure Ratio Study, and 4.2.6 Noise Assessment. There is a no-cost extension on Task 4.2.4 which will be reported on in a supplement to this final report.

An improved fidelity turbomachinery shielding method compatible with ANOPP was developed and implemented. To obtain the acoustic pressure in the geometric shadow region of an airframe, the geometric theory of diffraction was used to calculate edge-diffraction rays at sharp edges. Previous work showed that replacing the geometric theory of diffraction with Kirchhoff's diffraction theory can yield sufficient fidelity for a variety of geometries, including airframes. The first version of the method solved a contour integral around the outline of the geometry seen by the noise source based on the Maggi-Rubinowicz formulation of the Kirchhoff diffraction theory [1]. An algorithm was developed to generate the shadow contour for any 3-D geometry, making it applicable to a wide variety of applications. To remedy shortcomings of the Maggi-Rubinowicz formulation, such as spurious singularities and limitation to monopole sources, the method was reformulated borrowing ideas from geometrical optics. Using the Uniform Theory of Diffraction and a more general potential based on the framework described by Miyamoto and Wolf [2-3], an exact, analytical expression for the integral of the potential along a finite, linear edge was derived, reducing the problem to Fresnel integrals which can be treated analytically. The improved shielding method dramatically reduces computational cost, avoids spurious singularities, and allows for general source definitions (such as for example dipole or directional point source formulations). In addition, flight effects were incorporated based on the Prandtl-Glauert transformation.

The new shielding methodology was tested for canonical geometries such as a sphere and a cylinder, and the shielding results were compared with data from literature and with NASA fast scattering code results. Good agreement was achieved and, using the established methodology, the shielding capability of various airframe configurations was assessed. The shielding computations of the N2A aircraft indicate that this advanced configuration can potentially provide about 7 dB more noise attenuation than a conventional configuration. Furthermore, the results suggest that vertical tails provide additional 3 to 5 dB noise attenuation in the lateral direction.

Lastly, the FAR36 noise assessment was updated for the evolved N2A-EXTE aircraft configuration. Improved methods for airframe source noise, turbomachinary shielding and jet noise shielding were implemented and the noise audit was conducted for a range of fan pressure ratios. The results suggest that the NASA's N+2 noise goal can be met with a comfortable margin for a range of fan pressure ratios. The details of the assessment are discussed in this report and compared with previous noise audits from Phase I and Phase II.

2. Turbomachinery Noise Shielding Method

The previous version of the diffraction integral based shielding method, DIM v1.0, was developed in the first year of Phase II and was documented in [4, 5] and in the corresponding annual report. Thus, the details will not be repeated here. This report details the improvements and modifications to the previous version. The new version, DIM v2.0, includes: (1) directivity effects, such as dipole and directional point source descriptions, (2) flight effects, and (3) faster algorithm compatible with optimization framework computation time requirements and suitable for use in ANOPP.

2.1 Noise Shielding Framework and Method Overview

Figure 1 gives an overview of the improved turbomachinery noise shielding method, DIM v2.0. Similar to version v1.0 there is an offline and an online part. The offline part is comprised of three main modules two of which were newly developed.

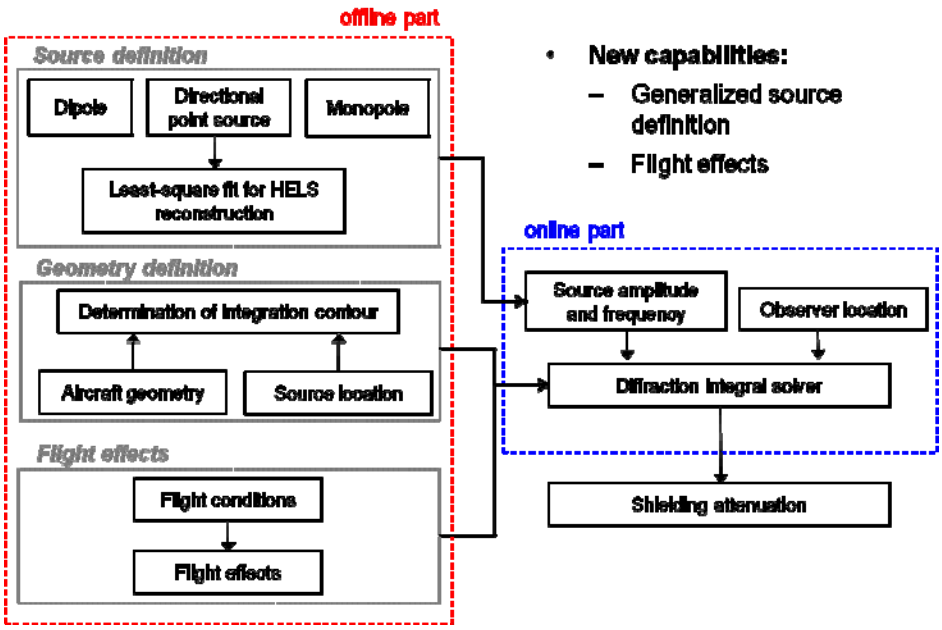

Figure 1: *Overview of new diffraction integral shielding method, version v2.0.*

In the source definition part either a monopole, or dipole, or a directional point source can be specified. For the directional point source a least squares method is used to reconstruct the near field source definition using directivity information in the far field. The module that defines the shielding geometry and source location is unchanged from v1.0. Based on the aircraft flight conditions, flight effects can be included in the shielding assessment. This information together with the location of observers is used in the diffraction integral solver to compute the shielding attenuation. The next section describes the theoretical development of the shielding method.

2.1.1 Theoretical Development

Consider the shielding geometry shown in Figure 2. For a given source and incident acoustic field $p_i(x)$, the field transmitted through an aperture can be written in terms of the following Kirchhoff diffraction surface integral

$$p_s(x) = -\frac{1}{4\pi}\iint_S \left(p_i \frac{\partial}{\partial n}\frac{e^{-jkR}}{R} - \frac{e^{-jkR}}{R}\frac{\partial}{\partial n}p_i\right)dS \qquad (1)$$

where S is the surface of the aperture.

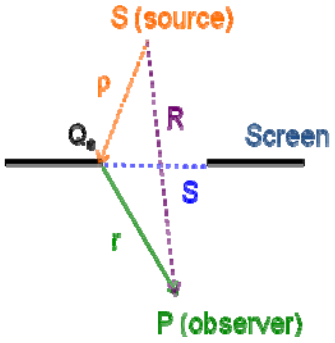

Figure 1: ***Relation between shielding geometry, source and observer location***

The total transmitted field through an aperture $p_s(x)$ is composed of the geometrical optics field $p_{GO}(x)$ and the boundary diffracted waves, which are the incident rays diffracted by the contour, $p_d(x)$. This can be written as

$$p_s(x) = p_d(x) + p_{GO}(x) = p_d(x) + \chi(\vec{R})p_i(x) \qquad (2)$$

where χ is the incident shadow indicator. This indicator is equal to 0 if $\vec{R}$ is in the shadow region and 1 otherwise. It follows that $p_d(x)$ can be expressed as a line integral along the contour of the aperture rather than a surface integral. Maggi and Rubinowicz, and successively Miyamoto and Wolf [2-3] derived an expression for $p_d(x)$ for a monopole source and for any scalar wave field respectively. With the notation in Figure 2 this becomes

$$p_d(x) = \frac{1}{4\pi}\oint_{\partial S}\frac{p_0(Q_e)}{r}\frac{(\vec{\rho}\times\vec{r}).d\vec{l}}{r\rho + \vec{r}.\vec{\rho}}e^{jk(r+\rho)} = \frac{1}{4\pi}\oint_{\partial S}\vec{W}.d\vec{l} \qquad (3)$$

where

$$p_i(Q) = p_0(Q)e^{jk\rho} \qquad (4)$$

In Eq. (3) the integrand yields a singularity for $r\rho + \vec{r}.\vec{\rho} = 0$. This region, where the potential goes to infinity, is called the transition region and corresponds to observer locations where χ transitions from 1 to 0. Because of this singularity the numerical integration of this integral is inaccurate and computationally expensive. To obtain an explicit expression for this line integral, the first step is to examine the integration along a linear segment Γ.

The diffracted field can be computed by discretizing any arbitrary diffraction contour into small linear edges Γ_i such that

$$p_d(x) = \oint_{\partial S} \vec{W}.d\vec{l} \approx \sum_i \int_{\Gamma_i} \vec{W}.d\vec{l} \tag{5}$$

Consider an arbitrary linear segment Γ, characterized by a unit vector $\vec{e}$, an arbitrary initial point $\vec{y}_0$ and a start and end point denoted by their curvilinear abscissae s_a and s_b. It can be shown that the boundary diffracted wave associated with a linear edge can be written per [6] as

$$\begin{aligned} p_d(P) &= \int_{s_a}^{s_b} f(s) e^{jkg(s)} ds = \\ &= \sqrt{\pi} e^{-j\frac{\pi}{4}} e^{jkg(s^*)} \left\{ G(s^*)[U(-\xi_a) - U(-\xi_b)] + G(s_a) F[|\xi_a|] - G(s_b) F[|\xi_b|] \right\} \end{aligned} \tag{6}$$

where f is the amplitude function defined as

$$f = \frac{p_0(Q_e)(\vec{\rho} \times \vec{r}).d\vec{l}}{4\pi r(r\rho + \vec{r}.\vec{\rho})} \tag{7}$$

and g is the phase function, $g = r + \rho$. F is a Fresnel integral defined as

$$F[x] = \frac{e^{-j\frac{\pi}{4}}}{\sqrt{\pi}} \int_x^\infty e^{jt^2} dt \tag{8}$$

and *U(x)* is the unit step function. The super script ***** and subscripts *a, b* denote stationary phase point and segment end points respectively. ξ is the so called 'detour' parameter,

$$\xi_\alpha = \sqrt{k\,|\,g(\alpha^*) - g(\alpha)\,|} \tag{9}$$

and

$$G(\alpha) = \frac{f(\alpha)}{h(\alpha)} \qquad , \quad h(\alpha) = \begin{cases} k\dfrac{g'(\alpha)}{2\xi} & if \quad \alpha \neq \alpha^* \\ \sqrt{\dfrac{kg''(\alpha)}{2}} & if \quad \alpha = \alpha^* \end{cases} \tag{10}$$

In summary, the first term in Eq. (6) is the stationary phase point contribution and the last two terms are the end point contributions.

2.1.2 Uniform Theory of Diffraction

Inspection of the previous derivation reveals that the potential still yields a singularity. In order to modify the topology of the integral and to avoid this singularity the Uniform Theory of Diffraction (UTD) [7] is applied. The theory postulates that in the transition region the diffracted field behaves like a Fresnel integral. Since this integral is continuous everywhere the potential must be as well. Eq. (6) can thus be rewritten as:

$$p_d(P) = 2\pi e^{jkR} \xi F[|\xi|]\left\{G(s^*)[U(-\xi_a) - U(-\xi_b)] + G(s_a)F[|\xi_a|] - G(s_b)F[|\xi_b|]\right\} \quad (11)$$

where $\xi = \sqrt{k\,|\,g(s^*) - R\,|}$. The above expression does not contain any singularities and forms the final formulation implemented in the shielding framework.

2.2. Implementation of Diffraction Integral Shielding Method

There are two key implementation steps: (i) stationary phase point location and derivatives of the phase function, and (ii) evaluation of the Fresnel integrals. In order to numerically evaluate the uniform, asymptotic expansions, the stationary phase point location and the first and second derivatives of the phase function need to be determined. On a linear edge, these quantities can be found via simple geometrical relations. The implementation and the numerical evaluation are straightforward and computationally inexpensive. Details of the code implementation can be found in Appendix A.

Having reduced the original line integral to Fresnel integrals, the main task in the method is to evaluate these integrals. There are two ways of evaluating such integrals. The first method is to make use of common routines that have been developed in the literature and are known to yield high accuracy (with errors less than 1e-8). One challenge with these numerical integrators is that extensive calling of such an external script from the main routine can significantly increase the computational cost. An alternative approach is to use an analytical expression [8]. It can be shown that the following two-term approximation

$$F[x] \approx \frac{1}{1 - e^{e^{-j\frac{\pi}{4}} 2\sqrt{\pi x}}} + \frac{e^{j\frac{\pi}{4}} e^{jx^2}}{2\sqrt{\pi}x} \quad (12)$$

yields sufficient accuracy. The largest errors occur near the origin and are of order 1e-2; everywhere else the errors are much below 1e-3. Both methods were assessed carefully and it was determined that the above analytical approximation is adequate.

2.3 Method Limitations and Assumptions

Before validating the diffraction integral method (DIM), its limitations and assumptions are briefly summarized:

1) The method is based on the Kirchhoff diffraction theory and is formulated as asymptotic expansions. The DIM is therefore a high frequency method and, as the assessment and validation in Section 2.4 will show, it is applicable for Helmholtz numbers as low as 90 which is equivalent to 300 Hz in the application of interest.

2) In line with the above assumptions, the method is based on edge diffraction for apertures and therefore does not capture creeping rays. This is illustrated and quantitatively assessed next.

3) A major consequence of these assumptions is that two objects that share the same outline yield the same insertion loss independent of their shape.

2.4 Method Validation

To quantify the limitations and to validate the method, two canonical test cases using a monopole noise source were considered: the shielding by a sphere and by a disk, as illustrated in *Figure 2*.

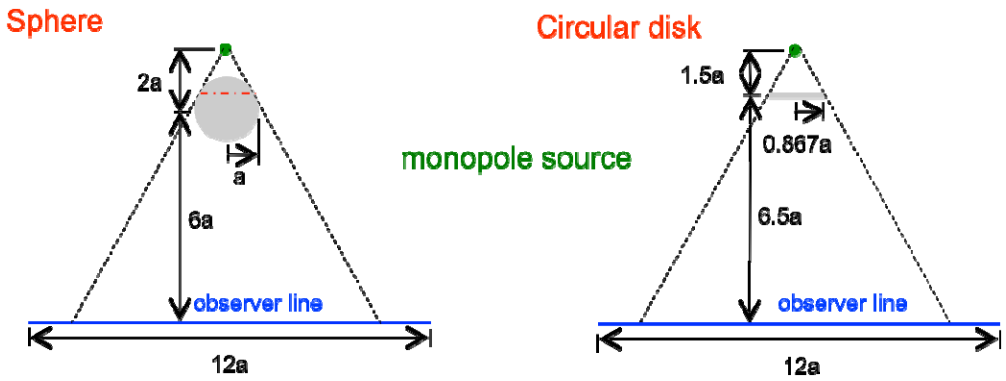

Figure 2: ***Canonical test cases: shielding by a sphere and by a disk with the same shielding contour.***

The diffraction integral method was compared to a high fidelity method, namely NASA's fast scattering code (FSC) based on the equivalent source method [12]. Shielding computations were conducted for both test cases at ka = 92, 150 and 400, where a is the radius of the sphere. If the sphere or the disk are scaled up to the size of the centerbody of the N2A aircraft, this Helmholtz number range corresponds to source frequencies ranging from 300 Hz to 1500 Hz. The fast scattering code results were kindly provided by NASA Langley, courtesy of Ana Tinetti. The results are shown in *Figure 3*. The disk and sphere results are plotted on the left- and right-hand side respectively. The noise attenuation is given as a function of non-dimensional distance from the centerline of the object along the observer line; Fast Scattering Code results are in red and Diffraction Integral Method results are in blue respectively.

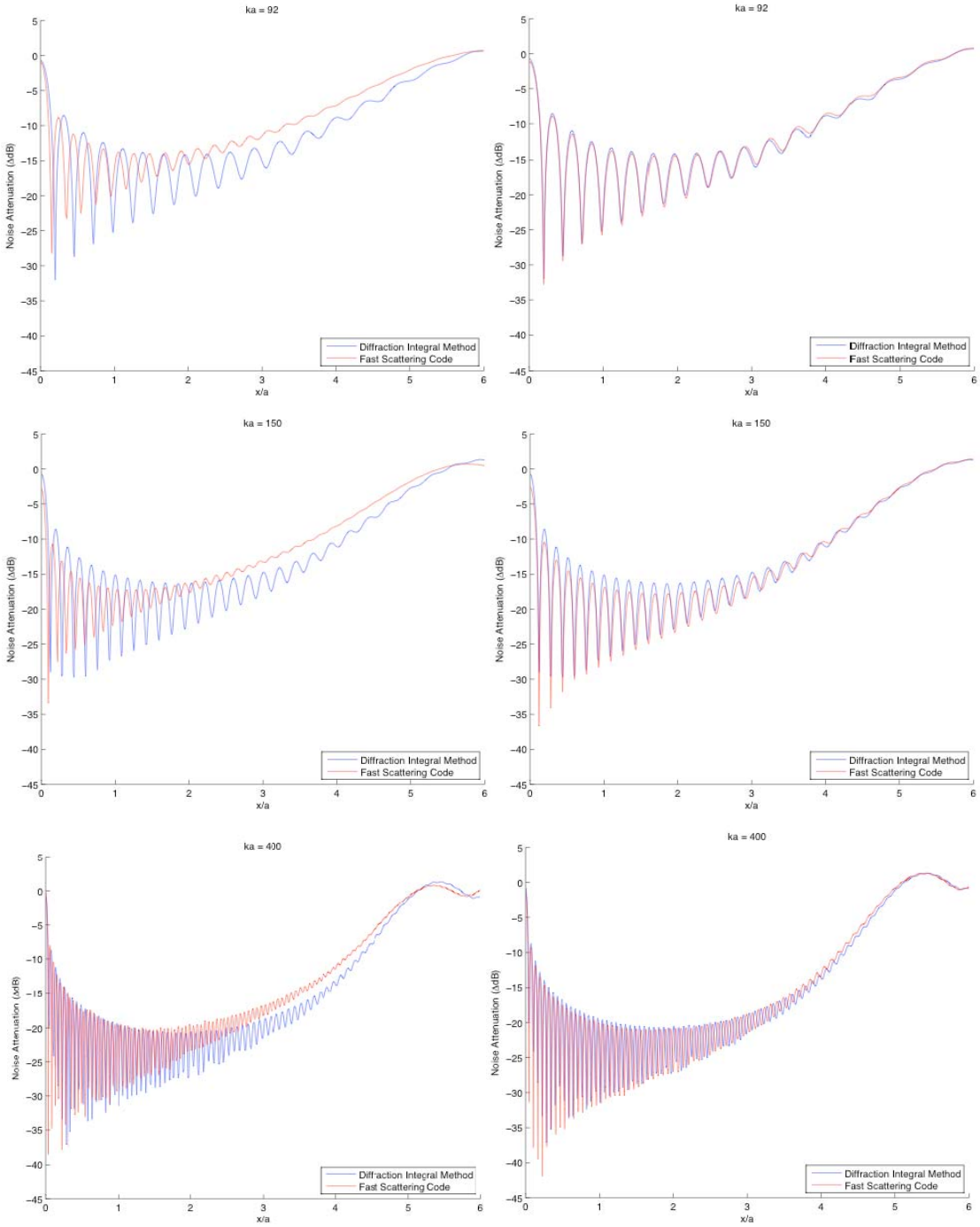

Figure 3: ***Monopole shielding by a sphere (left) and a disk (right) – Diffraction Integral Method (blue) compared with Fast Scattering Code (red).***

The noise attenuation from the diffraction integral method are in good agreement with the Fast Scattering method for the disk – for the sphere, discrepancies are observed consistent with the limitation that only edge-diffraction rays are captured. The difference of up to about 5 dB in the noise attenuation level between the disk and the sphere can be

attributed to creeping ray effects. The planform of a HWB aircraft is relatively flat, so the method is expected to yield adequate estimates of the noise shielding by the airframe, with the diffraction around the trailing edge being more accurate than that around the leading edge. Furthermore, the results for the different *ka* cases do not indicate any noticeable change in accuracy of the diffraction integral method over the range of frequencies considered. This suggests that, despite the high frequency approximation in the derivation, the diffraction integral method is applicable at relatively low frequencies down to about 300 Hz for a full-sized HWB airframe.

2.5 Source Noise Description

Four different source noise models were investigated and implemented in the diffraction integral method: (i) monopole, (ii) dipole, (iii) directional point source, and (iv) HELS directional point source. In the current implementation of the code, any of the above descriptions can be chosen by the user. More details can be found in the User Guide in Appendix B.

2.5.1 Monopole and Dipole Sources

The monopole and dipole source description can be formulated as

$$p_{monopole}(r) = Q\frac{e^{jkr}}{r} \tag{13}$$

$$p_{dipole}(r,\theta) = Q\frac{\cos\theta}{r^2}(1-jkr)e^{jkr} \tag{14}$$

where Q is the source strength. Both sources satisfy the Helmholtz equation. An omni-directional monopole source was first used in the development of the method and was then extended to a dipole source to assess the effects of directivity on shielding. While the dipole directivity is a useful diagnostic, it does not resemble the directivity pattern of a turbomachinery noise source. As such, a directional point source was explored and is discussed next.

2.5.2 Directional Point Source and HELS Representation

To capture a specific turbomachinery directivity pattern, a directivity function *D* can be introduced in combination with a point source. The directivity function can either be tabulated or a polynomial fit to measurements or a prescribed directivity pattern in the far field. The formulation becomes

$$p_{dir}(r,\theta,\varphi) = D(\theta,\varphi)\frac{e^{jkr}}{r} \tag{15}$$

It is important to note that this directional point source does not satisfy the Helmholtz equation and is therefore expected to yield significant errors in the near field.

To avoid these errors and to ensure that the Helmholtz equation is satisfied, spheroidal functions can be introduced [9, 10] and the directional point source can be written as

$$p_{HELS}(x) = \sum_{j=0}^{\infty} C_j \Psi_j(x) \approx \sum_{j=0}^{J} C_j \Psi_j(x) \tag{16}$$

where $$\Psi_j(x) = \psi_{n,l}(r,\theta,\phi) = h_n(kr) P_{n,l}(\cos\theta) e^{il\phi} \tag{17}$$

and J is the number of terms in the expansion, h_n is the n-th spherical Hankel function and $P_{n,l}$ is the associated Legendre polynomial. The coefficients can be determined via a least square fit on data available in the far field. This description is commonly referred to as a Helmholtz Equation Least Squares fitted point sources, or in short HELS.

Figure 5 depicts an example implementation of the HELS representation using ANOPP's Heidmann fan module to generate the far field data. For each 1/3 octave band frequency data was generated at kr = 1000 to ensure far field conditions for all frequency bands. An 11th order polynomial description was used in this example.

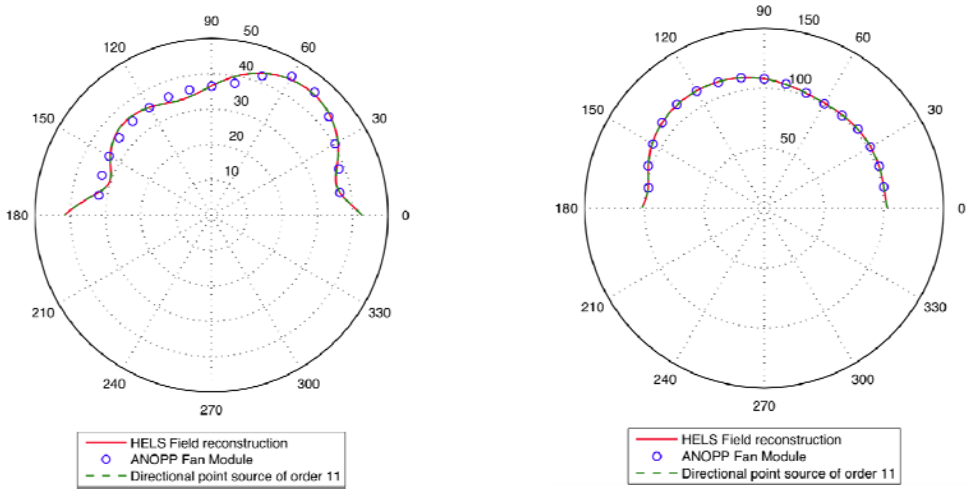

Figure 5: ***Directivity pattern using ANOPP's Heidmann fan module at 50 Hz (left) and 10 kHz (right)***

2.6 Near Field Error Assessment

2.6.1 Free-Field Comparison

To assess the near field error of the simple directional point source description of Eq. (15), the HELS reconstruction in Eqs. (16-17) is used for comparison. For both descriptions, the Heidmann fan noise directivity was implemented for a range of reduced frequencies kr.

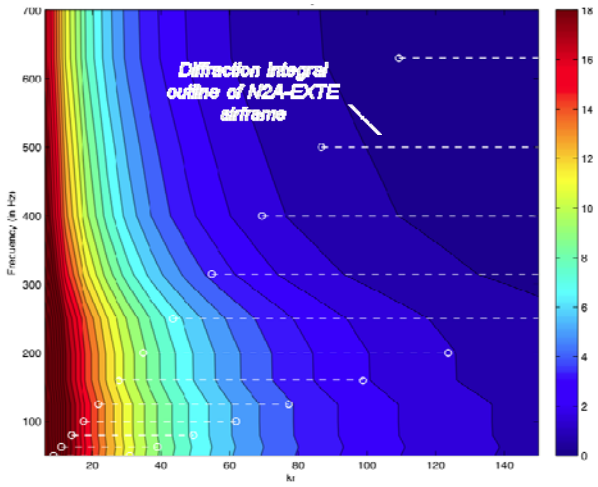

Figure 4: *Near field error in dB – simple directional point source vs. HELS representation.*

The results of the error analysis are shown in ***Figure 4***. The white dashed lines mark the range of *kr* corresponding to the outline of the N2A-EXTE airframe. As expected, significant discrepancies occur in the near field, which can amount to more than 18 dB..

2.6.2 Diffracted Field Comparison

Next, a shielding body is considered such as the N2A-EXTE airframe. For observers located in the far field, errors in the near field can impact the diffracted far field. To assess the far field error the directional point source and the associated HELS are compared and shown in *Figure 5*. Note that where the source is close to the diffracting edge the associated error in the far field is particularly high (up to 12dB for observers behind the vertical tails).

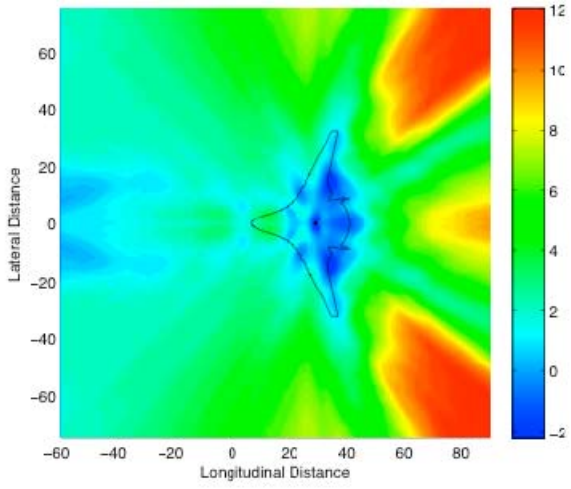

Figure 5: ***Noise attenuation pattern comparison: directional point source vs HELS description for N2A-EXTE***

The key conclusion is that directional point sources should be modeled using the HELS representation to accurately capture the directivity patterns of turbomachinery sources in the near field.

2.7 N2A-EXTE Turbomachinery Noise Shielding Assessment

To illustrate the range of source definitions that can be used in the shielding assessment, monopole, dipole and HELS directional point source shielding calculations were conducted for the N2A-EXTE airframe. The HELS directional point source description was based on ANOPP's Heidmann fan noise estimate, as described above. The results are depicted in Figure 8 below. Note the strong directivity pattern of the dipole with some amplification in the direction orthogonal to the dipole axis. This is due to the fact that in this region the incident field is silent whereas the diffracted field is not due to scattering around the shielding contour. It is also important to note that the monopole case is overestimating the insertion loss compared to the HELS directional point source case.

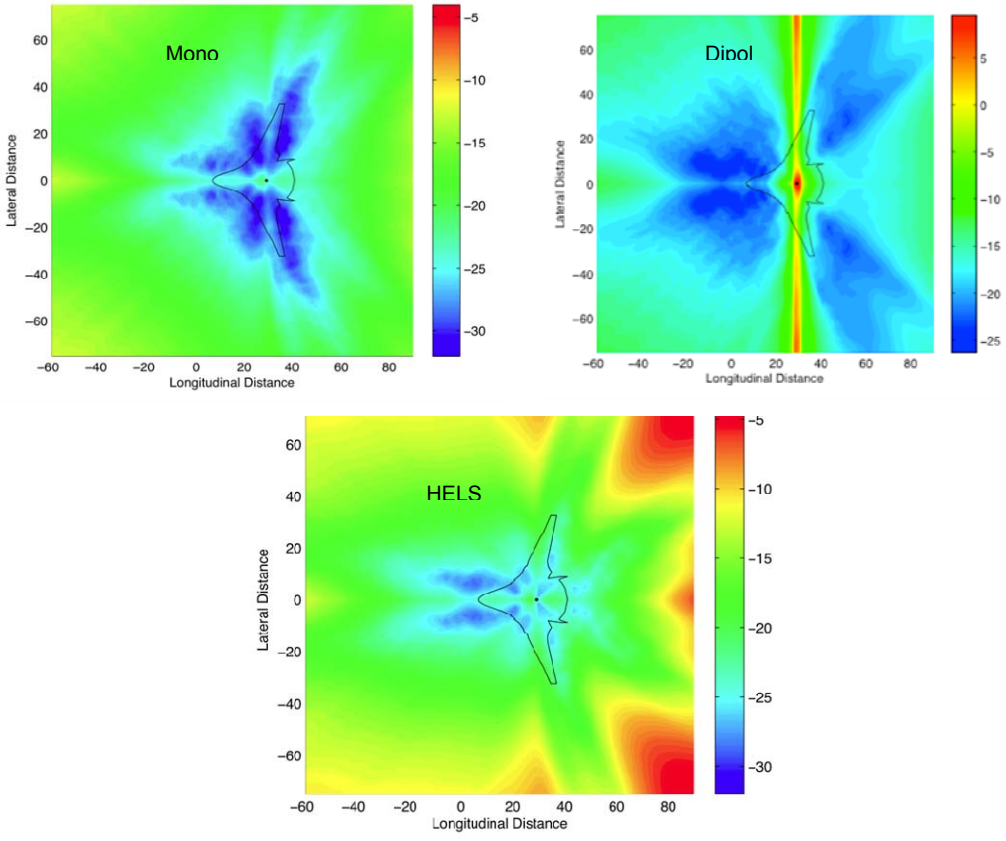

Figure 8: *N2A-EXTE shielding patterns for monopole (left), dipole (center), and HELS directional point source (right).*

To illustrate the difference between the shielding of a monopole source compared to that of the HELS directional point source representation, the difference in insertion loss is plotted in Figure 9.

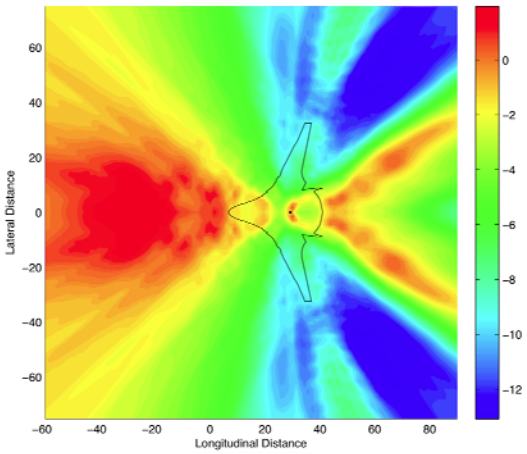

Figure 9: *Difference in insertion loss – monopole vs HELS directional point source.*

The monopole based shielding calculation over-estimates the insertion loss mostly in the lateral direction by about 10-12 dB. While this yields a significant difference in the shielding of the turbomachinery noise sources, it will be shown that the overall aircraft noise estimates at the FAR36 observer locations are impacted less. This is because airframe and jet noise sources dominate the acoustic signature.

2.8 Flight Effects

To model flight effects, the Prandtl-Glauert method for small acoustic disturbances in a uniform mean flow was implemented (see for example [12]). The method employs a Lorentz transformation according to

$$\vec{\xi} = (X, Y, Z) = B_0^{-1}(x, y, z) \tag{18}$$

where

$$B_0 = I + \frac{1-\beta_0}{\beta_0 M_0^{\,2}} \vec{M}_0 \vec{M}_0^{\,T} \tag{19}$$

The Helmholtz equation in the transformed domain then becomes

$$\nabla_X^{\,2} \tilde{p} + \kappa_0^{\,2} \tilde{p} = 0 \tag{20}$$

with the modified wave-number due to the Doppler shift

$$\kappa_0 = \frac{k_0}{\beta_0} = \frac{\omega_0}{c_0 \sqrt{1 - M_0^{\,2}}} \tag{21}$$

The acoustic pressure field with flight effects can then be written in terms of the acoustic pressure field at static conditions:

$$p_{M>0}(\vec{\xi}) = \frac{1}{\beta_0}\left[p_{M=0} + i\frac{M}{\kappa_0}\frac{\partial}{\partial X} p_{M=0}\right] e^{-i\kappa_0 M_0 X} \tag{22}$$

Note that in the

implementation, the spatial derivative of the acoustic pressure field at static conditions is required. The computation of this derivative was implemented in the method to account for simple flight effects. Figure 10 illustrates a monopole noise source at static conditions and compares it to flight conditions at M = 0.3.

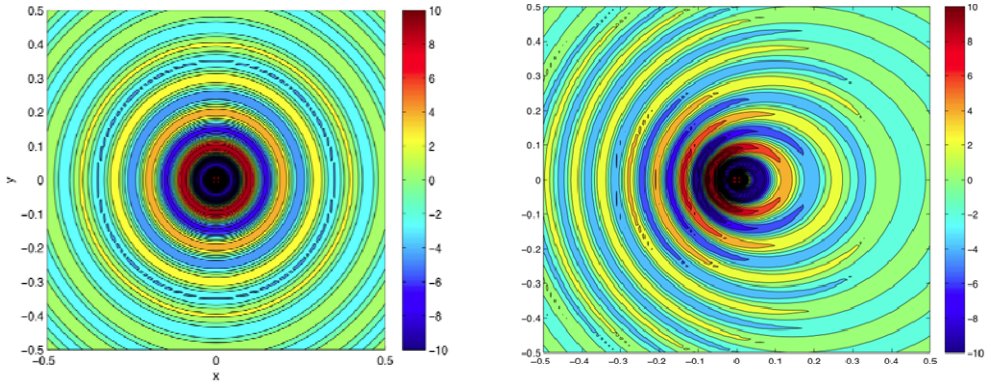

Figure 10: *Monopole at static (left) and M = 0.3 flight condition (right).*

It has to be pointed out that local flow accelerations around the airframe are not captured in this approach. Modeling these effects would require a ray tracing method at much increased complexity and computational cost. The diffraction integral framework used in the present approach offers high fidelity at high frequency and very low computational cost while capturing the bulk effects of mean flow.

To assess the effects of flight on shielding, a monopole source was placed on top of the N2A-EXTE airframe flying at M = 0.01 and M = 0.3. The difference in shielding compared to static conditions is plotted in Figure 11 below.

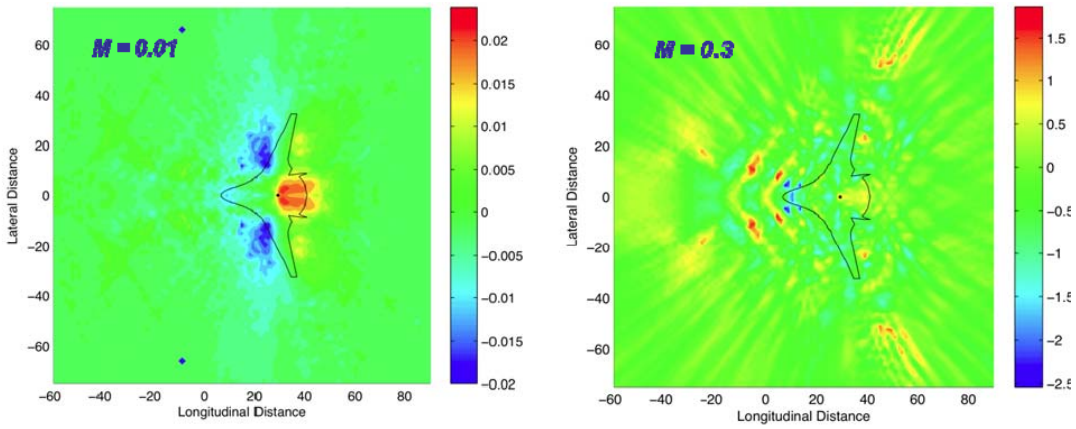

Figure 11: *Difference in shielding relative to static conditions for flight Mach number of M = 0.01 (left) and M = 0.3 (right) for monopole source.*

The results at M = 0.01 show relatively small insertion loss which can be shown to be consistent with an alternate approach using the transformation proposed by Taylor [11]. The Taylor transformation consists of computing the noise attenuation pattern in a time transformed domain where

$$T = t + \frac{M\Phi}{c_0} \tag{23}$$

and Φ is the potential of the mean flow

$$\vec{v}_\infty = \nabla\Phi \tag{24}$$

M and c_0 are the Mach number and speed of sound respectively. The advantage of this transformation is that the modified frequency in the transformed domain is equivalent to that in the original frame of reference, rending a more straightforward implementation.

The challenge is that Taylor's approach is limited to low Mach number and an in-depth analysis shows that it is equivalent to the first order term of the more general Prandtl-Glauert approach. More importantly this first order term scales with the reduced frequency times the square of the flight Mach number krM^2 further limiting the Taylor approach to yet smaller Mach numbers as the reduced frequency of interest is relatively high. For a flight Mach number of 0.3, Taylor's approach breaks down and the more general Prandtl-Glauert method shows that the flight effects can yield up to 3 dB difference in shielding compared to the static case as shown in Figure 11 on the right. In conclusion, the Prandtl-Glauert method was implemented in the diffraction integral shielding method and offers the assessment of flight effects over a relatively large range of Mach numbers. From a user perspective it is important to note that the method requires source data at the Doppler shifted 1/3-Octave band frequencies of the static source noise. This is described in Appendix B and implies that if the NPSS-WATE-ANOPP frame work is used to determine turbomachinery noise, the static source noise outputs must include these frequency shifts.

In summary, the improved integral shielding method yields three new capabilities: (1) a new diffraction integral solver (simpler and 40x faster compared to V1.0), (2) a source definition module that allows a more general source description (monopole, dipole and directional points source based on spheroidal wave functions using least-squares fits), and (3) the inclusion of flight effects based on the Prandtl-Glauert transformation. The V2.0 code and descriptions have been delivered to NASA LaRC for inclusion into ANOPP.

3. Aircraft Noise Assessment

The FAR36 noise assessment of the N2A-EXTE powered by two podded turbofan engines with fan pressure ratio 1.6 is discussed first. The potential noise benefit of different fan pressure ratio propulsion systems was also investigated and is presented at the end. In addition, a comparison of the final noise audit at fan pressure ratio 1.6 is given relative to the previous noise audit. In the final assessment, the turbomachinery shielding model based on the HELS directional point source and experimentally measured jet shielding results including chevrons and an external wedge are also included. With this, the N2A-EXTE configuration is estimated to meet the NASA N+2 noise goal with margin. The details are discussed in this section.

ANOPP-L28vMIT version was used for the final analysis and a summary of the noise source and shielding estimation methods is given in Table 1 below.

Noise Source	**Estimation Method**
Fan Forward	*ANOPP Heidmann Fan Module* *TREAT acoustic inlet liner increments* *DIM HELS directional point source shielding, flight effects*
Fan Rearward	*ANOPP Heidmann Fan Module* *TREAT acoustic fan duct liner increments* *DIM HELS directional point source shielding, flight effects*
Core	*ANOPP GE Core Module* *DIM HELS directional point source shielding, flight effects*
Jet	*ANOPP Stone 2 Jet Module* *UCI jet noise shielding*
Undercarriage	*Modified ANOPP Boeing Airframe Module for fairings* *Local Mach suppression based on CFD flow field results*
Elevon	*Outboard aileron model by Sen et al. [13]*
Airfoil (Wing)	*Physics based airfoil self-noise method (FW-Hall)*
Leading Edge Droop	*Droop effect on BL properties included in FW-Hall method* *Contribution of side edge not modeled*
Wing Tip	*Tip vortex noise model by Brooks and Marcolini*
Vertical Fins	*ANOPP Fink Airframe Module*

Table 1. *Summary of noise source and shielding estimation method.*

The landing gear noise estimate of the N2A-EXTE was updated using CFD flow field results available from Boeing to estimate the local flow Mach number around the nose and the main landing gear. The outboard aileron module by Sen et al. [13] was used to model elevon noise of the hybrid-wing body aircraft, since an update of the aileron module in ANOPP is not yet available. This model is currently being assessed and compared against conventional aircraft noise data. Due to this uncertainty and in order to give an upper and a lower bound on the overall FAR36 noise, the report includes results from audits conducted both with and without elevon noise. Jet noise shielding was included based on the N2A-EXTE experimental studies carried out by UCI. The nozzle was equipped with aggressive devices such as chevrons and a wedge that were essential in reducing the jet noise. Turbomachinery fan and core noise shielding was implemented through the diffraction integral shielding method (DIM) using the HELS representation of the Heidmann fan noise directivity. In addition, flight effects were included. This method was documented in the first section of this report.

3.1 FAR36 Assessment Procedure

The FAR 36 noise certification analysis was performed at International Standard Atmosphere (ISA) reference conditions +18F, 70% relative humidity, zero wind and at sea level.

The noise certification measurement locations are sideline, flyover and approach. These are shown in Figure 12. For sideline noise estimation, the observer is located at 450 m at sideline and at the point from brake release where peak sideline noise is encountered. For flyover noise estimation, the observer is located at 6,500 m from brake release on the runway centerline. For approach noise estimation, the observer is located 2,000 m from the runway threshold.

The overall noise level is measured in Effective Perceived Noise Level decibels (EPNdB) capturing the sound pressure level and accounting for tonal and duration effects on human perception of noisiness.

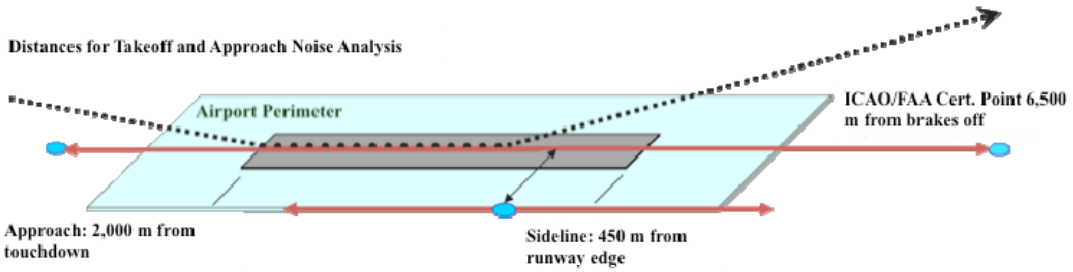

Figure 12: *FAR Part 36 noise measurement locations.*

3.2 N2A-EXTE FAR 36 Noise Audit at FPR = 1.6

The noise audit was first carried out for the N2A-EXTE aircraft configuration powered by two podded engines with fan pressure ratio1.6. The following assumptions and methods were used in the assessment:

1. Turbomachinery noise shielding based on DIM HELS directional point source definition using Heidmann fan directivity; flight effects included
2. Local Mach suppression of main and nose landing gear per Boeing CFD
3. Outboard aileron noise model by Sen et al. [13] for elevon noise
4. Sideline noise determined at peak noise location
5. Updated N2A-EXTE airframe aerodynamics for noise assessment purposes
6. Jet noise shielding data from UCI experimental studies on N2A-EXTE planform; nozzles equipped with aggressive chevrons and a wedge
7. Ground effects

Figure 13 depicts a three view of the N2A-EXTE configuration. Figures 14, 15 and 16 show the estimated noise histories for observers at sideline, flyover and approach conditions. Figure 17 summarizes the source noise breakdown for each certification location. For the case investigated the peak noise at sideline occurs for an aircraft altitude of 394 feet over the runway. At sideline, engine noise sources, mainly jet noise, are dominant. Based on this, sideline noise is expected to decrease when reducing the engine fan pressure ratio. The noise estimates for different fan pressure ratios are presented in a following section. At flyover both engine and airframe noise sources are dominant, especially jet noise and elevon noise. On approach airframe noise is the main noise contributor, mainly landing gear noise and elevon noise. The noise estimates at flyover and approach are considered an upper bound given the limitations and possible overestimation of the elevon noise model.

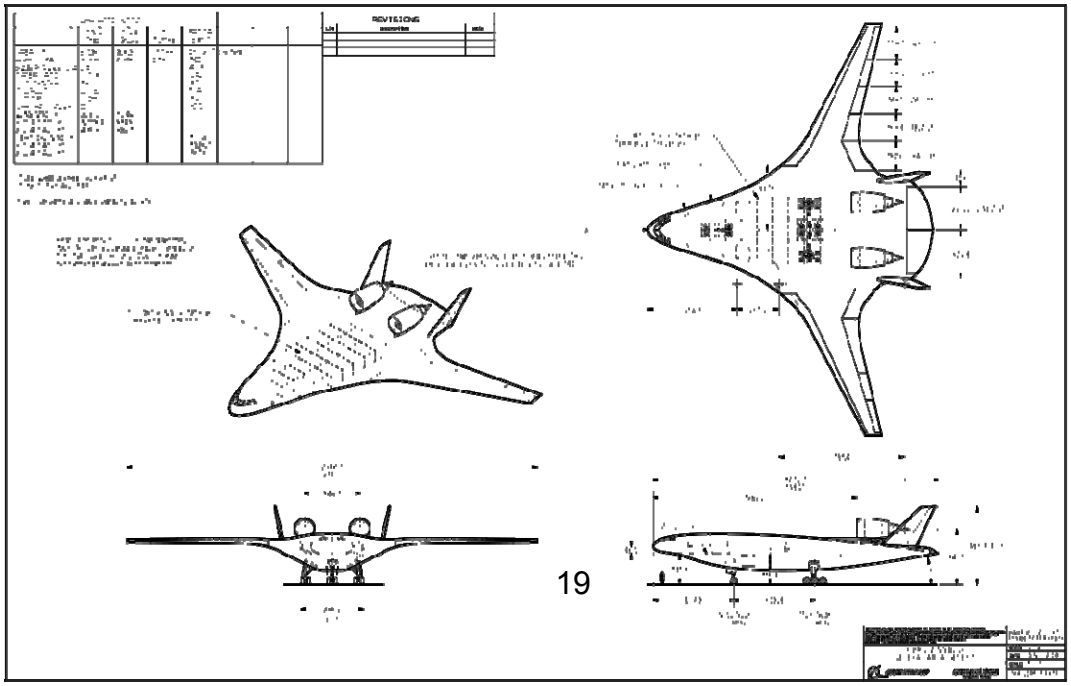

Figure 13. *Three view of the N2A-EXTE configuration.*

Table 2 summarizes the EPNL results, the cumulative noise and the N+2 noise goal. Given the uncertainties in the elevon noise model, the noise estimates are conducted for both cases, with and without elevon noise. This yields an upper and lower bound on the overall aircraft noise assessment with a difference of -6.7 EPNdB between the two cases.

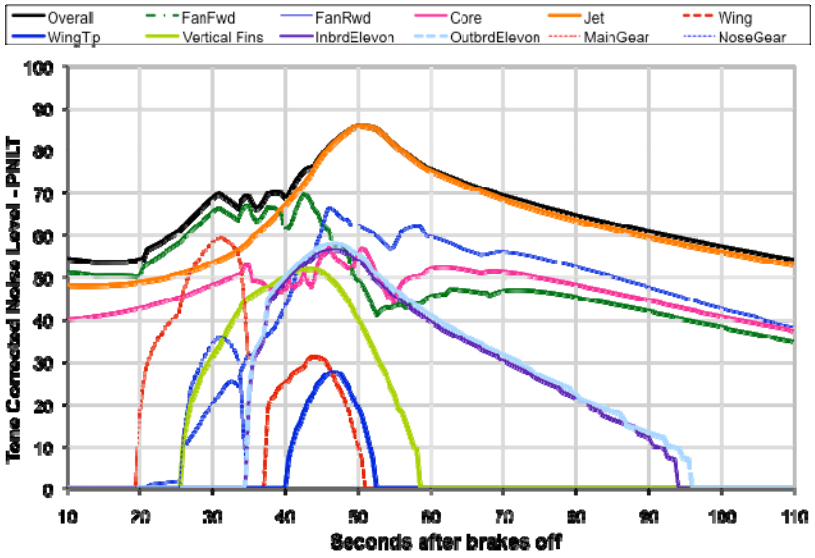

Figure 14. N2A-EXTE *FAR36 noise assessment at sideline observer location.*

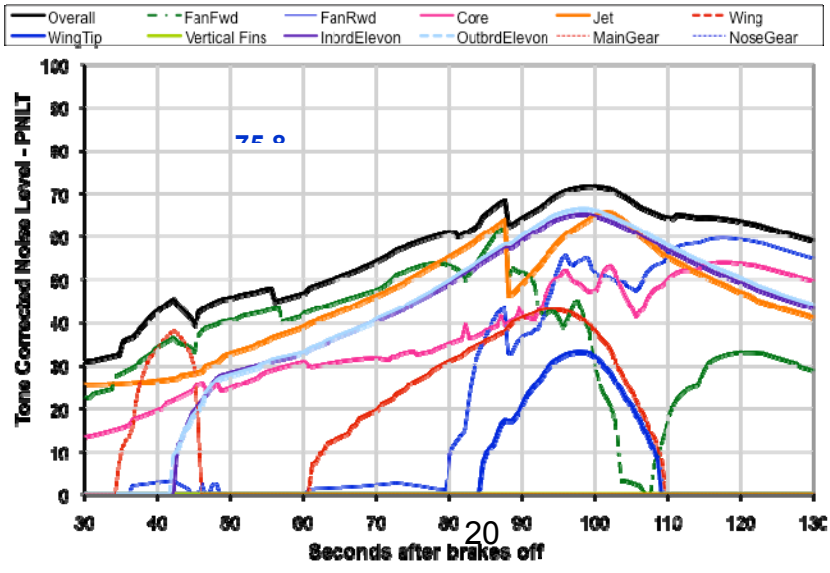

Figure 15. N2A-EXTE *FAR36 noise assessment at flyover observer location*

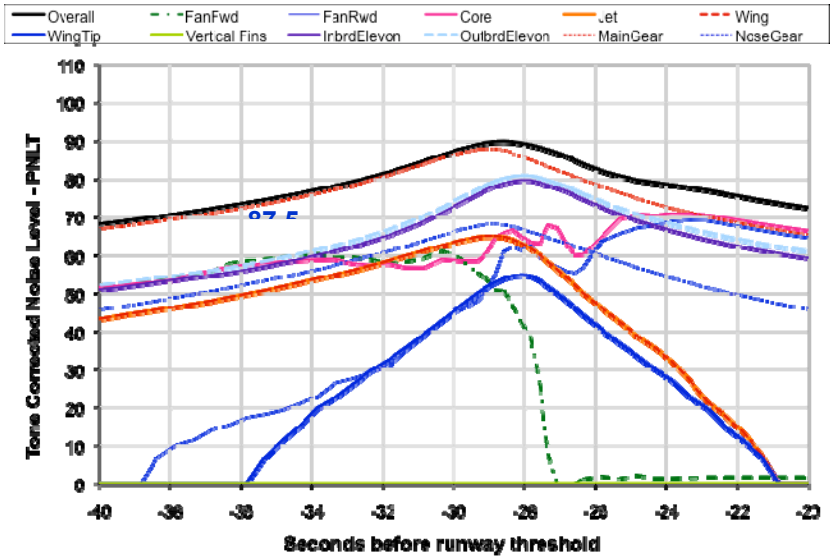

Figure 16. *FAR36 noise assessment at approach observer location*

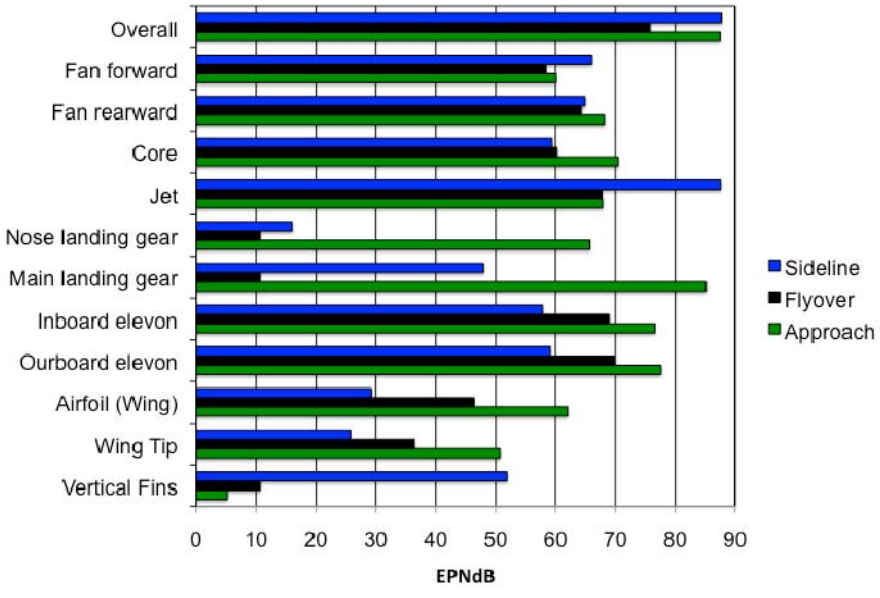

Figure 17. *Source noise breakdown for sideline, flyover and approach.*

Cumulative EPNdB with elevon noise (EPNdB)	251.0
Cumulative EPNdB without elevon noise (EPNdB)	244.3
N+2 Goal (EPNdB)	250.4
EPNdB Margin with elevon noise *(EPNdB)*	**+0.6**
EPNdB Margin without elevon noise *(EPNdB)*	**-6.1**

Table 2. *Summary of N2A-EXTE FAR-36 noise assessment.*

3.3 Comparison to Previous Noise Audits

To illustrate the evolution of the noise assessment and improvements in method fidelity, two noise audit comparisons are made. The noise audit results at the end of Phase I are briefly summarized first. Then, the noise estimates from the previous Phase II audit conducted in October 2010 for the NASA NRA review are compared with the final noise audit that includes all method improvements and updates made under Phase II.

3.3.1 Phase I Noise Audit Results

At the end of Phase I, the N2A noise estimates showed promise in meeting the NASA N+2 goal and were 5.3 EPNdB short of the goal. The sideline noise provided in Figure 18 had the most margin for improvement. The jet and fan rearward noise sources were 20 dB above the next loudest sources, core and fan forward noise. Since acoustic shielding and liners had already been applied to the engine noise sources, to further reduce engine noise, a lower FPR (1.4 or 1.5) engine was recommended.

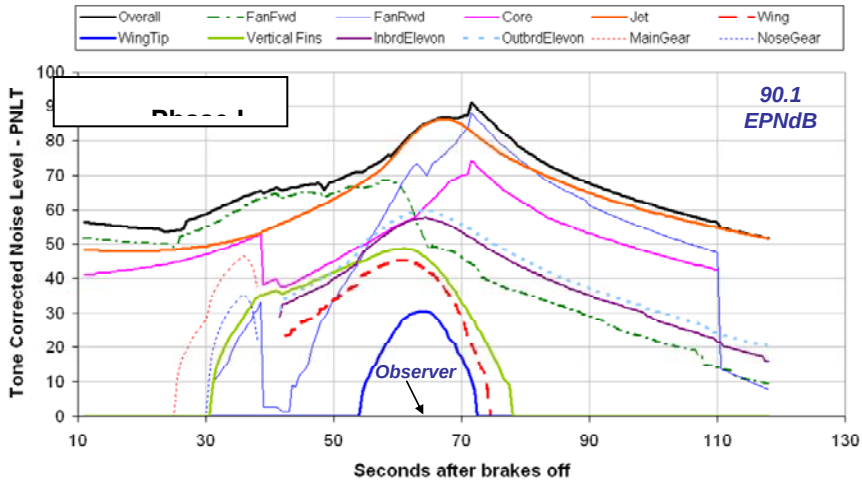

Figure 18: *Phase I N2A sideline PNLT and EPNdB estimates.*

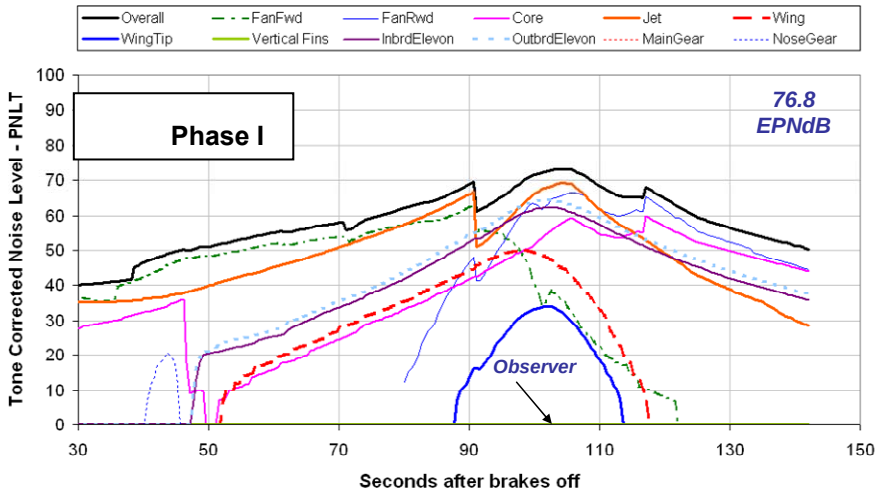

Figure 19: *Phase I N2A flyover PNLT and EPNdB estimates.*

The jet and fan rearward noise sources were also dominant in the flyover estimate shown in Figure 19. This motivated the improvement of jet and turbomachinery noise shielding assessment which were the key objectives in Phase II.

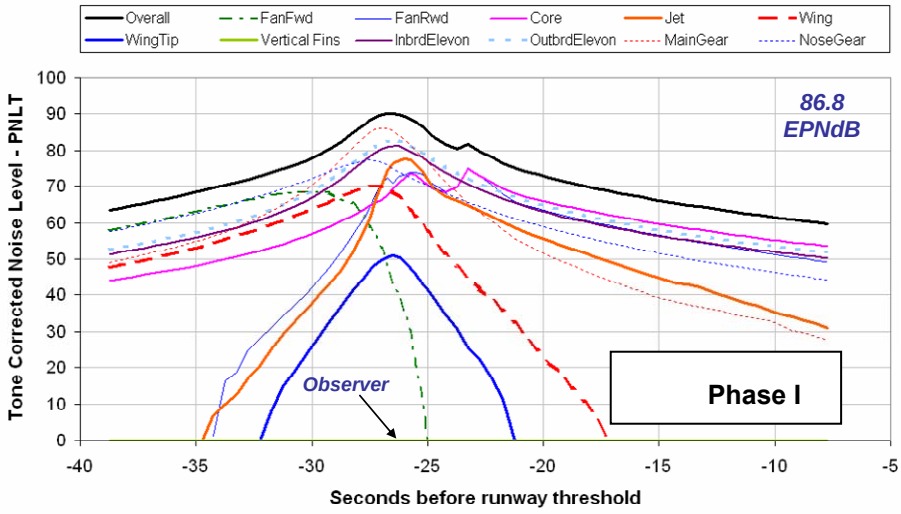

Figure 20: *Phase I N2A approach PNLT and EPNdB estimates.*

The main landing gear was the most dominant noise source on approach as depicted in Figure 20. The N2A configuration did not benefit from Mach suppression that most conventional aircraft experience. Fairings were utilized in this configuration which reduced their contribution by about 2.2 dB EPNL; however the benefit to the overall noise was less than 1 dB due to the jet and elevon noise levels. The Phase I N2A noise audit results are summarized and compared to the Phase II N2A-EXTE results in Table 3 below.

	Phase I – N2A	***Phase II – N2A-***

		EXTE
Sideline (EPNdB)	90.1	87.7
Flyover (EPNdB)	76.8	75.8
Approach (EPNdB)	86.8	87.5
Cumulative (EPNdB)	**253.8**	**251.0**
N+2 Noise Goal	**248.5**	**250.4**
EPNdB Margin	**-5.3**	**-0.6**

Table 3: *Phase I N2A and Phase II N2A EXTE noise audit results.*

Note that the noise goal of -42 dB below Stage 4 has slightly changed because of changes to the aircraft configuration. In summary, the fidelity of the noise assessment has been improved in the following key areas: (1) turbomachinery shielding method, (2) local Mach number effect of main and nose landing gear, (3) observer position for peak sideline noise estimation, and (4) jet noise shielding and nozzle design. These improvements are discussed in more detail below.

3.3.2 Preliminary Phase II N2A-EXTE Noise Audit Results

A preliminary Phase II noise audit was conducted in October 2010 and the results were presented at the final NRA review at NASA GRC. The final noise audit results are compared to these preliminary results to illustrate the changes. There were two key differences between the two audits. The DIM HELS turbomachinery noise shielding method was further improved by including flight effects. Also, for the final noise audit, the shielding results from the UCI experimental work for the N2A-EXTE were incorporated. These included nozzles with aggressive devices such as, chevrons and an external wedge[1].

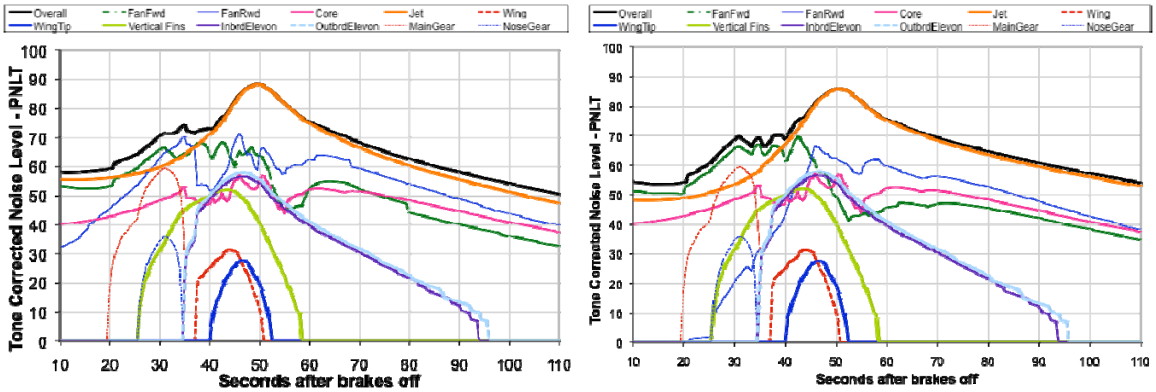

[1] The jet noise results presented at the Webex meeting on December 3, 2010 were amended and are updated here.

Figure 21. *Comparison of FAR36 noise assessment at sideline observer location for preliminiary N2A-EXTE noise audit (left) and final audit (right).*

Figures 21, 22 and 23 show the comparison between the two cases at sideline, flyover and approach.

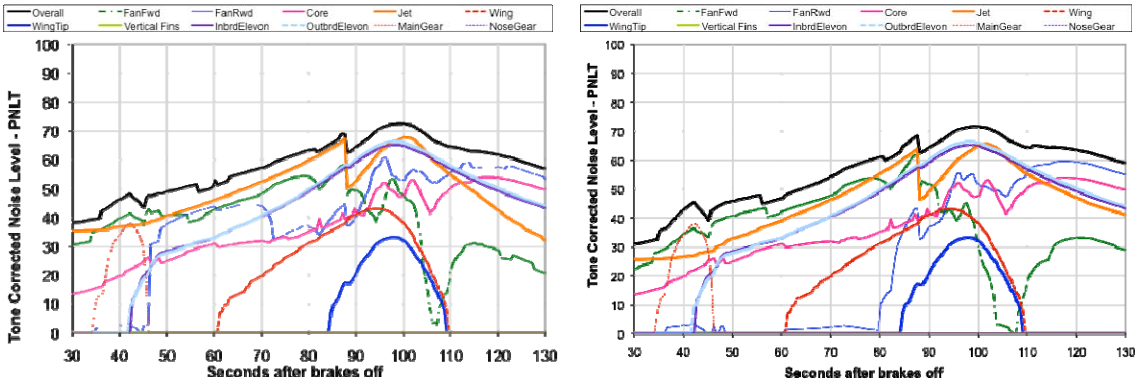

Figure 22. *Comparison of FAR36 noise assessment at flyover observer location for preliminary N2A-EXTE noise audit (left) and final audit (right).*

Table 4 shows the EPNL levels for the three certification points and the cumulative EPNL. The results show a decrease of 2.5 EPNdB in overall estimated noise. At sideline, there is a reduction of 1.9 EPNdB due to the improved of jet noise shielding with the N2A-EXTE platform and the implementation of aggressive nozzle devices. At flyover, the total noise level was only reduced by 0.6 EPNdB from 76.4 to 75.8 EPNdB although the jet noise was reduced by 2.7 EPNdB. This is due to the high levels of elevon noise at this observer location. At approach, there is no difference in noise because the airframe is the main noise source.

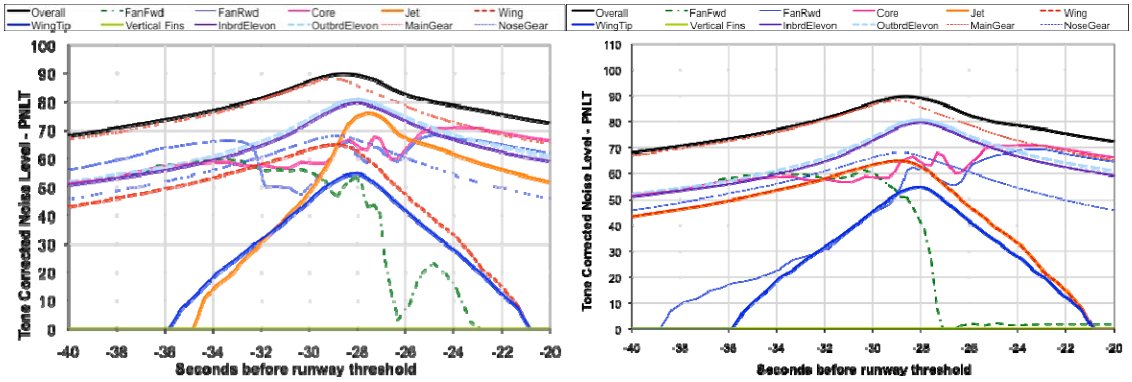

Figure 23. *Comparison of FAR36 noise assessment at approach observer location for preliminary N2A-EXTE noise audit (left) and final audit (right).*

N2A-EXTE	*DIM HELS without flight effect; N2A jet shielding data*	*DIM HELS with flight effects; jet shielding data with chevrons & wedge*
Sideline	89.6	87.7

(EPNdB)		
Flyover (EPNdB)	76.4	75.8
Approach (EPNdB)	87.5	87.5
***Cumulative** (EPNdB)*	**253.5**	**251.0**

Table 4. *N2A-EXTE noise comparison for FPR=1.6.*

3.4 Landing Gear Noise

The landing gear noise method in version ANOPP-v28MIT was used for the N2A-EXTE noise estimation. The model was updated using CFD flow field results available from Boeing to estimate the local flow Mach number around the nose and the main landing gear. The CFD results are shown in Figure 24. The nose landing gear Mach number is estimated to be around 0.9 of free stream Mach number while there is practically no Mach number suppression near the main landing gear. The results of the elevon and the nose and main landing gear noise for the N2A-EXTE configuration were compared to the experimental data reported by Rackl et al. [14] for a B767. This is shown in Figure 25. In general the trends are similar with the exception of the nose landing gear noise being quieter for the hybrid-wing body aircraft. This is conjectured to be due to the above mentioned local Mach number suppression.

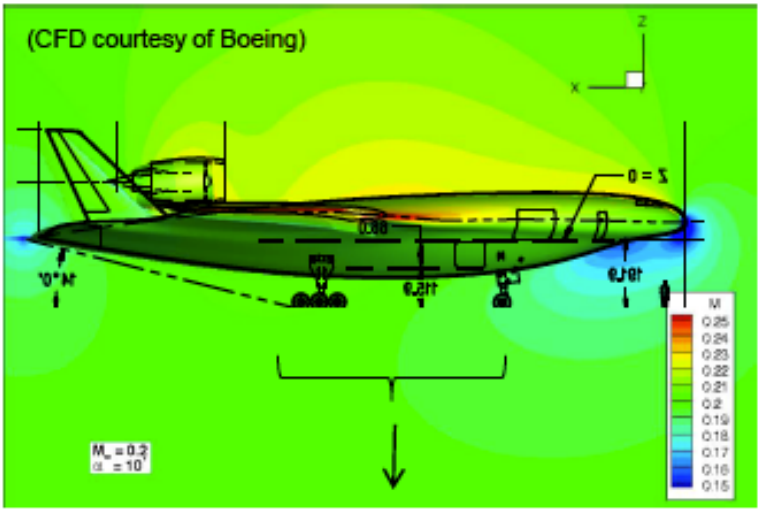

Figure 24. *Local flow Mach number results from CFD around N2A-EXTE.*

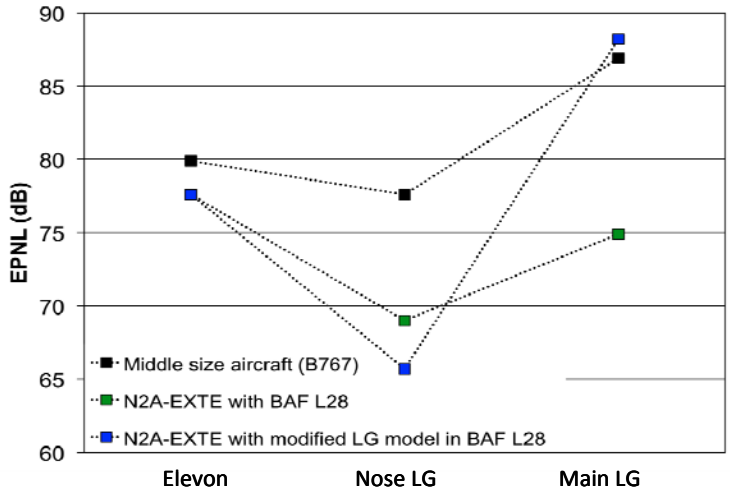

Figure 25. *Airframe component noise comparison at approach with ground effects, including local Mach suppression on landing gear; B767 data adopted from [14].*

3.5 Fan Pressure Ratio Sensitivity Study

A fan pressure ratio sensitivity study was carried out to investigate the potential noise reductions for lower fan pressure ratio propulsion systems.

Table 5 summarizes the key engine parameters and Figure 26 depicts the flight trajectories for the four fan pressure ratio cases investigated. The bypass ratio increases when decreasing the fan pressure ratio, as expected. The flight trajectories do not show significant differences between the four cases. Figures 27, 28 and 29 show the breakdown of the noise sources for the three certification points and the four fan pressure ratios investigated. The estimates include:

9. Turbomachinery noise shielding using DIM HELS directional point source definition based on Heidmann fan directivity; flight effects included

10. Local Mach suppression of main and nose landing gear

11. Outboard aileron noise model by Sen et al. [13] for elevon noise

12. Sideline noise determined at peak noise conditions

13. Updated N2A-EXTE airframe aerodynamics for noise assessment purposes

14. Jet noise shielding data from UCI experimental studies on N2A-EXTE; nozzles equipped with aggressive chevrons and a wedge

15. Ground effects

	FP R=1.4	*FP R=1.5*	*FP R=1.6*	*FP R=1.7*
BPR at Aerodynamic Design Point	20.5	15.5	12.3	10.1
OPR at Aerodynamic Design Point	36.6	29.1	27.8	26.8
Sea Level Static Thrust (klbs)	84.95	78.6	76.73	76.27
Cutback thrust (klbs)	27.30	26.67	26.57	26.65

Table 5. *N2A-EXTE engine parameters for four different fan pressure ratio cases.*

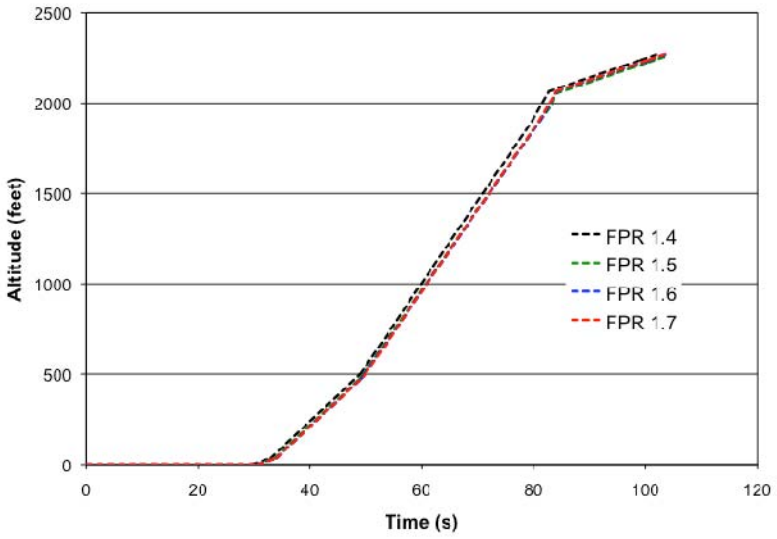

Figure 26. *Flight trajectory for the different fan pressure ratio cases.*

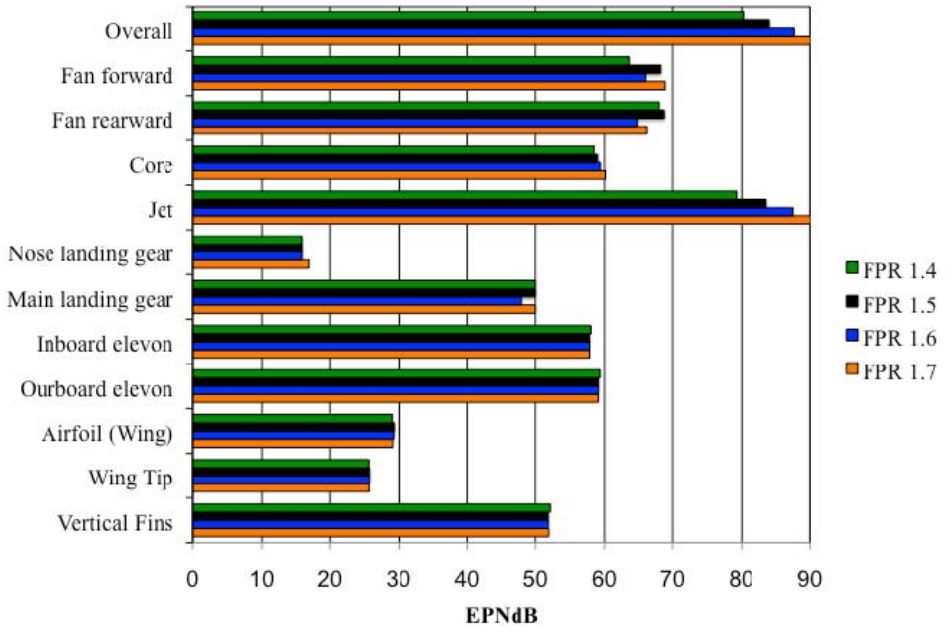

Figure 27. *Noise source breakdown at sideline for four fan pressure ratio cases.*

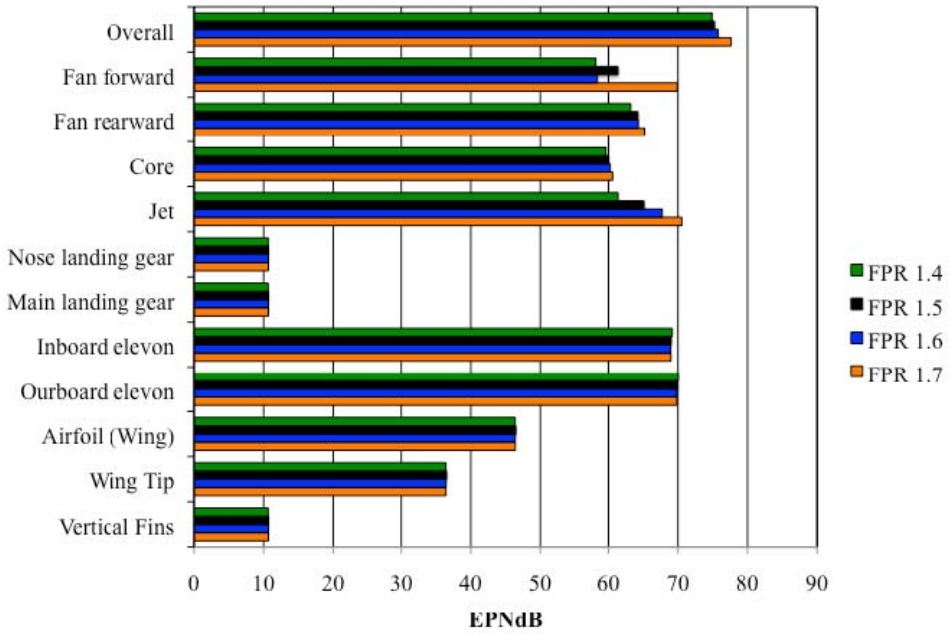

Figure 28. *Noise source breakdown at flyover for four fan pressure ratio cases.*

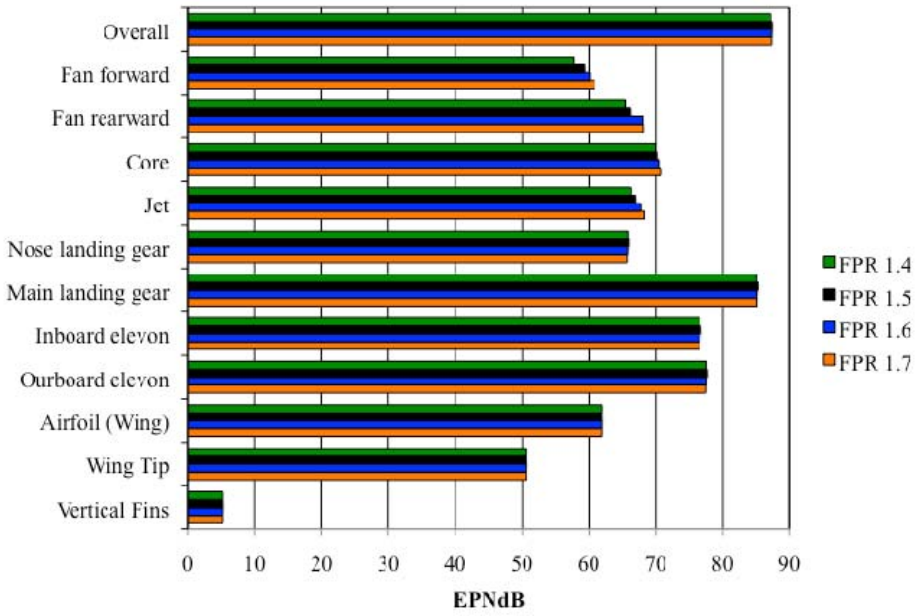

Figure 29. *Noise source breakdown at approach for four fan pressure ratio cases.*

Figure 30 shows the peak noise assessment at sideline observer location. The peak noise occurs at an aircraft altitude different from 1,000 ft. The 1,000 ft altitude, marked by the yellow dots, was used in previous noise audits based on a recommendation by Boeing guided by experience with conventional aircraft. The change in altitude is due to the change in aircraft configuration, changes in fan pressure ratio and in the flight trajectory. Table 6 shows a comparison of the sideline noise levels as well as the change in altitude. There is a difference of up to 2 EPNdB in sideline noise between peak noise and the previously used noise level at an altitude of 1,000 feet.

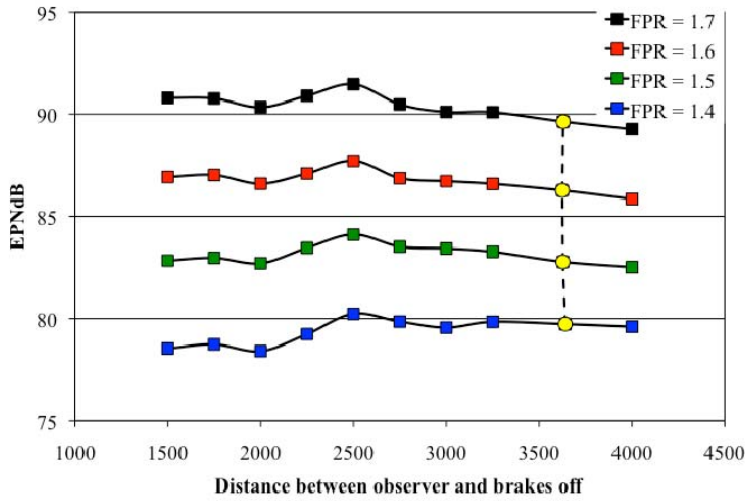

Figure 30. *Peak noise assessment at sideline observer locations.*

	FP R=1.4	*FP R=1.5*	*FP R=1.6*	*FP R=1.7*
Sideline noise at 1000 feet altitude	79.7	82.8	86.3	89.6
Sideline peak noise	80.2	84.1	87.7	91.4
Aircraft altitude at peak noise (ft)	393	395	394	392
Delta EPNdB	**+0.5**	**+1.3**	**+1.4**	**+1.8**

Table 6. *Comparison of sideline noise levels for different fan pressure ratios.*

Figure 31 summarizes the FAR36 noise levels at the three observer locations for the case with and without elevon noise. At sideline, the noise reduces significantly when decreasing the fan pressure ratio. Also, there is no effect when the elevon noise is suppressed. This is because the jet noise is the dominant source as can be observed in Figure 27. At flyover, there is also a reduction of the overall noise when the fan pressure ratio is decreased as jet noise together with the elevon noise are the dominant sources, as observed in Figure 28. As expected, there is a significant effect on flyover noise when the elevon noise is removed. Since airframe noise is the dominant noise source at approach, there is no effect on the overall noise when changing the fan pressure ratio. However, there is a reduction on the overall noise when suppressing elevon noise.

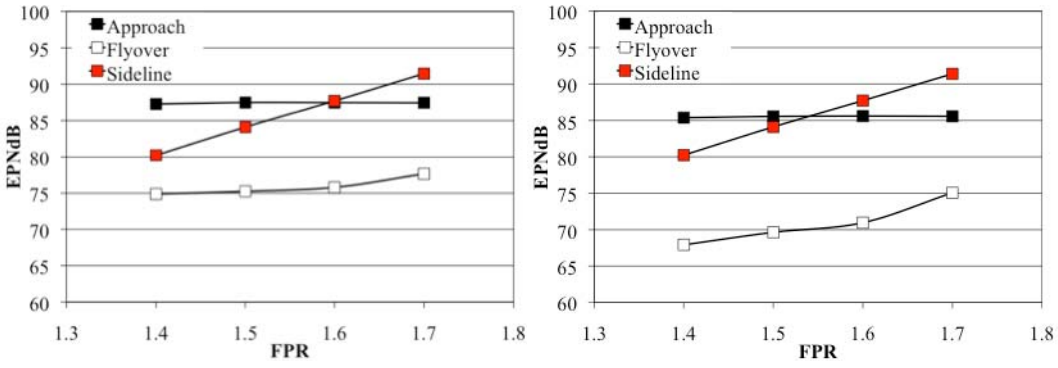

Figure 31. *Fan pressure ratio study with elevon noise (left) and without elevon noise (right).*

Table 7 summarizes the N2A-EXTE FAR-36 noise assessment for the four fan pressure ratio cases. The results suggest that, with a conservative estimate of elevon noise, the configurations with fan pressure ratio of 1.4 and 1.5 meet the N+2 noise goal, while a fan pressure ratio of 1.6 is just 0.6 EPNdB above the goal. For the optimistic scenario where elevon noise is below all other dominant noise source levels, the results suggest that all the configurations except the case for the fan pressure ratio of 1.7 can potentially meet the N+2 noise goal.

	FP R=1.4	*FP R=1.5*	*FP R=1.6*	*FP R=1.7*
Cumulative EPNdB with elevon noise	242.4	246.9	251.0	256.5
Cumulative EPNdB without elevon noise	233.5	239.3	244.3	252.0
N+2 Goal	250.7	250.4	250.4	250.4
EPNdB Margin with elevon noise	**-8.3**	**-3.5**	**+0.6**	**+6.1**
EPNdB Margin without elevon noise	**-17.2**	**-11.1**	**-6.1**	**+1.6**

Table 7: *N2A-EXTE FAR-36 noise assessment.*

4. Summary and Outlook

An improved fidelity turbomachinery shielding method compatible with ANOPP was developed and implemented. An algorithm was conceived to generate the shadow contour for any 3-D geometry, making it applicable to a wide variety of applications. To remedy shortcomings of the Maggi-Rubinowicz formulation, such as spurious singularities and limitation to monopole sources, a method was formulated borrowing ideas from geometrical optics. Using the Uniform Theory of Diffraction and a more general potential based on the framework described by Miyamoto and Wolf was derived, reducing the problem to Fresnel integrals which can be treated analytically. The improved shielding method dramatically reduces computational cost, avoids spurious singularities, and allows for general source definitions (such as for example dipole or directional point source formulations). In addition, flight effects were incorporated based on the Prandtl-Glauert transformation.

The new shielding methodology was tested for canonical geometries such as a sphere and a cylinder, and the shielding results were compared with data from literature and with NASA fast scattering code results. Good agreement was achieved and, using the established methodology, the shielding capability of various airframe configurations was assessed.

The FAR36 noise assessment was updated for the evolved N2A-EXTE aircraft configuration. Improved methods for airframe source noise, turbomachinary shielding and jet noise shielding were implemented and the noise audit was conducted for a range of fan pressure ratios. The results suggest that the NASA's N+2 noise goal can be met with a comfortable margin for a range of fan pressure ratios. With a conservative estimate of elevon noise, the configurations with FPR = 1.4 and FPR = 1.5 meet the N+2 noise goal with -8.3 and -3.5 dB margins respectively. It is likely that an improved elevon noise model will yield slightly reduced elevon noise levels potentially allowing the FPR = 1.6 configuration to also meet the target noise reduction. For the optimistic scenario where elevon noise is below all other dominant noise source levels, the results suggest that all configurations but the FPR = 1.7 case can potentially meet the noise goal.

The remaining challenges are jet noise at sideline, landing gear noise and elevon noise on approach. In order to further reduce these airframe noise sources aircraft operational changes such as reduced flight velocities and steeper glide-slopes but also noise reduction technologies need to be sought. In addition to further jet noise reduction studies, future research should focus on strategies to reduce landing gear noise and the development of an improved elevon noise assessment method. Finally, the experimental validation of the developed methods and new approaches is critical in the noise goal assessment. Experimental measurements on both the component and the aircraft system level need to be conducted.

References

[1] Lummer, M., "Maggi-Rubinowicz Diffraction Correction for Ray-Tracing Calculations of Engine Noise Shielding," AIAA-2008-3050, Vancouver, British Columbia Canada

[2] Miyamoto, K., Wolf, E., 'Generalization of the Maggi-Rubinowicz Theory of the Boundary Diffraction Wave - Part I', J. Opt. Soc. Am., June 1962, 6(52), pp 615-625.

[3] Miyamoto, K., Wolf, E., 'Generalization of the Maggi-Rubinowicz Theory of the Boundary Diffraction Wave - Part II', J. Opt. Soc. Am., June 1962, 6(52), pp 626-637.

[4] Ng, L., "Design and Acoustic Shielding Prediction of Hybrid Wing-Body Aircraft," MIT Master's thesis, department of Aeronautics and Astronautics, June 2009.

[5] Ng, L., Spakovszky, Z., "Turbomachinery Noise Shielding Assessment of Advanced Aircraft Configurations," AIAA paper 2010-3914 presented at the 16th AIAA/CEAS Aeroacoustics Conference (30th AIAA Aeroacoustics Conference), Stockholm, Sweden, June, 2010.

[6] Umul, Y. Z., 'Diffraction of evanescent plane waves by a resistive half-plane', J. Opt. Soc. Am., 10(24), October 2007, pp 3226-3232.

[7] Lewist, R. M., Boersma, J., 'Uniform Asymptotic Theory of Edge Diffraction', J. Math. Phys. 12(10), December 1969, pp 2291-2305.

[8] Umul, Y. Z., 'Equivalent functions for the Fresnel integral', Opt, Express, 21(13), October 2005, pp 8469-8482.

[9] Wang, Z., Wu, S. F., 'Helmholtz equation--least-squares method for reconstructing the acoustic pressure field', J. Acoust. Soc. Am., 4(192), October 1997, pp 2020-2032.

[10] Wu, S. F., Zhao, X., 'Combined Helmholtz equation–least squares method for reconstructing acoustic radiation from arbitrarily shaped objects', J. Acoust. Soc. Am. 2002 Jul, 112(1), pp 179-88.

[11] Taylor, K., 'A Transformation of the Acoustic Equation with Implications for Wind-Tunnel and Low-Speed Flight Tests', Proceedings of the Royal Society of London, Vol. 363, No. 1714 (Nov. 1, 1978), pp 271-281.

[12] Tinetti, A. F., Dunn, M. H., 'Aeroacoustic Noise Prediction Using the Fast Scattering Code', 11th AIAA/CEAS Aeroacoustics Conference (26th AIAA Aeroacoustics Conference), 23-25 May, Monterey, California, AIAA 2005-3061.

[13] Sen, R., Hardy, B., Yamamoto, K., Guo, Y., Miller, G.; Airframe Noise Sub-component Definition and Model, Boeing Commercial Airplane Company, NASA Contractor Informal Report, January 2000.

[14] Rackl, R. G., Miller, G., Guo, Y., Yamamoto, K.; Airframe Noise Studies: Review and Future Direction, Boeing Commercial Airplane Company, NASA Contractor Report, June 2005.

APPENDIX C

Hybrid Wing Body: Acoustic Test Planning
UTRC Phase II Summary Report: Task 4.2.3

In Support of NASA NNL07AA54C Phase II Contract:
Acoustic Prediction Methodology and Test Validation for an Efficient Low-Noise Hybrid Wing Body Subsonic Transport

Robert H. Schlinker and John C. Simonich

United Technologies Research Center

Hybrid Wing Body: Acoustic Test Planning
UTRC Phase II Summary Report: Task 4.2.3

In Support of NASA NNL07AA54C Phase II Contract:
Acoustic Prediction Methodology and Test Validation for an Efficient Low-Noise Hybrid Wing Body Subsonic Transport

Robert H. Schlinker and John C. Simonich

Summary

This report documents the development of test plans supporting the Hybrid Blended Wing Body (HWB) airframe shielding and airframe self-noise benchmark experiments to be conducted by NASA LRC using the 14x22 wind tunnel and a 1/16 scale airframe model with propulsion simulators representing the HWB podded engines. The test goals are to provide baseline data for: a) noise reduction by shielding, b) airframe noise contributions, and c) dual stream jet noise in addition to jet noise reduction concepts for the high bypass engine configuration selected for the HWB. New airframe engine-airframe shielding simulations being developed by NASA, MIT, and UCI as well as airframe noise models and jet noise models will be assessed and validated via the benchmark data. The current report evaluates these goals in the context of the requirements for facility hardware, airframe model, engine simulators, diagnostic instrumentation, microphone measurement stations, tunnel operating conditions, background noise, post-processing for validation of the simulation tools, and the 2012 test plan. Background details are reported in the 2009 UTRC Phase II Year 1 Summary Report for Task 4.2.3 in addition to a presentation package reported at the February 16 2010 ELNHWB Test Plan Review.

A. Primary Conclusions and Recommendations for 14x22 Tunnel Test

1. ***Select 14x22 tunnel forward flight speeds to maximize the ratio of source simulator-to-facility background noise when benchmarking BWB shielding characteristics with the impinging jet broadband source.***

   The aggressive shielding (20-35dB attenuation) may result in airframe attenuated noise levels below the tunnel background noise levels over most of the sideline and ceiling (ground plane) measurement domains available at forward flight conditions. The origin of this constraint is the impinging jet source strength which is insufficient for tunnel Mach numbers above 0.2. The impinging jet simulator acoustic source measurements acquired in the LRC SAJF facility (first reported at the August 7, 2009 ELNHWB WebEx) were combined with the static wing shielding predictions and then compared with the tunnel background noise levels (also reported by LRC) to determine the forward flight signal-to-noise ratio. Details are given in the 2009 UTRC Phase II Year 1 Summary Report for Task 4.2.3. The impinging jet source pressure has since increased somewhat and additional impinging jets are being added to the nacelle simulator suggesting that an updated analysis would be appropriate as the test plan is further developed. For jet noise shielding and source modification tests in the 14x22 facility, tunnel background limitations are not anticipated due to the dual stream jet noise simulators having sufficient acoustic output power. However, this should be confirmed prior to the test.

2. ***Conduct comprehensive static shielding mapping including sideline and forward panels to generate validation data bases for fan inlet noise in the transition region outside of the deep shadow regime on ceiling.***

   Since a key objective is to validate the shielding codes, it is recommended that microphone systems be installed to measure shielding in the forward and sideline directions. While the current NASA plan allows for measurements on the ceiling of the tunnel this region is in the deep shadow domain (20-35dB attenuation) and cannot be used to assess the progressive spatial transition from unshielded to full shielding. Measuring this transition is key to validating the overall shielding simulation methodology. A microphone system installed upstream of the model could be used to survey the shielded directivity pattern over the forward panel in the open jet test section of the tunnel. Mechanical implementation schemes have been discussed with NASA LRC. In the absence of such forward panel measurements, the ceiling survey will only provide shielding validation data in the deep shadow since this array maps a region approximately +/-45 degrees relative to a normal to the underside of the airframe model. At the +45 degrees in the forward direction (see Figure 2 in UTRC Phase II Year 1 Summary Report: Task4.2.3) airframe shielding has already decreased noise levels by over 20dB at the model scale BPF frequency (see Figure 28 of UTRC report). Validation of the transition region between 0dB

attenuation and 20dB attenuation would be lacking, hence, the recommendation of more comprehensive static shielding mapping. Characterization of the transition regime is just as critical as validating the shadow region since future designs may have milder shielding planforms with the engine sources located closer to the leading edge. A similar rationale applies for adding microphones in a sideline panel and aft panel.

3. ***Confirm the presence or absence of fine spatial detail in the diffraction field (peaks and valleys) using fine resolution spatial mapping/traversing during a subset of the impinging jet shielding measurements.***

Pretest predictions of shielding contours on the proposed measurement panels surrounding the airframe model demonstrated the presence of deep and narrow valleys in the spatially distributed shielding contours for the pure tone source models that are the basis of both the NASA and university codes. These predicted features are generated by interference between different discrete frequency diffracted propagation paths arriving at the far field microphone stations. Although such valleys are not currently expected in the experimental data when using the finite size impinging jet broadband source simulator, confirmation during a subset of the test plan is recommended. This check is motivated by the observation that time domain signals within 1/3 octave bands of the impinging jet source can be sufficiently coherent to generate cancellation among different diffracted paths arriving at each far field microphone station. If interference does exist, the overall plan to acquire acoustic data at fixed microphone stations should be reassessed since the measurement may be located within peaks and valleys.

4. ***Develop and validate a post-prediction frequency averaging scheme to allow comparing the computed discrete frequency shielding with the measured broadband impinging jet shielding.***

The fine spatial interference features described in Item 3 for the predictive methods may not be present in the shielded data generated with the broadband impinging jet source to be used in the 14x22 tunnel test. Validation of the simulation methods based on comparisons between predictions and measurements will then be complicated by the major peaks and valleys in the predictions. This complication exists irrespective of whether a monopole or multipole is used for the shielding prediction. The presence of inference features in the predictions suggests the need for a post-prediction processing scheme to remove the spatial interference effects. One approach involves averaging across large frequency bands (like 1/3 octave bands) at each microphone station in the spatial prediction. This approach smoothes the peaks and the valleys in the spatial domain similar to actually applying a spatial averaging scheme. The latter method could also be applied as demonstrated during the course of the current study, but, major features of the shielded

directivity pattern are not retained with a spatial averaging approach. The uniqueness of the frequency averaging results should be assessed by NASA LRC as the program continues in 2011.

5. Conduct selected discrete frequency static shielding test using a point source and fan tone simulator being developed as part of the canonical study being conducted by NASA GRC (Item 6).

In addition to the broadband impinging jet source, a scaled discrete frequency fan simulator is being developed by NASA GRC. Included in this effort is the development of a discrete frequency point source. It is recommended that LRC structure the 14x22 test plan to allow installation of the fan simulator and point source for a few selected test cases. The intent is to benchmark possible differences between airframe shielding based on broadband sources versus scaled BPF tones. The application of the point source will allow assessment of the fundamental point source premise in the simulation methods. The differences will be key to validation of the current diffraction/shielding simulation methods which are discrete frequency based. As noted in Item 5, the proposed comparisons will require addressing the spatially distributed peaks and valleys predicted by the simulations methods.

6. Conduct jet noise shielding and source modification tests at static conditions and include microphones stationed in an aft measurement plane to acquire directivity data beyond the PNLT directivity peak.

In the presence of tunnel flow aft jet noise directivity measurements will be limited by the 14x22 open jet shear layer restricting microphones to upstream stations outside of the turbulent shear layer. In this case, the resulting measurement stations are limited to angles upstream of the jet noise directivity peak. Tracking changes in the jet noise EPNL due to a) airframe shielding and b) chevron concepts proposed for shortening the jet source distribution will not be feasible. Hence, it is recommended that static jet noise shielding tests be conducted to acquire jet noise directivity data well beyond the PNLT directivity peak using microphones stationed in an aft measurement plane. It is recognized that the 14x22 tunnel does not currently have such a microphone survey system so this needs to be planned for. Concerns about the tunnel heating during static tests appear to be minimal based on the air exchange rate confirmed by NASA during the February 16 2010 ELNHWB Test Review.

B. Long Term Research Recommendations

1. Conduct a canonical experimental sensitivity study to assess the impact/importance of wing

leading edge radius on diffraction/shielding.

The influence of radius of curvature is not currently addressed in the MIT or UCI shielding codes. This technical issue, often designated as "creep," cannot be assessed during the 14x22 model scale test due to schedule and resource constraints. A canonical experimental sensitivity study has been recommended using a semi-infinite (approximately) barrier with a sharp edge and finite radius edge. A discrete frequency point source and a fan tone simulator are being developed as part of the study being conducted by NASA GRC.

2. Conduct a canonical experimental study to calibrate the directivity modification and shielding due

to HWB propulsor noise propagating through the airframe wake.

Schedule and resources will not allow a diagnostic test to calibrate these effects so a simplified test in the LRC open jet acoustic tunnel (QFF) is recommended to address this topic. Propagation through shear layers is known to modify far field directivity patterns and spectral shapes for discrete frequencies; hence, the proposed experiment could be conducted without interference to the mainline 14x22 tunnel test.

3. Develop and conduct an experimental sensitivity study directed at benchmarking the impact of

source wavefront coherence on diffraction/shielding.

The shielding methodologies developed for the HWB program currently assume spatial coherence over the acoustic wavefronts. This constraint does not replicate broadband fan sources or jet noise sources. Discrete frequency fan tones generated on actual engines will also have phase shifts between different modes at the fan inlet or exit plane. These physics based details will require future experimental assessment and updates to the current shielding simulation methods to properly account for these effects. It is recommended that tracking of the far field microphone spatial coherence be included in the test plan as a first step to interpreting the prediction versus measurement comparisons during post-test data analysis. Presumably, all microphone signals will be stored simultaneously in the time domain allowing coherence comparisons across the microphone stations.

C. Test Plan

1. Test Phases

During Phase 2 of the study, UTRC developed a detailed test matrix representing the primary goals of the program, the test requirements, and the test implementation framework. The goals and test requirements can be summarized as: 1)benchmark the Boeing HWB noise characteristics at the system level providing directivity and spectra, 2) determine the HWB EPNL

values, 3) validate the shielding simulation models for fan and jet noise, 4) evaluate shielding based noise reduction strategies such as using the aircraft verticals, 5) validate jet noise source modification and reduction concepts, 6) document the control surface and landing gear noise for validation of source self-noise models, and 7) provide benchmark data sets for ANOPP2. It is assumed that the microphone measurement configurations cited in the earlier Primary Conclusions & Recommendations Section, and discussed in detail during the February 2010 ELNHWB Test Plan Review, would be implemented to achieve these goals and meet the test requirements.

Acoustic tests addressing these specific goals must track the noise generation in different categories and configurations consisting of: 1) the individual propulsor/simulator component noise and airframe component noise, 2) the shielded simulator noise, and 3) the airframe system noise:

Component noise

- Fan simulator noise (inlet and exhaust)
- Jet simulator noise
- Control surface noise
- Landing gear noise

Shielded noise

- Installed fan or jet simulator noise
- Simulator location (Ex: dual stream jet location)
- Component location (Ex: vertical location)
- Airframe orientation (baseline, 30deg roll)

System noise

- Take-off
- Cut-back
- Approach

The test matrix must also recognize major hardware changes between the various acoustic tests cited above. Since shielding of the HWB propulsion component noise is essentially a transfer function applied to the isolated propulsor, the fan and jet simulator noise characteristics must first be documented in the absence of the airframe. Such tests would be conducted at static and forward flight conditions with the tunnel velocities selected to match, as a minimum, the takeoff, cutback, and approach aircraft Mach numbers as well as the angle of attack. These tests would be followed by installation of the airframe integrated with the fan or jet simulators. The delta between the isolated propulsor and the integrated system noise represents the attenuation due to shielding. Validation of the shielding computational methodologies can then be

conducted using the attenuation data while projection of the system noise levels to FAR36 conditions will provide EPNL levels.

The test sequence needed to conduct the shielding measurements is shown in **Figure S1** where configuration changes between a) to d) represent a natural progression of the hardware buildup. However, due to the multiday installation/conversion effort between major configurations, it is critical that the propulsor source characteristics (spectrum, directivity, SPL, and acoustic output power) be repeatable as the test progresses. To obtain accurate shielding validation data, source modification results, and high fidelity EPNL projections the simulator characteristic must be repeatable to within a few tenths of a dB as the test progresses from a) to d).

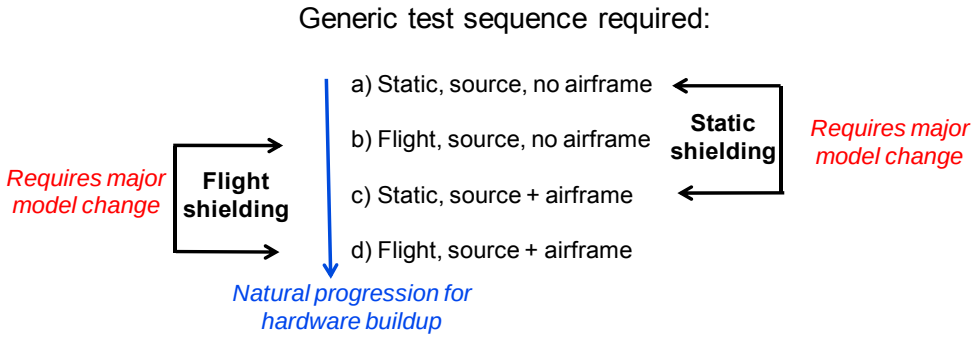

Figure S1: Generic Test Sequence

Combining the above requirements produces the test matrix shown in the **Table S1** below for which the key test parameters are specified in the columns.

Objective	Mach Number, M	Airframe Installed	Alpha: Airframe or Isolated Source	Roll: Airframe or Isolated Source	Leading Edge Config	Elevon angle	Vertical Installed	Vertical Axial Station	Vertical cant angle	Gear	Fan Inlet Axial Station	Fan Exit Axial Station	Fan 1&2 State	Jet Axial Station	Jet1&2 State	Cycle	Nozzle geometry
Static & flight; isolated fan	3 (0, 0.17, 0.22)	no	1 (0 deg)	1 (0 deg)	none	none	none	none	none	none	3	2	3	none	none	none	none
Static & flight; isolated round jet	3 (0, 0.17, 0.22)	no	1 (0 deg)	1 (0 deg)	none	none	none	none	none	none	none	none	none	1	3	3; takeoff, cutback, approach	round
Static & flight; isolated concept jet	3 (0, 0.17, 0.22)	no	1 (0 deg)	1 (0 deg)	none	none	none	none	none	none	none	none	none	1	3	3; takeoff, cutback, approach	2; chev, wedge
Static & flight shielding: fan & airframe	3 (0, 0.17, 0.22)	yes	1 (0 deg)	1 (0 deg)	1 (down)	1 (+10)	2 (out, in)	1	1 (80deg)	none	3	2	3	none	none	none	none
Static & flight shielding; round jet & airframe	3 (0, 0.17, 0.22)	yes	1 (0 deg)	1 (0 deg)	1 (down)	1 (+10)	2 (out, in)	1	1 (80deg)	none	none	none	none	1	3	3; takeoff, cutback, approach	round
Static & flight shielding; concept jet & airframe	3 (0, 0.17, 0.22)	yes	1 (0 deg)	1 (0 deg)	1 (down)	1 (+10)	2 (out, in)	1	1 (80deg)	none	none	none	none	1	3	3; takeoff, cutback, approach	2; chev, wedge
Airframe noise due to dual stream jet plume inter with elevons	1 (0.22)	yes	2 (0, 11.2 deg)	1 (0 deg)	2 (down, up)	3; (0, +10, +20)	none	none	none	none	none	none	none	1	1 (both jets on)	3; takeoff, cutback, approach	2; round, chev
Airframe noise due to LE controls; BL interactions with pylon & verticals, BL & wake interactions with TE, pylon & vertical self noise	2 (0.17, 0.22)	yes	2 (0, 11.2 deg)	1 (0 deg)	2 (down, up)	3; (0, +10, +20)	1	1	1 (80deg)	none	none	none	none	1	1 (match tunnel vel, temp)	1 (match tunnel vel, temp)	round
Airframe noise due to LE controls; BL interactions with TE	2 (0.17, 0.22)	yes	2 (0, 11.2, deg)	1 (0 deg)	2 (down, up)	5; (0, +10, +20, +/-10 split, +/-20 split)	none	none	none	none	none	none	none	none	none	none	none
Airframe noise due to BL, gear, gear wake interaction with TE, TE noise	2 (0.17, 0.22)	yes	2 (0, 11.2 deg)	1 (0 deg)	1 (up)	3; (0, -10, -20)	none	none	none	yes	none	none	none	none	none	none	none
Fan state: When using 2 fan simulators, each fan should run independently and then combined to understand shielding interference effects; total of 3 test points																	
Jet state: similar to fan state																	

Table S1: HWB Acoustic Test Matrix for LRC 14x22 Wind Tunnel: full parameter listing

The different test configuration groupings in the first column represent the sequential build-up of the hardware as proposed in **Figure S1.** The remaining columns contain the test parameters or components that are to be evaluated within the test group.

Table S1 is a comprehensive test matrix allowing for all possible combinations of parameters initially considered by the NASA, university, and industry team. The large number of test conditions is expected to exceed the test window and resources available for the 14x22 wind tunnel test. The next step to creating a feasible run plan is to prioritize the test parameters based on their impact on the system noise as well as key validation data required from the test. To facilitate the prioritization, each of the test parameters is discussed below after which subset test matrices will be defined focusing on fan noise shielding, jet noise shielding, jet noise reduction, and airframe self -noise.

2. Key Parameters

- **Wind tunnel Mach number, Mn**

  Values considered for this parameter span Mn=0, 0.17, 0.22 and possibly one higher value. Here the Mn=0.22 corresponds approximately to the aircraft velocity at takeoff, cutback, and approach.

  Mn=0 is a priority test condition since the primary shielding validation is recommended for static condition where comprehensive directivity patterns can be measured in the forward, ceiling, side, and aft panels. For the broadband impinging jet source representing fan noise sources, testing at Mn > 0.17 may encounter a low source-to-facility background noise ratio based on analyses presented later in this report. Hence, for the impinging jet propulsor simulator, Mn=0 & 0.17 are anticipated to be feasible for validating shielding.

  It is recognized that the Mn=0 & 0.17 test conditions do not emulate the Mn=0.22 flight speed expected at the FAR 36 noise certification measurement locations for the HWB. But, the impact of forward flight on shielding has been shown by the MIT simulations to be on the order of 1-2 dB so that testing at Mn< 0.22 provides representative validation. A similar rationale could be used to forgo the Mn=0.17 case and limit testing to strictly the static condition if the test plan requires aggressive paring. If the NASA GRC fan tone simulator and discrete frequency point source were tested in conjunction with the HWB model, the low acoustic output power expected from these simulators definitely suggests limiting testing to just static conditions.

  In the case of jet noise shielding and jet noise reduction via various forced mixing concepts, Mn=0, 0.17, & 0.22 are critical to establishing the effect of forward flight on the jet noise source mechanisms in the presence of the airframe. The sensitivity to flight effects is known to be significant based on semi-empirical scaling laws. When documenting airframe noise mechanisms (control surface or landing gear noise) forward flight is again key to the generation mechanism itself. In this case Mn=0.17 & 0.22 are recommended.

  In summary, forward flight is critical to the jet noise shielding and jet noise source reduction studies as well as benchmarking the airframe noise mechanisms which leads to testing at Mn=0.17 & 0.22. But, for fan noise shielding studies, conducted with the broadband impinging jet source and possibly the fan tone simulator, the low acoustic power generated by these sources, and the resulting signal-to-noise shortfall, may potentially limit testing to Mn=0 and Mn=0.17.

- **Airframe**

  Since shielding of the HWB propulsion component noise is essentially a transfer function applied to the isolated propulsor, the fan and jet simulator noise characteristics must first be documented in the absence of the airframe. These tests would be followed by installation of the airframe integrated with the fan or jet simulators. The delta between the isolated propulsor and the integrated system noise represents the attenuation due to shielding. Validation of the shielding computational methodologies can then be conducted using the attenuation data while projection of the system noise levels to FAR36 conditions will provide EPNL levels.

When benchmarking the airframe system and component noise, specific test conditions are noted in various columns of **Table S1.** These will be explained progressively in the discussion below.

- **Alpha: body angle of attack for airframe system/component noise and airframe shielding**

The airframe body angle of attack (alpha) relative to the flight path (or to the relative wind direction—see **Figure S2**) is the key parameter to track in the 14x22 wind tunnel when conducting airframe system or airframe component noise measurements. For the takeoff condition, alpha is approximately 11.6 deg after ground clearance occurs based on a Boeing tabulation of operating conditions specified in July, 2010. The angle increases to approximately 12.1 deg for a short time at the start of cutback and returns to 11.6 deg near the end of cutback. For the approach condition, alpha is approximately 10.8 deg after accounting for the -3 deg glide slope. These angles may change progressively as the HWB configuration evolves between NASA and Boeing.

To simplify airframe noise testing and avoid resetting alpha for each operating condition, it is suggested that the airframe angle of attack for takeoff, cutback, and approach be set at the average of the take off and approach conditions. This leads to alpha=11.2 deg for airframe noise testing. Other simplifications for the alpha angle selection are possible and can be pursued by NASA as the HWB operational characteristics evolve over time. It should be recognized that, in terms of the tunnel coordinates, the relative wind direction is aligned with the tunnel centerline.

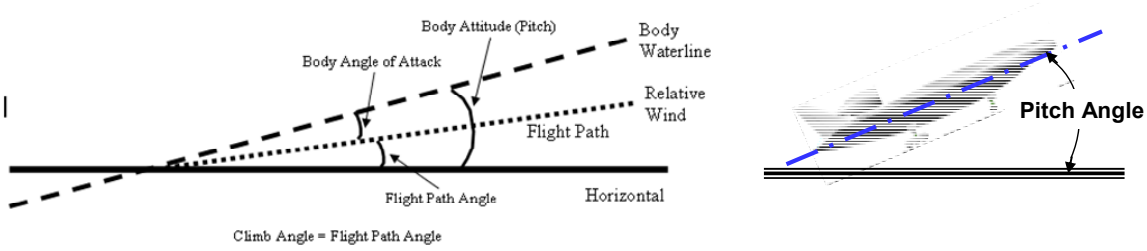

Figure S2: Airframe and flight path angles of attack

To broaden the airframe data base, it is recommended that airframe noise be measured at a second angle of attack corresponding to alpha=0 deg. This will allow monitoring how changes in the airframe boundary layer influence the turbulence interaction noise generated at the downstream landing gear, engine pylon, and the wing trailing edge control surfaces.

Once the airframe angle of attack is set, the polar angle location of the wind tunnel microphones can be designated relative to the airframe body water line for each operating condition. Since the microphone locations in the tunnel are expressed as polar angles referenced to the tunnel centerline translations between the different coordinate systems will be required. If

specific microphones are to be located at the FAR 36 stations, then the airframe water line reference would be used. In general, determining the microphone locations requires a 3 dimensional vector calculation since the microphones can be displaced laterally.

Due to the refraction of sound wavefronts while propagation through the 14x22 wind tunnel open jet shear layer the directivity pattern measured at the fixed microphone stations must be projected to the moving aircraft coordinate system. Refraction predictions can be used during post processing of data to correctly designate the microphone locations after which the aircraft directivity pattern can be constructed in terms of the emission angle.

When conducting airframe shielding measurements in the 14x22, the polar angle of the microphones relative to the water line is the primary parameter to track during the shielded directivity pattern measurement. In this case the aircraft angle of attack is not a direct controlling parameter. To simplify the testing, it is suggested that the sequence of isolated propulsor simulator followed by the shielded propulsor in **Figure S1** be conducted at alpha =0 deg. The airframe attenuation, based on the difference between these two configurations, can then be determined by subtracting the measured sound pressure levels at the same polar angles referenced to the aircraft waterline. These measurements can be then be translated to other angles, such at the aircraft emission angle, by accounting for the aircraft pitch angle. Refraction predictions can be used to track the attenuation pattern in the presence of forward flight in the wind tunnel.

Airframe shielding measurements are not recommended at non-zero alpha such as the alpha = 11.2 deg average angle suggested earlier for measuring airframe noise. While such measurements can be feasibly conducted in the tunnel and, thereby, avoid having to change angle of attack between airframe noise tests (11.2 deg) and airframe shielding tests (0 deg), the propulsion simulators would not be operating in a consistent flow field. For example, when testing the airframe + impinging jet simulator the local flow approaching the nacelle is aligned with the nacelle centerline based on engine-airframe integration criteria cited by Boeing. This results in zero incidence angle at the nacelle inlet, even though the airframe is at an angle of attack given by alpha=11.2 deg. Similarly, the dual stream exhaust nozzle centerline is aligned approximately with the local flow over the airframe. This suggests that when testing the isolated simulators, their angle of attack should be alpha=0 deg so as to align the tunnel flow with the centerline of the impinging jet nacelle or the dual stream jet, thereby, avoiding erroneous flow incidence angles. Hence, to maintain consistent approach flow conditions between the airframe + simulator configuration and the isolated simulator airframe shielding tests should be conducted at alpha = 0 deg.

The ability to actually achieve the approach and flyover measurement stations when benchmarking the HWB airframe shielding characteristics is dependent on conducting static directivity measurements with microphones located in a measurement plane forward of the airframe. The ceiling phased array will not be capable of measuring these stations even at static conditions. This led to the earlier recommendation to develop a microphone survey system for measuring the isolated propulsor (impinging jet nacelle or the discrete frequency fan simulator) and the airframe + propulsor in a plane forward of the airframe. Details supporting the inability of the ceiling array to measure the unshielded and shielded levels at the approach and flyovers stations are presented later in this report. For the sideline certification location, microphones

will be required on a side panel in the 14x22 tunnel. One approach being considered by LRC is installation of microphones on a possible gantry system which would translate axially outside of the tunnel flow and parallel to tunnel centerline.

- **Roll: roll angle for airframe or source**

Airframe roll angle is not a parameter in the FAR 36 certification. In this case, roll is a test option to augment the sideline microphone survey range beyond the side view available with the ceiling microphone array. By rotating the airframe through 30 deg, the ceiling phased array can measure sideline radiated noise over an additional 30 deg viewing angle. Sideline augmentation improves the shielding validation range associated with fan reward radiated noise and jet noise both of which peak outside of the ceiling panel measurement domain. This is based on a PNL tracing scheme developed during the current study to determine where rays from the aircraft-to-flyover observers intersect a virtual box surrounding the model scale airframe. Virtual test section panels represent the inlet, ceiling, sideline, and aft sections of the "box" surrounding the airframe. While the conclusions from these analyses suggest the need to rotate the airframe model, the conversion from 0 deg to 30 deg roll is a manual changeover in the 14x22 tunnel which may consume considerable test time. Also, the roll angle would be required for both the airframe+source and the isolated source to obtain the delta corresponding to this rotated shielding configuration. This becomes a complicated geometry set-up. Thus, it is suggested that the rotation not be applied and instead microphones be located on a possible gantry system for the sideline shielding measurements. Hence, roll=0 deg in the shielding test matrix.

The same recommendation for roll = 0 deg applies during airframe noise testing. The use of sideline microphones on a possible gantry can be used to measure landing gear noise instead of rolling the aircraft. Roll could be instituted as shielding and airframe component noise is pursued in follow-on studies beyond the 2012 test.

- **Leading edge configuration: airframe leading edge position (up or down)**

The HWB wing leading edge position is in the down orientation for the takeoff, sideline, and approach measurement conditions on the HWB. This configuration should be replicated on the 14x22 scale model during shielding validation measurements since the leading edge position determines the radius of curvature that the acoustic wavefronts encounter at the wing diffracting edge.

In the case of airframe noise tests, the leading edge orientation influences the pressure and suction side wing boundary layer development downstream. The boundary layer interacts with the landing gear on the pressure side generating turbulence interaction noise. On the suction side, the boundary layer interacts with the engine mounting pylon and more importantly, the wing trailing edge. The latter can produce significant trailing edge noise. Thus, the leading edge down position should be configured during the airframe noise benchmark testing. In addition, it is recommended that the up position be tested to broaden the interaction noise and trailing edge noise data base for future validations of simulation methods for these noise mechanisms. If the test plan requires aggressive paring the proposed up position could be skipped since it is not an operating configuration associated with FAR 36 certification conditions.

- **Elevon angle: angle for wing trailing edge elevon control surface**

The current elevon angle for the three FAR 36 certification conditions is +10 deg on the HWB. Boeing and NASA are considering using a split elevon during the approach condition to increase airframe drag resulting in a split/two piece elevon configuration with simultaneous +/- 10 deg to possibly +/- 20 deg. Such a split elevon configuration is expected to be noisy; hence, the test plan should include a subset of this geometry as a special case. Finally, the nacelle exhaust plume from the dual stream jet impinges on the elevons when deflected at +10 or +20. This could create an intense noise source. For this reason, jet-elevon interaction is a configuration during the airframe noise test.

- **Verticals: vertical control surface absent or installed**

The verticals have been shown by UCI to provide a jet noise shielding benefit; hence, it is recommended that the test plan include uninstalled and installed configurations. These surfaces are not expected to be effective for fan exit noise shielding as will be determined by the use of the impinging jet and possibly the fan tone simulator.

The verticals are potential turbulence interaction noise sites given the interaction of the wing boundary layer and the base of the vertical. However, the noise radiation pattern would be primarily lateral which would not reach the ground observer. Also, the turbulent wakes from the verticals are candidates for interaction with the wing trailing edge. However, these contributions would be spatially limited to a small section of the airframe trailing edge and qualitatively weak. The rudder deflection on the verticals is not considered a noise sources, hence, rudder position is not a parameter.

Vertical self noise generated at the trailing edge and side edge remains as a potential noise source. This series of noise sites on the vertical suggest that this component be included as a singular case in the test plan.

- **Vertical station: vertical control surface installation location on the wing planform**

To simplify the shielding test matrix, only one installation station is recommended for the vertical control surfaces. This will provide a data point for the jet noise shielding/reduction assessment and validation of the vertical shielding simulation prediction. The test can be conducted at static operating conditions to facilitate the set-up and changeover between no vertical and the proposed vertical installation station. The station is controlled primarily by the aircraft stability and control requirements so there is only minimal variability in the station options. A second station is optional and could be used to simulate fan exit plane shielding.

- **Vertical dihedral angle: vertical control surface angle**

Dihedral angle on the vertical has been a weak parameter so a single angle of ~80 deg is recommended based on UCI testing.

- **Gear: installed and uninstalled landing gear**

During approach, airframe noise is expected to be dominated by landing gear noise radiation, hence, landing gear retracted (not installed) and installed are two configurations that are critical to benchmarking the airframe noise.

In addition, subset diagnostic test are recommended during the installed case to evaluate the noise dependence on key subcomponents in the landing gear system. Such experiments are

best planned by NASA once the model scale landing gear is fabricated allowing evaluation and planning of key experiments. The objective in these additional tests would be to identify possible landing gear noise reduction strategies for the eventual HWB aircraft system. If the test schedule does not allow such additional experiments, it is possible that NASA could evaluate the landing gear system in the LRC QFF if the system fits into the open jet test section of the facility. This would avoid additions to the 14x22 test plan.

- **Fan Inlet Axial Station: location of impinging jet nacelle or discrete frequency fan simulator**

The fan simulators are used to benchmark airframe shielding and generate validation data for the various shielding methodologies. Multiple simulator mounting stations have been planned by NASA and Boeing with the option to orient the source either upstream or downstream in the 14x22 wind tunnel by alternately capping the ends of the nacelle. For the fan inlet noise shielding tests with the aft end of the nacelle capped, one station should correspond to the HWB nacelle inlet plane with two additional stations located further forward. While the actual HWB aircraft stability and control constraints will not allow such forward engine installations, the intent here is to benchmark the shielding dependence on source location and validate the airframe attenuation models across a broad range of engine locations. This objective is motivated by NASA's goal to develop a generic shielding model applicable to airframe geometries beyond the specific HWB engine locations being tested here.

It should be noted that whatever fan simulator stations are selected, noise measurements must be conducted at these stations with the isolated simulator at alpha=0 deg and with the airframe+ source at alpha=0 deg. This applies to static or forward flight. Shielding at each far field microphone station is then based on the delta between these two configurations.

- **Fan Exit Axial Station: location of impinging jet nacelle or discrete frequency fan simulator**

For fan exit noise shielding tests with the forward end of the nacelle capped, one station should emulate the actual HWB nacelle fan exit plane location. An additional station could be located further upstream to again provide a broad benchmarking of noise dependence on source location, although the current test plan only includes one exit plane station.

While the above fan inlet and exit simulator mounting stations suggest different stations the test schedule constraints may inhibit source testing at all of these stations if manual relocation is required to change stations. If the location change could be remotely controlled, then the five stations could be easily retained in the test plan. The choice of test points will be a local decision by NASA based on the pace at which model changes can be made in the 14x22 facility. Information on impinging jet or fan tone simulator model change over time was not available to UTRC or Boeing to allow down selecting the test configurations in this case.

As already noted for the fan inlet noise source locations, for each fan exit plane station selected, noise measurements must be conducted at alpha=0 deg for both the isolated simulator and the airframe+ simulator. This again applies to static or forward flight.

- **Fan 1&2 State: Fans 1 and 2 off/on status**

NASA is considering installation of two impinging jet nacelles to simulate the fan noise sources on the actual HWB aircraft for shielding assessment. Each source will generate its own diffraction interference pattern at a far field microphone which could have maxima and minima in the spectrum due to interference between different propagation paths diffracting to the same far field station. This follows from the discrete frequency monopole and multipole simulation model analyses conducted as part of the current study which demonstrated peaks and deep valleys for a singular source. It might be argued that individual broadband impinging sources will have minimal wavefront coherence so that interference between different diffracted propagation paths from the same source will be minimal; hence, there would be no maxima and minima. However, interference clearly occurs since wing shielding is aggressive and the shielding itself is diffraction and interference path dependent.

In addition, the dipole like directivity pattern of the impinging jet results in different directional "wavefront strengths" arriving at the same wing leading edge station from each source. This is based on the propagation path being different between each source and any common wing "edge point." Diffraction and scattering characteristics of the wavefronts at the common edge point will, therefore, be different when propagating towards the same far field microphone station. Hence, one cannot assume that the far field microphone station senses the same diffracted and scattered acoustic field from each of the individual sources.

Based on the above diffraction based physics, it is recommended that frequency dependent interference and individual scattered directivity be anticipated with the test plan structured to assess the presence or absence of these features. Frequency dependent interference will clearly be present if the two fan tone simulators being developed by NASA GRC are used in the test program.

Given these observations the impinging jet nacelles or fan tone simulators would be operated first as individual sources. This would allow validating the individual shielding predictions as each source-to-far field propagation path is different and the interference (or lack of interference) between these paths should not be assumed in advance. Once the individual contributions are recorded, then the two simulators can be operated simultaneously. This latter step will confirm or reject whether the contributions from the individual sources add linearly in the spectrum at each far field microphone station given the different diffraction paths. Also, this will confirm the ability to represent the individual source directivity pattern scattering and radiation to the far field microphone station. sequence is given by the following three (3) fan simulator "states":

i) Fan simulator 1 operational, fan 2 off
ii) Fan simulator 2 operational, fan 1 off
iii) Fan simulator 1 & 2 operational

- **Jet Axial Station: location of dual stream jet simulator**

For jet noise shielding, in addition to jet noise reduction testing, the range of nozzle exit plane axial stations is limited due to aircraft stability and control limitations on the engine installation location. Hence, only one or two stations are recommended. One station should emulate the current HWB nozzle exit plane location while a second station could be shifted

upstream by an additional nozzle diameter. Displacement of at least one diameter is necessary to impact the wing trailing edge shielding effectiveness. Smaller displacements have been shown analytically to be insensitive to changing the far field shielding as reported by UCI. Currently, the test plan includes only one axial station because of the weak sensitivity to axial location.

As already noted for the fan inlet/exit noise source locations, whatever jet exit plane stations are selected, noise measurements must be conducted at these stations with the isolated simulator at alpha=0 deg and with the airframe+ source at alpha=0 deg. This again applies to static or forward flight. Shielding at each far field microphone station is then based on the delta between these two configurations.

- **Jet 1&2 State: Dual stream jet 1 & 2 off/on state**

  Arguments similar the fan state discussion given above also apply to the jet on/off conditions. However, the broadband nature of the jet sources in addition to the large distributed source region reduces the possibility of any frequency based interference. On the other hand, the different directivity patterns incident at the wing edge point followed by diffraction and scattering does warrant assessment of the ability to represent these details. Hence, the following sequence of testing is recommended to minimize risk and confirm the operative physics:

  i) Jet simulator 1 operational, simulator 2 off
  ii) Jet simulator 2 operational, simulator 1 off
  iii) Jet simulator 1 & 2 operational

- **Cycle: Impinging jet pressure ratio and dual stream jet 1& 2 fan and core pressure & temperature conditions controlling the engine cycle**

  When using the impinging jet to calibrate airframe shielding only one pressure ratio is expected to be used, probably the highest pressure corresponding to the maximum acoustic output power of the system. This pressure ratio is designated as a "cycle point" in the test matrix when using the fan simulator. Similarly for the fan tone simulator one operating point/cycle point is expected although this device is not currently accounted for in the test matrix since it is not clear if it will be added to the 14x22 test plan. At most, the fan tone simulator would be used for shielding studies at static conditions since the acoustic output power is expected to be too weak compared to the tunnel background noise.

  To document the HWB jet noise contribution at the FAR 36 conditions will require setting the takeoff and cutback engine cycle conditions. Approach conditions are not considered since the jet noise is minimum in this case. Other fan/core pressure and temperature ratios are recommended, if feasible within the test plan, to provide generic jet noise sensitivity data as a function of nozzle operating condition and the various jet noise reduction concepts. Such additional conditions have not been included in the test plan presented here to minimize the number of data points. Additional data points are best selected by NASA during 2011 test planning.

  To diagnose the airframe noise associated with the airframe boundary layer/engine pylon interaction it is recommended that the dual stream nozzle fan and core velocities are set to match the tunnel free stream velocity during the airframe noise tests. This procedure will eliminate any jet noise contributions. This procedure will include a quantification of the pylon wake/trailing edge interaction noise. The ability to distinguish these sources, which are expected to be weak, will require the ceiling mounted phased array to spatially dissect the sources sites.

- **Nozzle geometry: Dual stream fan and core nozzle geometry**

The jet noise study is directed at both shielding and jet noise reduction concepts, the latter being based on nozzle modifications designed to rapidly mix the fan/core streams to achieve jet source reduction. Included in the rapid mixing is a second phenomenon: reduction of the axial extent of the jet source distribution. Decreasing the extent shifts the sources further upstream of the HWB wing trailing edge allowing more effective shielding. These multiple benefits will be tested in the 14x22 tunnel.

Two jet modification schemes have been successfully demonstrated by UCI: 1) aggressive chevrons and 2) an aggressive wedge. These schemes could also be combined to create a 3rd configuration. The sequence of testing becomes:

i) Baseline round nozzle
ii) Chevron nozzle
iii) Wedge nozzle
iv) Combined chevron + wedge

It is recommended that the down selection of configurations for testing be determined by direct measurements or prediction of thrust loss to assess the aircraft system level impact. The measurements could be conducted using larger scale nozzles combined with a balance system. At this time, these steps have not been completed so the proposed nozzle geometries are tentative. To minimize risk, concept iv) is not included in the **Table S1** test plan.

D. Subset Test Plans

The above described key parameters can now be assigned to subsets of the overall test matrix shown in Table S1 to provide a more detailed breakout leading to a test plan which NASA can extract from in response to the test window and resources that will be available in 2012. Included in the subset matrices are estimates of the number of test/data points. This provides visibility into where test configurations and data points must be pared to fit the test plan into the test window. The subset matrices presented below have reduced test conditions based on prioritizing the original overall test matrix with all parameters in **Table S1.**

1. Fan Noise Shielding Test Matrix

Config	Objective	Mach Number M	Airframe Installed	Alpha: Airframe or Isolated Source	Roll: Airframe or Isolated Source	Leading Edge Config	Elevon angle	Vertical Installed	Vertical Axial Station	Vertical Cant Angle	Gear	Fan Inlet Axial Station	Fan Exit Axial Station	Fan 1 & 2 State	Jet Axial Station	Jet 1 & 2 State	Cycle	Nozzle geometry	# Data Points
1	Isolated fan inlet, static	1 (0)	no	1 (0 deg)	1 (0 deg)	none	none	none	none	none	none	3	none	3	none	none	1	None	9
1	Isolated fan inlet, flight	1 (0.17)	no	1 (0 deg)	1 (0 deg)	none	none	none	none	none	none	3	none	3	none	none	1	None	9
2	Isolated fan exhaust, static	1 (0)	no	1 (0 deg)	1 (0 deg)	none	none	none	none	none	none	none	1	3	none	none	1	None	3
2	Isolated fan exhaust, flight	1 (0.17)	no	1 (0 deg)	1 (0 deg)	none	none	none	none	none	none	none	1	3	none	none	1	None	3
1a	Shielded fan inlet: static	1 (0)	yes	1 (0 deg)	1 (0 deg)	1 (down)	1 (+10)	2 (out, in)	1	1 (80 deg)	none	3	none	3	none	none	1	None	18
1a	Shielded fan inlet: flight	1 (0.17)	yes	1 (0 deg)	1 (0 deg)	1 (down)	1 (+10)	2 (out, in)	1	1 (80 deg)	none	3	none	3	none	none	1	None	18
2a	Shielded fan exhaust: static	1 (0)	yes	1 (0 deg)	1 (0 deg)	1 (down)	2 (+10, +20)	2 (out, in)	1	1 (80 deg)	none	none	1	3	none	none	1	None	12
2a	Shielded fan exhaust: flight	1 (0.17)	yes	1 (0 deg)	1 (0 deg)	1 (down)	2 (+10, +20)	2 (out, in)	1	1 (80 deg)	none	none	1	3	none	none	1	None	12
Fan state: When using 2 fan simulators, each fan should run independently and then combined to understand shielding interference effects; total of 3 test points when determining data points																			

2. Jet Noise Shielding and Jet Noise Reduction Test Matrix

Config	Objective	Mach Number M	Airframe Installed	Alpha: Airframe or Isolated Source	Roll: Airframe or Isolated Source	Leading Edge Config	Elevon angle	Vertical Installed	Vertical Axial Station	Vertical Cant Angle	Gear	Fan Inlet Axial Station	Fan Exit Axial Station	Fan 1&2 State	Jet Axial Station	Jet 1&2 State	Cycle	Nozzle geometry	# Data Points
3	Isolated round jet; static	1 (0)	no	1 (0 deg)	1 (0 deg)	none	none	none	none	none	none	none	none	none	2	3	2 (takeoff, cutback)	round	12
3	Isolated round jet; flight	2 (0.17,0.22)	no	1 (0 deg)	1 (0 deg)	none	none	none	none	none	none	none	none	none	2	3	2 (takeoff, cutback)	round	12
3a	Shielded round jet; static	1 (0)	yes	1 (0 deg)	1 (0 deg)	1 (down)	2 (+10, +20)	2 (out, in)	1	1	none	none	none	none	2	3	2 (takeoff, cutback)	round	24
3a	Shielded round jet; flight	2 (0.17,0.22)	yes	1 (0 deg)	1 (0 deg)	1 (down)	2 (+10, +20)	2 (out, in)	1	1	none	none	none	none	2	3	2 (takeoff, cutback)	round	24
4	Isolated chevron jet; static	1 (0)	no	1 (0 deg)	1 (0 deg)	none	none	none	none	none	none	none	none	none	2	3	2 (takeoff, cutback)	chevron	12
4	Isolated chevron jet; flight	2 (0.17,0.22)	no	1 (0 deg)	1 (0 deg)	none	none	none	none	none	none	none	none	none	2	3	2 (takeoff, cutback)	chevron	12
4a	Shielded chevron jet; static	1 (0)	yes	1 (0 deg)	1 (0 deg)	1 (down)	2 (+10, +20)	2 (out, in)	1	1 (80 deg)	no	none	none	none	2	3	2 (takeoff, cutback)	chevron	24
4a	Shielded chevron jet; flight	2 (0.17,0.22)	yes	1 (0 deg)	1 (0 deg)	1 (down)	2 (+10, +20)	2 (out, in)	1	1 (80 deg)	no	none	none	none	2	3	2 (takeoff, cutback)	chevron	24
5	Isolated wedge jet; static	1 (0)	no	1 (0 deg)	1 (0 deg)	none	none	none	none	none	none	none	none	none	2	3	2 (takeoff, cutback)	wedge	12
5	Isolated wedge jet; flight	2 (0.17,0.22)	no	1 (0 deg)	1 (0 deg)	none	none	none	none	none	none	none	none	none	2	3	2 (takeoff, cutback)	wedge	12
5a	Shielded wedge jet; static	1 (0)	yes	1 (0 deg)	1 (0 deg)	1 (down)	2 (+10, +40)	2 (out, in)	1	1 (80 deg)	no	none	none	none	2	3	2 (takeoff, cutback)	wedge	24
5a	Shielded wedge jet; flight	2 (0.17,0.22)	yes	1 (0 deg)	1 (0 deg)	1 (down)	2 (+10, +40)	2 (out, in)	1	1 (80 deg)	no	none	none	none	2	3	2 (takeoff, cutback)	wedge	24
Jet state: When using 2 jet simulators, each jet should run independently and then combined to understand shielding interference effects; total of 3 test points when determining data points																			

3. Airframe Noise Benchmarking Test Matrix

Objective	Mach Number, M	Airframe Installed	Alpha: Airframe or Isolated Source	Roll: Airframe or Isolated Source	Leading Edge Config	Elevon angle	Vertical Installed	Vertical Axial Station	Vertical Cant Angle	Gear	Fan Inlet Axial Station	Fan Exit Axial Station	Fan 1&2 State	Jet Axial Station	Jet 1&2 State	Cycle	Nozzle geometry	# Data Points
Airframe noise due to dual stream jet plume inter with elevons	1 (0.22)	yes	1 (0, deg)	1 (0 deg)	1 (down)	3; (0, +10, +20)	none	none	none	none	none	none	none	1	1 (both jets on)	2 (takeoff, approach)	2 (round, chev)	12
a) Leading edge control noise; b)wing side edge noise; c) BL interaction with pylon; d) pylon self noise	2 (0.17, 0.22)	yes	2 (0, 11.2 deg)	1 (0 deg)	1 (down)	1 (0 deg)	none	none	none	none	none	none	none	1	1 (match tunnel vel, temp)	1 (match tunnel vel, temp)	round	4
a) Leading edge control noise; b)wing side edge noise; c) pylon wake inter with TE; d) BL interaction with TE	2 (0.17, 0.22)	yes	1 (0 deg)	1 (0 deg)	1 (down)	3; (0, +10, +20)	none	none	none	none	none	none	none	1	1 (match tunnel vel, temp)	1 (match tunnel vel, temp)	round	6
a) Leading edge control noise; b)wing side edge noise; c) BL interaction with vertical; d) vertical self noise	2 (0.17, 0.22)	yes	2 (0, 11.2 deg)	1 (0 deg)	1 (down)	1 (0 deg)	1	1	1 (80 deg)	none	none	none	none	none	none	none	none	4
a) Leading edge control noise; b)wing side edge noise; c) vertical wake inter with TE; e) BL interaction with TE	2 (0.17, 0.22)	yes	1 (0 deg)	1 (0 deg)	1 (down)	3; (0, +10, +20)	1	1	1 (80 deg)	none	none	none	none	none	none	none	none	6
a) Leading edge control noise; b)wing side edge noise; c) BL interaction with TE	2 (0.17, 0.22)	yes	1 (0 deg)	1 (0 deg)	1 (down)	5; (0, +10, +20, +/-10 split, +/-20 split)	none	none	none	none	none	none	none	none	none	none	none	10
a) Leading edge control noise; b) BL interaction with gear; c) gear noise;	2 (0.17, 0.22)	yes	2 (0, 11.2 deg)	1 (0 deg)	1 (down)	1 (0 deg)	none	none	none	yes	none	none	none	none	none	none	none	4
a) Leading edge control noise; b)wing side edge noise; c) gear wake interaction with TE; d) BL interaction with TE	2 (0.17, 0.22)	yes	1 (0 deg)	1 (0 deg)	1 (down)	3; (0, -10, -20)	none	none	none	yes	none	none	none	none	none	none	none	6

REPORT DOCUMENTATION PAGE	*Form Approved OMB No. 0704-0188*

1. AGENCY USE ONLY (*Leave blank*)	2. REPORT DATE	3. REPORT TYPE AND DATES COVERED NASA Contractor Report

4. TITLE AND SUBTITLE Acoustic Prediction Methodology and Test Validation for an Efficient Low-Noise Hybrid Wing Body Subsonic Transport	5. FUNDING NUMBERS
6. AUTHOR(S) Kawai, R.	NASA Contract Number NNL07AA54C
7. PERFORMING ORGANIZATION NAME(S) AND ADDRESS(ES) The Boeing Company, Huntington Beach, CA	8. PERFORMING ORGANIZATION REPORT NUMBER
9. SPONSORING/MONITORING AGENCY NAME(S) AND ADDRESS(ES) National Aeronautics and Space Administration Langley Research Center Hampton, VA	10. SPONSORING/MONITORING AGENCY REPORT NUMBER

11. SUPPLEMENTARY NOTES

12a. DISTRIBUTION/AVAILABILITY STATEMENT Unclassified - Unlimited Subject Category Distribution: Nonstandard Availability: NASA CASI (301) 621-0390	12b. DISTRIBUTION CODE

13. **ABSTRACT** *(Maximum 200 words)*

This investigation was conducted to: (1) Develop a hybrid wing body subsonic transport configuration with noise prediction methods to meet the circa 2007 NASA Subsonic Fixed Wing (SFW) N+2 noise goal of -52 dB cum relative to FAR 36 Stage 3 (-42 dB cum re: Stage 4) while achieving a -25% fuel burned compared to current transports (re :B737/B767); (2) Develop improved noise prediction methods for ANOPP2 for use in predicting FAR 36 noise; (3) Design and fabricate a wind tunnel model for testing in the LaRC 14 x 22 ft low speed wind tunnel to validate noise predictions and determine low speed aero characteristics for a efficient low noise Hybrid Wing Body configuration.. A medium wide body cargo freighter was selected to represent a logical need for an initial operational capability in the 2020 time frame. The Efficient Low Noise Hybrid Wing Body (ELNHWB) configuration N2A-EXTE was evolved meeting the circa 2007 NRA N+2 fuel burn and noise goals. The noise estimates were made using improvements in jet noise shielding and noise shielding prediction methods developed by UC Irvine and MIT. From this the Quiet Ultra Integrated Efficient Test Research Aircraft #1 (QUIET-R1) 5.8% wind tunnel model was designed and fabricated.

14. SUBJECT TERMS Hybrid Wing Body, Fuel Efficient Low Noise Hybrid Wing Body	15. NUMBER OF PAGES
	16. PRICE CODE

17. SECURITY CLASSIFICATION OF REPORT	18. SECURITY CLASSIFICATION OF THIS PAGE	19. SECURITY CLASSIFICATION OF ABSTRACT	20. LIMITATION OF ABSTRACT
Unclassified	Unclassified	Unclassified	UL